

UNIVERSITÀ DEGLI STUDI DI TRENTO
DEPARTMENT OF PHYSICS
DOCTORAL SCHOOL IN PHYSICS - CONDENSED MATTER (XXV CYCLE)

Doctor Europaeus and PhD Degree Thesis

From materials science to astrophysics with electronic structure calculations

Simone Taioli

Tutor:

Prof. S. S. Saxena

Advisors:

Dr. M. Dapor
Prof. S. Giorgini
Dr. S. Simonucci

PhD committee:

Prof. D. Alfè (UCL)
Prof. M. Garavelli (ENS, Lyon)
Prof. F. Pederiva (UNITN)

*Ai miei genitori e Zsuzsanna,
grato in eterno*

“WHEN YOU HAVE ELIMINATED THE
IMPOSSIBLE, WHATEVER REMAINS,
HOWEVER IMPROBABLE, MUST BE THE
TRUTH”

Sherlock Holmes in The Sign of the Four

Acknowledgments

First and foremost, I would like to express my sincere gratitude to two friends and colleagues, dr. Maurizio Dapor and dr. Stefano Simonucci, for their continuous support to my study and research, in particular for believing sincerely in me.

The majority of the achievements and somehow good results written in this manuscript are largely due to their encouragement, guidance, patience, motivation, enthusiasm, and immense knowledge. I could not have imagined having better advisors and mentors throughout my scientific career.

Last but not least, they will always be an example of life and good ethics, a rare example of how a scientist has to behave to be an accomplished person beyond his/her work.

Besides them, the list of people and colleagues I should mention for their help and fruitful discussions tends rapidly to infinity and I would guiltily forget some of them. Thus, I just prefer to thank gratefully all of my group at the Interdisciplinary Laboratory for Computational Science (LISC) of the Center for Materials and Microsystems and colleagues at the University of Trento. Each of them have been always precious, and their encouragement, insightful comments, and hard questions have enormously contributed to this thesis. I am sure any of them could find a piece of their knowledge and time in this manuscript.

Furthermore, I am grateful to the Bruno Kessler Foundation for supporting me during my PhD course; to the University of Bologna (prof. M. Garavelli) for hosting my fellowship at the Institute of Advanced Studies; to University College London (prof. D. Alfè) and to Université Pierre et Marie Curie (dr. M. Casula) for their warm hospitality during my visit to London and Paris, respectively.

Finally, I would like to thank my family: my wife, for her beauty and truly unbelievable patience, and my parents, for supporting me in any way it is possible, even now that I am old enough, in my professional and private life.

Contents

1	Introduction	1
2	Electron spectroscopies	7
2.1	Outline of Electron spectroscopies	7
2.1.1	Electron Energy Loss Spectroscopy (EELS)	9
2.1.2	Photoelectron spectroscopy	9
2.1.3	Auger emission (AES)	11
2.1.4	Near edge X-ray absorption fine structure (NEXAFS)	12
2.2	Multichannel scattering and decay	12
2.2.1	Time-dependent vs. time-independent approach to scattering	13
2.2.2	Time-independent scheme for multichannel scattering in many-body systems	14
2.2.3	The T matrix and the Lippmann–Schwinger equation	16
2.2.4	The scattering states and cross sections	17
2.2.5	Time-dependent quantum mechanical approach	22
2.3	Spectral energy calculations	24
2.3.1	The Hartree–Fock method	26
2.3.2	Post Hartree–Fock methods	28
2.4	A new method for calculating excitation spectra	28
2.4.1	Our strategy for calculating excitation spectra in extended systems	30
2.4.2	On the use of the projection operator formalism in many-body scattering theory	31
2.4.3	Evaluation of spectroscopic quantities	34
2.4.4	Multisite correlations in CVV Auger transitions: the Cini–Sawatzky strategy	34
2.4.5	Our strategy to multisite correlations	36
2.4.6	<i>Ab-initio</i> calculation of electron spectra	37
2.5	A unified method to interpret electron spectra	42
2.5.1	Electron-Atom Elastic Scattering	43
2.5.2	Electron-Electron Interaction	45
2.5.3	The Monte Carlo Scheme	46
2.5.4	The unified method at work: Auger spectra from SiO ₂ including the energy loss	48
2.6	Conclusions	49

3	Epitaxy of SiC at Room Temperature	53
3.1	Introduction	53
3.2	The SuMBE experiment and state-of-the-art	54
3.3	Experimental findings	55
3.4	Theory and computation of SiC epitaxy: DFT, DFTB, TDDFT	62
3.4.1	Density Functional theory	62
3.4.2	Density functional tight-binding	63
3.4.3	Time-dependent DFT	63
3.5	BO-DFT simulation of the C ₆₀ -Si(111)-(7×7) collision	64
3.6	Non-adiabatic molecular dynamics	67
3.7	Conclusions	71
4	DFT vs. MBPT in carbon-based materials	73
4.1	Introduction	73
4.2	Methods beyond DFT	74
4.2.1	Methods beyond GW: excitonic effects	75
4.3	Band gap in carbon nanotubes from MBPT	77
4.4	Conclusions	82
5	Graphene: growth and functionalization	83
5.1	Introduction	83
5.2	The growth of graphene on Ni(111)	85
5.3	Tunable Gap in H-graphene	93
5.3.1	Core-Level Spectroscopy and X-ray Absorption	94
5.3.2	Angle-Resolved Photoemission	96
5.4	Electronic structure of H-graphene	100
5.5	Conclusion	109
6	ZIF for gas separation, storage and diffusion	111
6.1	Introduction	111
6.2	ZIF for gas separation	114
6.2.1	The materials studied	114
6.2.2	Potential models	115
6.2.3	Simulation of pure fluid adsorption	116
6.2.4	Simulation of mixture adsorption: selectivity	117
6.2.5	Permeance selectivity	119
6.2.6	Pure fluid isotherms	119
6.2.7	Mixture adsorption and selectivity	122
6.2.8	Dynamics of adsorbed molecules and permeation selectivity	123
6.3	Flexibility in MOF	125
6.3.1	Overview of the problem	125
6.3.2	Computational approaches	126
6.3.3	Vibrational densities of states	127
6.3.4	Barriers to diffusion of small molecules: CO ₂ and CH ₄ in ZIF-8	129
6.3.5	Barriers to diffusion of small molecules: H ₂ and CO ₂ in ZIF-7	132
6.4	Conclusions	133

7	IR spectra of Cu-resveratrol complexes	135
7.1	Introduction	135
7.2	Experimental methods	137
7.3	Theoretical and computational methods	138
7.4	Results	141
7.4.1	IRMPD spectroscopy	141
7.4.2	Theoretical results and comparison with experiments	143
7.5	Conclusions	147
7.6	Theoretical and Computational Methods	148
8	Ultra-cold Fermi gases	151
8.1	BEC-BCS crossover with contact interaction	151
8.1.1	<i>Ab-initio</i> calculation of the scattering length of alkali metals	153
8.1.2	Application of scattering theory to the solution of the Bogoliubov–de Gennes equations	155
8.2	Solution of the BdG equations	160
8.2.1	Calculation of the T matrix	160
8.2.2	Achieving self-consistency in the Bogoliubov–de Gennes equations	162
8.3	Ab-initio calculation of the multichannel T -matrix	163
8.4	Finite-range effects in the unitary limit for ${}^6\text{Li}$	163
8.5	Finite-range effects along the BEC–BCS crossover	166
8.5.1	The case of ${}^{40}\text{K}$	168
8.6	Conclusions	170
9	The half-life of ${}^7\text{Be}$ in Evolved Stars	173
9.1	Introduction	173
9.2	The electron captures on ${}^7\text{Be}$: state-of-the-art.	176
9.3	<i>Ab-initio</i> electron capture	176
9.3.1	Electronic screening	180
9.3.2	Decay rate from first principles	182
9.4	Li production and destruction	184
9.5	Conclusions	187
9.6	Transformation to relative coordinates	189
9.7	Thomas–Fermi and Debye–Hückel models	191
10	Final conclusions and future developments	193
10.1	Bird’s eye view on the achieved results	193
10.2	Visiting London for solving the puzzle of SiC growth by SuMBE	194
10.3	Ongoing work: the superconductivity puzzle of C_{60}K_3	195
10.3.1	Purpose of the visit to Université Pierre et Marie Curie	195
10.3.2	Description of the work carried out during the visit and of the results	197
10.3.3	Future collaboration with host institution	201
10.3.4	Projected publications resulting or to result from the grant	202
11	Publications	203

Chapter 1

Introduction

In the last few years, we have seen remarkable developments in two branches of condensed-matter physics. One is the study of the laws governing strongly correlated systems, notably low dimensional structures [1] and degenerate Fermi gases [2], with the growing realisation that electronic states other than simple Fermi liquids occur in several materials families. This area has been fuelled by the potential applications of materials such as high- T_c superconductors and carbon-based nanostructures to electronics, as well as by a fundamental desire to understand the ground and excited states of interacting many-fermion systems.

The other is the science of high-intensity, high-brightness synchrotron radiation sources in the soft X-ray region [3], notably the development of grazing incidence monochromators and high-resolution electron analysers [4, 5, 6], which allow unprecedented access to the investigation of optical and electronic properties of many-fermion systems with a total energy resolution considerably smaller than the width of the level investigated.

This thesis lies at the intersection between these two fields. First and foremost, we will use information from scattering experiments, notably from electron spectroscopies, in order to understand the ground and excited electronic states of systems behaving differently from a simple Fermi gas, such as graphene and carbon nanotubes. In particular, we aim at describing how the interplay between many-body scattering theories and experiments makes it possible to lay the foundation of a precise and general working model for our understanding of materials properties. This model will demonstrate its potential when further extended to take into account different conditions of temperature, from ultra-cold gases to ultra-hot plasmas, and pressures, as found in stellar environment.

Guided by our own interest in quantum collision theory, in this thesis we will consider a variety of many-body problems and describe a number of theoretical and computational approaches to electronic structure calculations within the framework of the scattering theory, ranging from classical Monte-Carlo and mean-field approaches to post-Hartree-Fock methods, from Density Functional Theories (in both Born-Oppenheimer and non-adiabatic flavors) to many-body perturbation theory. However, rather than presenting separate chapters discussing individually these methods of quantum many-body theory, we feel that it is more effective and meaningful for the reader to introduce them where required by the particular experimental technique. This description will be always accomplished by reducing the space given to well-established text-book methods in favour of the more recent and in-house developed approaches. Thus, particular emphasis will be delivered all through this thesis to benchmarking our general scattering framework against applications to realistic systems, starting from the analysis of electron spectra in a variety of materials, to the study

of ultra-cold and ultra-hot degenerate Fermi gases. In the end, we hope that this approach of mixing experiments, theory and calculations will better clarify the contribution of our work to the advancement of these techniques, be them experimental or theoretical.

In more detail, for interpreting resonant scattering processes involving many-particle systems, such as autoionisation, Auger emission, X-ray absorption and emission, plasmon excitation, or even Feshbach resonance in ultracold Fermi gases, we will extend the formal theory of scattering [7, 8] to include multichannel outcomes.

Electron spectroscopy investigations, for example, are based on scattering processes in which the initial state consists of a projectile, typically represented by a photon or an electron that collides with a target, and the final decay states are characterised by the presence of a few fragments, which asymptotically do not interact. In these processes, the system often goes through intermediate quasi-bound states having lifetimes longer than the collision times, and decay by fragmentation afterwards. The observation of the fragment types, as well as their angular and energy distribution, provides useful information on the dynamical properties of many-particle systems.

Indeed, decays are well known phenomena encountered in many physical contexts. They are usually classified in radiative, non-radiative and dissociative, if the process is accompanied or not by the emission of electromagnetic radiation and followed by dissociation. Decay processes analysed in this PhD thesis are typically radiation-less and of the latter kind, such as Auger, autoionisation, Feshbach resonances, molecular fragmentation, up to the electron capture in evolved stars. While each of these phenomena have its own peculiarities, nevertheless the common factor is the presence of the interaction with the continuum, via a resonant state, affecting the rate. The physical picture, under which all of these phenomena can be framed, is that of an intermediate, quasi-bound state produced by the initial scattering embedded in the continuum represented by one or more fragments. Correlation between the particles in the excited state is the driving force to the final decay. This is the case, for example, of the absorption spectroscopies (autoionization, XAS, NEXAFS [9]) that probe the unoccupied density of states with final electron emission to the continuum; or of beta decay in solar conditions occurring by electron capture from the continuum orbitals; or of the collision of ultra-cold alkali atoms leading to a resonant quasi-bound-state under certain conditions.

From the standpoint of theoretical modeling and computation, an ample body of time-dependent or time-independent many-body techniques was developed to study the ground state density of many-particle systems. *Ab-initio* methods, such as Hartree–Fock (HF) [10] and Density Functional Theory (DFT) [11], are mainly based on a mean-field treatment of the electron–electron repulsion, and follow the dynamics assuming that the system of electrons is always in its ground state, a situation which is far from realistic when analyzing the interaction of matter with external fields or in cluster collisions with solid surfaces. Thus, their outcomes usually need to be considerably corrected when they are applied to excited state properties, notably band gap and optical activity.

Nevertheless, theoretical and computational methods able to investigate accurately excited electronic states in solids are much less advanced. Among the most successful we mention Configuration Interaction (CI) [10], Many-Body Perturbation Theory (MBPT) [12, 13] plus Bethe–Salpeter treatment [14] to correct the self-energy for excitonic effects, and Time-Dependent Density Functional Theory (TDDFT) [15].

For a given accuracy, the computational cost of these methods, for treating both ground and excited states, scales exponentially with the number of particles and, thus, they are

often limited to a small number of atoms. This unfavorable scaling, furthermore, forces to represent the interaction between valence and core electrons by an effective pseudopotential, which considers the core electrons as frozen as they were in an isolated atom. This procedure, along with the approximate treatment of the electron correlation, compromises the accuracy and the reliability of the overall calculation and, of course, is not viable to model core-electron spectroscopy, where one has to describe the core-level energy shifts of atoms in a solid. To overcome this issue, in this thesis we present a recently developed method for calculating and interpreting electron spectra in solids. Our method does not suffer from limitations of previous approaches in treating the electronic correlation and treats bound and continuum states on the same grounds, at a cost comparable to molecules. Within this method, we further combine the theory of resonant multichannel scattering as developed by Fano [16] with a Monte Carlo treatment of the extrinsic energy loss mechanisms of the electrons on their way out of the solid. In this way we can compare our results directly to the ‘as-acquired’ experimental spectra.

While we will focus on the application of our method to the calculation of spectral properties in carbon-based materials, notably the recently discovered graphene and carbon nanotubes, our approach is sufficiently general to be applied to the analysis and interpretation of any electron spectra (XPS, autoionisation, Auger, EELS, NEXAFS) recorded from any kind of material, because its central feature is the ability of calculating wavefunctions for the continuum states.

Related, but in some ways even more puzzling, are the properties of ultracold Fermi gases, which represent the ideal playground for studying correlations within a scattering framework. In ultracold Fermi gases, the particles repel each other due to Pauli principle. Recent experimental developments [2] have opened the possibility of tuning the interaction using an external magnetic field. In this way the scattering length can be varied to values much larger than the mean interatomic distance, by forcing the system to undergo a so-called Feshbach resonance. Under these conditions, resonant scattering between two particles may occur, in which the closed bound channel becomes energetically close to the threshold of the continuum spectrum and may interact giving rise to discrete-continuum transitions. The theoretical methods used to describe this particular ‘unitary’ regime, which is a crossover between the situation of weakly paired fermions in BCS theory and strongly coupled bosons in Bose–Einstein condensation, are mainly based on Quantum Monte Carlo and mean-field approaches, notably the Bogoliubov-de Gennes (BdG) equations.

Thus, there are two ways in which scattering theory can be applied to study this regime. The first is the actual calculation of the relevant parameters describing the interaction (namely, the scattering length) from an *ab-initio* perspective. Secondly, the mean-field equations used to describe this system (that is, the Bogoliubov–de Gennes approach) can be naturally written in term of the T -matrix of the underlying potential. As we will show, many-body scattering techniques will shed a new light on the universal properties of this gas in the so-called “unitary” regime.

So far, the most used model to describe interactions or scattering in dilute Fermi gases is the contact (δ -like) potential, but this approach is questionable at unitarity because the magnitude of the interaction formally diverges. In this thesis we will analyse the mean-field approach to ultracold Fermi gases based on a contact potential and show that techniques borrowed from multichannel scattering theory can help in providing a rigorous definition of the contact potential even at unitarity, characterised by the divergence of the scattering length. Moreover, we will discuss how, in a consistent framework, the corrections due

to the finite size of the interaction potential on both the universal and the non-universal properties of various observables depend on the actual finite range of the potential. As a case-study, the self-consistent solution of the Bogoliubov–de Gennes equations in an homogeneous system of ${}^6\text{Li}$ and ${}^{40}\text{K}$ atoms at the BEC-BCS crossover with finite range interactions obtained from *ab-initio* calculations is investigated.

To appreciate further more the general nature of our theoretical framework, other than investigating materials properties, our approach to bound-continuum electronic structure will be used to explain the enrichment of Li in the Universe, a crucial problem to model the Galactic nucleosynthesis of Li that presents various puzzles to astrophysics. Our formalism goes beyond the previous ones, based on the Debye–Hückel (DH) approximation to the electronic screening, adopting a mean-field “adiabatic” approach to the scattering process. In particular, we will show how the mean field approach, combined with our treatment of the continuum channels, can be used to obtain reliable estimates for the decay rate of ${}^7\text{Be}$ in stellar conditions. Here, we only underline that the changes we find on respect to previously used approximations, in the electron density at the nucleus induce effects also on the electron screening (for p-captures on Li itself, as well as for other nuclei) so that our new approach might have rather wide astrophysical consequences.

Finally, in the ample body of applications tackled in this thesis, *ab-initio* electronic structure methods at different level of accuracy (actually including classical approaches) will be used to investigate: i) thermodynamical properties, such as adsorption and dynamics of gases in Zeolitic Imidazolate Frameworks (ZIF), ii) dynamical processes, such as barriers to diffusion of small molecules (hydrogen, carbon dioxide, and methane), in Metal-Organic Frameworks (MOF), iii) the chemical-physical mechanisms leading to the room-temperature growth of Silicon Carbide (SiC) thin films by supersonic molecular beam epitaxy technique.

The outline of this manuscript is organized as follows:

1. In chapter 2 we summarize, after a short introduction to inner shell and related spectroscopies, the basic definitions and notions of scattering theory (notably the Fano’s approach to multichannel scattering and resonant phenomena) and the standard notation of the photoionization and Auger processes. After a brief introduction to the experimental observables of interest in such investigations, we present our method for calculating *ab initio* electronic spectra in solids, including the generalization of the theory to describe the energy loss of the electrons in their way out of the solid (plasmon peak). We will present illustrative experiments and applications of photoionization, Auger and NEXAFS to the characterization of materials properties.
2. In chapter 3 we discuss both the experimental evidence and the theoretical interpretation of a new approach to the growth of Silicon Carbide (SiC) at room temperature, named Supersonic Molecular Beam Epitaxy technique (SuMBE). In particular, we will tackle the modeling of SiC epitaxy by a number of theoretical and computational tools at different level of accuracy until a reliable description of the experimental findings will allow us to gain insights into the mechanisms leading to the C_{60} cage breaking.
3. In chapter 4 we calculate spectroscopic properties of carbon-based nano-materials, discussing in particular the electronic and optical properties, such as band gap and

light absorption, in small semiconductor carbon nanotubes via a new developed many-body perturbative approach to the self-energy.

4. In chapter 5, using the model described in chapter 1 and DFT calculations we will tackle the problems of the growth of graphene by CVD on nickel, and of a possible route to open a band-gap in pristine graphene by hydrogenation for microelectronic applications, showing the insurgence of mid-gap states.
5. In chapter 6 we investigate by classical and *ab-initio* techniques the thermodynamical and dynamical properties of novel material types, i.e. Zeolitic Imidazolate Frameworks (ZIF) and Metal-Organic Frameworks (MOF). In particular, we justify the use of classical approaches for the calculation of dynamical properties in these classes of materials on respect to the *ab-initio* ones without a significative loss of accuracy.
6. In chapter 7 we use infra-red multiple-photon dissociation spectroscopy and density functional perturbation theory to investigate vibrational spectra of charged copper-resveratrol complexes.
7. In chapter 8 we investigate, by using our scattering approach, the finite-density effects on the properties of ultra-cold Fermi gases, such as gap function, critical temperature and chemical potential at the BEC-BCS crossover. We apply a new approach, going beyond the widely used contact-interaction, to study ${}^6\text{Li}$ and ${}^{40}\text{K}$ ultracold gases at the BEC-BCS cross-over.
8. In chapter 9, a novel mean-field method, however based on the scattering framework previously outlined, for calculating the electronic charge density at the nucleus in a hot plasma, as found in solar and intermediate mass stars is developed. Our method goes beyond the usual Debye-Hückel approach and will be applied in this chapter to a problem of current interest in astrophysics, that is the electron decay rate of ${}^7\text{Be}$ in evolved stars.
9. Conclusions, an overview of the activity performed during the PhD course and the on-going developments, based on a combination of the previously described electronic structure methods, for investigating other properties of interest in materials science, notably superconductivity in alkaly-doped fullerenes, are finally presented in Chapter 10.

Chapter 2

Electron spectroscopies

Since we have chosen electron spectroscopy as one of the fields of application for the theoretical methods discussed in this thesis, this chapter is intended to provide a short overview over experimental and theoretical techniques in electron spectroscopy. It will not be exhaustive as will not cover all the issues related to electron spectroscopy and the entire range of spectroscopy techniques currently available. Rather, we will provide a basic introduction to a few widely used techniques which will be considered by examples and applications, and an overview of the main theoretical issues concerning theoretical decay rates.

2.1 Outline of Electron spectroscopies

The term electron spectroscopy includes all techniques where electrons, let's call them signal electrons, are the carriers of information, with the latter obtained from analysis of the energy distribution of electrons. These techniques have found increasing application in several branches of materials science and solid state physics. Among the reasons for this success, we remember that:

1. electrons can be handled by electromagnetic fields, and hence analysed with respect to energy and angular distribution;
2. using electrostatic lenses and analysers electrons can be easily detected and counted;
3. at the typical energies involved in most electron spectroscopy techniques (below 2–3 keV), signal electrons are only emitted from a tiny layer (a few Å) beneath the surface, a feature which makes the techniques sensitive to the surface region;
4. electrons carry useful information about the electronic structure of materials and, specifically, about electronic excitations. Electron spectra are generated by recording electrons as a function of the kinetic energy. Moreover, angular resolved and time resolved spectra can be acquired;
5. signal electrons are emitted from many electron systems. Gathering the conveyed information is therefore essentially a many-body problem which, in a perturbative approach, is the study of how particle-particle interactions change the picture of non-interacting particles.

Historically, the most fruitful and widely adopted approach towards electron spectroscopy has been to understand measured spectra within the framework of a one-electron picture. This amounts to hide electron-electron interactions by introducing the concept of quasi-particle, defined as a real particle (e.g. the signal electron) dressed with its interaction with the remaining electrons in the system. Electron spectra are thus quasi-particle spectra and what we measure on them (e.g. binding energy in core-level photoemission) refers to quasi-particles. Usefulness of the approach is not only in that it keeps the familiar one-electron description, but also in that it enables one to address and to describe the great variety of many-body effects associated with electron emission. Alternatively, one could also view electron spectra as a means to learn about electron-electron interactions. In this case, it is the many-body excitation spectrum that we try to extract from measured spectra, while leaving the one-particle picture in the background.

Generally, measured electron spectra are in qualitative agreement with Hartree-Fock calculations. However, electron correlation effects are easily observed through the appearance of satellites, together with energy shifts and changes in the spectrum profile with respect to expectations from the one-electron picture.

The main effects on the spectral lineshape of the many-body interaction as probed by the scattering event are the following:

1. *Change in line widths*

In a typical atomic spectrum, line-widths range from 0.1 to 1 eV. On the contrary, in molecules or solids several vibrational levels, very close in energy, exists, so that the spectrum is characterised by the presence of vibrational progressions that can be nearly overlapping. Therefore broad lines are quite often observed, if the spectral resolution is not enough. A further source for line broadening in molecules and solids is the existence of intermediate and final states with a dissociative character.

2. *Shift in energy positions*

The energy levels of a given atom are shifted when the atom is part of a molecule or a solid. This effect, called *chemical shift*, is due to the chemical environment and it changes the kinetic energies of the emitted electrons.

3. *Change in spectral intensities*

Since the wave function of an atom in a molecule or solid is quite different from that of the isolated atom, also the intensities of spectral lines, which depend on the shape of the electronic wave functions, are substantially changed.

4. *Appearance of secondary peaks*

Electrons emitted in the primary ionisation and those emitted in the following decay process can lose their energy by colliding with atoms, electrons or other particles. This effect is particularly relevant in solids, where the probability of inelastic scattering is very high and the emitted electrons can excite plasma oscillations. The electrons, which have lost an amount of energy equal to a plasmon, produce secondary smaller peaks, while the electrons which undergo several collisions present a distribution in energy that is quite uniform apart for the low energy region where it blows up. Other satellite lines at different energies and with smaller intensities [17] are produced by *shake-up* and *shake-off* processes (or *monopole excitations*) which take place when the

primary ionisation process is accompanied by simultaneous ionisation (shake-off) or excitation (shake-up) of a valence electron. Usually these secondary processes give a global contribution to the spectrum that is of the order of 20%. Their appearance, together with the presence of perturbations, due, for example, to spin-orbit coupling in molecules containing heavy atoms or to interband effects in solids, makes the interpretation of photoemission and Auger spectra very difficult and requires the use of quantum multichannel scattering theory.

5. *Initial state effects*

In molecules or solids, spectral profiles are strongly dependent on the position of the initial hole produced in the primary ionisation, even if the final dicationic states produced by the decay process are the same. This is due to the localised character of both the intermediate electronic state and several final states of the doubly ionised system.

To fully account for electron correlation, one should not only consider the response of the surrounding electrons to the creation of signal electrons, but also the electron response to the perturbation caused by signal electrons during their way out of the solid. Many-body effects are referred to as intrinsic in the former case and extrinsic in the latter case. Intrinsic effects are only observed when signal electrons are generated inside the solid, as in the case of photoemission or Auger emission. On the other hand, extrinsic effects are best singled out when electron transport is decoupled from electron generation. This is the case of electron energy loss spectroscopy, where electrons are generated outside the solid.

2.1.1 Electron Energy Loss Spectroscopy (EELS)

If a monochromatic electron beam (probe) is sent to a solid, electrons in the beam undergo elastic and inelastic interactions, thereby changing momentum and losing energy. If the electron loses energy into a characteristic excitation of the solid, its energy is decreased by a characteristic amount from the energy of the primary beam. The EELS technique focuses on the spectrum of electrons which have undergone one or more inelastic scattering event. Distinct information is derived by considering two distinct energy ranges. For energy losses greater than ~ 50 eV, core-level excitations are possible, giving rise to characteristic features in the spectrum at threshold energies. Investigation of the energy region just above threshold probes the density of empty states in the conduction band, analogously to Near Edge X-ray Absorption Spectroscopy (see below). On the other hand, for energy losses below ~ 50 eV, electrons lose energy into interband transitions (single particle excitations) and collective excitations of valence electrons. The particle-like features of such collective excitations are emphasised by referring to them as quasi-particles, e.g. phonons and plasmons. For this range of energy losses, a many-body approach is mandatory and spectra are interpreted in terms of the statistical properties of valence electrons, represented by the energy and momentum dependent dielectric function of the material.

2.1.2 Photoelectron spectroscopy

Photoemission from atoms, molecules or solid surfaces consists in the creation, by an incident photon of energy $h\nu$, of an electron-hole pair whereby the electron is imparted

sufficient energy to be emitted from the solid. Electrons can be excited from localised core levels or from extended valence states. Denoting by E_0^N the ground state energy of an N -particle system, and by E_n^{N-1} the energy of the system after removing a particle from a single-particle-state n , conservation of energy for the photoemission process is given, within a one-electron picture, by:

$$h\nu + E_0^N = \epsilon_{kin} + E_n^{N-1} \quad (2.1)$$

The photoelectron binding energy is defined as:

$$\epsilon_b = h\nu - \epsilon_{kin} = E_n^{N-1} - E_0^N \quad (2.2)$$

where all energies are referred either to the Fermi level (more used) or to the vacuum level (less used). If, as it is sometimes the case, binding energies are referred to the Fermi level, while kinetic energies are referred to the vacuum level, the work function (vacuum barrier) W has to be introduced:

$$\epsilon_b = h\nu - \epsilon_{kin} - W \quad (2.3)$$

The one-electron-picture interpretation of this process (the so-called frozen-orbital approximation), assumes that the $N - 1$ system electrons, left behind by photoemission, remain frozen in their original ground state orbitals. The approximation amounts to disregarding electron-electron interactions, responsible for a whole range of effects:

1. relaxation of the remaining $N - 1$ electrons to screen the hole charge (core-hole relaxation): in the solid state, the process involves intra-atomic (inside the atom where the photoelectron has been created) and extra-atomic charge and leads the system to a new energy state, lower than E_n^{N-1} by an amount δE_{relax} .
2. correlation among electrons: it affects both initial and final states. Correlation is described via the so-called Coulomb hole (reduced charge density, in the electron neighbourhood, due to Coulomb interaction) and the so-called exchange hole or Fermi hole (reduced density of electrons with the same spin, in the electron neighbourhood, because of the Pauli principle). Correlation modifies the energy of both the N and $N - 1$ electron systems, with an overall effect on the binding energy described by δE_{corr} .

As a consequence, the photoelectron binding energy becomes:

$$\epsilon_b = h\nu - \epsilon_{kin} - W - \delta E_{relax} + \delta E_{corr} \quad (2.4)$$

The specific relaxation path associated with a photoemission event depends on the photoelectron kinetic energy, as well as on the electronic structure of the solid. As the photoelectron kinetic energy increases from nearly zero (at the photoionisation threshold), a continuous transition between the adiabatic and the sudden limit is observed.

For an energy of the photon close to the photoionisation threshold, the kinetic energy of the emitted photoelectron is so low that it remains in the region of the core-hole for a long time as compared to the response time of the surrounding electrons, and therefore the system has the opportunity to relax towards the new ground state of the $N - 1$ system.

For an energy of the photon much higher than the photoionisation threshold, the so-called sudden limit, the kinetic energy of the photoelectron is so high that it leaves the region of the core-hole in a short time compared to the response time of the surrounding

electrons. In this case, the hole potential is switched on instantaneously and relaxation results in excitations, either collective (phonons, plasmons) or single-particle (shake-up and shake-off processes, i.e. excitation to a bound or to a continuum state, respectively).

In general, though, the photoelectron kinetic energy depends on the energy absorbed by the excitations, giving rise to tails and satellites on the high binding energy side of the main photoelectron spectrum.

While shake processes leave the core hole in its original shell, an alternative response of the solid to the sudden creation of a core hole involves a transition of the core hole to a different shell, followed by either radiative or non-radiative decay. Non-radiative decay is known as Auger electron emission.

2.1.3 Auger emission (AES)

Auger electrons can be recorded from atoms, molecules and solids as a result of non-radiative transitions driven by the electrostatic interaction between two electrons in an atom which is singly ionised (as a consequence of photon or electron impact). Specifically, an initial state hole in, say, level a is filled by an electron from level b , thus shifting the hole from a to b . Then, autoionisation of the atom occurs with emission of an Auger electron from level c . Two holes (in levels b and c) are left in the final state. Clearly, Auger emission involves only excited states and it is, as such, a rich probe for many-electron effects. Auger transitions are designated via the three energy levels involved, using the X-ray notation (e.g. K-LL, L-MM, ...). They are also broadly categorised as core-core-core (CCC), core-core-valence (CCV), core-valence-valence (CVV), depending on whether the electronic states involved are localised core states or extended valence states. The lifetime of the initial core hole ($\simeq 10$ fs) is generally long enough, so that hole creation and decay can be considered as independent processes (two-step model for Auger emission). Within this framework, the kinetic energy of Auger electrons in one-electron picture is given by:

$$\epsilon_{kin} = E_a^{N-1} - E_{bc}^{N-2} \quad (2.5)$$

where E_a^{N-1} is the energy of the system after removing one particle from a single-particle-state a and, analogously, E_{bc}^{N-2} is the energy of the system after removing two particles from the single-particle states b and c .

Most often, the Auger kinetic energy is written, approximately, in terms of single particle binding energies:

$$\epsilon_{kin} = (\epsilon_a - \epsilon_b) - \epsilon_c \quad (2.6)$$

thus making clear that it is basically given by the difference between the energy released in the relaxation of the excited ion and the energy required to remove the Auger electron from its orbit. A correction term is then needed to account for the approximations involved in doing so. As for photoemission, many-body effects (core-hole relaxation and electron-electron correlation) shift the apparent Auger kinetic energy from the above value (see Eq. (2.5)). Therefore, corrective terms have to be introduced to reproduce measured energies. An example in this regard, proposed within the two-step model of the Auger process, is the relation:

$$\epsilon_{kin} = \epsilon_a - \epsilon_b - \epsilon_c - F_{bc} + R^{sa} + R^{sea} - W \quad (2.7)$$

where the term F_{bc} accounts for the hole-hole final state interaction (Coulomb and spin-orbit); R^{sa} , referred to as static relaxation, accounts for the response of the surrounding

electrons to emission of the Auger electron and it is atomic in origin; R^{sea} is the extra-atomic static relaxation describing the environmental contribution to the Auger energy, and W is the vacuum barrier needed, as above, in case binding energies are referred to the Fermi level while kinetic energies are referred to the vacuum level.

Equations of this kind clearly result from forcing the description of Auger emission within approximations (two-step model, single-particle picture). They nonetheless have the merit of depicting the wide range of many-body effects accompanying electron emission. As in the case of photoemission, satellites appear in Auger spectra, due to non-adiabatic relaxation. They are associated with shake processes which can occur before (initial state shake) or together (final state shake) with Auger emission, both decreasing the kinetic energy of the Auger electron. Additional satellites are associated with resonant excitation which occurs under electron impact or for photon energies around the core level ionisation threshold. In this case, creation of the core hole does not result in electron emission. Rather, the electron is resonantly excited into a bound state, so that Auger emission takes place in the presence of this localised electron (spectator Auger transition). Alternatively, the excited electron can take part in the recombination process (participator Auger transition).

2.1.4 Near edge X-ray absorption fine structure (NEXAFS)

As for photoemission, NEXAFS is based on the absorption of an X-ray photon by a core level. Differently from photoemission experiments, where the photon energy is kept fixed, in NEXAFS experiments the photon energy is scanned, thus requiring the use of synchrotron radiation sources and the absorbed X-ray intensity is measured.

Two strategies are possible in this regard. The first consists in measuring directly X-ray absorption after transmission through thin films (which requires careful sample preparation). The alternative consists in measuring X-ray absorption indirectly via detection of electrons (Auger electrons, inelastically scattered photoelectrons) generated by X-ray absorption. Such electron yield measurements, in principle possible for any kind of sample, can consider the total electron current (total electron yield, TEY), or just a part of it, e.g. only Auger electrons (partial electron yield, PEY). As the photon energy is scanned over core level absorption edges, jumps in X-ray absorption are observed in the spectrum. Focus of the technique is the energy region extending around 30 eV above the absorption edge. Here, considerable fine structure arises, associated with excitation of core level electrons into conduction band states, which makes NEXAFS a probe of the unoccupied states.

2.2 General theories of multichannel scattering and decay processes

In order to calculate *ab initio* the main parameters which characterise the scattering, one has to apply the general theory of scattering to the analysis of the transitions involved. The Hamiltonian operator may have both discrete (bound or quasi-bound states) and continuum spectrum and the system may undergo a transition through a metastable state or resonance.

The principal information that can be deduced from the analysis of a scattering experiment are: partial and total cross sections of several transitions, partial decay rates into various channels, energy levels of target and fragments to probe many-body interactions,

and total decay rate. This last quantity is the most difficult to be calculated and is related to the lifetime of the resonance or intermediate bound state. When the electronic transitions are the only possible decay paths, as in the case of atoms, the total decay is proportional to the linewidth, but, in other cases, several processes contribute to the broadening of the lines and one cannot measure directly the total decay rate of a given state.

Resonant decay states can be formed either by exciting an inner-shell electron to an empty bound orbital (autoionization [18]) or two electrons of the outermost shells to discrete states, while an Auger state [19] is created by inner-shell ionisation. Notably, Auger and autoionising states are excited, quasi-bound states embedded in the continuum of the next higher charge state of the system. They can decay either by radiation emission or by electron emission (radiationless transition). The latter decay mode is called an autoionising or Auger transition, depending on whether the excited quasi-bound state occurs in a neutral or in a core-ionised system.

Such discrete-continuum interplay is the fingerprint of the many-body interaction in scattering experiments. Scattering excitation and decay are inherently many-body processes: their theoretical analysis, considered beyond the single-particle framework, provides the opportunity to unravel the intricacies of many-body interactions.

In this section we aim at describing the theoretical methods developed for dealing with the complexity arising from this many-body interaction and finding the evidence of such interaction on the spectral properties of molecular and solid state systems. These tools can be described in both the time-independent and time-dependent frameworks [20]. While yielding physically equivalent description, we will investigate the aspects that make one approach more appealing than the other by applying the theory to a specific set of phenomena, notably dissociative attachment of water [21], core-level photoemission [22], autoionisation and Auger decay in molecular and condensed matter systems [23].

2.2.1 Time-dependent vs. time-independent approach to scattering

The goal of any theoretical method in scattering theory is the calculation of the scattering wavefunction. In order to get the measurable parameters from the Hamiltonian, notably the cross sections for different scattering experiments, the theoretical analysis may proceed through two complementary approaches:

- by considering the evolution of the scattering process in a time dependent scheme;
- by studying the currents of the stationary waves in a time independent framework.

In conventional time-independent schemes, one prepares target and probe very far each other in the remote past ($t = -\infty$) and calculates the probability that a scattering event has taken place at a time where the final part of the system are well separated by an asymptotically large distance ($t = +\infty$). In this way, a time-independent steady-state description of the scattering is obtained. In time-dependent theories, by contrast, the evolution of the wavefunction of the system is followed for a large time interval, but no extrapolation to infinity can be made. This difference already divides the application range of these two schemes.

Time-dependent approaches are more suited to describe chemical reactive collisions, where one follows the reagents and the products at any stage of the scattering, or to particle-driven chemistry, such as in photodissociation and attosecond physics, where Hamiltonians are explicitly time-dependent. Time-independent methods are better suited to describe experimental conditions where the impinging particle and the detector are at very large distance from the scattering centre, as found in electron spectroscopy.

Therefore in a time-dependent description the system is simulated in a length and time intervals characteristic of the collision process, while time-independent methods only consider the asymptotic regime of the process. These differences in the approach reflect the fact that in time-independent description of scattering the energy or momentum spread of the initial projectile is ideally zero, while it is finite in the time-dependent formulation. Following the time evolution of a wavepacket starting from some known initial conditions seems the most intuitive and natural frame for studying quantum scattering and dynamics, since this description is analogous to that obtained by classical mechanics. In fact, one can represent snapshots of such evolution at different times by plotting the probability density, which is the square modulus of the wavepacket, obtaining a close-up view on the dynamics. Furthermore, a single wavepacket evolution gives information on a finite energy region, while the time-independent approach is energy peaked, as the projectile is prepared in the remote past and the scattering detected in the remote future. This is a consequence of the fact that the relation between the time-dependent wave packet and the time-independent wave function is given by a Fourier transform.

Time-independent scattering approaches are still preferred in condensed matter applications due to the high computational cost of studying wavepacket evolution on scattering potentials of systems with many interacting degrees of freedom. In some sense, time-independent methods are preferred since the time variable has been dropped. Therefore, the numerical solution of the time-dependent Schrödinger equation has been possible only in simple cases, for small molecules, particularly in studying chemical reactions [24, 25] or electron-driven chemistry [26, 21].

2.2.2 Time-independent scheme for multichannel scattering in many-body systems

In the time-independent scheme, instead of following the evolution of the wavepacket, calculations are performed in the framework of stationary-state quantum mechanics.

We will consider only the electrons as dynamical particles, described by the Hamiltonian

$$H = -\frac{\hbar^2}{2m} \sum_{i=1}^N \nabla_i^2 + \sum_{i<j}^N \frac{e^2}{|r_i - r_j|} - \sum_{i=1}^N \sum_{k=1}^n \frac{Z_k e^2}{|r_i - R_k|} \quad (2.8)$$

where we have indicated with N the total number of electrons of mass m , identified by the coordinates r_i , and n the total number of nuclei (each with charge Z_k and identified by the coordinates R_k). In the following, we will assume that the kinetic energies of the incident particles are smaller than mc^2 and that Z_k is not too large, so that the non-relativistic formulation of quantum mechanics is appropriate.

As usual in the study of scattering processes it is useful to express the Hamiltonian (2.8) as the sum of an “asymptotic” Hamiltonian and an interaction part. The asymptotic

Hamiltonian describes the initial (or final) state of the system as a collection of non-interacting bodies. The particular set of particles that are being considered as initial (or final) state of the scattering process is generally called a *channel*.

It is important to notice that the asymptotic Hamiltonians describing the initial or final states of the system might in general be different. For example, in the Auger process, a single energetic photon interacts with a solid. Assuming the usual “two-step” description, the photon removes one core electron and, subsequently, another electron is emitted from the system. In this case, the asymptotic “in” Hamiltonian for the second step describes a ionised crystal lattice with $N - 1$ electrons, whereas the asymptotic “out” Hamiltonian describes one free electron and a crystal lattice with $N - 2$ electrons. Scattering processes are characterised by the fact that the state of the system in the infinite past can be described in the factorised form (not taking into account the antisymmetrization at the moment)

$$|\Psi_{\text{in}}\rangle = |\psi_{\text{probe}}\rangle|\Phi_{\text{target}}\rangle. \quad (2.9)$$

where $|\psi_{\text{probe}}\rangle$ is the state of the incoming probe and $|\Phi_{\text{target}}\rangle$ is the initial state of the system to be probed. The probe and the target interact according to the Hamiltonian of equation (2.8), producing a time-dependent state $e^{-iHt/\hbar}|\Psi\rangle$, where $|\Psi\rangle$ is the state of the system at a certain time. Since the state (2.9) is the asymptotic condition at $t \rightarrow -\infty$ of the actual interacting state, one has that in the $t \rightarrow -\infty$ limit the following equation holds:

$$e^{-iHt/\hbar}|\Psi\rangle = e^{-iH_{\text{in}}t/\hbar}|\Psi_{\text{in}}\rangle. \quad (2.10)$$

where H_{in} is the asymptotic Hamiltonian of the “in” channel.

This property can be used to define the Møller operator Ω_+^α relative to the incoming channel α as the operator mapping the initial state described by $|\Psi_{\text{in}}\rangle$ onto the interacting state at a certain time t , that is

$$|\Psi\rangle = \lim_{t \rightarrow -\infty} e^{iHt/\hbar} e^{-iH_{\text{in}}t/\hbar} |\Psi_{\text{in}}\rangle \equiv \Omega_+^\alpha |\Psi_{\text{in}}\rangle \quad (2.11)$$

A similar definition can be used to map the interacting state at a time t to the asymptotic out state (described the Hamiltonian H_{out}), which is also assumed to be separable, that is

$$|\Psi_{\text{out}}\rangle = |\psi'_{\text{emitted}}\rangle|\Phi'_{\text{system}}\rangle. \quad (2.12)$$

Using an argument similar to that leading from equation (2.10) to equation (2.11), one can define a Møller operator connecting the asymptotic “out” states in the channel β to the full interacting states as:

$$|\Psi'\rangle = \lim_{t \rightarrow \infty} e^{iHt/\hbar} e^{-iH_{\text{out}}t/\hbar} |\Psi_{\text{out}}\rangle \equiv \Omega_-^\beta |\Psi_{\text{out}}\rangle. \quad (2.13)$$

Given the definitions of the Møller operators, the probability of observing the outgoing state $|\Psi_{\text{out}}\rangle$ given the incoming state $|\Psi_{\text{in}}\rangle$ under the dynamics described by the Hamiltonian H of equation (2.8) is proportional to the squared modulus of the overlap between the states $|\Psi\rangle$ and $|\Psi'\rangle$, that is

$$P_{\text{in} \rightarrow \text{out}} \propto |\langle \Psi' | \Psi \rangle|^2 = \left| \langle \Psi_{\text{out}} | \Omega_-^{\beta\dagger} \Omega_+^\alpha | \Psi_{\text{in}} \rangle \right|^2. \quad (2.14)$$

The previous equation leads naturally to define the scattering matrix $S_{\beta,\alpha}$ connecting the “in” and “out” states in the channels α and β , respectively, as:

$$S_{\beta,\alpha} = \Omega_-^{\beta\dagger} \Omega_+^\alpha. \quad (2.15)$$

2.2.3 The T matrix and the Lippmann–Schwinger equation

The principal problem in multichannel scattering theory is therefore determining the matrix elements of the scattering matrix $S_{\alpha,\beta}$ as a function of the possible ingoing and outgoing channels, as well as the interaction potential V of the many-body system. In general, one is interested in the matrix elements of $S_{\alpha,\beta}$ with eigenstates of the asymptotic Hamiltonians, that is

$$H_\alpha|\Psi_\alpha\rangle = E_\alpha|\Psi_\alpha\rangle \quad (2.16)$$

$$H_\beta|\Psi_\beta\rangle = E_\beta|\Psi_\beta\rangle \quad (2.17)$$

An equation determining $\langle\Psi_\beta|S_{\beta,\alpha}|\Psi_\alpha\rangle$ can be obtained from the definition of the scattering matrix in terms of the Møller operators (see equation (2.15)), which can be rewritten as

$$S_{\beta,\alpha} = \lim_{\substack{t \rightarrow \infty \\ t' \rightarrow -\infty}} e^{itH_\beta/\hbar} e^{-itH/\hbar} e^{it'H/\hbar} e^{-it'H_\alpha/\hbar} \quad (2.18)$$

$$= \lim_{t \rightarrow \infty} e^{itH_\beta/\hbar} e^{-itH/\hbar} e^{-itH/\hbar} e^{itH_\alpha/\hbar} \quad (2.19)$$

$$= 1 - \frac{i}{\hbar} \int_0^\infty dt \left(e^{itH_\beta/\hbar} V_\beta e^{-2itH/\hbar} e^{itH_\alpha/\hbar} + e^{itH_\beta/\hbar} e^{-2itH/\hbar} V_\alpha e^{itH_\alpha/\hbar} \right) \quad (2.20)$$

where we have used the identity $f(t) = f(0) + \int_0^t dt' df(t')/dt'$ passing from equation (2.19) to equation (2.20). The matrix elements of $S_{\beta,\alpha}$ are therefore given by

$$\begin{aligned} \langle\Psi_\beta|S_{\beta,\alpha}|\Psi_\alpha\rangle &= \langle\Psi_\beta|\Psi_\alpha\rangle + \\ &\frac{1}{2}\langle\Psi_\beta|V_\beta G\left(\frac{E_\alpha + E_\beta}{2}\right) + G\left(\frac{E_\alpha + E_\beta}{2}\right)V_\alpha|\Psi_\alpha\rangle \end{aligned} \quad (2.21)$$

where we have introduced the *resolvent operator* of the full Hamiltonian H , given by

$$G(z) = (z - H)^{-1}. \quad (2.22)$$

The resolvent is not defined when z becomes one of the eigenvalues of the Hamiltonian H . In this case we will interpret equation (2.22) as the limit

$$G(z) = \lim_{\varepsilon \rightarrow 0^+} (z + i\varepsilon - H)^{-1} \quad (2.23)$$

which corresponds to write the time integral in equation (2.20) as the limit of the regularised integral

$$\int_0^\infty dt \dots \equiv \lim_{\varepsilon \rightarrow 0^+} \int_0^\infty dt e^{-\varepsilon t} \dots \quad (2.24)$$

Using the identities

$$A^{-1} = B^{-1} + B^{-1}(B - A)A^{-1} = B^{-1} + A^{-1}(B - A)B^{-1} \quad (2.25)$$

we can write an equation relating the resolvent (2.22) to the interaction potential and the resolvent $G^\alpha(z)$ of the asymptotic Hamiltonian H^α in a given channel, that is

$$G(z) = G^\alpha(z) + G^\alpha(z)V^\alpha G(z) = G^\alpha(z) + G(z)V^\alpha G^\alpha(z). \quad (2.26)$$

The operators appearing in equation (2.21) can be written as

$$G(z)V^\alpha = [G^\beta(z) + G^\beta(z)V^\beta G(z)]V^\alpha \quad (2.27)$$

$$= G^\beta(z) [V^\alpha + V^\beta G(z)V^\alpha] \quad (2.28)$$

$$\equiv G^\beta(z) T^{\beta,\alpha} \quad (2.29)$$

and

$$V^\beta G(z) = V^\beta [G^\alpha(z) + G(z)V^\alpha G^\alpha(z)] \quad (2.30)$$

$$= [V^\beta + V^\beta G(z)V^\alpha] G^\alpha(z) \quad (2.31)$$

$$\equiv T^{\beta,\alpha} G^\alpha(z). \quad (2.32)$$

where we have defined the T matrix relative to the scattering process in the α and β channels.

As a function of the T matrix, the matrix elements of the scattering operator S are given by

$$\begin{aligned} \langle \Psi_\beta | S_{\beta,\alpha} | \Psi_\alpha \rangle &= \langle \Psi_\beta | \Psi_\alpha \rangle + \left(\frac{1}{E_\beta - E_\alpha + i\varepsilon} + \frac{1}{E_\alpha - E_\beta + i\varepsilon} \right) \times \\ &\quad \langle \Psi_\beta | T | \Psi_\alpha \rangle \end{aligned} \quad (2.33)$$

$$= \langle \Psi_\beta | \Psi_\alpha \rangle - 2\pi i \delta(E_\beta - E_\alpha) \langle \Psi_\beta | T | \Psi_\alpha \rangle. \quad (2.34)$$

The T matrix satisfies an equation which can be obtained using equations (2.29) and (2.32) to give

$$T^{\beta,\alpha} = V^\alpha + V^\beta G^\beta T^{\beta,\alpha} \quad (2.35)$$

which is the Lippmann–Schwinger (LS) equation in multichannel scattering [27]. Notice that the T matrix is defined in terms of the channel potential and the resolvent of the asymptotic Hamiltonian, which is usually simpler to calculate than the full resolvent $G(z)$.

The two inequivalent definitions of the multichannel T -matrix given in equations (2.29) and (2.32) give the same matrix elements when then asymptotic states have both the same energy (on-shell scattering), as is required by the appearance of the δ function in equation (2.34).

The LS equation (2.35) can be formally resolved by the multichannel Born series as:

$$T^{\beta,\alpha} = V^\alpha + V^\beta G^\beta V^\alpha + V^\beta G^\beta V^\beta G^\beta V^\alpha + \dots \quad (2.36)$$

which has been proved to be quite useful in the context of single-channel scattering. However, in the case of multi-channel scattering, the Born series is not easily amenable of a direct solution. A much more useful approach is the one developed by Fano, described below and based on the interference between the continuum and discrete states during the scattering process.

2.2.4 The scattering states and cross sections

The LS equation can be equivalently expressed in terms of the asymptotic states. For example, using the same procedure leading to equation (2.20), one can rewrite equation (2.10)

as

$$|\Psi\rangle = \Omega_+^\alpha |\Psi_{\text{in}}\rangle = |\Psi_{\text{in}}\rangle + GV^\alpha |\Psi_{\text{in}}\rangle \quad (2.37)$$

$$= |\Psi_{\text{in}}\rangle + G^\alpha V^\alpha |\Psi\rangle \quad (2.38)$$

where we have used equation (2.26) to express the right-hand side as a function of the asymptotic propagator.

The definition of the T matrix given in equation (2.32) shows that

$$\langle \Psi_{\text{out}} | T^{\beta,\alpha} | \Psi_{\text{in}} \rangle = \langle \Psi_{\text{out}} | V^\beta (1 + GV^\alpha) | \Psi_{\text{in}} \rangle = \langle \Psi_{\text{out}} | V^\beta | \Psi \rangle \quad (2.39)$$

so that the knowledge of the scattering state $|\Psi\rangle$ allows one to calculate the matrix elements of T and therefore, from equation (6.9), the elements of the scattering matrix S . Equation (2.38) is also known as the Lippmann-Schwinger equation for the scattering state.

Many important conclusions on the structure of the scattering wavefunction can be drawn from the LS equations [8], and, for the sake of illustration, we will consider the particular case $\alpha = \beta$. Inserting a complete set of states between the operators G^α and V^α in equation (2.38), one finds out that for an incoming state (2.9) with a plane-wave having wavevector \mathbf{k} , the wavefunction of the scattering state $|\Psi\rangle$ has the form

$$\langle \mathbf{x}, \mathbf{X} | \Psi \rangle \propto \left[e^{i\mathbf{k}\cdot\mathbf{x}} \Phi_{\text{target}}(\mathbf{X}) + \sum_{\beta} f(\text{target}, \mathbf{k} \rightarrow \beta, \mathbf{k}_{\beta}) \frac{e^{i\mathbf{k}_{\beta}r}}{r} \Phi_{\beta}(\mathbf{X}) \right] \quad (2.40)$$

which is straightforwardly interpreted as the superposition of a situation where no scattering takes place (that is, the product of the incoming plane wave and the initial state of the target) with states describing an outgoing plane wave with wavevector \mathbf{k}_{β} and a corresponding state $\Phi_{\beta}(\mathbf{X})$ of the target system, each one weighted by a scattering amplitude $f(\text{target}, \mathbf{k} \rightarrow \beta, \mathbf{k}_{\beta})$. Notice that, although the overall energy is conserved during the scattering process, the target system might be left in an excited state and, consequently, the momentum of the scattered probing particle does not necessarily have the same magnitude as the momentum of the incoming particle. The derivation of equation (2.40) shows that the scattering amplitude can be written as

$$f(\text{target}, \mathbf{k} \rightarrow \beta, \mathbf{k}_{\beta}) = \langle \mathbf{k}_{\beta}, \Phi_{\beta} | V^\alpha | \Psi \rangle = \langle \mathbf{k}_{\beta}, \Phi_{\beta} | T^{\alpha,\alpha} | \mathbf{k}, \Phi_{\text{target}} \rangle \quad (2.41)$$

The differential cross section of the process through which the target goes from the initial state to state β , $d\sigma$, is then defined analogously to the elementary scattering theory as the ratio between the current flow through the solid angle Ω , that is

$$I \propto |f(\text{target}, \mathbf{k} \rightarrow \beta, \mathbf{k}_{\beta})|^2 |\mathbf{k}_{\beta}| d\Omega \quad (2.42)$$

and the incident flux

$$J \propto |\mathbf{k}| \quad (2.43)$$

where the constants of proportionality are the same in both cases, and are related to the choice of the normalisation of the incoming states. The cross section is therefore

$$\frac{d\sigma}{d\Omega} = |f(\text{target}, \mathbf{k} \rightarrow \beta, \mathbf{k}_{\beta})|^2 \frac{|\mathbf{k}_{\beta}|}{|\mathbf{k}|}, \quad (2.44)$$

with analogous expressions for the most general case $\beta \neq \alpha$.

The time-independent Fano's approach to resonant multichannel scattering

A fruitful description of the scattering wavefunction (2.38) of a many-body system – from which T -matrix elements can be obtained via (2.39) – has been put forward by Fano who developed his approach to describe the excitation spectra of molecules [16].

Fano interpreted resonant photoemissions as the result of the interaction between the intermediate metastable state created in the initial excitation and the continuum of states.

To describe the Fano's interpretation of resonant multichannel scattering theory we will assume that the incident photon beam impinging the target is energetic enough that the scattering process can be decomposed in primary photoionisation and following decay (Static Exchange Approximation [28, 29, 30]). The many-body Hamiltonian, which describes the system and its interaction with the electromagnetic field, reads in atomic units ($\hbar = m = e = 1$) [31]:

$$\hat{H}(1, \dots, N) = \sum_{i=1}^N [\hat{T}(i) + \hat{V}^{en}(i)] + \frac{1}{2} \sum_{i \neq j}^N \hat{v}(i, j) + \frac{1}{c} \sum_j \mathbf{A}(\mathbf{r}_j, t) \cdot \mathbf{p}_j \quad (2.45)$$

$$= \hat{H}_0 + \hat{V}_{ee} + \hat{H}_{int} = \hat{H}_s + \hat{H}_{int} \quad (2.46)$$

where

$$\mathbf{A} = A_0 \mathbf{e}(e^{i(\mathbf{k} \cdot \mathbf{r} - \omega t)} + \text{Hermitean conjugate}) \quad (2.47)$$

is the vector potential in Coulomb gauge $\nabla \cdot \mathbf{A} = 0$ [32] and

$$\hat{T}(i) = -\frac{1}{2} \nabla_i^2; \quad \hat{V}^{en}(i) = \sum_{\mu} \frac{Z}{|\mathbf{r}_i - \mathbf{R}_{\mu}|}, \quad \hat{v}(i, j) = \frac{1}{|\mathbf{r}_i - \mathbf{r}_j|}, \quad \mathbf{p}_j = -i \nabla_j. \quad (2.48)$$

In Eqs. (2.46) and (2.48), \hat{H}_0 is the free Hamiltonian, containing the electron kinetic energy \hat{T} and the electron-nuclei interaction \hat{V}^{en} , $v(i, j)$ is the electron-electron repulsion, \hat{H}_{int} is the coupling or dipolar operator, H_s is the system total Hamiltonian and \mathbf{p}_j is the electron momentum. The resonant multichannel scattering theory [33, 34, 31, 35, 36] aims to find positive energy solutions of the Hamiltonian (2.46):

$$(\hat{H} - E) |\Psi_{\alpha, \epsilon}^{-}\rangle = 0 \quad (2.49)$$

where the scattering wavefunction $|\Psi_{\alpha, \epsilon}^{-}\rangle$ describes the motion of a particle with kinetic energy $\epsilon_{\alpha} = E - E_{\alpha}$, asymptotically not interacting with the scattering centre in the state Θ_{α} at energy E_{α} . The final channels $|\Psi_{\alpha, \epsilon}^{-}\rangle$ are thus classified according to the quantum numbers α of the single (autoionisation) or double (Auger) ionised system and kinetic energy ϵ_{α} of the released fragments. Defining the initial state wavefunction $|\Psi_0\rangle$ of the system, usually assumed in the ground state, the goal of our analysis will be to assess the transition probability:

$$T_{0 \rightarrow \alpha, \epsilon} = 2\pi \left(\frac{A_0}{c} \right)^2 |\langle \Psi_{\alpha, \epsilon}^{-} | \mathbf{e} \cdot \mathbf{p} e^{i\mathbf{k} \cdot \mathbf{r}} | \Psi_0 \rangle|^2. \quad (2.50)$$

Furthermore, in photoemission and Auger spectroscopy, emitted electrons are collected in detectors at large distance from the target. Their asymptotic state are conveniently normalised according to the *incoming wave* boundary conditions: [33]

$$\psi(r \rightarrow \infty) \simeq \sum_{\gamma=1}^{N_e} \frac{\Omega_{\gamma}}{2ir} \sqrt{\frac{2}{\pi k_{\beta}}} (\delta_{\gamma\alpha} e^{+i\theta_{\gamma}} - S_{\gamma\alpha} e^{-i\theta_{\gamma}}) \quad (2.51)$$

where θ_γ is the phase shift for long range Coulomb interactions, $k_{\alpha\gamma}$ is the electron momentum and Ω_γ are symmetry adapted wave functions of the ionised target. In Eq. (2.51) the asymptotic behaviour of the wave function is characterised by the scattering matrix S , whose element $S_{\gamma\alpha}$ gives the probability amplitude for the emission of one electron into channel γ . Using this representation of the final state wavefunction, Fano explained the observation of anomalous line shapes (Fano profiles) as due to the interference between the direct ionisation channel and the resonant path. Therefore, Fano's configuration-interaction theory remains one of the clearest example of the many-body interaction fingerprint on spectral properties. In Fano's approach the scattering wavefunction $|\Psi_{\alpha,\epsilon}^- \rangle$ is obtained by linear combining the discrete quasi-bound state $|\Phi \rangle$, excited by the scattering of the impinging beam, with the continuum many-body channels of the ionised target, $\{|\chi_{\beta,\epsilon}^- \rangle\}$, chosen to fulfill the asymptotic condition (2.51):

$$|\Psi_{\alpha,\epsilon}^- \rangle = a_\alpha(\epsilon)|\Phi \rangle + \sum_{\beta=1}^{N_c} \int_0^\infty |\chi_{\beta,\tau}^- \rangle C_{\beta,\alpha}(\tau, \epsilon) d\tau \quad (2.52)$$

where ϵ is the escaping electron kinetic energy. The decay channels $\{|\chi_{\beta,\epsilon}^- \rangle\}$ interact via the many-body Hamiltonian

$$\langle \chi_{\beta\epsilon'}^- | H - E | \chi_{\alpha\epsilon}^- \rangle = (\epsilon + E_\alpha - E) \delta(\epsilon' + E_\beta - \epsilon - E_\alpha) \delta_{\beta\alpha} + V_{\beta\alpha}(\epsilon, \epsilon', E). \quad (2.53)$$

The scattering problem is therefore reduced to the calculation of the expansion coefficients $a_\alpha, C_{\beta,\alpha}$ in Eq. (2.52), which can be obtained from equation (2.49) as the solution of the set of equations

$$\langle \Phi | H - E | \Psi_{\alpha,\epsilon}^- \rangle = \langle \chi_{\beta,\epsilon}^- | H - E | \Psi_{\alpha,\epsilon}^- \rangle = 0. \quad (2.54)$$

By using the Dirac technique for treating the singularities which appear in the definitions of the coefficients $\{a_\alpha, C_{\beta\alpha}\}$, the scattering wavefunction is finally written as:

$$|\Psi_{\alpha,\epsilon}^- \rangle = |\chi_{\alpha,\epsilon}^- \rangle + \frac{M_\alpha^-(\epsilon, E)}{E - E_r - i\frac{\Gamma}{2}} \left[|\Phi \rangle + \lim_{\nu \rightarrow 0} \sum_{\beta} \int_0^\infty \frac{|\chi_{\beta,\tau}^- \rangle M_\beta^-(\tau, E)^*}{E - E_\beta - \tau - i\epsilon} d\tau \right] \quad (2.55)$$

while $M_\beta^-(\epsilon_r, E)$, Γ , and E_r are respectively:

$$M_\beta^-(\epsilon, E) = \langle \Phi | H - E | \chi_{\beta,\epsilon}^- \rangle \quad (2.56)$$

$$\Gamma = \sum_{\beta} \Gamma_\beta = 2\pi \sum_{\beta} |M_\beta^-(\epsilon_r, E)|^2; \quad \epsilon_r = E_r - E_\alpha \quad (2.57)$$

$$E_r = \langle \Phi | H | \Phi \rangle + \Delta; \quad \Delta = \sum_{\beta} \mathcal{P} \int_0^\infty \frac{|M_\beta^-(\tau, E)|^2}{E - E_\beta - \tau} d\tau. \quad (2.58)$$

By knowing the stationary state $\{|\Psi_{\alpha,\epsilon}^- \rangle\}$ one can obtain the cross section of multichannel scattering processes from the state α into channel β by squaring the transition matrix. If the direct term is negligible in comparison to the resonant excitation, the cross section reduces to the Breit–Wigner cross section [37].

The concept of autoionisation and Auger effect as resonant multichannel scattering

The calculation of photoemission (or autoionisation) and Auger cross sections is a straight application of Fano's multichannel resonance approach [34, 16, 38]. In the former case, the differential cross section for a ionisation process in which the target in the ground state $|\Psi_0\rangle$ is ionised by a linearly polarised, monochromatic photon beam at frequency ω , can be evaluated by:

$$T_{fi}(\epsilon) = \langle \chi_{\alpha,\epsilon}^-; N-1, \omega | \hat{H}_{int} | \Psi_0; N, \omega \rangle + \frac{\langle \chi_{\alpha,\epsilon}^- | \hat{H}_s - E | \Phi \rangle \langle \Phi^-; N-1, \omega | H_{int} | \Psi_0; N, \omega \rangle}{\epsilon - \epsilon_r + i\frac{\Gamma}{2}} \quad (2.59)$$

where:

$$|\Phi^-\rangle = |\Phi\rangle + \lim_{\nu \rightarrow 0} \sum_{\beta=1}^{N_c} \int_0^\infty \frac{|\chi_{\beta,\tau}^-\rangle M_\beta^-(\tau, E)^*}{E - E_\beta - \tau - i\varepsilon} d\tau; \quad \epsilon = \omega - (E_\alpha - E_0). \quad (2.60)$$

The first term in the right hand side of Eq. (2.59) represents the direct electron emission, while the resonant formation of inner-shell vacancies is described by the second term. By neglecting the direct contribution, the cross section of the process is:

$$\frac{d\sigma_{fi}(\epsilon)}{d\epsilon} = \frac{4\pi^2\omega}{N_c} |T_{fi}(\epsilon)|^2 = \sigma(\omega) \frac{1}{2\pi} \frac{\Gamma_\alpha}{(\epsilon - \epsilon_r)^2 + \Gamma^2/4} \quad (2.61)$$

where $\sigma(\omega) = \frac{(2\pi)^2\omega}{N_c} |\langle \Phi^-; N-1, \omega | H_{int} | \Psi_0; N, \omega \rangle|^2$ is the cross section for the excitation process $|\Psi_0\rangle \rightarrow |\Phi\rangle$. The probability amplitude for the resonant ionisation is therefore distributed according to a Lorentzian profile peaked at ϵ_r , in which the width Γ_α and Γ represent weakly energy dependent partial and total decay rates. If the energy of the incident beam is such that the direct term cannot be neglected, autoionising states interfere with the direct ionisation path. In this case Lorentzian distributions with characteristic half-widths are substituted by asymmetric probability distributions (Fano profiles). The description of an autoionisation process is still valid for an Auger process, the only difference being that in the latter the resonant metastable state is single ionised while the continuum is represented by a linear combination of double-ionised states. For this process the T matrix is thus the following:

$$T_{\alpha i} = \langle \chi_{\alpha,\epsilon_1\epsilon_2}^-; N-1, \omega | \hat{H}_{int} | \Psi_0; N, \omega \rangle + \int_0^\infty \frac{\langle \chi_{\alpha,\epsilon_1\epsilon_2}^- | \hat{H}_s - E | \Phi_\tau \rangle \langle \Phi_\tau; N-1, \omega | H_{int} | \Psi_0; N, \omega \rangle d\tau}{\epsilon_1 + \epsilon_2 - \epsilon_r - \tau + i\Gamma/2}$$

where $\epsilon_{1,2}$ are the photoemitted and Auger electron kinetic energies related by the energy conservation relation, $\epsilon_1 + \epsilon_2 = \omega - (E_\alpha - E_0)$. When the incident beam energy is such that $\omega \gg E_\alpha - E_r$, the intermediate metastable state $|\Phi_\tau\rangle$ can be approximated by the antisymmetrized product $\hat{A}\{|\Phi\rangle|\tau\rangle\}$ of the ket of the photoemitted electron $|\tau\rangle$ and of the ionised target. Neglecting the direct double-ionisation process (first terms in the right-hand side of Eq. (2.62)), the Auger cross section is:

$$\frac{d\sigma_\alpha(\epsilon)}{d\epsilon} = \sigma(\bar{\epsilon}) \frac{1}{2\pi} \frac{\Gamma_\alpha}{(\epsilon - \epsilon_r)^2 + \Gamma^2/4}; \quad \bar{\epsilon} = \omega - (E_r - E_0) \quad (2.62)$$

where $\sigma(\bar{\epsilon})$ is the photoionisation cross section, Γ_α and Γ are still interpreted as the partial and total Auger non-radiative decay rates.

2.2.5 Time-dependent quantum mechanical approach

In time-dependent scattering approaches one interprets differential cross sections in terms of the scattering of a plane wave packet, which is prepared with a finite spread of momenta (or energies) at a distance R from the target such that the interaction potential can be neglected (typically 10 – 20 a.u.):

$$|\Psi_I(t)\rangle = \int d^3\mathbf{p} a(\mathbf{p}) \exp[-iE(\mathbf{p})t/\hbar]|\mathbf{p}\rangle \quad (2.63)$$

where $\int |a(\mathbf{p})|^2 d^3\mathbf{p} = 1$ for a wave packet describing a single particle. Under these conditions, the free non-relativistic time evolution of the wave-packet before and after scattering is determined by the Hamiltonian $H_0 = \mathbf{p}^2/2m$. Assuming that the spread in $\mathbf{p} = \mathbf{p}_0 + \Delta\mathbf{p}$ is large enough to localise the initial positions of the collision partners but such that the variation of $a(\mathbf{p})$ in Eq. (2.63) has a negligible effect on the calculated quantities when compared to experiments ($\partial^2 E/\partial^2 p \simeq 0$), the wave packet behaves like a rigid body (modulo an insignificant phase factor) having a well defined velocity $\partial E/\partial p|_{p_0}$. The condition for the validity of this approximation is $\delta = R\lambda/(\Delta R)^2 \ll 1$ where $\lambda = \hbar/p_0$ is the reduced de Broglie length and ΔR being the space extension of the wavepacket. Such a condition is normally satisfied in the usual operating conditions of nuclear and atomic collisions, as R is a macroscopic quantity (typically $R = 10^2$ cm), while $\Delta R = 10^{-1}$ cm and $\lambda = 10^{-8}$ cm (corresponding to an electron of 10 eV, typically of the order of an hydrogen atom). In this case $\delta \simeq 10^{-4}$. In nuclear collisions δ is usually of the order of 10^{-9} since $\lambda = \hbar c/(2Emc^2)^{1/2}$ and $\hbar c = 200$ MeV fm, but even for thermal neutrons $\delta \simeq 10^{-5}$ as $E \simeq 0.025$ eV. Notably, while a spatial spreading of the wavepacket will occur during the free evolution, immediately out of the scattering region, velocity will force all momentum components to leave the source and reach the scattering centre. In the scattering region, where the interaction potential between target and projectile is not negligible, the wavepacket evolves in time according to the scattering potential. Depending on the scattering mechanisms under investigation, the wavepacket may disappear (absorbing potential) or decay (complex potential) into different final channels. To extract the observables of the system, notably the differential cross section, and find the connection with the time-independent view, the wavepacket evolution can be mapped directly onto a set of plane waves of given momentum.

Collecting the wavepacket in the final asymptotic state means to project it onto a particular state $|\beta\rangle$. The probability amplitude of finding the state $|\beta\rangle$ when we have prepared the system in the initial state $|\alpha\rangle$ is given by

$$S_{\alpha\rightarrow\beta} = \lim_{t\rightarrow\infty} \langle\beta|\psi_I(t)\rangle = \langle\beta|\Omega_+^- \Omega_+|\alpha\rangle \quad (2.64)$$

since $|\psi_I(0)\rangle = \Omega_+ \psi_I(-\infty) = \Omega_+|\alpha\rangle$.

Wave-packet propagation in the excited states

The time evolution of a quantum mechanical system is ruled by the time-dependent Schrödinger equation (TDSE)

$$i\hbar\partial/\partial t\Psi(t) = \hat{H}\Psi(t) \quad (2.65)$$

where H is the N -body Hamiltonian of the system. Eq. (2.65) is a first-order differential equation in the time variable, which can be solved once an initial condition is fixed. In this sense, time-dependent approaches deal with initial values problems and propagate the wavefunction in time, while the time independent picture faces the diagonalization of the Hamiltonian. Any time-dependent wavepacket approach involves the following three steps:

1. generation and representation of the initial wavepacket
2. propagation of the wavepacket until the end of the dynamical event
3. analysis of the final wavepacket

The representation of the initial wavefunction is usually performed by the Discrete Variable Representation (DVR) [39, 40, 41], in which the initial wavefunction is expanded in a basis of orthonormal functions with time-dependent coefficients:

$$\Psi(x, t) = \sum_i^N a_i(t) \phi_i(x) \quad (2.66)$$

and a quadrature rule is employed to discretize the continuous variables on a point grid. Alternatively, a Fast Fourier Transform (FFT) basis can be used to expand the wavefunction [42, 43, 44, 45]. The differences among the methods developed in time-dependent approaches are mainly in the time propagation stages. Second-order difference scheme [46], split-operator method [47, 48], Chebyshev polynomial expansion method [49], Lanczos recursion scheme [50] are the principal methods used over the years to follow the dynamics of the wavepacket on a many-body potential. The whole of these methods usually performs very well within the Born–Oppenheimer approximation, where the coupling between different electronic states is weak. Unfortunately, in many processes, such as molecular dissociation or photo-excitation, one has to go beyond this approximation due to the crossing at some distance of the potential curves. The idea is to use multi-configurational time-dependent wavefunctions approximated by a number of Hartree products [51]. In this way one can take into account more accurately the correlation among different electronic levels and solve the time-dependent Schrödinger equation by a variational method, leading to a set of coupled equations for the electronic levels used to build the multi-configuration wavefunction.

In the adiabatic representation of the TDSE, the potential energy operator is diagonal and the kinetic energy operator is not. The opposite situation characterises the diabatic representation. In the diabatic representation $\psi_{1,2}$ therefore the TDSE reads

$$i\hbar \frac{\partial}{\partial t} \begin{pmatrix} \psi_1(t) \\ \psi_2(t) \end{pmatrix} = \left\{ \begin{pmatrix} \hat{T}_1(R) & 0 \\ 0 & \hat{T}_2(R) \end{pmatrix} + \begin{pmatrix} \hat{V}_{11} & \hat{V}_{12} \\ \hat{V}_{21} & \hat{V}_{22} \end{pmatrix} \right\} \begin{pmatrix} \psi_1(t) \\ \psi_2(t) \end{pmatrix} \quad (2.67)$$

where \hat{T}_1 and \hat{T}_2 are the kinetic energy operators for nuclear motion on surface 1 and 2, respectively, and V_{ij} are the potential energy matrix elements in the diabatic basis, where the potential energy curves do not touch anywhere. The perturbation arising from the electronic coupling is given by the off-diagonal terms in the potential matrix. The time evolution on the coupled electronic states in the diabatic representation is performed at any point of the spatial grid by using different propagation schemes, such as Lanczos or

Chebyshev, depending upon the nature of the nonadiabatic dynamics or by a wave packet perturbation theory [52], in which the adiabatic Hamiltonian is divided into a perturbed and unperturbed part and the recursive integral equation for the time-evolution operator is solved. A similar approach based on a Chebyshev recursion relation has been used by Taioli and Tennyson [21, 53] to calculate the dissociative attachment of water on the complex triatomic potential of the X^2B_1 resonance state of the water anion, which is known to be dissociative for a kinetic energy of the impinging electron equal to 6.4 eV. In this case, the complex potential forces the system to decay into channels different from those reached via the initial excitation and the coupling between the resonant and the ground electronic level is caused by the nuclear kinetic term. The real and imaginary part of the wavepacket are evolved by using an efficient Chebyshev recursion scheme, which allows to use a large time step. A plot of the density evolution on the X^2B_1 excited state of water at different time snapshots, starting from the roto-vibrational ground state of water, is reported in Fig. 2.1 and shows the wavepacket dissociation in $\text{OH} + \text{H}^-$ along the Jacobi radial coordinates in about 21 fs.

2.3 Calculation of the spectral energy in electron spectroscopy

One of the central problems of calculating spectral properties is the accurate quantum-mechanical treatment of the electronic structure of the target system. For example, the kinetic energy of an Auger electron (ϵ_A) emitted into the channel α has to be calculated as the difference between the energy (E_Φ) of the intermediate resonant state $|\Phi\rangle$ and the energy (E_α) of the final state $|\alpha\rangle$ of the doubly ionised target: $\epsilon_A = E_\Phi - E_\alpha$.

In order to follow this approach, one has to calculate the electronic excited states of systems. Specifically to condensed matter applications, methods based on Density Functional Theory [11] are not applicable since they are rigorously valid only to study the ground state.

Recently, new methods, notably time-dependent density functional theory (TDDFT) [54], many-body perturbation theory [13, 12], density matrix Renormalization group [55, 56, 57, 58, 59, 60, 61] have been developed to investigate the dynamics of many-body systems in the presence of time-dependent potentials, such as electric or magnetic fields.

The most accurate approaches to the calculation of excited states are still the methods derived from quantum chemistry, such as Configuration Interaction (CI) and Green's function based approaches [10], which goes beyond a mean-field treatment of the electron-electron interaction. These have been extensively used to predict absorption spectra and Auger energies and the results are generally in fairly good agreement with the experimental data [62, 63, 22, 64]. However, the range of application of such methods has been limited to the simulation of simple atomic and molecular spectra by the unfavorable computational scaling, in terms of both computational time and memory, to reach the chemical accuracy (below 0.05 eV).

In this section we will briefly summarise the main features of a few methods proposed for calculating bound and excited state energies, based on the use of one-configuration wave function (HF method) and those based on the use of multi-configuration wave functions (CI). In chapter 3 a short introduction to methods based on many-body perturbation techniques [65, 66] will be provided. Finally we will present a recently implemented theo-

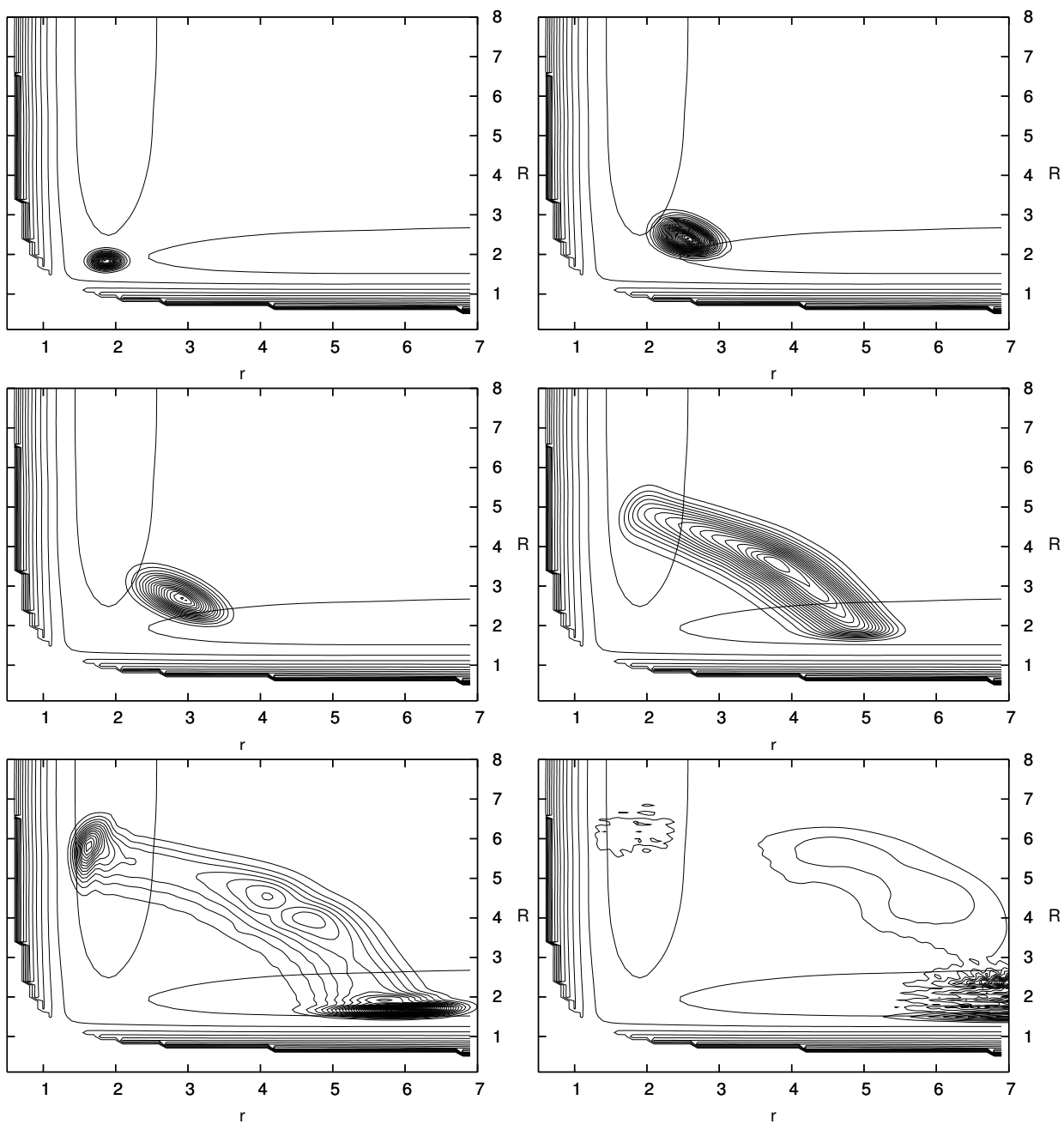


FIGURE 2.1: Time snapshots of the wavepacket evolution from the rovibrational ground state of water on the X^2B_1 excited state, whose square real part is plotted on the figures.

retical method for calculating excitation spectra, able to deal with the complexity arising in condensed matter applications at a computational cost similar to that of molecules.

2.3.1 The Hartree–Fock method

The aim of this method is to construct the wave function that minimises the electronic energy in the space of one-configuration wavefunctions. For closed-shell systems this function is a single Slater determinant of spin-orbitals, while for open-shell systems is a linear combination of few Slater determinants having a correct spin treatment and spatial symmetry. The search for an energy minimum with orthonormality constraints among occupied and virtual orbitals leads to a family of coupled differential equations for the orbitals $\{\phi_j\}$ appearing in the Slater determinant. These equations are non linear and, for a closed shell, can be decoupled [10] to give

$$\hat{F}|\phi_j\rangle = (\hat{h} + \hat{G})|\phi_j\rangle = \epsilon_j|\phi_j\rangle \quad (2.68)$$

where \hat{F} is the HF operator, \hat{h} its one-electron part and \hat{G} the effective potential due to the other electrons:

$$\hat{h} = -\frac{1}{2}\nabla^2 + \sum_l^{nuclei} \frac{Z_l}{|\mathbf{r} - \mathbf{R}_l|} \quad (2.69)$$

$$\hat{G} = \sum_j^{occ} (2\hat{J}_j - \hat{K}_j). \quad (2.70)$$

In Eq. (2.70) \hat{J}_j and \hat{K}_j are, respectively, the Coulomb and exchange operators defined in terms of the orbital ϕ_j by the matrix elements

$$\langle\phi_i|\hat{J}_j|\phi_m\rangle = \int dr_1 dr_2 \phi_i(r_1)\phi_j(r_2) \frac{1}{|r_1 - r_2|} \phi_m(r_1)\phi_j(r_2) \quad (2.71)$$

$$\langle\phi_i|\hat{K}_j|\phi_m\rangle = \int dr_1 dr_2 \phi_i(r_1)\phi_j(r_2) \frac{1}{|r_1 - r_2|} \phi_j(r_1)\phi_m(r_2). \quad (2.72)$$

In case of open shell systems the problem is complicated by the fact that not all the orbitals are doubly occupied and, therefore, the HF equations cannot be decoupled through unitary transformations among the occupied orbitals, as in the case of a closed shell. Several procedures have been proposed to solve the HF equations, for both closed and open shell systems, and they are summarised in Ref. [67].

In order to give an idea of the quality of the Auger energies obtainable using the HF method, we compare in Tab. 1 the HF values, calculated by Kelly [68] for the Auger spectrum of the Ne atom, with those obtained using the CI method and with the experimental results [69]. As one can see, the largest discrepancies between Hartree–Fock energies and experimental data are of the order of 2 eV, a value that one has to compare with energies of order of 800 eV and differences between energies of the order of 30 eV. This error is small in percentage, but can be too large for the assignment of the spectral lines when several transitions are close in energy. A similar comparison between HF and CI energies is performed in Tab. 2 for a different system, the H_2O molecule [70, 71]. In this case the calculated values cannot be compared with the experimental energies since the assignment of the Auger transitions in the experimental spectrum [72] is not very clear. However, also

TABLE 1: Hartree–Fock and CI transitions energies for the Auger decay process from the state (${}^2S : 1s^{-1}$) of the Neon, calculated by Kelly [68] and compared with the experimental values (E_{expt}) [69]. All the quantities are given in eV.

State	E_{HF}	E_{CI}	E_{expt}
${}^1S (2s^{-1}2s^{-1})$	746.99	748.15	748.0 ± 0.1
${}^1P (2s^{-1}2p^{-1})$	770.86	771.71	771.4 ± 0.1
${}^3P (2s^{-1}2p^{-1})$	783.01	782.45	782.0 ± 0.1
${}^1S (2p^{-1}2p^{-1})$	800.97	801.27	800.4 ± 0.1
${}^1D (2p^{-1}2p^{-1})$	806.04	804.51	804.2 ± 0.4

TABLE 2: Hartree–Fock and CI transition energies for the Auger decay process from the (${}^2A : 1a_1^{-1}$) state of the H_2O molecule, calculated by Ågren *et al.* [70]. All the quantities are given in eV.

State	E_{HF}	E_{CI}
${}^1A_1 (2a_1^{-2})$	451.45	458.31
${}^1A_1 (2a_1^{-1}3a_1^{-1})$	473.46	472.06
${}^3A_1 (2a_1^{-1}3a_1^{-1})$	480.66	483.48
${}^1B_2 (2a_1^{-1}1b_2^{-1})$	467.26	467.57
${}^3B_2 (2a_1^{-1}1b_2^{-1})$	478.83	476.57
${}^1B_1 (2a_1^{-1}1b_1^{-1})$	474.02	475.66
${}^3B_1 (2a_1^{-1}1b_1^{-1})$	482.14	482.14
${}^1A_1 (3a_1^{-2})$	496.40	494.55
${}^1B_2 (3a_1^{-1}1b_2^{-1})$	493.79	492.14
${}^3B_2 (3a_1^{-1}1b_2^{-1})$	496.35	494.42
${}^1B_1 (3a_1^{-1}1b_1^{-1})$	499.57	497.96
${}^3B_1 (3a_1^{-1}1b_1^{-1})$	502.62	500.67
${}^1A_1 (1b_2^{-2})$	488.32	487.39
${}^1A_2 (1b_2^{-1}1b_1^{-1})$	495.72	494.42
${}^3A_2 (1b_2^{-1}1b_1^{-1})$	497.74	496.37
${}^1A_1 (1b_1^{-2})$	500.77	499.39

in this case one can see that, the differences between Hartree–Fock and CI energies are of the order of $2 \div 3$ eV, apart for the transition to the $^1A_1(2a_1^{-2})$ state, where the difference is of about 7 eV.

Finally, one should remember that, for energy calculations on heavy atoms, the usual electrostatic Hamiltonian is no longer appropriate and other terms, obtained from relativistic quantum theory and due to the coupling among spin and orbital angular momentum of electrons and nuclei, have to be taken into account. For a general review on this subject see Ref. [67].

2.3.2 Post Hartree–Fock methods

Configuration interaction method

From the solution of the Hartree–Fock equations one obtains, in principle, a complete set of orbitals among which the lowest in energy are chosen to construct the one-determinant wave function that represents the ground state of the system. In order to improve the quality of this representation, one can add to the HF wavefunction other Slater determinants, built with HF excited state orbitals. Using all the orbitals of a complete set, one gets, in principle, an exact expansion of the wave function, but the rate of convergence is very slow since many Slater determinants are necessary to obtain an energy more accurate than the HF one.

The process of including other configurations to minimise the energy is known as Configuration Interaction method (CI) and it is based on the diagonalization of the Hamiltonian matrix whose elements, $H_{jl} = \langle \Phi_j | H | \Phi_l \rangle$, are constructed using Slater determinants $\{\Phi_j\}$. The eigenvalues of this matrix represent upper bounds to the exact energies of ground and excited states of the system. The quality of the results can be improved by their extrapolation through perturbative approaches.

CI calculations have been carried out by Kelly [68] - see Tab. 1 - to interpret the Auger spectrum of the Ne atom and by Ågren [70] - see Tab. 2 - for the Auger spectrum of the H_2O molecule. CI calculations are shown to improve the accuracy of the theoretical predictions, usually making them consistent with experimental results.

2.4 A unified method for calculating excitation spectra in solids

Over the last few years it has become possible to obtain electron spectra with a total energy resolution (monochromator plus electron spectrometer) considerably smaller than the linewidth of the core/valence-hole level investigated [73]. This fact allows the accurate determination of the intensity distribution also for those transitions which are split into a large number of sub-levels due to the coupling of the emitted electrons with spectator electrons, with the nuclear motion (in the case of molecules) and with plasmons (in the case of nanoclusters and solids).

Therefore, it is now possible to measure the combined effects of the intrinsic and extrinsic dynamical properties of the system on the spectral lineshape. For a quantitative interpretation of electron spectra recorded on solids, problems mainly arise in the accurate treatment of the electronic correlation, in the localisation of the electron emission, in the

degree of localisation over the entire valence band of the Auger process, and in the energy losses suffered by the electrons in their way out of the solid.

Recently, Taioli and coworkers proposed a unified theoretical method for calculating electron spectra in solids [62]. This method provides an extension of Fano's resonant multi-channel scattering, allowing the construction of the continuum wavefunction of the emitted electron with appropriate boundary conditions, accurately including the main correlation effects, and treating the extrinsic electron energy losses with the surrounding electronic cloud. Within this approach, the general theoretical framework for interpreting electron spectra can be summarised as a three-steps procedure: firstly, a minimum-size cluster embedded in the solids is identified. This cluster is chosen to be large enough to include the range of interactions of interest in electron spectroscopies and to reproduce the electronic structure of the system. The effect of the electron bath, in which the cluster is embedded, is treated by using an inexpensive mean-field approach. Secondly, first-principle calculations are used to obtain transition energies and intensities. Finally, Monte Carlo is used to simulate the effect of inelastic losses on the original line-shape [62, 64]. With the last step, the calculated intrinsic spectrum is convoluted with the spectrum of extrinsic losses, so that it can be directly compared to the 'as-acquired' experimental spectrum [74, 75].

At variance with Fano's theory, several intermediate quasi bound states and many interacting decay channels can be included in our calculations. Moreover, shake processes, electron-hole and hole-hole interactions are considered without semiempirical parameters such as those appearing in Hubbard-like models [76, 77, 78]. The steps undertaken by this theoretical method are summarised in Fig. 2.2.

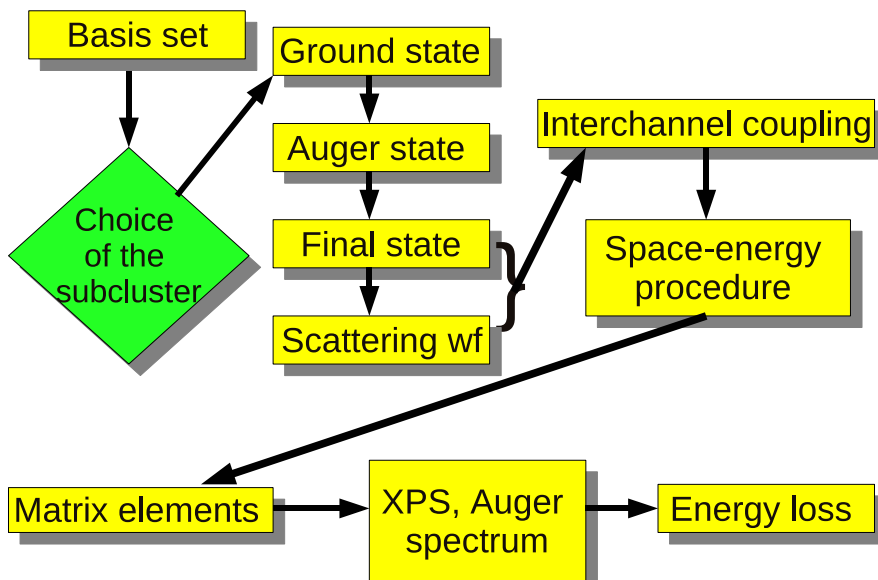


FIGURE 2.2: Structure of the quantum mechanical/Monte Carlo method for calculating excitation spectra.

2.4.1 Our strategy for calculating excitation spectra in extended systems

The bottleneck of many *ab-initio* approaches to scattering for condensed matter applications is the size of the functional space used to represent the wavefunctions, be them plane waves or Gaussians. Furthermore, the larger the extension of the system, the bigger the number of coupled decay channels. Fortunately, electron correlations have a range of a few atomic diameters and this allows one to use a reasonably small number of atoms to calculate the properties of matter. This is particularly true for core-electron spectra, which are affected only by the local density of states. There are two ways of reducing the functional space: the supercell method, in which the chosen cluster of atoms is surrounded by periodically repeated self-images, or the cluster method, whose size is increased until the properties of interest (spectroscopic observables in our case) cease to vary.

Our method follows the latter approach. Inside the cluster, electronic correlation is accounted for by any of the post-HF methods previously described (CI, MP2, GW, DMRG, ...) while the embedding environment is treated at a lower level of accuracy, by using – for example – mono-electronic HF orbitals. Special care has to be paid to the interactions between the two sub-structures as the cluster is bound to the surrounding medium and should be thus let free to exchange electrons.

A rigorous partitioning of the two functional subspaces can be obtained by orthogonalizing the Hilbert space of the cluster to that one of the environment. To this goal, localised basis sets of symmetry adapted Hermite Gaussian functions (HGF) [79, 80], centered on the nuclei of the system, are used to represent the wavefunctions.

By defining two suitable projectors, the HF solution of the complete system for the occupied and virtual orbitals are projected onto the cluster subspace. By diagonalising these projectors, only eigenvectors having a large overlap with the cluster orbitals will be selected to be used in the CI procedure; in this way doubly and singly occupied, bonding and virtual orbitals localised in the cluster (in the sense that they have a not-negligible projection on the cluster functional space) will be included in the CI calculation, while orbitals outside the cluster will be clamped down and treated at the HF level.

After this selection procedure, electronic structure calculations of the cluster for different charge and excitation states are performed by using quantum chemistry methods. As a result, the wavefunctions representing neutral (absorption spectroscopy or autoionisation), singly (photoemission spectroscopy) and doubly (Auger spectroscopy) ionised states can be written as a linear combination of Slater determinants whose elements have been obtained by self-consistent procedures.

After the calculation of bound states, a central difficulty in scattering calculations is represented by the construction of the continuum wavefunctions $\{\chi_{\alpha,\mathbf{k}}^-\}$ with proper boundary conditions [33]. Such a wavefunctions are the eigen-solutions of a Schrödinger equation at positive energy and have to be antisymmetrized with the bound states of the remaining ion. In principle, one could solve a HF-like equation at a specific positive energy with the effective potential due to the charge on the nuclei and on the bound electrons in the remaining ion; unfortunately such an approach, as pointed by Kelly *et al.* [68], suffers errors and numerical instabilities already in the case of atoms, preventing its use in condensed matter applications. In order to avoid all these difficulties, we proposed an alternative approach based on the observation that the HF equation in the continuum is equivalent to

the following Lippmann-Schwinger (LS) equation:

$$\eta_{\alpha,\mathbf{k}}(\mathbf{r}) = \mathbf{e}^{i\mathbf{k}\cdot\mathbf{r}} + \hat{\mathbf{G}}_0^-(\epsilon)\hat{\mathbf{V}}_\alpha(\mathbf{r})\eta_{\alpha\mathbf{k}}(\mathbf{r}) \quad (2.73)$$

$$\hat{\mathbf{G}}_0^-(\epsilon) = \lim_{\epsilon \rightarrow 0} \left[\epsilon - i\epsilon - \hat{H}_0 \right]^{-1}; \quad \hat{H}_0 = -\frac{1}{2}\nabla^2 \quad (2.74)$$

where $\hat{V}_\alpha(\mathbf{r}, \{\mathbf{R}\}) = \hat{\mathbf{V}}_{\text{en}}(\mathbf{r}) + \sum_{\mathbf{j}} \left[\mathbf{a}_{\alpha\mathbf{j}}^{(c)} \hat{\mathbf{J}}_{\mathbf{j}}^{(\alpha)}(\mathbf{r}) - \mathbf{c}_{\alpha\mathbf{j}}^{(c)} \hat{\mathbf{K}}_{\mathbf{j}}^{(\alpha)}(\mathbf{r}) \right]$. In electron spectroscopies \hat{V}_α is a long range potential:

$$\hat{V}_\alpha(\mathbf{r}) \rightarrow \hat{V}_\alpha^{LR}(\mathbf{r}) = -\frac{q}{r} + \mathcal{O}\left[\frac{1}{r^n}; n > 1\right]; \quad q = 1 \text{ or } 2 \quad (2.75)$$

with a tail represented by a Coulomb potential plus higher-order corrections that depend on the type of system considered. The presence of this long-range potential, forces one to include the Coulomb and static dipole components of the potential in the zero-order Hamiltonian (\hat{H}_0), a fact that is very difficult to be implemented in a condensed matter context. To by-pass this difficulty we will use the projection operator formalism.

2.4.2 On the use of the projection operator formalism in many-body scattering theory

The many-body Hamiltonian written in Eq. (2.8) is valid also in the case of a N -electron system with one electron in the continuum spatially close to the system. In the scattering process two different spatial regions can be identified: an asymptotic region where analytical hydrogenic-like solutions are appropriate and a scattering volume where the interaction among the indistinguishable electrons cannot be neglected. At variance with R -matrix-type approaches [81], we proposed to define an ‘‘Heaviside potential’’ \hat{V}_α^t , such that correctly reproduces the effect of the true potential \hat{V}_α inside the interaction region when applied to the scattering wavefunction $\eta_{\alpha\mathbf{k}}(\mathbf{r})$ and is zero outside. Viceversa, a second ‘‘Heaviside potential’’ $\hat{V}'_\alpha(\mathbf{r}) \simeq \hat{V}_\alpha^{LR}(\mathbf{r})$ can be defined, which is zero inside the the interaction region and equal to the long-range potential in the outer region. These definitions guarantee the correct form of the scattering wavefunction both inside the volume, where $\hat{V}_\alpha(\mathbf{r}) \neq \hat{V}_\alpha^{LR}(\mathbf{r})$ and the discrete-continuum coupling plays an important role, and in the outer region, where $[\hat{V}_\alpha(\mathbf{r}) - \hat{V}_\alpha^{LR}(\mathbf{r})]\eta_{\alpha\mathbf{k}}(\mathbf{r}) \simeq 0$ and the continuum orbital can be represented by linear combination of hydrogenic wavefunctions. Such a division in scattering and asymptotic regions is operatively reached by projecting the scattering potential onto a finite set of L^2 functions:

$$\hat{V}_\alpha \sim \hat{V}_\alpha^t = \sum_{\lambda\mu\nu\tau} |\lambda\rangle S_{\lambda\mu}^{-1} \langle \mu | \hat{V}_\alpha | \nu \rangle S_{\nu\tau}^{-1} \langle \tau | \quad (2.76)$$

$$S_{\lambda\mu} = \langle \lambda | \mu \rangle \quad (2.77)$$

The elements of this basis set are chosen to minimise the difference $(\hat{V}_\alpha - \hat{V}_\alpha^t)|\eta_{\alpha\mathbf{k}}\rangle$ inside the region of interest. The replacement $(\hat{V}_\alpha \rightarrow \hat{V}_\alpha^t)$ allows one to solve Eq. (2.73) as follows:

$$\eta_{\alpha\mathbf{k}}(\mathbf{r}) = e^{i\mathbf{k}\cdot\mathbf{r}} + \hat{\mathbf{G}}_0^-(\epsilon)\hat{T}_\alpha(\epsilon)e^{i\mathbf{k}\cdot\mathbf{r}} \quad (2.78)$$

where \hat{T}_α is the transition operator defined by the equation:

$$\hat{T}_\alpha = \hat{V}_\alpha^t + \hat{V}_\alpha^t \hat{G}_0^-(\varepsilon) \hat{T}_\alpha \quad (2.79)$$

The corresponding matrix equation, defined in the space spanned by the basis set $\{|\lambda\rangle\}$, gives:

$$\hat{T}_\alpha = \hat{V}_\alpha^t \frac{1}{\hat{V}_\alpha^t \hat{G}_0^-(\varepsilon) \hat{V}_\alpha^t} \hat{V}_\alpha^t \quad (2.80)$$

It follows that one can write $\eta_{\alpha\mathbf{k}}$ in the form

$$\eta_{\alpha\mathbf{k}} = e^{i\mathbf{k}\cdot\mathbf{r}} + \sum_{\lambda} c_{\lambda}(\mathbf{k}, \varepsilon) \mathbf{f}_{\lambda}(\varepsilon, \mathbf{r}) \quad (2.81)$$

with

$$c_{\lambda} = \sum_{\mu, \nu, \tau} S_{\lambda\mu}^{-1} \langle \mu | \hat{T}_\alpha(\varepsilon) | \nu \rangle S_{\nu\tau}^{-1} \langle \tau | \mathbf{k} \rangle \quad (2.82)$$

$$f_{\lambda}(\varepsilon, \mathbf{r}) = \hat{G}_0^-(\varepsilon) |\lambda\rangle \quad (2.83)$$

Therefore, a general expression of the continuum wavefunction is obtained by applying the free-particle Green function to a finite set of L^2 functions. Nevertheless, the previous expressions, along with the LS Eq. (2.73), are based on the projection of the N -body Hamiltonian except for the kinetic term as follows:

$$\hat{H}(1, \dots, N) = \sum_{i=1}^N [\hat{T}(i) + \hat{V}_\pi^{en}(i)] + \frac{1}{2} \sum_{i \neq j}^N \hat{v}_\pi(i, j) \quad (2.84)$$

$$\hat{T}(i) = -\frac{1}{2} \nabla_i^2; \quad \hat{V}_\pi^{en}(i) = \hat{\pi}(i) \hat{V}^{en}(i) \hat{\pi}(i) \quad (2.85)$$

$$\hat{v}_\pi(i, j) = \hat{\pi}(i) \hat{\pi}(j) \hat{v}(i, j) \hat{\pi}(i) \hat{\pi}(j) \quad (2.86)$$

$$\hat{\pi}(i) = \sum_{l=1}^m |g_l(i)\rangle \langle g_l(i)| \quad (2.87)$$

where $\hat{\pi}$ is the identity operator of a m -dimensional space (\mathcal{G}) of $L^2(R^3)$ -functions, spanned by the orthonormal set $\{|g_l\rangle; l = 1, \dots, m\}$. We use $\hat{\pi}$ to project both $\hat{V}^{en}(i) = -\sum_{\mu} \frac{Z_{\mu}}{|\mathbf{r}_i - \mathbf{R}_{\mu}|}$, i.e. the electron-nuclei attraction potential, and $\hat{v}(i, j) = \frac{1}{|\mathbf{r}_i - \mathbf{r}_j|}$, i.e. the electron-electron repulsion operator. In this framework, the continuum is recovered by the kinetic term and the use of this projected representation of the potential, that necessarily can be appropriate only inside a finite volume, allows a drastic simplification of the problem. By choosing an initial set of functions given by the antisymmetrized products:

$$\chi_{\alpha\mathbf{k}}(1, 2, 3 \dots) = \hat{A} [\varphi_{\alpha\mathbf{k}}(1) \Theta_{\alpha}(2, 3, \dots)] \quad (2.88)$$

where \hat{A} is the antisymmetrizer that contains also the normalisation constant, Θ_{α} is a Slater determinant representing the excited state α of the molecule (which can be singly or doubly ionised depending on the type of spectroscopy) and $\varphi_{\alpha\mathbf{k}}$ is the spin-orbital for the outgoing electron:

$$\varphi_{\alpha\mathbf{k}}(1) = \eta_{\alpha\mathbf{k}}(\mathbf{r}_1) \sigma_{\alpha}(s_1) \quad (2.89)$$

one can look at the eigen-solutions of the Hamiltonian (2.84) inside the Hilbert space spanned by these functions. The continuum orbitals $\{|\eta_{\mathbf{k}}\rangle\}$ can be obtained as eigenfunctions of the kinetic energy operator \hat{T} , which satisfy the orthogonality constraint $\langle\eta_{\alpha\mathbf{k}}(j)|\Theta_{\beta}(1, \dots, j, \dots, N-1)\rangle_j = 0$; $\forall \alpha, \beta, j, \mathbf{k}$, where $\{|\Theta_{\beta}\rangle\}$ are solutions of the secular problem for the $N-1$ -electron bound system. This means that they are solutions of the eigenvalue equation:

$$\hat{T}_q|\eta_{\mathbf{k}}\rangle = \frac{k^2}{2}|\eta_{\mathbf{k}}\rangle \quad ; \quad \langle\eta_{\mathbf{k}}|\eta_{\mathbf{p}}\rangle = (2\pi)^3\delta(\mathbf{k}-\mathbf{p}) \quad , \quad \forall \mathbf{k}, \mathbf{p} \quad (2.90)$$

$$\hat{T}_q = (\hat{1} - \hat{P})\hat{T}(\hat{1} - \hat{P}) = \hat{T} + \hat{V}_{PK} \quad ; \quad \hat{P} = \sum_j^n |\theta_j\rangle\langle\theta_j| \quad (2.91)$$

where $\hat{V}_{PK} = -\hat{P}\hat{T} - \hat{T}\hat{P} + \hat{P}\hat{T}\hat{P}$ is an effective potential, due to the orthogonality constraints, that has the typical structure of a Phillips–Kleimann potential [82]. The single-channel wavefunction defined as the antisymmetrized product of Eq. (2.88), with the continuum orbital $\eta_{\mathbf{k}}$ given in Eq. (2.90), are mixed by the electron-electron correlation

$$\langle\chi_{\alpha\mathbf{k}}|\hat{H}^N|\chi_{\beta\mathbf{p}}\rangle = (2\pi)^3\delta(\mathbf{k}-\mathbf{p})\delta_{\alpha\beta} \left(\frac{k^2}{2} + E_{\alpha} \right) + \langle\varphi_{\alpha\mathbf{k}}|\hat{V}_{\pi}^{en}\delta_{\alpha\beta} + \hat{W}_{\pi}^{\alpha\beta}|\varphi_{\beta\mathbf{p}}\rangle \quad (2.92)$$

where

$$\hat{W}_{\pi}^{\alpha\beta}(1) = \sum_{j=2}^N \langle\Theta_{\alpha}(2, \dots, j, \dots, N)|\hat{v}_{\pi}(1, j)(\hat{1} - \hat{\mathcal{P}}_{1,j})|\Theta_{\beta}(2, \dots, j, \dots, N)\rangle \quad (2.93)$$

and $\hat{\mathcal{P}}_{1,j}$ is the operator that interchanges the $(1, j)$ variables. Assuming that the bound-state problem has been solved, the matrix elements in Eq. (2.92) can be looked as the representation of an effective one-particle Hamiltonian with internal degrees of freedom (α, β) . Therefore, the N -particle problem can be reduced to an effective single particle problem, in which the scattering states can be obtained from the solution of a LS equation with the proper boundary conditions. Furthermore, the evaluation of matrix elements in Eq. (2.92) requires the knowledge of the components of the continuum orbitals $\{|\eta_{\mathbf{k}}\rangle\}$ only inside the space that has $\hat{\pi}$ as the identity operator and where the projected potential has the following structure

$$\hat{V} = \sum_{\alpha, \beta}^M \sum_{i, j}^m |g_i\rangle\langle\alpha|V_{ij}^{\alpha, \beta}\langle\beta|\langle g_j|, V_{ij}^{\alpha, \beta} = \langle g_i| \left[\hat{V}_{\pi}^{en}\delta_{\alpha\beta} + \hat{W}_{\pi}^{\alpha\beta} \right] |g_j\rangle \quad (2.94)$$

where $\{|g_j\rangle\}$ and $\{|\alpha\rangle\}$ are orthonormal basis sets. To summarise the findings of this formal description, the problem of solving the Eq. (2.84) for positive energies has been reduced to the solution of the LS equation

$$|\chi_{\alpha\mathbf{k}}^{-}(E)\rangle = |\varphi_{\alpha\mathbf{k}}(E)\rangle + \hat{G}_0^{-}(E)\hat{V}|\chi_{\alpha\mathbf{k}}^{-}(E)\rangle \quad (2.95)$$

where

$$\hat{G}_0^{-}(E) = \lim_{\epsilon \rightarrow 0} [E - i\epsilon - \hat{h}_0]^{-1} = \frac{\hat{\mathcal{P}}}{E - \hat{h}_0} + i\pi\delta(E - \hat{h}_0) \quad (2.96)$$

and $\hat{\mathcal{P}}$ is the Cauchy principal value. The formal solution of this problem can be expressed in terms of the wave operators ($\hat{\Omega}_-$) [7] (see Eq. (2.11)):

$$|\chi_{\alpha\mathbf{k}}^-(E)\rangle = \hat{\Omega}_-(E) |\varphi_{\alpha\mathbf{k}}(E)\rangle \quad (2.97)$$

$$\hat{\Omega}_-(E) = [\hat{1} + \hat{G}^-(E)\hat{V}] = [\hat{1} - \hat{G}_0^-(E)\hat{V}]^{-1} \quad (2.98)$$

where $\hat{G}^-(E)$, that is defined as in Eq. (2.96) with \hat{h}_0 replaced by \hat{h} , is related to $\hat{G}_0^-(E)$ by:

$$\hat{G}^-(E) = \hat{G}_0^-(E) + \hat{G}^-(E)\hat{V}\hat{G}_0^-(E) \quad (2.99)$$

Furthermore, we observe that, due to the structure of the projected potential, the correction to any given free-particle state $|\varphi_{\alpha\mathbf{k}}(E)\rangle$ is represented by a linear combination of $\hat{G}^-(E)|f_{j\alpha}\rangle$, where $\{|f_{j\alpha}\rangle = |g_j\rangle|\alpha\rangle\}$ is the tensorial product of two arbitrary orthonormal basis sets. Finally, one can demonstrate that the functional space spanned by the free scattering eigenstates is finite and isomorphous to the functional space changed by the projected potential. This property reduces considerably the computational cost of this approach when applied to condensed matter.

2.4.3 Evaluation of spectroscopic quantities

Once the scattering wavefunction has been calculated, as by Fano's approach, the main theoretical feature characterising core-electron spectroscopies is the interaction between one or more metastable states created in the initial excitation process and the continuum of states. Considering only one discrete intermediate state $|\Phi_j\rangle$ and several continuum decay channels $|\Psi_{\alpha\epsilon}^-\rangle$, the many-body scattering process is governed by the matrix elements

$$M_{j\alpha}(\epsilon, E) = \langle\Phi_j|\hat{H} - E|\Psi_{\alpha\epsilon}^-\rangle \quad (2.100)$$

coupling discrete and continuum states.

The interpretation of electron spectra, thus, requires a computational method able to represent accurately the electronic correlation among bound electrons in the intermediate quasi-bound states of the system and the interaction between bound and escaping electrons, represented by the projected scattering potential $\hat{V}_\alpha(\mathbf{r})$ in eq. 2.94.

2.4.4 Multisite correlations in CVV Auger transitions: the Cini–Sawatzky strategy

In solid state applications, the number of decay channels, mixed by the interchannel interaction, may become prohibitively high and computationally not treatable. However, neglecting correlation effects in final states leads to discrepancies between computed and experimental lineshapes, thus calling for the development of suitable theoretical methods.

Let us examine this point for the particular case of Auger spectroscopy. When transitions involve the valence band (CCV or CVV transitions), Auger spectroscopy is in principle a probe of the valence density of states local to the atomic site where the initial core-hole has been created.

Focusing in particular on CVV transitions, Lander [78] showed that they can be basically interpreted as the self-convolution of the Local Density of States (LDOS), provided the possible variation of transition matrix elements across the valence band can be neglected.

CVV spectra from several materials (Si, alkaline and alkaline-earth metals) were indeed reasonably interpreted within this framework. Characteristic feature of CVV spectra from such materials is a broad peak extending around twice the width of the valence band, as expected for the self-convolution of the Valence Band DOS. This fact gained them the name of ‘band-like’ spectra.

It soon became clear however that a band-like picture was not able to generally account for CVV spectra. Spectra from a number of elements, notably some of the transition metals (such as Cu, Zn, Cd, In, Sn, . . .), exhibit in fact the same multiplet structure both in the gas and in the solid phase [83] and, for this reason, they were referred to as ‘atomic-like’. Between these two extremes, CVV spectra from a whole range of materials exhibit a superposition of band-like and atomic-like features.

Criteria for predicting the band-like or atomic-like character of CVV spectra were devised by Antonides *et al.* [84] on the basis of two critical energies, namely the effective Coulomb interaction, U_{eff} , between the two final-state holes localised on one atomic site and the valence band width. As long as the former is smaller than the latter, band-like character of CVV spectra is ensured by the ability of the two final-state holes to delocalize onto different atomic sites. On the other hand, when hole-hole repulsion exceeds the valence band width, CVV spectra acquire atomic-like character due to localisation of the two holes on the same atomic site. By the end of the 70’s, Cini [76] and, independently, Sawatzky [77] developed a theory based on a Hubbard model which explains the occurrence of band-like and atomic-like CVV spectra in terms of the ratio between the effective Coulomb interaction U in the Hubbard Hamiltonian and the width of the valence band, W . The Cini-Sawatzky theory is based on assumptions which restrict its application, the most important constraint being that the theory holds only for systems with filled bands derived from closed atomic shells. The theory was later extended to treat systems with partially filled bands [85, 86, 87, 88, 89].

As an empirical measure of the effective hole-hole correlation energy, U_{eff} , Antonides *et al.* [84] proposed to use the Auger parameter, ξ , introduced by Lang and Williams [90]:

$$\xi = U_{\text{eff}}^{a,b,c} = \epsilon^a - \epsilon^b - \epsilon^c - \epsilon_{\text{kin}}^{bc} \quad (2.101)$$

The binding energies of levels a , b , and c are taken from XPS measurements and they are referred to the same energy as the kinetic energy of the Auger electron, $\epsilon_{\text{kin}}^{bc}$. Defined in this way, U_{eff} represents the total additional energy (with respect to the two one-hole excitation energies) required to excite two holes in levels b and c on the same atom, with a given final state configuration.

Measurements of U_{eff} derived from experimental spectra were proposed by several authors. As an example, we consider here the C KVV spectrum from graphite, known to belong to the class of band-like CVV spectra. A detailed study on it was performed by Houston *et al.* [91] who interpreted the graphite KVV spectrum in terms of the self-fold of partial components (π_p , σ_p , σ_s) of the density of states. Partial density of states were empirically derived from valence band photoemission and from X-ray emission spectra. Discrepancies between the KVV spectrum and the self-folded partial density of states were ascribed to several many-body effects, such as static and dynamic screening in the initial and in the final state. Moreover, using the Cini-Sawatzky expression to account for hole-hole interaction in the final state, they were able to measure effective hole-hole interaction energies of 2.2 eV for two holes in the σ band, 1.5 eV for one hole in the σ band and one hole in the π band and 0.6 eV for both holes in the π band.

2.4.5 Our strategy to multisite correlations

While the Cini–Sawatzky approach described in subsection 2.4.4 can be very useful in order to gain insight on these scattering processes, excluding some of the most complicated effects, the main drawback remains the use of a phenomenological parameter (U_{eff}).

To include these effects and avoid unwanted semi-empirical parameters, Taioli and coworkers [62] have generalized the use of the projected potentials by defining a model Hamiltonian in which final valence-valence hole states are firstly localized on the atom where the initial core-hole is found and multisite interactions enter naturally in this Hamiltonian as a perturbation. This idea stems from the quasi-atomic nature of core level photoemission and Auger transitions, that forces the holes to remain on the atom where the initial core-hole is created.

The diagonalization of the interchannel interaction (see eq. 2.92), including hole delocalization on valence bands and electronic excitations, is computed by using a so called *space-energy similarity procedure* [62]. In this procedure the direct diagonalization of the large and sparse Hamiltonian found in solid state applications of multichannel scattering is avoided by selecting among the open channels a number of localized states at different energies, which account for the majority of the total decay probability. The interchannel interaction is diagonalised within this subspace, and each resulting channel is overlapped with all the possible configurations generated by electronic excitations from the selected configuration. Only states presenting a high overlap with the selected channel will be kept to generate the band-like part of the spectrum.

The dimension of the initial multichannel space, where the model Hamiltonian is firstly diagonalized, is a trade-off between computational load and ability to reproduce accurately transition energies and intensities; this dimension can be further increased if the interchannel procedure does not recover important parts of the correlation energy. Transition matrix elements are fixed during space-energy similarity steps to the values obtained after the interchannel procedure and the square modulus of the overlap enters as a multiplicative factor in the lineshape analysis. Such analysis, which is the core of our method, significantly reduces the computational effort to calculate core level photoemission and non radiative decay in large systems. With regard to scaling performances, the calculation cost of the interchannel procedure scales as the third power of the number of channels, whereas the memory cost scales as the second power. Symmetry may be used to further reduce the computational scaling, particularly in the interchannel procedure. Finally, the analytic expressions for the autoionisation and Auger cross sections derived in Eqs. (2.61) and (2.62) can be used to calculate the theoretical lineshape.

The approach has been applied to calculate the C KVV spectrum of graphite which is compared to the experimental spectrum (obtained from Highly Oriented Pyrolytic Graphite) in Fig. 2.3. The intrinsic spectrum, i.e. deconvoluted of extrinsic losses, was obtained according to standard procedures [92, 93]. The calculated and measured spectra are normalised to a common height. No energy shift was required to obtain the agreement shown in the figure. The spectrum consist of three resolved features. On moving from high to low kinetic energy, we find the most intense peak slightly below 270 eV, followed by a shoulder in the region 250-270 eV and by a much less intense shoulder in the region 230-250 eV. These three spectral regions are interpreted as due to transitions leaving p-p, s-p and s-s holes in the final state, respectively [91, 94].

The computed spectrum is in good agreement with the experimental one regarding its

basic structure and the transition energy. Calculations overestimate the spectral intensity at the low kinetic energy side of the main peak (s-s and s-p region) and they underestimate it at the high energy side of the main peak. However, by enlarging the basis set used in the calculation (blue line), the agreement in the s-p region improves.

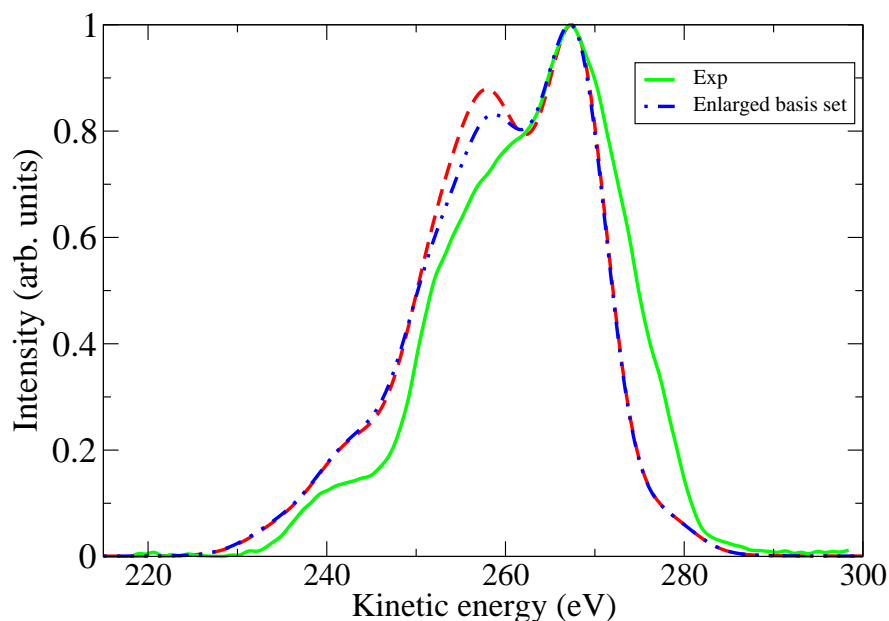


FIGURE 2.3: Comparison between the theoretical (blue and red lines) and experimental (green line) Auger spectrum of graphite.

2.4.6 *Ab-initio* calculation of electron spectra

Chemical shifts in photoemission

The existence of core level chemical shifts in photoemission is the origin of the great popularity of the technique as an analytical tool and gained it, in its infancy, the name ESCA, i.e. electron spectroscopy for chemical analysis. Chemical shifts result from a combination of many-body effects taking place in the initial and in the final state of the photoemission process. Initial state effects are associated with the mean ground state electrostatic potential: depending on the chemical environment, and hence on the charge on the atom, the binding energy of a core level can increase or decrease as compared to the free atom. Final state effects are associated with the response of the electron system to the core-hole potential. This relaxation causes a decrease in the total energy of the system which is taken off by the photoelectron, thereby reducing its measured binding energy.

As examples in this regard, let us examine the C 1s spectrum from propene and from graphene. While graphene growth and functionalization will be extensively treated in the next chapter, here we anticipate some details relevant to our method for calculating electron spectra.

Propene. Propene (C_3H_6) is used as a precursor gas for chemical vapor deposition (CVD) of graphene on Ni [95]. The molecule, sketched in figure 2.4, contains three inequivalent C atoms.

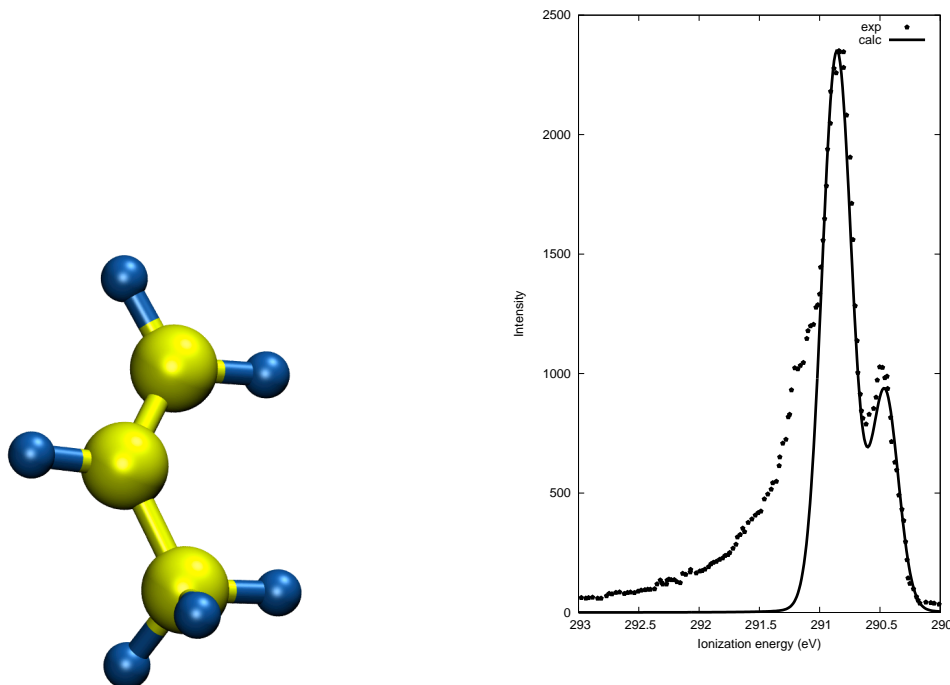


FIGURE 2.4: Left: geometrical structure of propene, showing C (yellow) and H (blue) atoms. Right: experimental vs. theoretical C 1s photoelectron spectrum of propene. The experimental spectrum was obtained with 310 eV excitation energy.

The C 1s spectrum from gas-phase propene was measured by Saethre *et al.* [96] at a photon energy of 310 eV. Fig. 2.4 compares this spectrum (dotted curve), digitised from Fig. 3 of Ref. [96], to the C 1s spectrum (continuous line) we have calculated for the propene molecule in terms of the *ab-initio* method described above. Calculate energies assume that the removed electron is brought infinitely far from the system (vacuum level). Both spectra are normalised to a common height of their most intense feature. At the low ionisation-energy end of the spectrum we see a well resolved peak, while the main peak is slightly below 291 eV with a shoulder on its high energy side. It was demonstrated [96] that the high energy shoulder has to be assigned to energy loss into phonon excitations, while the three inequivalent C sites give rise to just two resolved peaks, because the ionisation energy for two of the three atoms is too near to be resolved in the spectrum. Our calculation, which does not account for vibrational energy losses, reproduces the two high energy peaks very well both with respect to difference in energy and relative intensity.

Graphene. We have calculated the C 1s spectrum from graphene [95] for several situations, namely:

1. after chemical vapor deposition on Ni (111)
2. after intercalation of Au into the graphene/Ni interface
3. after H exposure

	graphene/Ni		H-graphene/Au		
	top	hollow	C1	C2	C3
exp.	284.7	284.8	284.2	283.9	284.7
calc.	284.8	284.89	284.33	283.59	284.61

TABLE 3: Experimental and theoretical C1s binding energies for graphene/Ni and graphene/Au. For graphene/Ni, the carbon atoms are located above top and hollow Ni sites. If 1 ML of Au is intercalated between graphene and Ni, the binding energy of graphene is given by C1. The values C2 and C3 denote binding energies of extra peaks that appear upon hydrogenation and the formation of C-H bonds (see sketches in Fig. 2.5)

Fig. 2.5 illustrates these three situations in (a), while measured C 1s spectra (dotted curves) are given in (b). Fitting components (Doniach–Sunjic lineshapes) to the spectra are given as continuous lines. Calculations of the C 1s binding energies are indicated by vertical lines on the energy axis. Experimental and calculated C 1s peak positions for all spectral components are summarised in Table 3.

We see that the C 1s lineshape markedly depends on the chemical environment of C atoms. The initial C 1s peak for graphene on Ni is contributed by two unresolved components, assigned to C atoms located on top of Ni atoms and in fcc hollow sites, respectively. As Au intercalation proceeds, this original peak gradually disappears and a second peak, 0.5 eV lower in binding energy, grows. Both peaks are visible after 0.5 ML Au intercalation. However, after intercalation of 1ML Au, the original peak disappears, thus indicating that the graphene-Ni interaction is substantially removed. We remain with the peak at lower binding energy (referred to as C1 peak), which we assign to sp^2 bonded C atoms in quasi-free-standing graphene. Partial hydrogenation of graphene brings about a dramatic change in the C1s spectrum. Lineshape analysis reveals the presence of two additional components (C2 and C3) separated by 0.5 eV from the C1 peak and on either side of it. Calculations assign the lower binding energy peak (C2) to C atoms which are next to a hydrogenated C atom (see figure 2.5(a)), while the C3 peak is assigned to sp^3 bonded C atoms that form an out-of-plane C-H bond (see figure 2.5(a)). By comparing the relative area of components associated with sp^2 and sp^3 carbon atoms in the C 1s spectrum, we obtain a maximum hydrogen coverage of about 25%. Finally, heating to 600 K brings about the removal of all components associated with the H interaction and the spectrum of quasi-free-standing graphene (peak C1) is recovered, thus proving that hydrogenation-dehydrogenation of graphene is a fully reversible process. A deeper analysis of these spectra will be delivered in chapter 5.

NEXAFS spectrum from graphene and hydrogenated graphene

NEXAFS spectra have been measured [97] from graphene obtained by chemical vapor deposition on Ni(111) thin films epitaxially grown on W(110) and after deposition of 1 ML Au, intercalated into the graphene/Ni interface by annealing. It is known [95] that this procedure removes the graphene/Ni interaction, making the graphene quasi-free-standing. Fig. 2.6 shows angle resolved C 1s NEXAFS spectra relative to both pristine graphene and partially hydrogenated graphene, where the H coverage is estimated to be around 15%. These spectra, which to a first approximation probe the density of empty states above

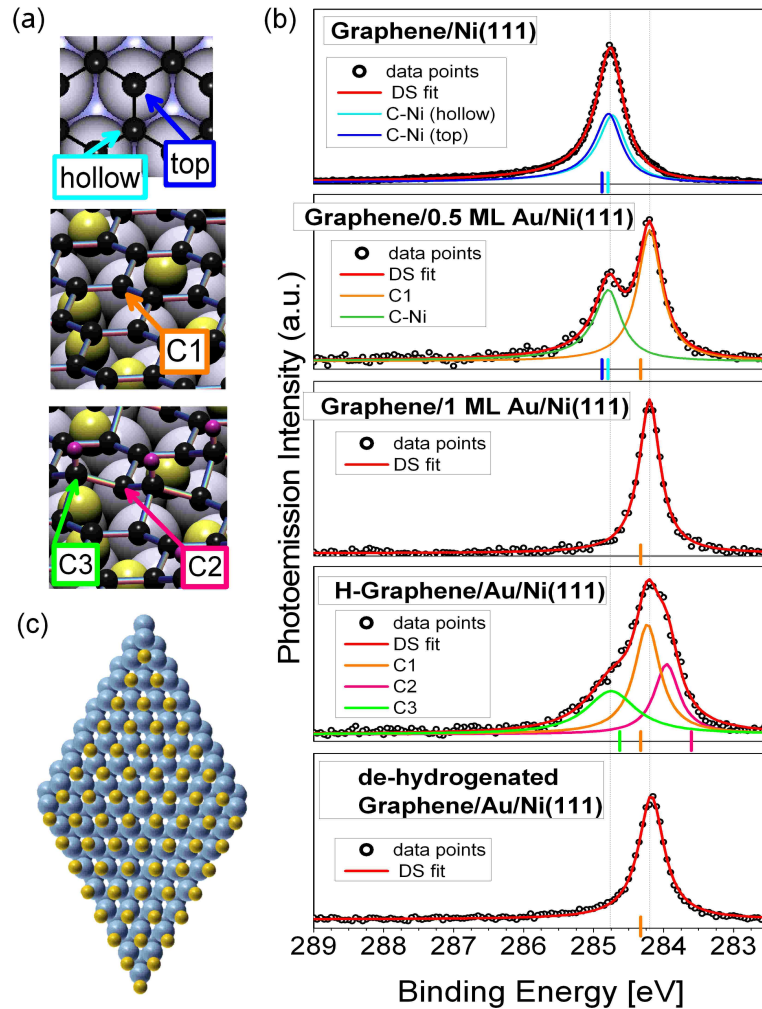


FIGURE 2.5: (a) From top to bottom: graphene on Ni(111), Au intercalated between the graphene/Ni interface and hydrogenated graphene on Au. The hydrogen atoms are marked in violet. C1 and C2-C3 indicate chemical environments for graphene/Au and hydrogenated graphene, respectively. (b) C1s core level spectra of graphene on Ni and on Au (0.5 and 1 ML of Au) and fully hydrogenated graphene. The bottom panel depicts the C 1s spectrum after dehydrogenation of graphene. All C 1s features were fitted with Doniach–Sunjic (DS) lineshapes with components for graphene/Ni (top and hollow sites), graphene/Au (C1) and hydrogenated graphene (C2-C3). The vertical lines on the energy axis correspond to the calculated C1s energies of these components (the same colour code applies). From the integrated area of the C-H component, we estimate a $\sim 25\%$ hydrogen load. (c) Optimised superstructure of one monolayer Au (8×8) on a Ni(111) surface (9×9).

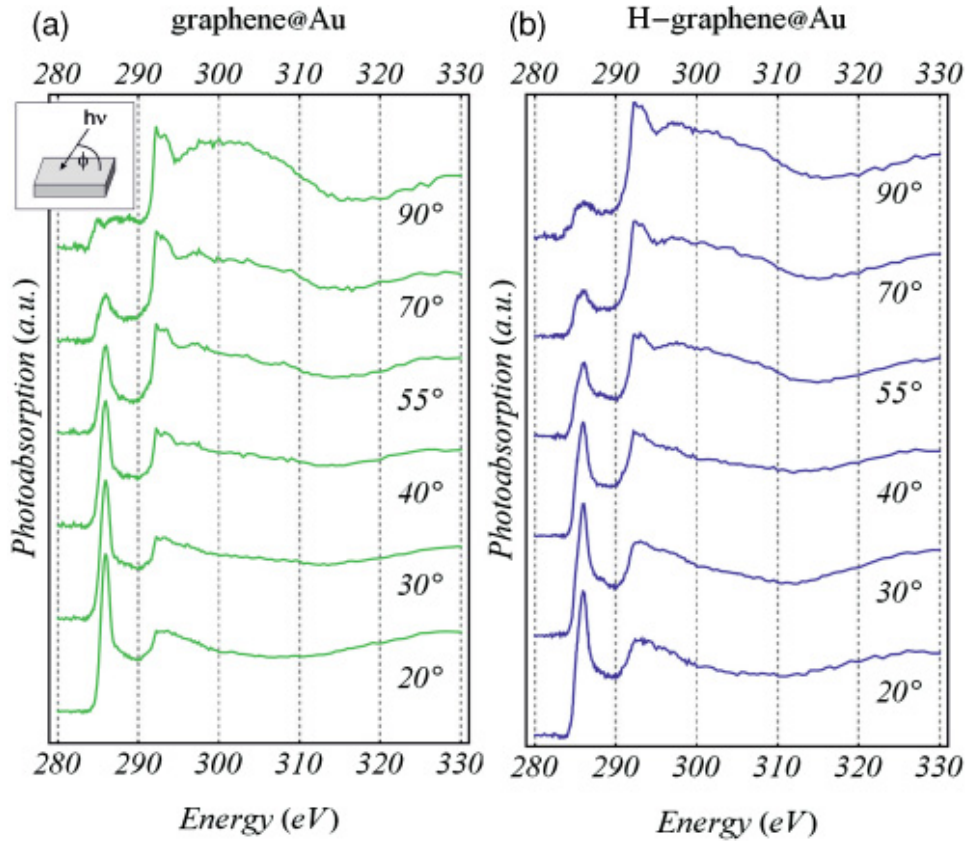


FIGURE 2.6: NEXAFS spectra of pristine (a) and hydrogenated graphene with coverage in hydrogen around 15% (b).

the Fermi level, show the well-known fact that the π^* band is better probed at grazing incidence, while the opposite occurs for the σ^* band. For fully hydrogenated graphene, up to saturation coverage, spectra are strongly modified [98]. On the other hand, changes are barely observed in the present case, where the H coverage is around 15%. They nonetheless consistently show a reduction in the intensity of the π^* band, understood in terms of the formation of sp^3 C-H bonds at the expenses of the original sp^2 C-C bonds.

For partially hydrogenated (15%) graphene, spectra were calculated for incidence angles of 20°, 55° and 90° and for an energy range extending from the C 1s edge up to 295 eV. They are compared to measured spectra in Fig. 2.7, where measured and calculated spectra are normalised to a common height of the most intense feature. No energy shift was required to obtain the kind of agreement shown in the Figure. We see that the energy position and relative intensity of the σ^* and π^* bands are well reproduced, apart from a small overestimation of the π^* intensity for the 55° spectrum. Most interestingly however, we see the presence of a small feature, possibly not resolved in the experimental spectra in the region between the π^* and the σ^* band for the 20° and 55° spectra. This feature was previously shown [98] to be absent on spectra from pristine graphene and to form upon hydrogenation, so that it was assigned to C-H bonds. Moreover, it was shown [98] that the feature is easily observed for spectra acquired at grazing incidence, whereas it disappears on moving to normal incidence. The result, consistent with our calculations, is understood as a demonstration that C-H bonds are oriented perpendicular to the graphene plane. A deeper analysis of these spectra will be delivered in chapter 5.

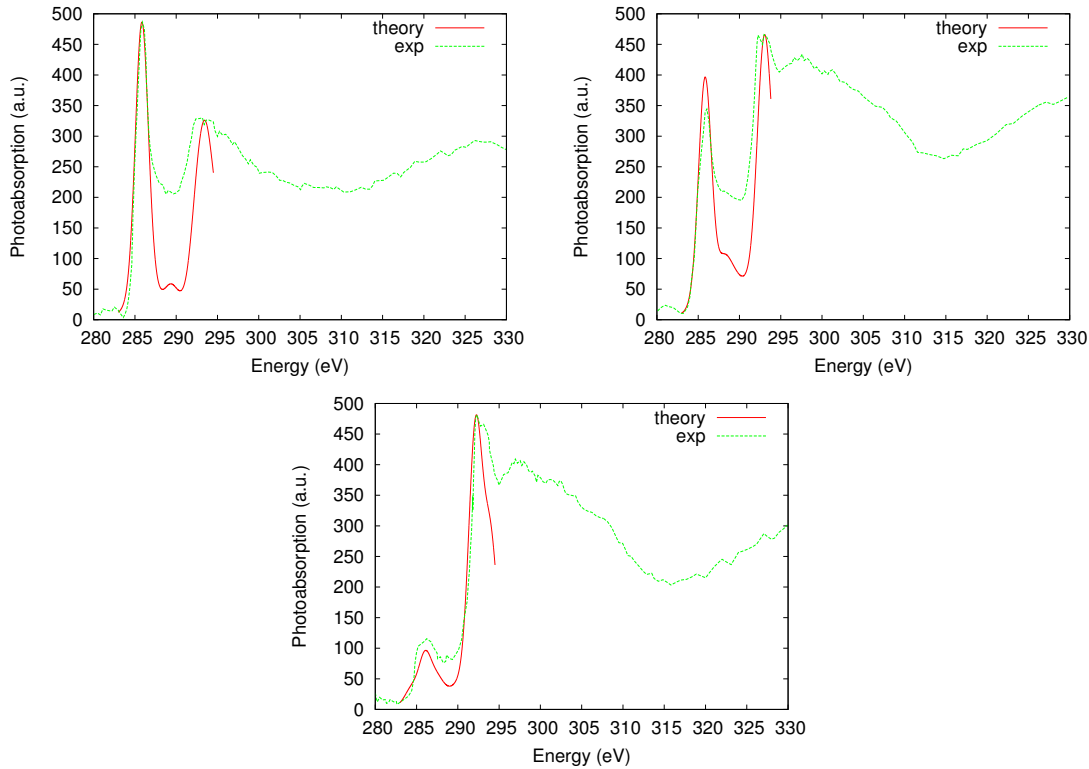


FIGURE 2.7: Comparison between the experimental (green lines) and theoretical (red lines) C 1s NEXAFS spectra from hydrogenated graphene for (from top to bottom) 20° , 55° , and 90° incidence angles, defined as in Fig.(2.6).

2.5 EEL spectra for quantitative understanding of Electron Spectra

The construction of the theoretical spectrum of primary or secondary electrons would not be complete without taking into account the energy loss suffered by the electrons due to single particle excitations or, in the case of solids, to the interaction with collective excitations, notably phonons and plasmons. To compare measured electron spectra to computed spectra, one could move along two independent directions.

On the one hand, one could recover the ‘true’ spectrum by conventional deconvolution procedures [74, 75, 92, 93] starting from the ‘as-acquired’ experimental spectrum. While such deconvolution procedures are routinely used, they are not free from uncertainty, as different background subtraction techniques may affect the final result and thus the line-shape.

Reversely, one could generate computed spectra where extrinsic energy losses are superimposed to the intrinsic spectrum, so that computed spectra can be directly compared to ‘as-acquired’ measured spectra. The basic idea is to use the *ab initio* Auger or photoemission spectrum as a source of electrons which undergo inelastic processes. Extrinsic energy losses into collective excitations (plasmons, phonons, polarons) are treated by statistical methods (Monte Carlo approach [99]) after computing the *ab initio* spectrum (which can include the intrinsic energy loss). We will show an application of this unified method to the

calculation of the Si K–LL and O K–LL Auger spectra from SiO₂ in Sec. 2.5.4. In order to describe the processes that occur when an electron beam penetrates in a solid target, we need to calculate the elastic and the inelastic collisions suffered by the electrons travelling in the solid. In each collision event the incident electron both loses energy and changes its travelling direction. The nuclear collisions, due to the large mass difference between the electron and the atomic nucleus, are nearly elastic: they strongly affect the direction of the incident electron, while the energy transfer is negligible. The energy dissipation of the incident electron mainly occurs through atomic electron excitations or ejections, plasmon excitations, phonons creation, and electron-polaron interactions. These scattering processes also influence the electron trajectory in the solid.

In the following, the inverse inelastic mean free paths relevant for describing all these phenomena are briefly described.

2.5.1 Electron-Atom Elastic Scattering

The electron-atom elastic scattering can be treated using the partial wave expansion method. It is based on the solution of the Schrödinger equation in a central field. The Mott theory [100] (relativistic partial wave expansion method) is based on a similar approach but requires, instead of the solution of the Schrödinger equation, the solution of the Dirac equation (in a central field). In reference [101, 102] one can find details of the present numerical calculations, based on the Mott theory [100]. An excellent review about the subject of the electron-atom elastic scattering cross section calculation was proposed by Jablonski, Powell and Salvat [103].

The Mott theory allows to calculate the differential and the total elastic scattering cross section by the knowledge of the phase shifts of the scattered electron wave. These phase shifts are calculated solving the Dirac equation up to a distance from the centre of the nucleus so large that the atomic potential can be ignored.

If θ is the angle of scattering, then the differential elastic scattering cross section is given by

$$\frac{d\sigma_{el}}{d\Omega} = |f|^2 + |g|^2, \quad (2.102)$$

where $f = f(\theta, E)$ is the direct scattering amplitude, $g = g(\theta, E)$ is the spin-flip scattering amplitude, E is the incident electron kinetic energy, and

$$d\Omega = 2\pi \sin\theta d\theta \quad (2.103)$$

is the infinitesimal solid angle. The direct and spin-flip scattering amplitudes are given by [104]

$$f(\theta, E) = \frac{1}{2iK} \sum_{l=0}^{\infty} \{(l+1)[\exp(2i\delta_l^-) - 1] + l[\exp(2i\delta_l^+) - 1]\} P_l(\cos\theta), \quad (2.104)$$

$$g(\theta, E) = \frac{1}{2iK} \sum_{l=1}^{\infty} [-\exp(2i\delta_l^-) + \exp(2i\delta_l^+)] P_l^1(\cos\theta). \quad (2.105)$$

In these equations, $K^2 = (E^2 - m^2c^4)/\hbar^2c^2$, E is the electron kinetic energy, m the electron mass, c the speed of light, P_l are the Legendre's polynomials, and

$$P_l^1(x) = (1 - x^2)^{1/2} \frac{dP_l(x)}{dx}. \quad (2.106)$$

The phase shifts δ_l^- and δ_l^+ can be computed by using the equation

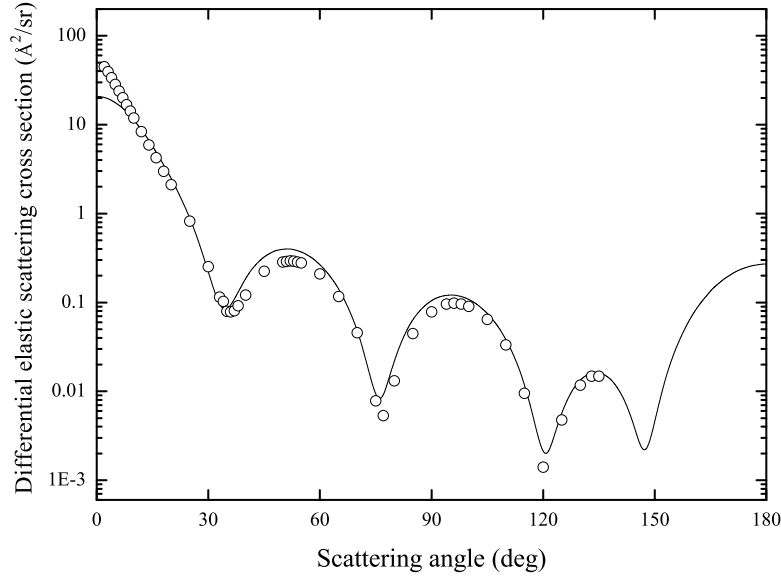


FIGURE 2.8: Differential elastic scattering cross-section of 300 eV electrons scattered by Hg. Solid line represents the present numerical calculation. Circles represent the Holtkamp *et al.* experimental data [105].

$$\tan \delta_l^\pm = \frac{K j_{l+1}(Kr) - j_l(Kr)[\zeta \tan \phi_l^\pm + (1 + l + k^\pm)/r]}{K n_{l+1}(Kr) - n_l(Kr)[\zeta \tan \phi_l^\pm + (1 + l + k^\pm)/r]}, \quad (2.107)$$

where

$$\zeta = \frac{E + mc^2}{\hbar c}. \quad (2.108)$$

In equation (2.107), $k^+ = -l - 1$, and $k^- = l$, j_l are the regular-spherical Bessel functions, and n_l the irregular-spherical Bessel functions. ϕ_l^\pm has to be computed as:

$$\phi_l^\pm = \lim_{r \rightarrow \infty} \phi_l^\pm(r), \quad (2.109)$$

where $\phi_l^\pm(r)$ is the solution of the Dirac's equation which can be reduced, as shown by Lin, Sherman, and Percus [106] and by Bunyan and Schonfelder [107], to the first-order differential equation:

$$\frac{d\phi_l^\pm(r)}{dr} = \frac{k^\pm}{r} \sin[2\phi_l^\pm(r)] - \frac{mc^2}{\hbar c} \cos[2\phi_l^\pm(r)] + \frac{E - V(r)}{\hbar c}. \quad (2.110)$$

Here, $V(r)$ is the electron-atom potential. A comparison between experimental and calculated differential elastic cross section is reported in Fig. 2.8.

2.5.2 Electron-Electron Interaction

Many details about the inelastic scattering theory and calculations can be found, for example, in Refs. [108, 109, 110, 111, 112, 113, 114, 64, 93] so that we will limit in the following to describe the main topics.

Penn [110] and Ashley [111] calculated the energy loss function using the experimentally determined optical dielectric function. Ashley [111] suggested, in particular, to calculate the inverse inelastic mean free path λ_{inel}^{-1} of electrons penetrating solid targets as follows

$$\lambda_{inel}^{-1}(E) = \frac{me^2}{2\pi\hbar^2 E} \int_0^{W_{max}} \text{Im} \left[\frac{1}{\varepsilon(0, w)} \right] L \left(\frac{w}{E} \right) dw. \quad (2.111)$$

In this equation m is the electron mass, e is the electron charge, $\hbar = h/2\pi$ (h is the Planck constant), E is the incident electron energy, and $W_{max} = E/2$. Note that in equation (2.111) the momentum transfer \mathbf{k} in the dielectric function $\varepsilon(\mathbf{k}, w)$ is set to 0 because the ε dependence on \mathbf{k} was factorised through the function L , given by [111]

$$L(x) = (1-x) \ln \frac{4}{x} - \frac{7}{4}x + x^{3/2} - \frac{33}{32}x^2. \quad (2.112)$$

The differential inverse inelastic mean free path $d\lambda_{inel}^{-1}(w, E)/dw$ – necessary for both the computation of the inelastic mean free path and of the probability $P_{inel}(W, E)$ providing the fraction of electrons losing energies less than or equal to W – can be calculated using experimental optical data for the evaluation of $\varepsilon(0, w)$, as follows

$$\frac{d\lambda_{inel}^{-1}(w, E)}{dw} = \frac{me^2}{2\pi\hbar^2 E} \text{Im} \left[\frac{1}{\varepsilon(0, w)} \right] L \left(\frac{w}{E} \right). \quad (2.113)$$

Notice that the dielectric function (and hence the differential inverse inelastic mean free path) can also be calculated by introducing an energy $\hbar\omega_k$ related to the dispersion relation so that

$$\varepsilon(k, \omega) = 1 - \omega_p^2 \sum_n \frac{f_n}{\omega^2 - \omega_n^2 - \omega_k^2 - i\gamma_n\omega}, \quad (2.114)$$

where γ_n are positive damping coefficients, f_n are the fractions of the valence electrons bound with energies $\hbar\omega_n$, and ω_p is the plasma frequency given by

$$\omega_p^2 = \frac{4\pi n e^2}{m}. \quad (2.115)$$

The dispersion relation has to be established taking in mind the Bethe ridge which imposes that $\hbar\omega_k$ should approach the value $\hbar k^2/2m$ as $k \rightarrow \infty$. The simplest way to achieve this results is, of course, to require that, according to Yubero and Tougaard [112] and to Cohen-Simonsen *et al.* [113],

$$\hbar\omega_k = \frac{\hbar k^2}{2m}. \quad (2.116)$$

Ritchie [108] and, then, Ritchie and Howie [109] proposed instead

$$\hbar^2 \omega_k^2 = \frac{3\hbar^2 v_F^2 k^2}{5} + \frac{\hbar^4 k^4}{4m^2}. \quad (2.117)$$

where v_F is the Fermi velocity.

Others important mechanisms of electron energy loss – particularly relevant when the electron energy is low (few eV) – are represented by the interaction of the electrons with the optical modes of the lattice vibrations or with the polarons. Notice that this kind of interactions are responsible of electron energy gain or loss with a probability of occurrence much lower than that of electron-electron energy loss, and almost negligible at the energy of interest in this thesis.

2.5.3 The Monte Carlo Scheme

If r_0 is a random number uniformly distributed in the interval $(0, 1)$, every step length Δs of each electron travelling in the solid is calculated assuming a Poisson distribution, so that $\Delta s = -\lambda \ln r_0$. In this equation, λ is the electron mean free path including all the scattering mechanisms. Its reciprocal, called inverse inelastic mean free path, can be expressed as the sum of all the inverse mean free paths of the interactions of the electrons with the target

$$\lambda^{-1} = \lambda_{el}^{-1} + \lambda_{inel}^{-1} \quad (2.118)$$

where

$$\lambda_{el}^{-1} = \frac{1}{N \sigma_{el}}, \quad (2.119)$$

$$\sigma_{el} = \int \frac{d\sigma_{el}}{d\Omega} d\Omega = \int (|f|^2 + |g|^2) d\Omega, \quad (2.120)$$

and N is the number of atoms per unit of volume in the target. Random numbers establish the kind of collision. Let $p_{el} = \lambda_{el}^{-1}/\lambda^{-1}$ be the probability that the collision is elastic, $p_{inel} = \lambda_{inel}^{-1}/\lambda^{-1}$ the probability that the scattering is an electron-electron inelastic collision. In what follows we will neglect energy loss mechanisms different from the latter, as, in the energy window we are interested in, the occurrence of electron-phonon or electron-polaron interaction is very unlikely. Before each collision the algorithm generates a random number r_1 uniformly distributed in the range $[0,1]$, so that, if it is less than or equal to p_{el} then the next collision will be elastic. If, on the other hand, $p_{el} < r_1 \leq p_{el} + p_{inel}$ then it will be an electron-electron inelastic collision.

If the collision is inelastic, the energy loss is calculated according to the specific inelastic scattering cross section (electron-electron, electron-phonon, or electron-other quasi-particle). If the collision is elastic, the scattering angle is calculated according to the Mott cross section. If the collision is elastic, the polar scattering angle ϑ is selected assuming that the probability of elastic scattering into an angular range from 0 to ϑ is a random number r_2 , uniformly distributed in the range $(0, 1)$. In other words, the integrated probability for scattering in the angular range from 0 to ϑ equals r_2 :

$$r_2 = \frac{1}{\sigma_{el}} \int_0^{\vartheta} \frac{d\sigma_{el}}{d\Omega} 2\pi \sin \theta d\theta. \quad (2.121)$$

In each inelastic collision, in order to find the energy loss W of an incident electron with kinetic energy E , it is necessary to calculate the function providing the fraction of electrons losing energies less than or equal to W . In each inelastic collision, indeed, the energy loss W is computed by utilising a random number r_3 , uniformly distributed in the range $(0, 1)$, so that

$$r_3 = \lambda_{inel} \int_0^W \frac{d\lambda_{inel}^{-1}}{dw} dw . \quad (2.122)$$

If one has to include different types of energy loss mechanism, in the case of electron-phonon interaction, the energy loss is given by the energy of the created phonon, while if a polaron is created, the electron is trapped in the solid.

Limiting our description to the cases of electron-electron scattering collisions, the polar scattering angle ϑ can be calculated by the use of the classical binary-collision model:

$$\frac{W}{E} = \sin^2 \vartheta . \quad (2.123)$$

The azimuth angle, for both elastic and inelastic collisions, is calculated as a random number uniformly distributed in the range $(0, 2\pi)$. When a slow electron reaches the target surface, it can be emitted only if its energy E and its direction Θ with respect to the normal to the surface satisfy the condition

$$E \cos^2 \Theta \geq \chi , \quad (2.124)$$

where χ is the potential energy barrier between the vacuum level and the minimum of the conduction band, the so-called *electron affinity*. Each electron is followed until it is trapped in the target or until it emerges from the target surface.

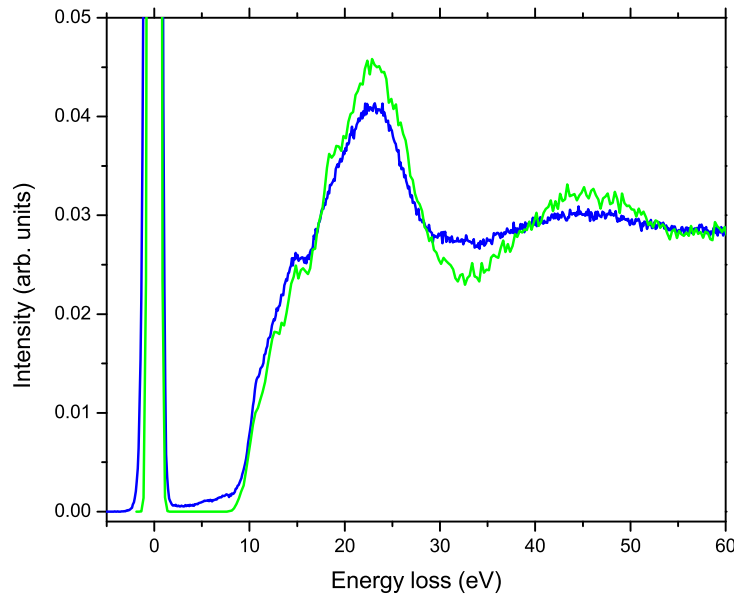


FIGURE 2.9: Experimental (blue line) and MC simulated (green line) EEL spectra excited by 2 keV electrons in SiO_2 . All spectra are normalized to a common area of the zero loss peak.

The REEL spectrum from SiO_2 was simulated by the Monte Carlo method, according to the strategy illustrated above. In this case, the energy loss function was calculated from optical data obtained from the atomic scattering factors by Henke et al. [115]. For energies

lower than 40 eV, the Buechner experimental energy loss function [116] was used. The energy loss function was extended beyond the optical limit using the Ashley approximation [111]. Surface effects were neglected.

A comparison between the experimental and simulated spectra, obtained under these approximations, is shown in Fig. 2.9 for electrons with 2 keV energy. Both spectra are normalized to a common area of the zero loss peak and loss energies up to 60 eV are considered. The figure shows that the simulated spectrum (green line) reproduces, though with higher intensity, the basic loss features of the experimental spectrum (blue line), i.e. the plasmon peaks corresponding to single (~ 23 eV) and double (~ 46 eV) excitations. In the energy region below 10 eV on the other hand, while the simulated spectrum shows the zero loss intensity expected for an ideal wide gap material, the experimental spectrum exhibits nonzero intensity, thus revealing the existence, for the real material, of defect-related states within the gap. These defect states are most likely due to electron-induced rupture of Si-O bonds, leading to O desorption from the SiO₂ surface. For a more detailed discussion of the Monte Carlo energy loss scheme and some applications, the reader is referred to [114].

2.5.4 The unified method at work: Auger spectra from SiO₂ including the energy loss

By treating the generation of the intrinsic spectrum and the superposition of extrinsic losses within a unified framework, Taioli and coworkers [62, 64], by using the mixed *ab initio* and Monte Carlo methods outlined above, have calculated the Si K-LL and O K-LL Auger spectra from SiO₂. The process under investigation is:



Electronic structure calculations have been carried out for the optimized geometries of the clusters shown in Fig. 2.10 by using a basis set of Hermite Gaussian functions with (s, p, d)-type character centered on the nuclei variationally optimizing the exponents of 6-31G* basis sets for oxygen and silicon atoms taken from a standard basis set [149]. In Table 4, we report the results obtained for the energies, referred to the vacuum level, and the relative decay rates after applying the space-energy similarity procedure.

In Fig. 2.11 we report the simulation of the Auger transitions, before and after superimposing energy losses to Auger emissions, with the initial core-hole in Si (left) and in O (right) (a detailed lineshape analysis can be found in Refs. [62, 64]). To account for the width of the incident radiation and for the analyzer resolution, computed spectra are convoluted with a Voight profile ($\Sigma_g = 1$ eV, $\Sigma_l = 0.1$ eV). Both spectra are normalised to unit height of the main peak without applying energy shifts. From Fig. 2.11 one can appreciate both the initial state dependence of the secondary spectrum and the clearly visible plasmon peaks, which enhance and broaden the Auger signal. For both spectra, Auger emission (satellite processes are not included in these calculations) is distributed over three groups of features, due to singlet transitions to the core-hole level of the atom initially excited, and less intense shoulders due to triplet transitions. The ‘band-like’ part of the spectrum, including all possible transitions from SiO₂ is recovered by the multi-site procedure described in Sec. 2.4.5.

On the right panel of Fig. 2.11, the O-KLL theoretical spectrum with superimposed energy losses (continuous line) is compared to its experimental analogue (dashed line), i.e.

the ‘as-acquired’ spectrum [64], which is in good agreement with previous measurements [117, 118, 119, 120, 121]. The overall good agreement between theory and experiments demonstrates the accuracy and the generality of our approach to the many-body scattering from solids.

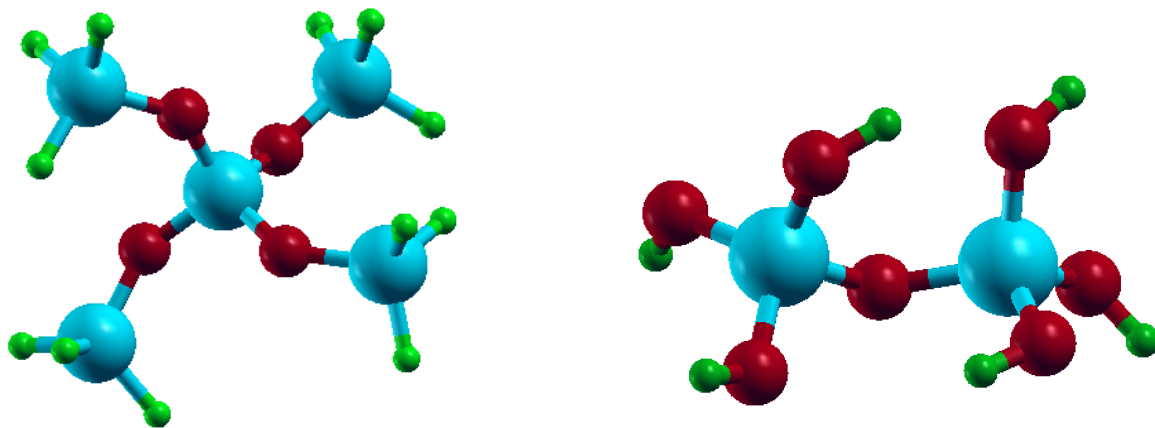


FIGURE 2.10: Sketch of the $\text{Si}_5\text{O}_4\text{H}_{12}$ (left) and $\text{Si}_2\text{O}_7\text{H}_6$ (right) nanocluster optimized structures. Oxygen is in red, silicon in light blue, hydrogen in green.

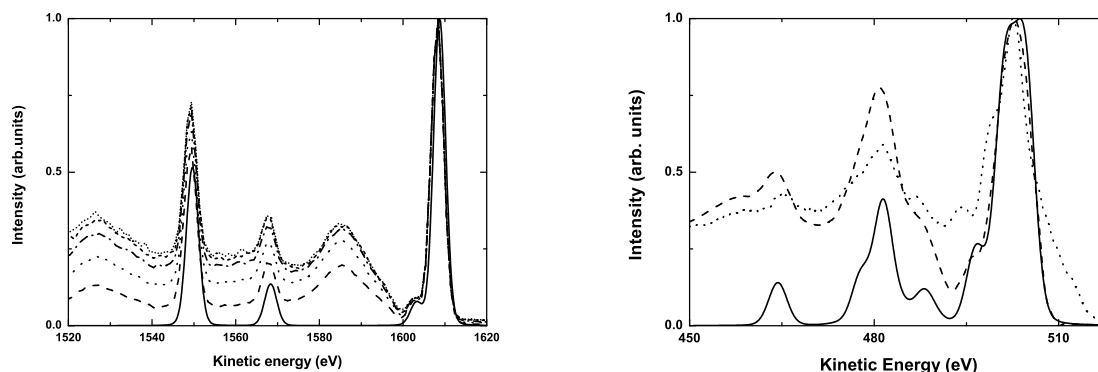


FIGURE 2.11: Left: Si $K - LL$ Auger spectrum in $\text{Si}_5\text{O}_4\text{H}_{12}$. Comparison between the quantum mechanical first principles calculation (continuous line) and the Monte Carlo results for different SiO_2 layer thickness increasing from the bottom to the top: 5 nm (dashed line), 10 nm (spaced point line), 15 nm (point-dashed line), 20 nm (small-dashed line), 25 nm (point line). Right: O $K - LL$ Auger spectrum in $\text{Si}_2\text{O}_7\text{H}_6$. Comparison between the Quantum Mechanical theoretical data (continuous line), the Monte Carlo results (dashed line) and the experimental data from Taioli et al. [64] (point line).

2.6 Conclusions

In this first chapter, we presented experiments and a critical overview of theoretical methods for interpreting electron spectra of atoms, molecules and solid-state systems. The general

TABLE 4: Kinetic energies (E_{kin}) in eV, referred to the vacuum level, and probabilities (Γ_α) in arbitrary units, normalised to the maximum peak, for the O $K-LL$ (left) and Si $K-LL$ (right) Auger localized states of the SiO_2 nanoclusters under investigations according to the double holes configurations (O $K-LL$, Si $K-LL$ columns) in the central silicon atom (oxygen) and final total spin S^2 (0=singlet, 1=triplet).

O K-LL	S^2	E_{kin}	Γ_α	Si K-LL	S^2	E_{kin}	Γ_α
$2s-2s$	(0)	458.75	0.570	$2s-2s$	(0)	1499.99	0.335
$2s-2p$	(0)	473.4	0.511	$2s-2p$	(0)	1544.66	0.860
$2s-2p$	(0)	477.41	0.653	$2s-2p$	(1)	1563.35	0.226
$2s-2p$	(0)	477.99	0.624	$2p-2p$	(0)	1598.19	0.362
$2s-2p$	(1)	481.64	0.156	$2p-2p$	(0)	1603.72	0.998
$2s-2p$	(1)	484.96	0.182	$2p-2p$	(0)	1603.73	1
$2s-2p$	(1)	485.73	0.190	$2p-2p$	(0)	1661.11	0.051
$2p-2p$	(0)	493.94	0.670	$2p-2p$	(0)	1714.15	0.039
$2p-2p$	(0)	497.89	0.801	$2p-2p$	(0)	1716.26	0.404
$2p-2p$	(0)	498.74	0.862				
$2p-2p$	(0)	500.28	0.829				
$2p-2p$	(0)	501.98	0.975				
$2p-2p$	(0)	502.45	1.0				

theoretical framework for this analysis has been the resonant multichannel scattering theory. Electron spectroscopies are, in fact, based on scattering processes in which the initial state consists of a projectile, typically photons or electrons, exciting a target to a resonant state, which has long lifetimes if compared to the collision time. This metastable state is embedded in the continuum of final states characterized by the presence of a few fragments, whose observation provides useful information on the properties of the system under study.

Even if the general theory of scattering and decay phenomena has been largely developed, its specific application to electron spectroscopies in condensed matter and, in several cases also to atoms and molecules, presents difficulties that have hindered the production of high quality theoretical spectra until recently. This is mainly due to computational problems related to treating a large number of decay channels, which prevent one from using numerical techniques for representing the electron as it moves outward through the field of the ionized system. Furthermore, another issue is represented by the need to account for shake processes and extrinsic energy losses due to the coupling with collective excitations.

To overcome these issues, in this chapter we presented a new theoretical method which does not suffer from the limitations of previous approaches, and allows one to reproduce accurately the experimental results in solids. This method provides an extension, useful in condensed matter applications, of Fano's formulation of the interaction between discrete and continuum states. It includes the combined effects of intrinsic and extrinsic features on spectral lineshapes so that computed spectra are directly comparable to acquired spectra, avoiding background subtraction or deconvolution procedures. This approach is sufficiently general to be applied not only to the analysis and interpretation of autoionization, Auger, NEXAFS and photoemission spectra in the variety of systems under consideration in this thesis, notably carbon-based nanostructures, but also to the study of other processes, as

we will see in the following chapters, since its central feature is the ability of calculating accurate wavefunctions for continuum states of extended systems.

Chapter 3

Epitaxy of nanocrystalline Silicon Carbide on Si(111) at Room Temperature

In this chapter we investigate the processes leading to the room-temperature growth of silicon carbide thin films by supersonic molecular beam epitaxy technique. We present experimental data showing that the collision of fullerene on a silicon surface induces strong chemical-physical perturbations and, for sufficient velocity, disruption of molecular bonds and cage breaking with formation of nanostructures with different stoichiometric character. We show that in these out-of-equilibrium conditions it is necessary to go beyond the standard implementations of density functional theory, as ab-initio methods based on the Born–Oppenheimer approximation fail to capture the excited-state dynamics. In particular, we analyse the C_{60} -Si collision within the non-adiabatic nuclear dynamics framework, where stochastic hops occur between adiabatic surfaces calculated with time-dependent density functional theory. This theoretical description of the C_{60} impact on the Si surface is in good agreement with our experimental findings.

3.1 Introduction

A fundamental problem in materials science is the understanding and control of epitaxy mechanisms for the production of high-quality crystals. In this chapter, we will focus on thin film crystal growth of silicon carbide (SiC). SiC has unique properties making it suitable for hard and protective coatings, optoelectronics and sensing [122]. It is the most promising alternative to Si for electronics devices working at high power/high frequency or in prohibitive conditions [123]. A new perspective is now being pursued for SiC as material for biomedical applications [124]. Being the substrate for synthesizing high quality graphene, SiC is expected to be one the most promising interface for Graphene-based electronics [125]. Despite the use of different growth approaches, SiC synthesis of high quality/low defects crystalline films still represents an open challenge [123, 126]. In particular, SiC epitaxy on Si is interesting for the cubic (3C) polytype synthesis, having potentially the best electrical properties [122]. In this case, Molecular Beam Epitaxy (MBE) has demonstrated to be a viable approach to 3C-SiC/Si synthesis at ~ 1200 K, using buckminsterfullerene (C_{60}) as C precursor. However, the epitaxy is critically affected by three factors: high lattice/thermal

mismatches between SiC and Si, the high material processing temperature ($T \geq 1100$ K), and Si diffusion through the SiC film, creating defects at the nano and micro-scale [126]. Even, in the usual thin film growth processes, a deposition temperature in excess of 1000 K is used to synthesize this material and speed up growth and nucleation.

Unfortunately, a higher growth temperature results in a larger number of crystallographic defects, such as voids, stacking faults and dislocations. The presence of these defects represents a substantial drawback as strongly influences the electronic and optical properties of SiC in a uncontrollable way. In SiC growth this temperature issue is emphasized, as one has to deal with the different thermal expansion (8% larger in SiC) of lattice-mismatched substrates (20% larger in Si) inducing stress and strain in the grains.

Therefore, synthesizing SiC at lower T is highly desirable to reduce side-growth processes, film defectivity and production costs. In this chapter we demonstrate the room T ($RT = 300$ K) synthesis of nanocrystalline 3C-SiC on the Si(111) 7×7 surface using the Supersonic Molecular Beam Epitaxy (SuMBE) approach. In this experiments, C_{60} translational kinetic energy (KE) reaches values of 30-35 eV by aerodynamic acceleration in vacuum [127, 128, 129, 130], activating chemical processes on the Si surface. Furthermore, we simulate the C_{60} -Si(111) 7×7 collision by Density Functional Theory (DFT) showing that the reason of the failure in explaining the C_{60} cage rupture at the observed kinetic energy is the neglect of the coupling between the electronic and nuclear degrees of freedom within the widely used Born–Oppenheimer (BO) approximation. To overcome this limitation, we decided to describe the coupled electronic-nuclear dynamics via a non-adiabatic approach [141]. In fact, recent modeling efforts point out the importance of non-adiabatic effects in describing various physical and chemical phenomena occurring at surfaces [142, 143, 144].

3.2 The SuMBE experiment and state-of-the-art

The study of high-energy cluster beam impact on solid surfaces is an old topic [131], both from a theoretical and experimental point of view, with many applications ranging from materials science, for sputtering [132] or thin film deposition [133], to chemistry, for initiating reactions [134, 135], and even nuclear fusion experiments [136]. Nevertheless, state-of-the-art experimental and theoretical investigations in high-energy cluster beam impacts are far from being conclusive on the nature of the chemical and physical processes occurring at the surface.

In this context, we put forward our approach as a viable way to grow materials, and we show how the studies of C_{60} impact on semiconductor surfaces might be important in materials science for the growth of carbon-based nanostructures.

In the SuMBE approach, by seeding a carrier gas, such as H_2 , He and Ar, within an injection chamber with the material to deposit (in our case carbon), and by using aerodynamical acceleration to reach supersonic velocities out of the injection cell, high fluence and directionality of the particles towards the Si surface can be obtained with a substantial freezing of the internal degrees of freedom to typical temperatures of a few kelvins [128]. In this way, different processes, such as cage disruption, covalent bond formation and, finally, growth can be activated. A sketch of the SuMBE experiment is reported in Fig. 3.1.

Notably, we apply this experimental technique to the hetero-epitaxy of SiC using su-

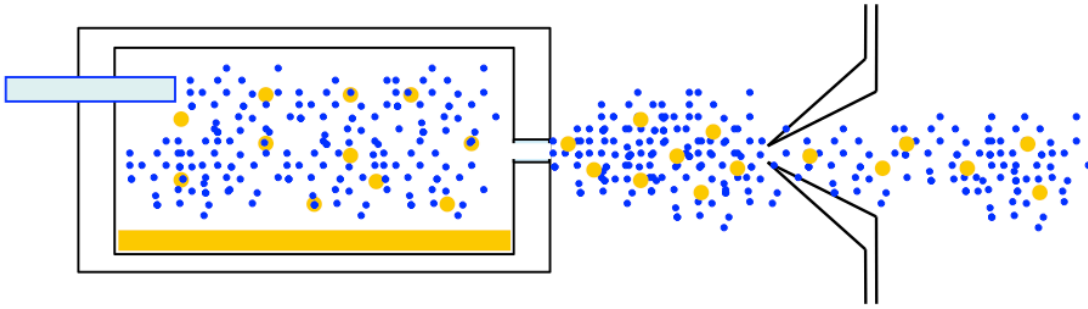


FIGURE 3.1: Layout of the SuMBE experiment.

personic fullerene.

Several reasons make C_{60} a very good precursor for SiC epitaxy. Firstly, C_{60} is the most abundant among fullerenes, and can be inexpensively obtained either by a discharge between two nearby graphite electrodes in an inert atmosphere or by other self-assembly mechanisms that have been recently proposed [137]. Secondly, this molecule has a large total mass and thus can be accelerated in the SuMBE experiment by exploiting the aerodynamical acceleration mechanism [129, 130, 138]. Finally, hydrogen is not present in pristine fullerene, avoiding the presence of an undesired chemical element into a SiC growing film.

While SiC epitaxy has been already achieved in experiments [129, 130, 138], the right stoichiometric ratio was obtained only above 800 K and for a beam kinetic energy of 5 eV. On the theoretical side, available computer simulations based on classical molecular dynamics (MD) [139] or tight-binding approach [140] are in complete disagreement with these experiments. In these studies Si structural order is maintained, with simple superficial permeation and no evidence of C_{60} cage breaking up to an energy per atom three times the experimental value obtained by SuMBE.

3.3 Experimental findings

C_{60} sub-monolayer (ML) films were deposited with two different precursor KEs of 30 eV (0.30 ML, 0.65 ML) and 35 eV (0.35 ML, 0.70 ML). The chemical/physical properties of the C_{60} films were investigated by in-situ X-ray (XPS) and ultraviolet (UPS) photoelectron spectroscopies. The C 1s core level (CL) analysis reveals different characteristics for the 35 (Fig. 3.2a, b) and 30 (Fig. 3.2c, d) eV KEs film, but all peaks can be well reproduced by the same four components, labeled P1, P2, P3 and P4. P1 is located at a binding energy (BE) of 283.03 eV and represents photoemission of C in SiC, amorphous/stoichiometric carbide [145, 146] and 3C-SiC [147]. P2 (BE = 283.73 eV) is associated to nonstoichiometric SiC compounds [148] or to hexagonal SiC polytypes [149]. P3 (BE = 284.46 eV) and P4 (BE = 285.10 eV) are related to C_{60} forming few covalent bonds [150, 145, 151, 152, 153, 129, 130, 146] or weak interaction with Si. P1 and P2 were observed only in experiments of C_{60} on Si at $T \geq 1000$ K, P3 at $T = 700$ K, while P4 is typical of physisorbed cages. As shown in Fig. 3.2e, at 35 eV C_{60} KE, the reacted species peak areas (P1+P2) represent more than 50% of total C 1s CL for both films, with P2 being always the most intense peak. Differently, at 30 eV C_{60} KE the reacted species decrease their weight going from 0.30 to 0.65 ML, with P4 becoming the most intense. In terms of absolute intensity, at the higher coverage all peaks show a significant increase at 35 eV C_{60} KE, while at 30 eV

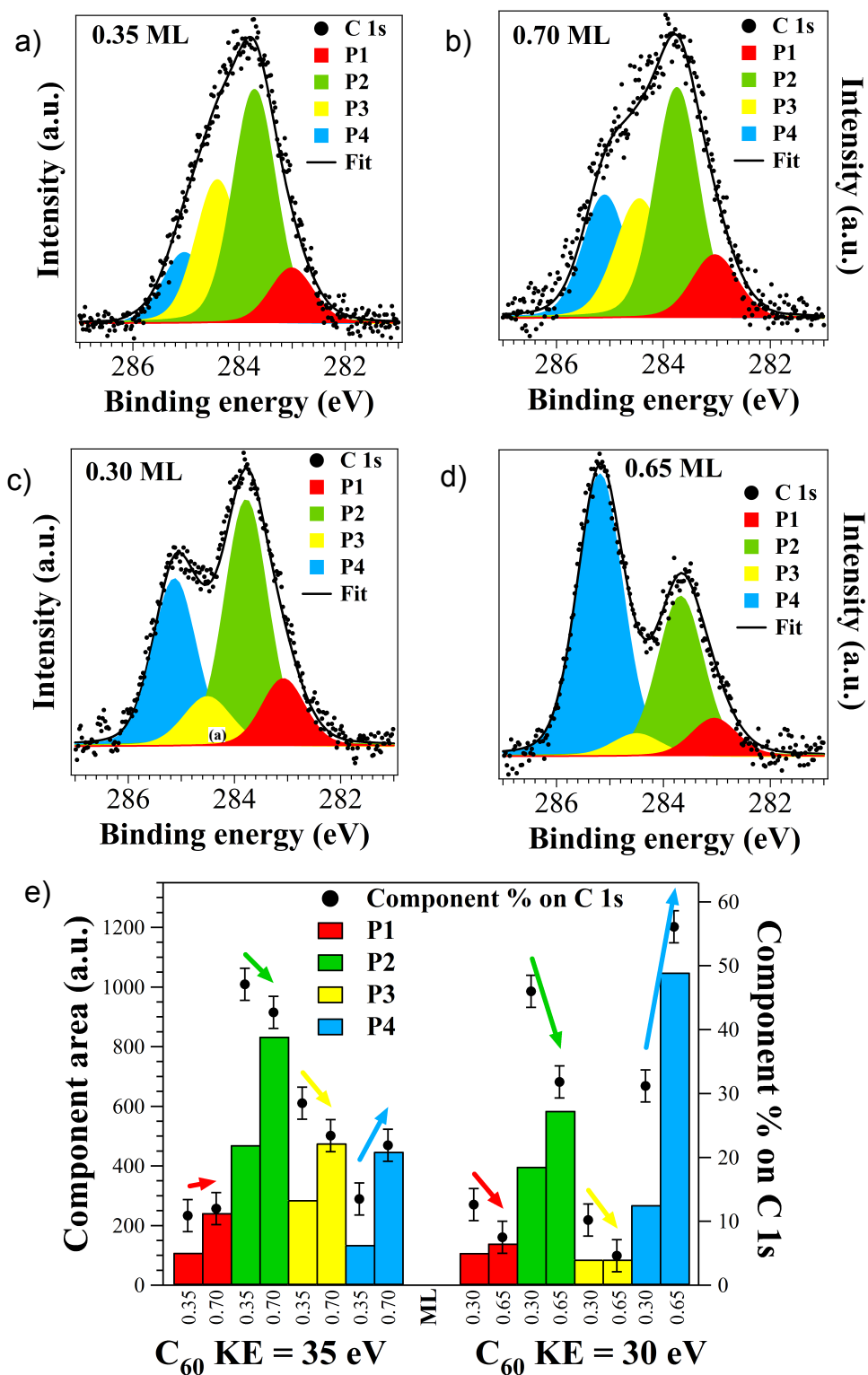


FIGURE 3.2: C 1s CLs (peak normalized in height) of films grown at C₆₀ KEs of 35 eV (a, 0.35 ML; b, 0.70 ML) and 30 eV (c, 0.30 ML; d, 0.65 ML). Components correspond to C in 3C-SiC (P1), SiC (P2), reacted (P3) and physisorbed (P4) C₆₀. (e) Component area and percentage (variation followed by arrows) on C 1s area.

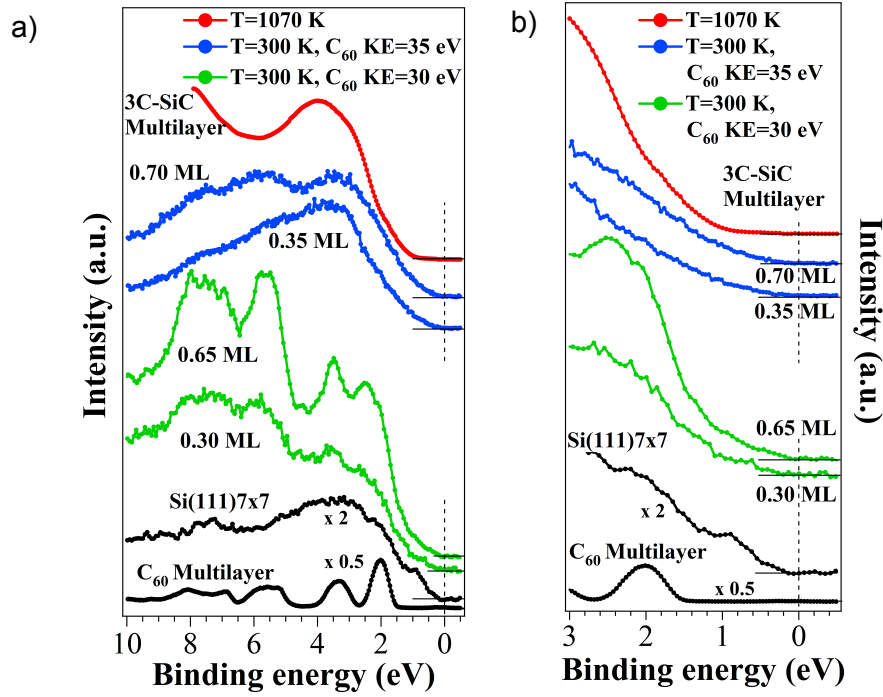


FIGURE 3.3: (a) VBs of films grown at C_{60} KEs of 35 eV and 30 eV, and of substrate, C_{60} multilayer and 3C-SiC film, zoomed in the 0-3 eV BE range (Fig. 3.2e). (b).

the slight gain of the reacted species results in a strong enhancement of those physisorbed (Fig. 3.2e).

Fig. 3.3a shows the valence band (VB) spectra from UPS for C_{60}/Si films at 35 and 30 eV KEs, together with typical VB of 3C-SiC, C_{60} multilayer and Si(111) 7×7 . The 3C-SiC VB is characterized by two broad structures at about 4 and 9 eV, related to the p-like and sp-like molecular orbitals (MO). The C_{60} spectrum has several distinct features, with peaks at 2.0 and 3.4 eV attributed to the highest occupied molecular orbital (HOMO) and to the so-called HOMO-1. The Si(111) 7×7 VB shows a metallic character, with surface states at 0.2 and 0.9 eV (Fig. 3.3b) and an overall intensity lower than C_{60} and SiC, leading to VB of C_{60}/Si films mainly dominated by the organic features. VBs of films at 30 eV C_{60} KE partially resemble the organic multilayer structures with a +0.3 eV BE shift, differently from what observed in MBE experiments at RT [145, 151, 154] and $T = 670$ K [151, 145]. C_{60} features are superimposed to an intense broad band with increasing intensity from 0.35 ML to 0.65 ML, thus not representative of the Si(111) 7×7 substrate but other carbon species. The Si surface states are depleted or absent, while two structures are present at 2.0 and 2.4 eV. Considering the observed BE shift, the 1.7 eV feature represents the former HOMO while the 2.1 eV peak has been assigned to C_{60}/Si chemical interaction at RT [153, 151, 155] and at $T = 570$ K [150, 145, 151]. Therefore, these films are mainly due to cages physisorbed and showing Si-C covalent bonds.

VBs of films at 35 eV C_{60} KE are characterized by intensity higher than for bare Si.

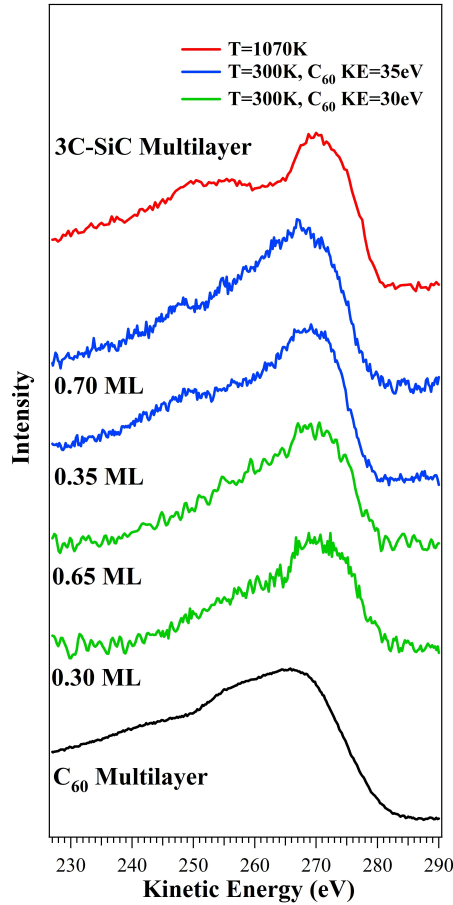


FIGURE 3.4: Auger analysis of the 0.35-0.70 ML films at 35 eV C₆₀ KE, 0.30-0.65 ML films at 30 eV C₆₀

A main structure is present at ~ 3.7 eV, while the Si(111) 7×7 surface states are absent. C₆₀ MOs are detectable only in the 5-10 eV range at 0.70 ML. Similar VB has been found only for C₆₀/Si(111) 7×7 MBE experiments at $T \geq 1140$ K [150, 145, 151] when synthesis of 3C or amorphous SiC islands is achieved. The bands in the 4-10 eV range at 0.70 ML resemble those of C₆₀ but with major broadening. A similar picture has been found only at $\simeq 1070$ K and is evidence of cage breaking [150, 145, 151]. Thus, SiC is present in both films, and broken cages at 0.70 ML. Comparing with MBE experiments, XPS and UPS analysis clearly highlights the role of the C₆₀ KE in activating chemical/physical processes otherwise forbidden in thermal equilibrium conditions at RT.

Further confirmations of the SiC growth come from Auger electron spectroscopy analysis. The AES analysis has been performed at a primary electron energy of 3 keV and a retarding ratio = 20. The Si LVV emission is dominated by the signal coming from the substrate surface, and it is not possible to extract reliable information about the overlayer. Therefore, we focus our analysis on the C-KVV peaks of the 0.35-0.70 ML films at 35 eV C₆₀ KE, and of the 0.30-0.75 ML films at 30 eV C₆₀ KE, which are shown in Figure 3.4. The typical Auger emission in the 250-270 eV kinetic energy range from a C₆₀ multilayer is

characterized by a broad band, while 3C-SiC shows a narrower and better defined feature shifted to higher KEs, together with other two bands in the 240-255 eV range that are absent in case of physisorbed fullerenes (see Fig. 3.4).

The 0.35 and 0.70 ML films at 35 eV C_{60} KE show the typical features of 3C-SiC in the 240-255 eV range and a well defined band at about 270 eV, becoming broader and shifted to lower KEs at the higher coverage. This suggests the presence of the carbide in both films, together with other chemical species becoming dominant at 0.70 ML, leading to an Auger emission more similar to that of physisorbed C_{60} . The 0.30 and 0.65 ML films at 30 eV C_{60} KE show less defined features, however the broadening and shifting to lower KEs of the main peak at $\simeq 270$ eV at increasing fullerene coverage unambiguously put in evidence the presence of SiC and physisorbed carbon species, the latter becoming dominant at 0.70 ML. We are dealing with SiC islands and not a well defined film, considering the very low C_{60} layer thickness. Physisorbed fullerenes are present, but the differences with the multilayer Auger emission lineshape suggest they are the dominant carbon chemical species only in the 0.65 ML film at C_{60} 30 eV KE. The AES analysis further stress the results obtained by XPS and UPS. The presence of SiC can be found in all films, with a more significant quantitative contribution for the 35 eV KE fullerene films. At increasing coverage, the weight of physisorbed cages raises but the complexity of the AES peaks lineshape clearly suggests the presence of other carbon chemical species, better identified in the XPS and UPS analysis.

The higher efficiency observed at 35 eV suggests the presence of a C_{60} KE threshold close to 30 eV, while the presence of crystalline 3C-SiC envisages a role of the precursor KE in improving also the film structural order. Low T SiC growth by Ionized Cluster Beam deposition has been studied before, but the debate on this technique [156] is still great and the one order of magnitude higher KE of the clusters leads to chemical and physical processes different from those typical of MBE and SuMBE.

Low energy electron diffraction (LEED, 50 eV) analysis has been performed on the four C_{60} sub-monolayer films. Si(111)7 \times 7 shows the well known sharp diffraction pattern (Fig. 3.5a). The two films at lower coverage have LEED pattern with a diffused background superimposed to the Si 7 \times 7 features, while the 0.65 ML at C_{60} KE = 30 eV shows only the Si 1 \times 1 hexagonal spots. Similar results have been reported for RT MBE experiments [145, 151, 157], suggesting that the Si surface structure is hardly affected by the presence of the physisorbed C_{60} layer. The 0.70 ML film at C_{60} 35 eV KE (Fig. 3.5b) shows features of the 7 \times 7 surface but also new hexagonal 1 \times 1 extraspots, wider than the Si corresponding features. Subtracting the Si pattern to that of the 0.70 ML film (Fig. 3.5c), we obtain black and white features corresponding to the Si(111)7 \times 7 and new 1 \times 1 patterns. The lattice parameter of the new pattern is typical of a 3C-SiC(111)1 \times 1 structure [122]. In MBE experiments, LEED analysis revealed an ordered carbide only at $T \geq 1300$ K [145], while at $\simeq 1100$ K SiC amorphous islands are formed [150, 157]. The observed superposition of Si and SiC LEED patterns suggests presence of 3C-SiC/Si islands, with lateral dimensions of few tens of nm, considering a typical 10-20 nm LEED electron coherence length [158]. As chemical analysis has shown the presence of the carbide in its cubic phase in all films, thus the SiC pattern absence in the remaining three films suggests the presence of smaller 3C-SiC islands, not detectable by LEED analysis.

Ex-situ atomic force microscopy (AFM) and transmission electron microscopy (TEM) analysis were performed on the 0.65 ML deposited at 30 eV KE, that is characterized by $\geq 50\%$ of physisorbed C_{60} and $\sim 7.5\%$ of SiC (from XPS analysis), but absence of 3C-SiC

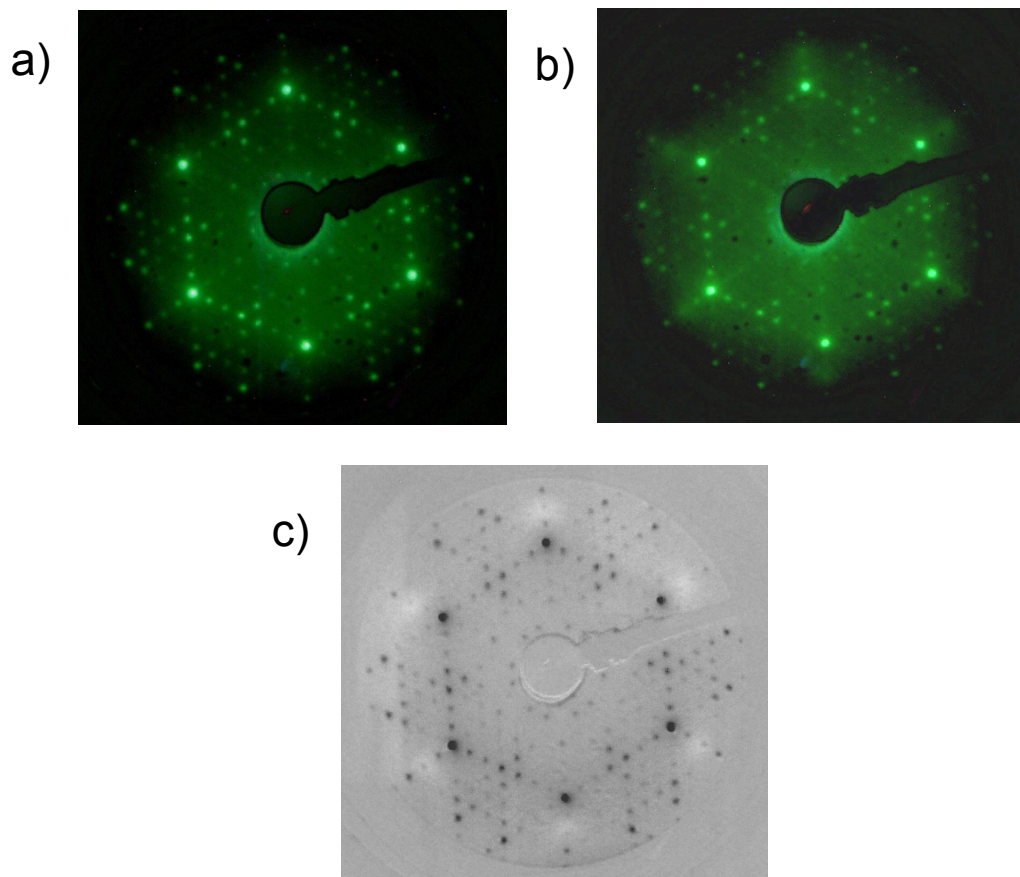


FIGURE 3.5: (a-c) 50 eV LEED patterns. (a) Si(111)7 \times 7. (b) C₆₀/Si(111)7 \times 7 film, 0.70 ML, 35 eV KE, showing 3C-SiC 1 \times 1 extraspots. (c) Subtraction of image (a) to image (b): dark areas belong to the 7 \times 7 pattern, white spots to the new 3C-SiC 1 \times 1.

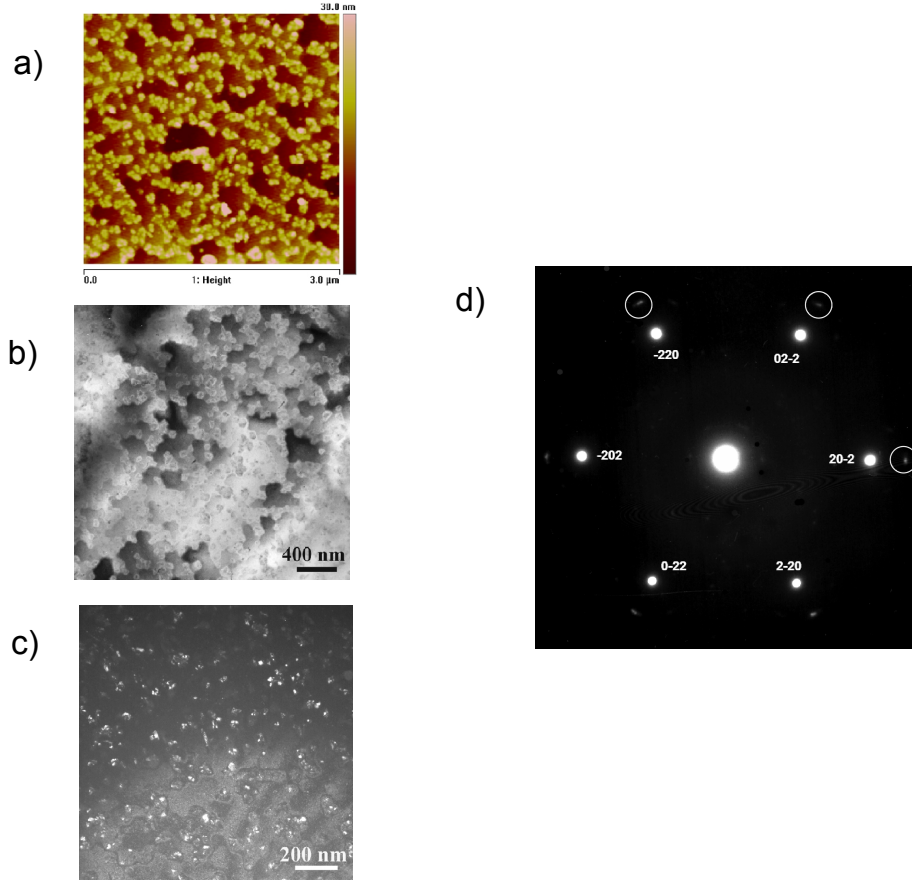


FIGURE 3.6: a-d) $C_{60}/Si(111)7\times 7$ film, 0.65 ML, 30 eV KE. (a) AFM image. (b) TEM diffraction pattern, with Si(111) bright spots and 3C-SiC phase weak reflections (circled spots). (c) Bright-field TEM image. (d) Dark-field TEM image.

LEED pattern. The surface morphology (Fig. 3.6a) shows the typical Si(111) terraces separated by multiple-atomic steps. A high density of nanometer-sized island grains along the step edges, some tens of nm wide and about 10 nm high, are revealed on the terraces. In TEM analysis, the diffraction pattern in the (111) Si zone axis (Fig. 3.6b) shows spots that can be unambiguously attributed to 3C-SiC, epitaxially grown on Si(111) and with lattice parameters of a completely relaxed structure. Bright-field TEM image (Fig. 3.6c) shows terraces and nanograins mainly deposited along the step edges, according to AFM. Dark field TEM image (Fig. 3.6d), taken using one of the the (220) reflection of the 3C-SiC phase, indicates that the small grains at the Si terrace edges are nanometer-sized 3C-SiC islands. Their small size, ~ 10 nm, is probably below the detectability of our LEED set up. The low Si and C mobility at RT would suggest the carbide formation of one or very few layers on Si surface. Due to the lattice mismatch between 3C-SiC and Si(111), a single epitaxial carbide layer would be characterized by a strained structure, but we have found 3C-SiC ~ 10 nm high islands with a completely relaxed lattice. This envisages the presence of a non negligible C but also Si atom mobility induced by C_{60} KE. The differences in chemical

and structural properties for the films grown at the two C_{60} KEs confirm the presence of a precursor energy threshold close to 30 eV in inducing several physical processes at the film surface at RT, first and foremost the cage breaking. This process triggers all further developments and thus we tackled the C_{60} -Si collision modeling by a number of theoretical and computational tools to obtain a reliable description of the experimental findings.

3.4 Theory and computation of SiC epitaxy: DFT, DFTB, TDDFT

The problem of the SiC epitaxy by SuMBE technique has been approached by several techniques at different level of accuracy in order to gain a satisfactory, even though mostly qualitative, insight into the mechanisms leading to the C_{60} cage break. In the following subsections we briefly outline the main features of the methodologies applied to the description of the C_{60} -Si(111) surface impact.

3.4.1 Density Functional theory

Initially, calculations have been performed within the framework of density functional theory (DFT), using the *ab-initio* total-energy and molecular dynamics program VASP [159, 160, 161, 162].

The DFT approach is based on the minimization of the Kohn–Sham energy functional

$$E[n] = \sum_i \left\langle \psi_i \left| -\frac{1}{2}\nabla^2 + V_{\text{ext}}(r) + \frac{1}{2}V_{\text{H}}[n](r) \right| \psi_i \right\rangle + E_{\text{xc}}[n] + E_{\text{II}}, \quad (3.1)$$

where

$$n(r) = \sum_i |\langle r | \psi_i \rangle|^2, \quad (3.2)$$

$$V_{\text{H}}[n](r) = \int d^3r' \frac{n(r')}{|r - r'|}, \quad (3.3)$$

$$V_{\text{ext}}(r) = -\sum_k \frac{Z_k}{|R_k - r|}, \quad (3.4)$$

$$E_{\text{II}} = \frac{1}{2} \sum_{k \neq n} \frac{Z_k Z_n}{|R_k - R_n|}. \quad (3.5)$$

In the previous equations, $|\psi_i\rangle$ are the Kohn–Sham (KS) orbitals, $n(r)$ is the electronic density of the system, $E_{\text{xc}}[n]$ is the exchange-correlation functional, E_{II} is the ion-ion Coulomb potential, Z_k is the charge for the k -th nucleus, and we have used atomic units.

Thermal excitations of electrons have been included via the finite-temperature formulation of DFT [166] in which the variational quantity to be minimized is the free energy of the electrons, $F_V(T) = E_V(T) - TS_V(T)$ where E is the sum of the kinetic, electron-nucleus, Hartree and exchange-correlation energies and $S = -k_{\text{B}}T \sum_i [f_i \ln f_i + (1 - f_i) \ln(1 - f_i)]$ is the electronic entropy, k_{B} being the Boltzmann constant and f_i the Fermi-Dirac occupation number of orbital i .

Molecular dynamics simulations (with the exception of the non-adiabatic molecular dynamics) were performed in the micro-canonical ensemble, using a time step of 1 fs. The simulations used an efficient charge density extrapolation which speeds up the simulations by approximately a factor of two [167].

3.4.2 Density functional tight-binding

The density-functional tight-binding (DFTB) method [168, 169, 170] is based on a second-order expansion of the density appearing in the full DFT approach to electronic structure calculations. In this approach the energy of a system of atoms is expressed as a sum of tight-binding-like matrix elements, a Coulomb interaction, and a repulsive pair-potential. The parameters appearing in the formulae expressing these contributions are evaluated using high-level electronic structure methods, and are highly transferable to different physical and chemical environments.

In the DFTB approach, the density is written as $n(r) = n_0(r) + \delta n(r)$, where $n_0(r)$ is the superposition of the *isolated* atomic electron densities. Expanding Eq. (3.1) to the second order in $\delta n(r)$, one can rewrite the DFT energy functional as [171, 172]

$$\begin{aligned}
 E[n_0 + \delta n] &= \sum_i \left\langle \psi_i \left| -\frac{1}{2} \nabla^2 + V_{\text{ext}}(r) + V_{\text{H}}[n_0](r) + V_{\text{xc}}[n_0](r) \right| \psi_i \right\rangle \\
 &+ \int d^3r d^3r' \left(\frac{\delta^2 E_{\text{xc}}}{\delta n(r) \delta n(r')} - \frac{1}{|r - r'|} \right) \delta n(r) \delta n(r') \\
 &- \frac{1}{2} \int d^3r V_{\text{H}}[n_0](r) n_0(r) + E_{\text{xc}}[n_0] + E_{\text{II}} - \int d^3r V_{\text{xc}}[n_0](r) n_0(r) \quad (3.6)
 \end{aligned}$$

where $V_{\text{xc}}[n_0](r)$ is the functional derivative of the exchange-correlation energy $E_{\text{xc}}[n]$. Equation 3.6 is the starting point of the tight-binding approach, where the atomic-centered KS orbitals $|\psi_i\rangle$ are expressed in a local basis of tightly-bound electrons. The matrix elements of the first term in Eq. (3.6) in this basis can be evaluated using high-level DFT calculations, whereas the last four terms are usually lumped together in a *repulsive potential* dependent only on the properties of the isolated atoms [172]. The second term should be in principle evaluated self-consistently, and is sometimes neglected. Its inclusion gives rise to the so-called Self Consistent Charge (SCC) DFTB method [173].

The computational cost of this approach to electronic structure calculation is at least two orders of magnitude cheaper than the corresponding full DFT. As a result of these substantial speed gain, DFTB may be used to investigate much larger systems than those accessible by DFT, and – for what concerns the motion of the nuclei – it is possible to follow their evolution for much longer timescales. Recently, DFTB-based approaches have been benchmarked for many systems, including the calculation of stable fullerene isomer structures [174], where they have displayed an accuracy comparable to DFT. We used the DFTB+ program [175] to perform the DFTB calculations described below. The tight-binding parameters that we have adopted are the `mio` and `znorg` sets, obtained from the website <http://www.dftb.org>.

3.4.3 Time-dependent DFT

Time-dependent density functional theory (TDDFT) generalizes DFT to time-dependent problems. In this approach, the density of a complex interacting many-body system is

thus time-dependent and the goal is to solve the Schrödinger equation with a frequency-dependent exchange-correlation functional in the presence of external fields. The time-dependent density is calculated within linear response theory, and its evolution includes in principle an unlimited number of excited states of the system. Excitation eigenvalues ω_k and eigenvectors $|\phi^{LR}\rangle$ have been obtained by solving the secular equation in the Tamm-Dancoff approximation [176]:

$$\sum_{ij}^{N_{occ}} (H^{KS} \delta_{ij} - \epsilon_{ij}) |\phi_j^{LR}\rangle + \delta V(\omega) |\phi_i\rangle = 0 \quad (3.7)$$

where N_{occ} is the number of occupied orbitals, $|\phi_i\rangle$ and ϵ_{ij} are the Kohn-Sham eigenvectors and eigenvalues, H^{KS} and $\delta V(\omega)$ are the DFT Kohn-Sham Hamiltonian and the linear response effective potential. The latter represents the correction to the DFT energies of the first-order perturbation in the density. TDDFT calculations have been performed using the CPMD code [177]. Further details on the actual implementation of the above described approaches for the description of SiC epitaxy will be outlined in the following sections.

3.5 BO-DFT simulation of the C₆₀-Si(111)-(7×7) collision

While our experiments of deposition at the kinetic energy of ~ 35 eV on Si provide evidence of the C₆₀ cage breaking at room temperature, available theoretical results are in complete disagreement with this finding.

A first attempt at modeling was made by Averback [139] using the Tersoff potential [178] in the framework of classical molecular dynamics simulations. Cage disruption was found occurring only for an impinging kinetic energy larger than 100 eV. Similar results have been obtained by Galli and coworkers [140], in a more refined model using a tight-binding approach. In this case, the minimum impact kinetic energy to obtain heavy damage of the diamond surface and fragmentation of the C₆₀ cage is predicted to be above 200 eV.

Both of these predictions are many times higher than our experimental value. In the light of these results, it is clear that a theoretical explanation of the fragmentation mechanism is missing and a number of open questions remain unsolved. In the following we will address these issues by progressively increasing the level of accuracy of the computational modeling, in order to understand the cage breaking mechanism, which initiates all the physical-chemical processes of the SiC growth.

We ran a first set of simulations looking for a possible mechanical explanation of the cage fragmentation, namely a mechanism based on highly-excited vibrational states, bringing about the breaking of the bonds on a timescale of picoseconds, within the reach of *ab-initio* molecular dynamics.

As a first step, we chose the density-functional tight-binding (DFTB) method [168, 169, 170], which is a computationally low-cost and systematically improvable approximation of the full density-functional theory (DFT), with generally only modest compromises on the accuracy.

We performed simulations on a series of initial kinetic energies in the range 35 eV to 450 eV. The Si(111) surface reconstructed (7 × 7) was simulated by means of a slab containing 494 atoms, passivated by 49 hydrogen atoms, as shown in Fig. 3.7.

We found that for energies less than 300 eV the C_{60} molecule undergoes large distortion upon impact onto the surface, but does not fragment. The cage breaking occurs only from 300 eV upwards.

This conclusion is strongly inconsistent with our experimental data. In order to check whether a possible reason for this failure was due to the limited accuracy of the forces calculated in the DFTB framework, we performed a number of trials using full DFT. DFT-based simulations, indeed, have been used successfully to investigate a wide spectrum of phenomena, ranging from the response to macroscopic electric fields [179, 21], melting [62], and adsorption [95, 97], although several known failures exist, such as underestimation of the band-gap in insulators and semiconductors [180, 181].

The unit cell we used in the calculation measures 26.9 Å along the short diagonal, while the spacing between the adatoms is 7.68 Å within the triangular subunit, 6.65 Å across the boundary of the triangle and the diameter of the corner hole is 13.3 Å. The dimension of the cell along the collision direction, orthogonal to the surface plane, depends on the number of Si layers in the simulation cell, ranging from 30 to 50 Å for 5 and 8 layers, respectively. In all DFT calculations, the ion-electron interaction has been described using the projector augmented (PAW) technique [163] with single-particle orbitals expanded in plane waves with a cutoff of 400 eV, which ensures convergence of the electronic structure (band gap) and of the total energy within chemical accuracy (0.01 eV). Only the Γ -point has been used to sample the Brillouin zone, due to the large number of atoms in the unitary cell (several hundreds). We tested different exchange-correlation functionals, notably based on the Local Density Approximation (LDA) [164] and generalized-gradient correction (GGA-PBE) [165], and we found that the dynamics of the system, calculated as described in Sec. IV, is independent on the choice of the functional.

We found that even this more accurate level of theory does not modify the previous picture, although we tested various impact angles, different surface impact sites, several orientations of the impinging molecule, and defects on the fullerene cage enhancing the reactivity, such as found in $C_{57,58,59}$ [182] without finding appreciable changes in the energy required for breaking the cage.

Furthermore, we ran a simulation with a negatively charged cell to take into account possible charge transfer due to clustering between fullerenes or scattering with the carrier gas.

The charge transfer from Si to fullerene is then facilitated by the lowering of the HOMO-LUMO gap, decreasing from 1.65 eV to 0.8 eV at the penetration stage. Nevertheless, cage rupture is still observed at energies much higher than the experimental one.

Finally, we tried to increase the fullerene flux by simulating a collision of two C_{60} impinging one on top of the other on the Si(111) surface, as shown in Fig. 3.8. Even in this case, the minimum kinetic energy needed to obtain the cage rupture was around 300 eV. While a mechanical disruption of the C_{60} cage can be safely ruled out based on the previous analysis for the kinetic energies observed in the experiments, BO-MD simulations reported in the literature [183, 184] show that a break may occur some time after a collision if the total internal energy of C_{60} (defined as the difference between the kinetic energy of the bouncing fullerene and the center of mass kinetic energy) is between 30 and 40 eV. This is a further clear indication that this approach must be missing some crucial physical process: the experimental evidence of the breaking of C_{60} at 35 eV of initial translational kinetic energy cannot obviously be consistent with a final internal kinetic energy of the molecule of 30 – 40 eV. However, we performed an investigation of the dependence of the

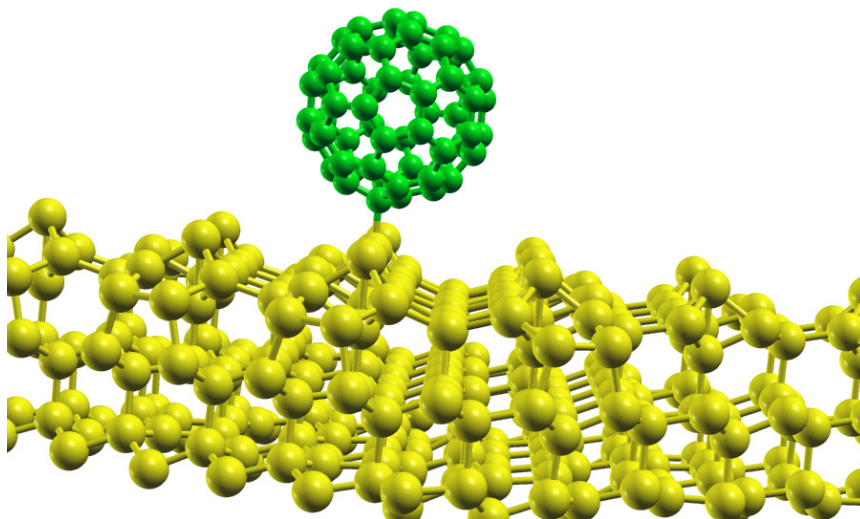


FIGURE 3.7: Layout of the experiment. Silicon surface cleaved along the (111) direction and reconstructed (7×7), highlighting the 12 adatoms protruding from the surface plane. At some distance from the surface we depict the impinging C_{60} molecule.

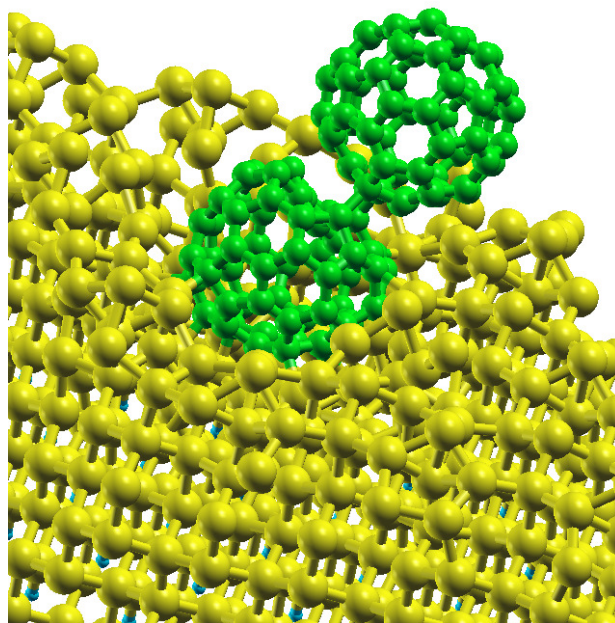


FIGURE 3.8: Two C_{60} molecules impinging on the Si surface one on top of the other.

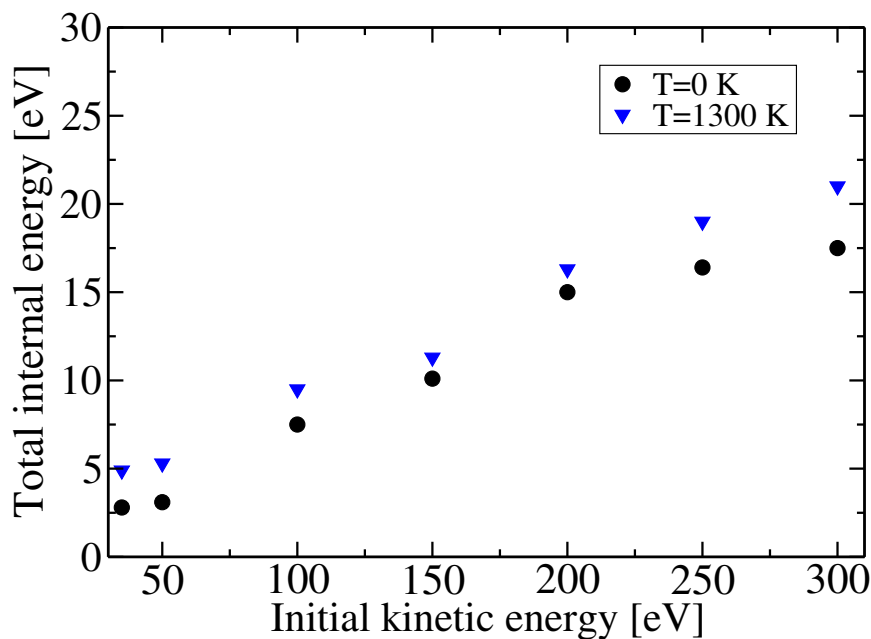


FIGURE 3.9: Internal kinetic energies of fullerene after bouncing back from the surface for room temperature (300 K, black circles) and 1300 K (downward blue triangles) from BO-DFT calculations. Temperature is the same for both surface and C_{60} .

final internal kinetic energy of fullerene as a function of impinging kinetic energy. The results are reported in Fig. 3.9, and show that for the impinging kinetic energies under investigation (35 to 300 eV), the fullerene internal energy after the collision ranges from 3 to 17.5 eV, as shown by the circles in Fig. 3.9. An enhancement of the substrate temperature to 1300 K increases the internal kinetic energy (downward triangles, blue in the on-line version in Fig. 3.9) but not so much as to cause a rupture in a short time.

We also hypothesized that cage breaking could happen on a longer timescale than that one simulated by *ab-initio* MD. To investigate this possibility, long ($\simeq 50$ ns) classical MD simulations were performed by employing the Brenner–Tersoff empirical potential [178]. For the impinging kinetic energies under investigation (35 to 300 eV) we did not observe any fragmentation, whereas we did observe the fullerene chemisorption. Of course, the absence of fragmentation within a time-scale which is still relatively short does not prove that the process might be kinetically hindered, but it provides further indications that some important feature is missing in BO-MD.

3.6 Non-adiabatic molecular dynamics

The results reported so far exclude a simple mechanical picture for the fragmentation of the cage at the kinetic energy experimentally measured. Therefore, this failure must be due to physical processes that are not considered in the BO-DFT description of the collision. The first hint that electronic excitations may be important to break the C_{60} cage comes from the observation that strong radiation fields lead to charge photo-excitation, ionization and plasmon excitation inducing the fragmentation of buckminsterfullerene [185, 186]. In particular, upon high-intensity femtosecond laser excitation, C_{60} undergoes a ‘giant’ plasmon resonance at 20 eV. This collective charge excitation leads to an efficient

energy transfer to the vibrational modes of the molecule and to a possible rupture of the cage via two-plasmon excitation [187]. In our case, the role of the external electromagnetic field is played by the intense dipole moment created by the impact on the metallic surface of Si. Due to the short duration of the impact, electrons cannot instantaneously follow the nuclear positions, and therefore ‘lag behind’ the nuclei during the collision. In order to explore this alternative route to cage breaking it is necessary to take into account electronic excitations and their coupling to nuclear motion. Consequently, our computational modeling should go beyond BO-DFT and therefore adopt a method capable of treating excited electronic states.

The BO approximation relies on the assumption that ionic and electronic motion proceeds on decoupled timescales. In C_{60} the 1.6 eV band-gap corresponds to emission in the frequency region of 10^{15} Hz, and the collisional time scales in our case are of the order of few tens of femto-seconds, $\simeq 10^{14}$ Hz. The Massey parameter, defined as the ratio between nuclear (τ_p) and electronic characteristic times (τ_e), is of the order of $\xi = \tau_p/\tau_e \simeq 1 - 10$. In this range the BO cannot be expected to be valid (ξ should be much greater than one for the BO approximation to hold).

An accurate model of the C_{60} -silicon surface impact must take into account that the nuclear and electronic timescales are comparable, and the electrons cannot relax fast enough to the ground state relative to the instantaneous configuration of the nuclei. Therefore, the potential energy surface on which the nuclear motion evolves changes significantly, possibly allowing for cage breaking at lower kinetic energy. These considerations, along with the results described so far, led us to conclude that the BO-DFT approximation is not sufficiently accurate to describe this high-energy collision. In order to have a first indication of the importance of the electronic excitations, we first used the Car–Parrinello approach to MD, as implemented in the CPMD code suite [188, 177]. In this method the electronic wave function is not optimized at each MD step but is propagated in time by means of a fictitious classical Lagrangian [189], where the electronic degrees of freedom are given a fictitious mass. This does not guarantee that the wave function is exactly on the BO surface, but it stays reasonably close. For higher fictitious electronic mass, the wavefunction responds less promptly to the change in the nuclei configuration. We exploited this feature, intentionally increasing the fictitious electronic mass, in order to allow for a sizeable deviation from the BO surface, thus effectively including excited components in the wave function. Within this approach, the minimum kinetic energy required to break the cage dropped to 120 eV. This result gave us a strong hint that electronic excitation effects may play an important role in breaking the cage at lower energies than those required by classical MD.

However, a full quantum treatment of electrons and nuclei is unfeasible for the size of our problem. Therefore we decided to use a non-adiabatic MD method. In this approach, the non-adiabatic dynamics is approximated by performing stochastic hops between adiabatic surfaces constructed with the excited states of the system, which have been calculated by using time-dependent density functional theory (TDDFT) in the Tamm–Dancoff approximation [176].

The nuclei are propagated using Newton’s equation of motion on the current adiabatic electronic state and the probability of surface hopping is evaluated by means of the Landau–Zener theory [190, 191]. Forces used in the MD simulation are calculated on the adiabatic surfaces populated at the present MD step and constructed with the excited states of the system [192]. We verified that the TDDFT approach was able to reproduce

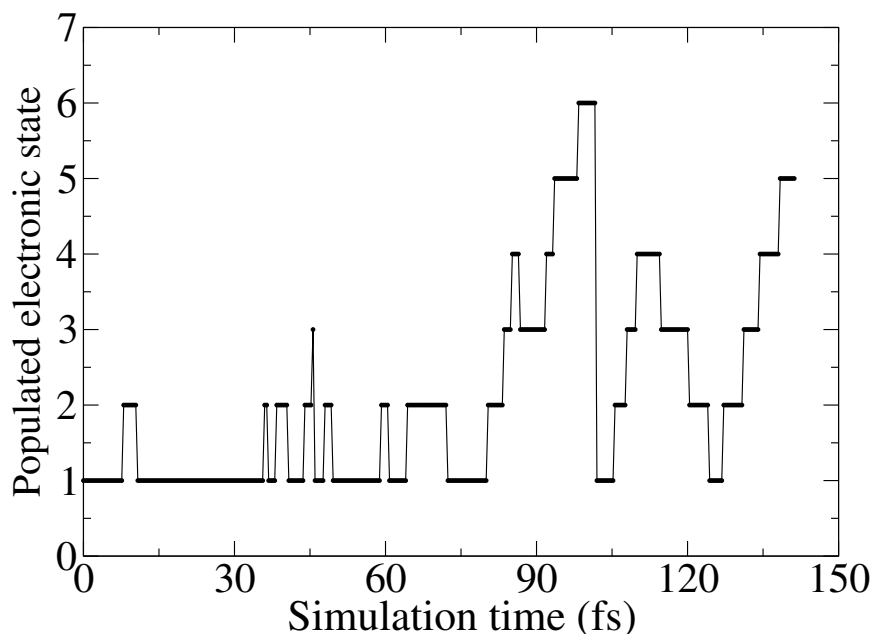


FIGURE 3.10: Surface-hopping evolution on the first six excited states during the non-adiabatic MD simulation.

the experimental electronic excitation spectrum of fullerenes.

Unfortunately, we estimated that the computational cost for simulating the excited-state dynamics of C_{60} impinging on Si(111)-(7 \times 7) surface would have been too high to obtain a result in a reasonable time. Therefore we considered a smaller yet realistic system. We used a three-layer Si(100)-(2 \times 1) slab composed of 48 silicon atoms, passivated with hydrogen atoms. The six lowest lying singlets were included in the calculation of the adiabatic surfaces. All of them were found to be visited during the dynamical evolution of the system.

From the result of our BO-DFT simulations, this crystallographic surface is equivalent, with regards to the impact of the fullerene molecule, to the Si(111)-(7 \times 7) surface. The two bottom layers were held fixed during the MD run. Due to the smaller transversal size of the slab, we chose to simulate the impact of a C_{20} molecule, in order to avoid unphysical interactions with periodic images. The main differences between C_{20} and C_{60} consist in the HOMO-LUMO energy difference (0.54 eV vs. 1.64 eV) and the cohesive energy per carbon atom (6.26 eV/atom vs. 7.15 eV/atom). Classical MD simulations of the impact of C_{20} on graphite, with empirical potentials, are reported in the literature [193] and the kinetic energy needed for the fragmentation of the C_{20} molecule exceeds 25 eV (at least 1.25 eV/per atom). Our BO-DFT calculations agree with this value of the kinetic energy for the cage breaking upon impact with the Si surface. We performed four simulations of C_{20} , with initial kinetic energies of 35, 22.6, 11.5 and 5.0 eV (corresponding to 105, 67.8, 34.5 and 16.5 eV for C_{60} having the same initial velocity) to find the kinetic energy threshold. Each simulation lasted 0.2 ps with a time-step of 0.5 fs. The fragmentation of the cage happened in all of the first three cases, while it was not obtained in the last one.

In this simulation, we clearly observe fragmentation of C_{20} impinging with a kinetic energy of 11.5 eV on the Si(111)-(7 \times 7) surface on a timescale spanning \sim 150 fs. This very short timescale confirms that a non-adiabatic description is needed for a proper modeling of the phenomena resulting from fullerene impacts.

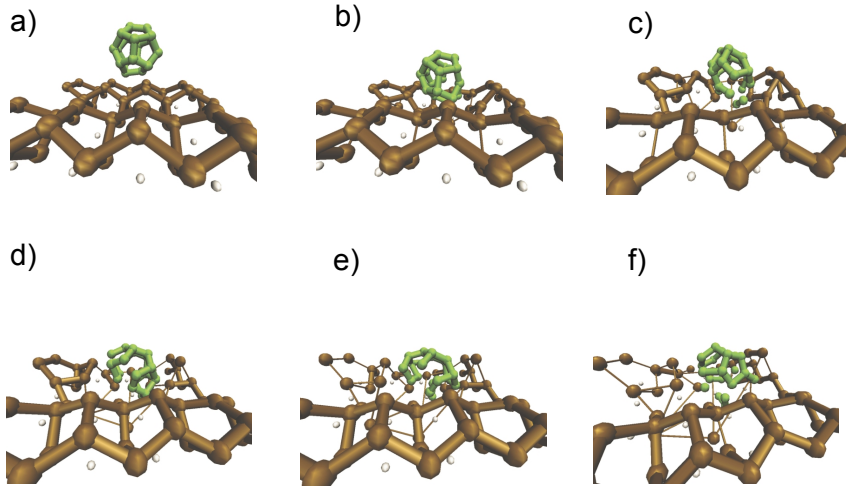


FIGURE 3.11: (a-f) Snapshots of the C_{20} trajectory impinging on Si(100) 2×1 at 11.3 eV from NA-MD calculations. Frames are taken every 22 fs, starting from (a).

We report in Fig. 3.10 the visited electronic state as a function of the simulation time. The impact between C_{20} and the surface, defined as the instant when the distance between the fullerene and the surface is at a minimum, occurs at $t = 36$ fs. It is clearly seen that from this moment on, the system visits excited surfaces. At $t = 56$ fs another carbon atom impacts with the surface and at $t = 80$ fs a considerable distortion of the C_{20} cage occurs. From this moment onwards, the energy transfer between the carbon atoms and the surface is particularly intense, as evidenced by the fact the excited states of progressively higher energy are visited along the trajectory. Interestingly, the cage rupture occurs via the ejection of a C–C dimer, which we observe in the last part of our trajectory beyond 130 fs, when hopping occurs between many excited energy surfaces. This finding is compatible with experimental evidence on fragmentation due to high-energy impacts of fullerenes. [194] C_{20} trajectory all the way from the initial condition to breaking is reported in Fig. 3.11a-f.

As a check, we also performed a BO-DFT simulation of C_{20} impact at an initial kinetic energy of 11.3 eV and we did not observe the fragmentation, enforcing once more the role of the electronic excitations on the cage breaking.

Following the epitaxy of SiC thin films is computationally not feasible due to the time-scale out of reach of MD simulations, but could in principle could be tackled by methods such as Dominant Reaction Pathways [195]. However, based on the much higher solubility of carbon at the surface with respect to the bulk and the stability of SiC, it could be argued that the system, after the cage breaking, will evolve into the state corresponding to the crystal phase without steep energy barriers.

3.7 Conclusions

In this chapter, experiments on the epitaxy of SiC by SuMBE technique and a first-principle model of the collision of C₆₀ with Si(111)-(7×7) surface have been described. SuMBE has been used to grow high quality crystalline SiC thin films. In this experimental method the formation and disruption of bonds and the activation of surface processes are kinetically driven. Experiments of deposition at high kinetic energy ($\sim 30 - 35$ eV) on Si gave evidence of SiC ordered domain formation at room temperature. In-situ electron spectroscopy measurements confirm the epitaxy of SiC nano-islands.

Simulations using DFT based on the Born–Oppenheimer and Car–Parrinello approximations are not able to capture the dynamics of the impact, predicting a minimum kinetic energy for the cage breaking of one order of magnitude higher than the experimental value. This failure is due to the neglect in BO-DFT of the excited electronic states, populated upon the high-energy collision with the Si surface. In order to properly capture the dynamics of the system, it is mandatory to explicitly include the excited electronic states in the calculation.

Therefore, non-adiabatic MD has been used with the inclusion of several electronic excited states, so as to reproduce the coupling between the electron and nuclear dynamics through the surface hopping in the calculation of the forces. From our results, we may infer that the mechanism which makes it possible to break the fullerene cage at energies as low as 0.6 eV per atom is the change in the force field felt by the nuclei, due to the spawning of excited electronic states of the molecule upon impact with the surface.

While our theoretical approach and the calculations have been performed specifically in the case of SiC growth, we believe that the underlying model and computational tools are rather general, and can be applied to other cases of material epitaxy or organic molecule interaction by SuMBE with inorganic surfaces.

Finally, we would like to comment on the computational cost of performing these *ab-initio* simulations. All of the BO-DFT calculations presented above required roughly 10^5 CPU hours on modern 2.3 GHz processors of a high-end computing terascale resource. All of the non-adiabatic simulations required twice as much. The considerable computational requirements of non-adiabatic simulations allowed us to follow only the initial stage of the processes leading to SiC formation. Nevertheless, this model agrees with the experimental finding of an energy threshold for C₆₀ fragmentation close to 35 eV.

Chapter 4

Towards an accurate treatment of correlation in extended systems: from density functional to many-body perturbation theory of carbon-based materials

Mean-field theories, such as HF, usually represent a good starting point for more accurate calculations of spectral properties. Particularly in condensed matter applications where one deals with systems having many degrees of freedom, the accurate calculation of the excited state energies is still a challenge for theory. In this chapter we discuss the development of novel computational and theoretical methods to go beyond mean-field and density functional approaches, notably many-body perturbation theory, to treat accurately the excited states properties. In particular we will describe a novel approach to GW and use it for calculating electronic band gaps for optically allowed transitions of a series of semiconducting single-walled zig-zag carbon nanotubes of increasing diameter. The dependence of the evaluated gaps with respect to tube diameters is then compared with those found from previous experimental data for optical gaps combined with theoretical estimations of exciton binding energies. We find that our GW gaps confirm the behavior inferred from experiments. The relationship between the electronic gap and the diameter extrapolated from the GW values is also in excellent agreement with a direct measurement recently performed through scanning tunneling spectroscopy.

4.1 Introduction

The design of electronic devices based on n-doped graphene and carbon nanotubes (CNTs), as possible semiconductor materials in the 2025 time-frame, has been the subject of significant effort during the last decade. To control and engineer novel devices using these carbon nanostructures, it is essential to have a good understanding of the relation between the band gap and the corresponding geometrical structure, in the case of the carbon nanotubes, or as a function of the doping (as we will see in the next chapter), in the case of graphene. In particular, for semiconducting single-walled tubes, the knowledge of the electronic gap

dependence on the chirality and diameter is the fundamental key to determine transport properties. However, the direct measurement of electronic band gaps in semiconducting CNTs is cumbersome due to difficulties in performing combined direct/inverse photoelectron measurements and the large exciton energies in these one-dimensional systems when the optical gap is probed [196]. Indeed, when band gaps are optically probed the recorded energies account not only for the electronic band gaps but also for the exciton binding energies [197]. The electronic band gaps could in principle be obtained just by subtracting the exciton energies but these cannot be easily measured. Hence, for extracting the electronic gaps from the optical ones, it is necessary to rely on theoretical models for the excitons [198, 199].

4.2 A very short introduction to methods beyond Density Functional theory

To access electronic band gaps, the most common methods so far are based on density functional theory (DFT) within local approximations for the exchange and correlation functional. Usually this method yields a significant underestimation of electronic gaps and cannot provide reliable estimations for CNTs. DFT demonstrated its potentiality in obtaining the total energy of a system of many-interacting electrons in its ground state [11]. As by section 3.4 of the previous chapter, DFT states firstly that the knowledge of the ground-state electron density $n(\mathbf{r})$ for an arbitrary external potential completely defines the many-body properties of the system and, secondly, that the ground state energy of the system can be obtained by minimising the energy functional with respect to such charge density and by solving a set of linear equations for independent particles.

Unfortunately, being a theory for the ground state, the use of DFT orbitals for the calculation of the excited states has not a clear physical meaning at variance with the HF wavefunctions. Known failures of DFT in predicting excited state properties, such as underestimation of the band gap in semiconductors and low-dimensional systems [200, 201], discontinuity in the exchange-correlation potential of an insulator when adding an electron [202] and wrong prediction of the density of states (DOS) in metals [203], rule out the use of local, energy-independent functionals as a tool to access the dynamics. To correct the pathological behaviour of DFT, a time-dependent version of DFT, TDDFT, based on an extension of the Hohenberg–Kohn theorem [15], has been proposed. Within TDDFT, excited state calculations are performed via time-dependent effective potentials, using a linear response theory of the density. However, the majority of TDDFT applications are limited to molecules or small systems [204, 205, 206, 207], with very few notable results in condensed matter.

On the other hand, many-body perturbation theory (MBPT), based on Green’s function approach [65, 208], is a general, though unwieldy, framework for studying excitation spectra in solids. The whole of Green’s function approaches rely on the consideration that electronic states in a weakly correlated system can be described as quasi-particle states and that the one-particle Green’s function has the poles at the energies the electrons are added and removed. MBPT provides a formally exact approach for addressing quasi-particles, though approximations are required for performing actual calculations [217]. Even in this case, the computational load is such to limit the range of applications to a very small number of atoms [209, 210, 211, 212, 213]. Within the MBPT framework, the equation of motion of the one-

particle Green's function $G(\mathbf{r}, \mathbf{r}', \omega)$ is analogous to the DFT Kohn-Sham equations where a non-local, energy-dependent interaction $\Sigma(\omega)$ replaces the exchange-correlation potential:

$$[-1/2\nabla^2 + V_{\text{ext}}(\mathbf{r}) + V_{\text{Hartree}}(\mathbf{r}) + \Sigma_{xc}(\mathbf{r}, \mathbf{r}'; \omega) - \omega]G(\mathbf{r}, \mathbf{r}', \omega) = \delta(\mathbf{r} - \mathbf{r}'). \quad (4.1)$$

The self-energy Σ_{xc} accounts for the 'dressed' interaction among the electrons acted on by a screened Coulomb potential. A systematic, though computationally very expensive method for calculating such electron self-energy is based on the combined self-consistent solution of five closed equations, introduced by Hedin [65]. To reduce the computational cost approximate, not self-consistent forms of the self-energy have been proposed, the most successful so far being the GW approximation:

$$\Sigma(\mathbf{r}, \mathbf{r}'; \omega) = i G(\mathbf{r}, \mathbf{r}'; \omega)W(\mathbf{r}, \mathbf{r}'; \omega) \quad (4.2)$$

where W is the screened Coulomb interaction. The quasi-particles corrections to DFT-LDA energies are obtained by solving the self-consistent equation:

$$\varepsilon_n^{GW} = \varepsilon_n^{LDA} + \langle \psi^n | \Sigma^{GW}(\omega = \varepsilon_n^{GW}) - V_{xc}^{LDA} | \psi^n \rangle \quad (4.3)$$

The so-called diagonal G_0W_0 or *one-shot* [218] GW approximation can be seen as the simplest of such approximations. The G_0W_0 scheme permits to apply many-body corrections to a starting DFT calculation and in many cases with great success. According to the G_0W_0 approximation, Σ is found from the convolution of the one-body Green's function G_0 , obtained from the DFT calculation, with the correlation part of the screened Coulomb potential W_0^c , which is obtained through the random-phase approximation [219]

$$W_0^c = W^{RPA} = \varepsilon^{-1}v \quad (4.4)$$

where v is the bare Coulomb interaction and $\varepsilon = 1 + vG_0G_0$. It should be noted that the G_0W_0 approximation is an approximation to the fully self-consistent GW method and in principle different results could be found [220, 221, 222, 223]. However, the latter is still in its phase of development and an approach for performing self-consistent GW calculations avoiding explicit sums over empty states has still to be conceived. Despite the apparent simplicity of this approach, its application requires a considerably larger effort than the starting DFT calculation. Not only does it involve the evaluation of operators at several frequencies but also the evaluations of G_0 and W_0 contain sums over a large, in principle infinite, number of unoccupied Kohn-Sham states. These are the origins of the difficulties in obtaining well converged GW calculations [213].

Recently, we could present a GW scheme which allows one to avoid these two difficulties: we express the bare and screened polarizability operators through reduced (optimal) basis sets in the Wannier scheme [66, 180, 215], retaining good accuracy, and we eliminate any explicit sum over empty unoccupied states through an approach [214] based on Lanczos chains. In this approach all the operators are first evaluated on imaginary frequencies and then the expectation values of the self-energy operator are obtained upon analytic continuation [224], avoiding the use of the so-called plasmon-pole approximation.

4.2.1 Methods beyond GW: excitonic effects

GW approach works very well for ionisation potential calculation but, in many experiments, notably NEXAFS, resonant photoemission and EELS, neutral excitations play an important role. In this case, particularly for low dimensional materials, excitonic effects are not

negligible and GW-based approaches fail in predicting the spectral properties, notably the optical response. Within MBPT, the most successful method so far for taking into account the binding energy of the particle-hole pair relies on the solution of the four point Bethe–Salpeter equation (BSE) [14], describing the correlated motion of two particles. It turns out [201] that good agreement between theory and experiment can be achieved, particularly in semiconductors or insulators excitation spectra. However excitonic effects turn out to be important surprisingly even in metals, where the excitons should be screened out. The main problem in using the BSE is the computational load and, in this sense the propagation of a two-point quantity, such as the density in TDDFT, would bring to less computationally expensive calculations. An example of the kind of agreement in the absorption spectrum of bulk silicon between different level of theories, namely DFT-LDA, RPA, GW-RPA, BSE [225] and experimental measurements is sketched in Fig. 4.1, where one can appreciate the improvements with respect to experiments obtained by introducing the electron-hole interaction.

A completely different approach used to treat electronic correlation in quantum chemistry

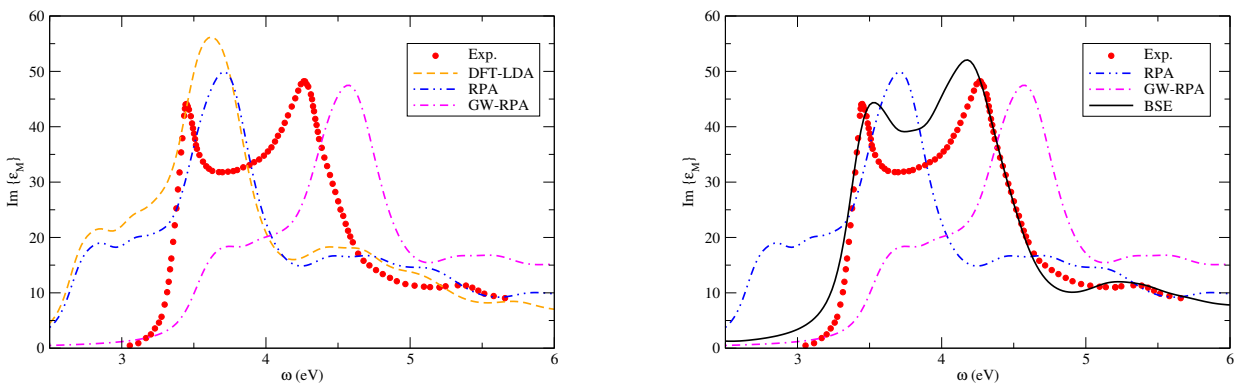


FIGURE 4.1: Left: absorption spectrum of solid silicon. DFT-LDA, RPA and GW-RPA results [226] compared to the experiment [225]. Right: absorption spectrum for bulk silicon. RPA, GW-RPA and BSE results [226] compared to the experiment [225]. Reprinted from [226] with kind permission of F. Sottile.

is the Density Matrix Renormalization Group (DMRG)[55]. This method is a combination of ideas from the renormalisation group and the one-body density matrix theory. Generally speaking, renormalisation is a procedure which allows one to describe properties of a system on a large scale, without explicitly taking into account all the degrees of freedom or by integrating out the degrees of freedom in between two different length scales. In this way the dynamics seen at a longer length scale differs from that one observed at shorter length scale by an effective or ‘renormalized’ behaviour. Renormalization procedures have a long history and dates back to the golden age of Kadanoff and Wilson in the ‘60-’70, who respectively solved the uni-dimensional Ising model by a block spin technique [227] and the Kondo problem [228]. In the DMRG approach one uses as block variables the eigenstates of the density matrix, that is $\rho(\mathbf{r}', \mathbf{r}) = \langle \hat{\psi}^\dagger(\mathbf{r}') \hat{\psi}(\mathbf{r}) \rangle$, where $\hat{\psi}(\mathbf{r})$ is the field operator.

The real space version of DMRG, in particular, has proven extremely successful in calculating the residual electronic interaction for finite Fermi systems. This method has a computational scaling of the order of $O(n^4 m^2)$ where n is the total number of basis states and m is the number of states kept in the iterative DMRG procedure, which is much

lower than that of CI. In this case DMRG is applied within the conventional chemical framework of a finite basis set with non-orthogonal basis functions centered on the nuclei (e.g. Gaussians). As in standard CI approach, HF is initially used to generate a basis set of orthogonal n orbitals. Since HF self-consistent field procedure has a small polynomial scaling, this step can be performed in almost all the systems of interest. Then, DMRG is used to include correlation beyond HF. To this goal, each orbital, which can be empty, single or double occupied is treated as a ‘site’ in a 1D lattice. HF orbitals in a chosen order, usually with an energy driven criterion, are blocked together and the most relevant orbitals are selected via the density matrix. DMRG algorithm assumes that the eigenstates of the density matrix of the block with the highest eigenvalues correspond to the most relevant block states. The number of eigenstates kept after the diagonalization of the density matrix of the block influences the accuracy of the calculation. This procedure is then iteratively repeated until convergence or a fixed point is reached.

Case studies on methane [229], using a minimal basis set and $m = 50$ per block, and water [59], with 25 HF orbitals and $m = 400$ per block, give results for the ground state energy already comparable to CAS(8,8) and an accuracy of $10^{-4}\mu\text{Hartree}$ in comparison to the full CI calculation, respectively. Excited state properties, notably the dynamics of excitons or the optical absorption edge in dendrimers, have been studied by DMRG as well obtaining very good agreement with experimental data. In this calculation, each monomer has been considered as one block of the DMRG algorithm [58]. For an exhaustive description of DMRG methods in quantum chemistry, excellent reviews are given by Dukelsky *et al.* [60] and Chen *et al.* [57].

4.3 Electronic band gaps of semiconducting zig-zag carbon nanotubes from MBPT

Taioli *et al.* applied the G_0W_0 method described in section 4.2 for investigating the dependence of electronic band gaps with respect to tube diameter for the case of semiconducting single-walled zig-zag carbon nanotubes. We have addressed tubes with diameters ranging

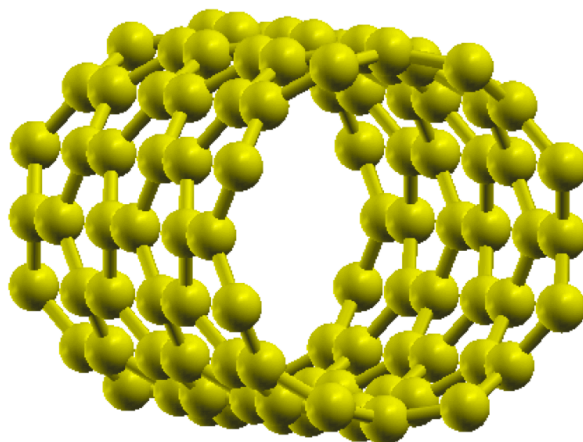


FIGURE 4.2: A simulation cell of a (8,0) CNT.

(m,n)	#cells	#atoms	dimension (Bohr)
(7,0)	4	112	30.0 x 32.0 x 30.0
(8,0)	3	96	30.0 x 24.3x 30.0
(10,0)	3	120	34.0x 24.0 x 34.0
(11,0)	3	132	36.0 x 24.0 x 36.0
(13,0)	2	104	39.0 x 16.0 x 39.0
(14,0)	2	112	40.0 x 16.0 x 40.0
(16,0)	2	128	40.0 x 16.0x 40.0

TABLE 1: Parameters for the simulation cells adopted in the GW calculations: chirality indices (m,n), number of primitive cells defining the supercell ($\#cells$), number of atoms in the supercell ($\#atoms$), and dimension of the supercells.

from 0.56 nm to 1.27 nm. We have considered here the single-walled zig-zag CNTs with chirality indices: (7,0), (8,0), (10,0), (11,0), (13,0) (14,0), (16,0) which are semiconducting [230]. An example of a simulation cell for a (8,0) CNT, used in these calculations, is sketched in Fig. 4.2. We adopted periodic simulation cells setting a distance of 10 Å between the next periodic replica of the tubes. We considered simulation cells comprising from 2 to 4 replica of the primitive cell along the tube direction. This choice led to a number of atoms in the simulation cells varying from 96 to 128. Details of the dimensions of the adopted simulation cells are reported in Table 1. The starting DFT calculations were performed using the local density approximation (LDA) for the exchange and correlation functional as described in Ref. [231]. We used the pw.x code of the QUANTUM-ESPRESSO suite of DFT packages [232]. Within this package, wave-functions and charge-densities are expressed through plane-waves basis sets and the interaction between valence and core electrons is modeled through pseudo-potentials.

We applied a normconserving pseudopotential for the carbon atoms [233] and an energy cutoff of 40 Ry. The G_0W_0 calculations have been performed with the GWL code [234] which has been implemented as a package in QUANTUM-ESPRESSO. This code uses a k-point mesh for sampling the Brillouin zone only for the long-range terms of the symmetric dielectric matrix. For this reason we used supercells containing up to four primitive cells. The DFT charge densities and the long-range terms of the symmetric dielectric matrix have been calculated using meshes from 4 to 9 k-points along the reciprocal direction of the tube.

For the GW calculation we built a basis for the polarizability operators as described in Ref. [214], using a cutoff $E^* = 3$ Ry and a threshold q^* varying from 1.8 Bohr³ to 8.6 Bohr³ yielding basis consisting of 4000 vectors in each case. The calculations were first carried out in imaginary frequency [224] using a grid consisting of 256 steps on the positive imaginary axis up to 20 Ry. Then the expectation values of the self-energy operator were obtained on real frequency through analytic continuation using three-poles expansion. We estimate a final global accuracy of 0.1 eV for the calculated quasi-particle energy levels.

In Table 2 we display the calculated band gaps relative to optically allowed electronic transitions for the tubes we have considered. In the tubes (7,0) and (8,0) the fundamental electronic band gap refers to transitions which are not optically allowed. We note that while the fundamental gap for the (8,0) tube, 1.80 eV, is in good agreement with the previous GW

(m,n)	LDA (eV)	GW(eV)	Ref. GW(eV)
(7,0)	0.16	1.98 (1.47)	(0.60 ^a –1.12 ^b)
(8,0)	0.5	2.24 (1.80)	2.54 ^c (2.12–1.75 ^c –1.51 ^d)
(10,0)	0.80	1.72	
(11,0)	0.95	1.66	
(13,0)	0.65	1.52	
(14,0)	0.74	1.36	
(16,0)	0.56	1.21	

TABLE 2: Electronic band gaps from LDA, GW, and reference literature values, for selected semiconducting zig-zag CNTs of chirality indices (m,n). The gaps are relative to optically allowed transitions. When the electronic band gap for optically allowed transitions differs from the fundamental electronic band gap, we have reported also the latter in parenthesis both in the GW and in the reference column. Literature data are from: (a) Ref. [211], (b) Ref. [180], (c) Ref. [196], and (d) Ref. [210]

results of 1.75 eV from Ref. [196] and of 1.51 eV from Ref. [210], our result for the (7,0) tube, 1.47 eV, is higher than the value 0.60 eV reported in a previous GW investigation [211]. However, for the latter case, in the literature different values are reported already at the LDA level possibly depending on subtleties in the structural optimization [235, 236]. The calculated gap for the (8,0) tube relative to optically allowed transitions (2.24 eV) is in agreement with the value of 2.54 eV from Ref. [196]. The calculated gaps for the (7,0) and (8,0) CNTs are also in agreement with the results in Ref. [180], where we used a preliminary version of our method still requiring sums over empty states.

In Fig. 4.3 we present the quasi-particle DOS for the (8,0) CNT. The opening of the gap at the Fermi energy ($E_F=0$) is clearly visible in the picture. As our calculated electronic gaps have been obtained using periodic boundary conditions, we have estimated the maximal changes in the electronic gaps when the intertube distance goes towards infinity. We considered a (8,0) tube with a simulation cell comprising 32 atoms and varied the intertube distance. By extrapolating the gap/distance behavior we estimate a maximal increase in the electronic gaps in the isolate tube limit varying from 0.2 eV for the (8,0) tube to 0.1 eV for the (16,0) tube. We note that such extrapolations could be avoided using a more complex approach involving the cylindrical truncation of the Coulomb interaction [196, 237]. The electronic band gap of semiconducting nanotubes corresponds to the energy difference, usually indicated as E^{11} , relative to the van-Hove singularities appearing in the density of electronic states closest to the Fermi level. The energy difference relative to the second closest singularities is referred as E^{22} . When the band gap are investigated experimentally through optical spectroscopies, fluorescence lines do not match the electronic band gap E^{11} as electrons and holes in CNTs show strong correlated motion and their binding energy produces significant band gap renormalisation. In practice, experiments measure the energies of the lowest (E_{1A2}) and of the second lowest (E_{2A1}) optically active exciton states and their difference.

In principle, scanning tunneling spectroscopy (STS) could give a direct measure of electronic band gaps. However, in such a case a model is required for the estimation of the screening effects arising from the metal substrate on which the nanotube is dispersed and the final error bars are quite large [238]. Therefore, accessing electronic band gaps usually

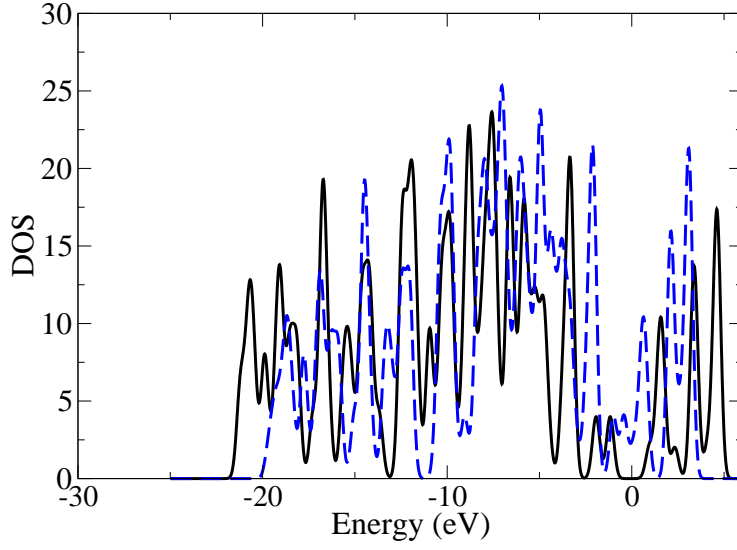


FIGURE 4.3: Electronic density of states for (8,0) CNT: LDA (blue dashed line) and GW (black solid line). A Gaussian broadening of 0.2 eV has been used.

relies both on optical measurement and theoretical modeling. The edges for fluorescence emission have been measured for several tubes and then their dependence with respect to the diameter has been fitted with model functions [197, 198]. In Ref. [198], the authors report the following behavior for the optical first emission gap E_{op}^{11}

$$E_{op}^{11} = \frac{1.11eV}{d_t + 0.11} \quad (4.5)$$

where the diameter d_t is expressed in nanometers. Slightly different values for E_{op}^{11} are reported in Ref. [197], where the dependence of the optical gap with respect to the tube chirality is considered. Indeed, the gap versus diameter function changes whether $mod(n - m, 3)$ equals 1 or 2 (mod1 or mod2 species, respectively):

$$\begin{aligned} E_{op}^{11}(\text{mod1}) &= \frac{1.241 \times 10^3 eV}{157.5 + 1066.9d_t} - \frac{0.0957 [\cos(3\alpha)]^{1.374}}{d_t^{2.272}} \\ E_{op}^{11}(\text{mod2}) &= \frac{1.241 \times 10^3 eV}{157.5 + 1066.9d_t} + \frac{0.04307 [\cos(3\alpha)]^{0.886}}{d_t^{2.129}} \end{aligned} \quad (4.6)$$

where α is the chiral angle [230]. For zig-zag CNTs we have $\alpha = 0$. The tubes we have examined, (7,0), (10,0), (13,0) and (16,0) are of mod1 kind, while (8,0), (11,0), (14,0) are of mod2 kind. In Ref. [197], fits for the second fluorescence gap and E_{op}^{22} are also reported:

$$\begin{aligned} E_{op}^{22}(\text{mod1}) &= \frac{1.241 \times 10^3 eV}{145.6 + 575.7d_t} + \frac{0.1651 [\cos(3\alpha)]^{0.828}}{d_t^{1.809}} \\ E_{op}^{22}(\text{mod2}) &= \frac{1.241 \times 10^3 eV}{145.6 + 575.7d_t} - \frac{0.1764 [\cos(3\alpha)]^{1.110}}{d_t^{2.497}} \end{aligned} \quad (4.7)$$

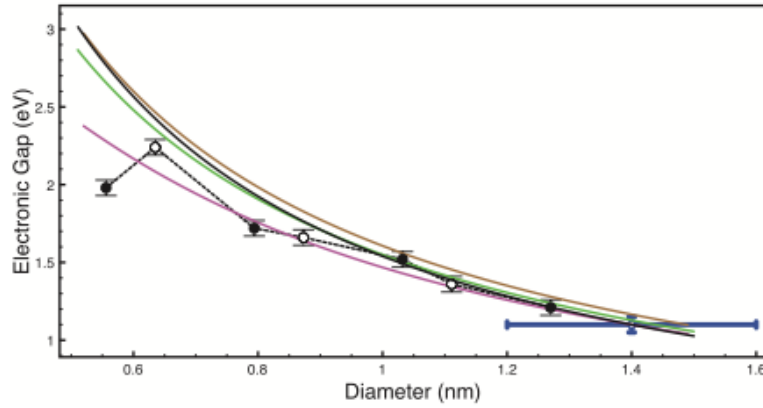


FIGURE 4.4: Electronic band gaps for semiconducting carbon nanotubes of diameter d_t , corresponding to optical transitions. Black discs: first-principles GW results for mod1 zig-zag nanotubes (see text). Open circles: first-principles GW results for mod2 zig-zag nanotubes. The error bars refer to the final estimated accuracy of the GW energy levels. The dashed black line is a guide for the eye. Bold black line: fit of GW results for large tubes (see text). Theoretical estimates for semiconducting nanotubes are obtained from: Eqs. 4.9 and 4.5 (green line), Eqs. 4.6, 4.7 and 4.8 for zig-zag tube with mod1 (purple line) and mod2 (brown line). The experimental STS measurement of Ref. [238] is reported together with error bars (blue).

In Ref. [199], Deslippe and co-workers proposed a model for the electron-hole exciton Hamiltonian which yields exciton binding energies in agreement with accurate GW-Bethe-Salpeter first-principles calculations [239]. Moreover, they found for semiconducting CNTs that the binding energy E_{1A2}^{bind} for the lowest 1A2 exciton could be expressed as:

$$E_{1A2}^{\text{bind}} \approx 2.3 (E_{\text{op}}^{22} - E_{\text{op}}^{11}) \quad (4.8)$$

Eq. 4.8 combined with the data of Ref. [198] leads to the following expression for E_{1A2}^{bind} :

$$E_{1A2}^{\text{bind}} \approx \frac{0.55\text{eV}}{d_t} \quad (4.9)$$

The electronic band gap E^{11} corresponding to optical transition can now be found from the Eqs. 4.6-4.9 through:

$$E^{11} = E_{\text{op}}^{11} + E_{1A2}^{\text{bind}} \quad (4.10)$$

In Figure 4.4, we compare our GW results with combined theoretical-experimental estimates using the result of Eq.4.8 combined with either the experimental values from Ref. [198] or from Ref. [197]. The latter are reported for the case of zig-zag semiconducting tubes ($\alpha = 0$) for both mod1 and mod2 cases. We note a very good agreement of the calculated GW electronic gaps with the previous estimates for the entire diameter range excluding the thinnest tube (7,0). It should be noted that LDA results, not shown in this figure, would be very far from the theoretical/experimental lines as can be seen from Table 2. The GW results for the largest tubes we have considered here are also in excellent agreement with the direct measurement of an electronic gap [238] which in turn is in good agreement with the experimental/theoretical lines.

As, usually, the nanotubes which are used in devices have diameters which are larger than those studied here, it is interesting to fit our GW results for extrapolating the electronic gap-diameter function. For the purpose of extrapolating our data for larger tubes we fitted the GW results for tubes larger than 1.0 nm with the simple relation $E^{11} = \frac{a}{d_t}$ which goes towards a closed gap in the large diameter limit as expected from the observed closed gap in graphene. We find a value a of 1.54 eV*nm. From Fig. 4.4, we see that our fitted behavior agrees well with the previous mixed theoretical/experimental estimates. At smaller diameters evidence of hybridization further reduces the band gap from this relationship [235, 236].

4.4 Conclusions

In conclusion, we have studied the electronic band gap of zig-zag semiconducting carbon nanotubes using a new developed GW approach and have found agreement with estimations from optical measurements coupled with theoretical modeling for the exciton binding energies. We could extrapolate the gap/diameter behavior for larger diameters with a $1/x$ function. As for larger semiconducting CNTs the dependence of the gap on the tube chirality becomes smaller our relation $E_{gap} = 1.54 \text{ eV} \times \text{nm}$ can be used for providing estimates for electronic gaps of generic semiconducting tubes.

Chapter 5

Graphene: growth, functionalization and characterization

A growth model of graphene on Ni(111) is proposed in this chapter. Our experimental data, based on time-dependent photoemission spectroscopy, and ab initio calculations point towards a growth model strikingly different from the standard two-dimensional film growth. We observe a catalytic growth process that is self-limiting and stops completely as soon as the Ni surface is covered by a monolayer of graphene. Comparison between our calculations and the experiments yields excellent agreement and highlights that graphene nucleates from propene fragments and then proceeds by adsorption of carbon atoms.

Following the growth of a complete monolayer, to use graphene in microelectronics applications one needs to open a band gap, which we obtain by hydrogenation. We show by angle-resolved photoemission spectroscopy that a tunable gap in quasi-free-standing monolayer graphene on Au can be induced by hydrogenation. The size of the gap can be controlled via hydrogen loading and reaches 1.0 eV for a hydrogen coverage of 8%. The hydrogen induced gap formation is completely reversible by annealing without damaging the graphene. Calculations of the hydrogen loading-dependent core level binding energies and the spectral function of graphene are in excellent agreement with photoemission experiments.

Finally, we produce evidence of the emergence of a new energy band in the electronic structure of electron-doped hydrogenated monolayer graphene, largely composed of hydrogen 1s orbitals. This band remains extended for low H-coverage despite the random chemisorption of H. Further evidence for the existence of a hydrogen state is provided by x-ray absorption studies of undoped H-graphene which are clearly showing the emergence of an additional state in the vicinity of the π^ resonance. Some data and pictures on graphene growth are courtesy of A. Grüneis, University of Vienna.*

5.1 Introduction

The discovery of 2D graphene has led to a dramatic increase in research effort due to its remarkable physical properties [240]. Graphene is a zero gap semiconductor with a linear energy band dispersion around the Fermi energy (E_F), so that the charge carriers mimic massless Dirac fermions with a Fermi velocity of 1×10^6 m/sec [241, 242]. This allows one to address basic questions of quantum electrodynamics in a bench-top experiment [243, 244].

It is also one of the candidates for post silicon area in nanoelectronics and, as such, has received and still receives large attention from the research community. Following its discovery considerable efforts have been spent in order to facilitate high throughput and large area synthesis of graphene layers. A promising way to achieve this goal is chemical vapour deposition (CVD) on a number of metal surfaces, such as Ni(111) [245, 246, 247]. This geometry is most suitable for spin filter devices [248] which might become important for organic spintronics applications. The growth dynamics of graphene are very similar to the nucleation step of carbon nanotube growth and a detailed understanding of the growth mechanism of graphene will shed some light on the nanotube growth which remains poorly understood a decade following their discovery.

In this chapter, we firstly present an in-situ time-resolved photoemission study during the growth of a graphene monolayer. A phenomenological growth model based on rate equations and ab-initio calculations is introduced that captures all the essential processes and reproduces the experimental data over all measured time and temperature ranges. Nevertheless, the application of graphene in semiconductor devices requires a band gap in order to switch the conductivity between on- and off-states.

Besides growing a large area high-quality monolayer, to use graphene in microelectronics applications one needs to open a band gap. Physical and chemical approaches for opening a gap are under discussion. First, size quantization of about 1 nm induces band gaps of $\simeq 1$ eV in graphene nanoribbons [249, 250, 180], nanotubes [230], and quantum dots [251]. However, in the case of nanotubes, the preparation of samples with Ohmic contacts is still challenging. Similarly, in the case of nanoribbons, the electronic properties are determined by the edges [252], making this approach technologically very demanding. An alternative strategy is the chemical functionalization of graphene which induces band gaps and can even be reversed [253, 254, 255, 256, 257, 258, 257]. This approach was already successfully demonstrated before the discovery of graphene. For example, in hydrogenated amorphous carbon (a-C:H) [259] an optical gap has been observed which increases with the hydrogen content [260, 261]. Fully hydrogenated graphene, also referred to as graphane, has been suggested recently as an insulator with a band gap of 3.5 eV [262] and doped graphane as a possible high- T_c superconductor [263].

For partially hydrogenated graphene, Duplock et al. reported the appearance of a substantial band gap of 1.25 eV accompanied by a spin-polarized midgap state [264]. With transport measurements, a metal to insulator transition (MIT) was observed after cleaved graphene on SiO_x was exposed to atomic hydrogen [265]. Much less is known about the band structure and the nature of the MIT. Furthermore, the amount of applied hydrogen could not be directly accessed by transport measurements. Hydrogenated graphene on SiC was investigated with angle-resolved photoemission spectroscopy (ARPES), suggesting an electron localization as the mechanism responsible for the MIT [266]. The transition itself was already observed at H coverages of $\simeq 0.1\%$. However, graphene on SiC is intrinsically heavily electron doped (E_F is $\simeq 0.5$ eV above the Dirac point) and thus is not the model system to be compared to the transport experiments on cleaved graphene.

Similarly, scanning tunneling measurements of hydrogenated epitaxial graphene on an Ir substrate indicated graphene quantum dot formation and therefore a band gap opening that is determined by the quantum dot size [267]. In the above case, the strong interaction of graphene to the Ir and the patterned hydrogen chemisorption prevents a tunability of the electronic band gap. These profound limitations call for a different system from graphene on Ir and on SiC for studying hydrogenation. In the following sections we demonstrate how

it is possible to open a tunable band gap in hydrogenated quasi-free-standing graphene on Au (E_F is at the Dirac point). The size of the gap depends exclusively on the H/C ratio and obtainable band gaps of up to 1 eV make this approach extremely appealing for applications in nanoelectronics and optics. The hydrogen induced gap formation is also fully reversible by modest annealing without damaging the graphene. Furthermore, both, the graphene on SiO_x and on Au have an identical doping level and a very similar electron energy band structure. Therefore hydrogenated quasi-free-standing graphene provides important input for understanding the transport experiments of hydrogenated graphene on SiO_x .

Furthermore, by using Near Edge X-Ray Absorption Fine Structure spectroscopy (NEXAFS) a hydrogen-derived midgap state in H-graphene can be found. NEXAFS measurements provide access to unoccupied electronic states above the Fermi level by measuring the x-ray absorption which is caused by transitions from the C 1s core level to the π^* and σ^* energy bands. For undoped H-graphene the impurity band is located within the emerging gap at the Fermi level and is therefore hardly accessible with ARPES since this method probes only the occupied electronic states of the band structure. Using potassium intercalated n -doped graphene, the hydrogen-derived state becomes available for electron occupation and acts as an acceptor level for π^* electrons which can be directly observed in ARPES. Density functional theory (DFT) calculations suggest that the midgap state is largely derived from H 1s orbitals. Calculations of the typical and average density of states (DOS) using the kernel polynomial method (KPM) with a tight-binding (TB) band structure calculation [268, 269, 265, 266, 267, 270] indicate that the new state does not localize easily despite the randomness in the H chemisorption sites.

5.2 The growth of graphene on Ni(111)

In Fig. 5.1(a) and (b) we show C1s core level spectra during the growth of graphene for two different synthesis temperatures.

As we will show later in detail, the lower binding energy feature is from C_3H_6 fragments and the higher binding energy feature that appears at a later time comes from graphene. The graphene peak increases with time and saturates, which highlights that the catalytical activity decreases and approaches zero as the whole surface is covered by a graphene layer. This was also evidenced by previously recorded ARPES spectra, following the growth [245]. The insets in Fig. 5.1(a) and (b) denote the integrated PE intensity for the graphene and fragment peaks.

Temperatures above 650°C cause the desorption of graphene from the Ni surface. In Fig. 5.1(c) the time resolved desorption process of graphene is shown and it can be seen that the graphene intensity disappears completely after 200 s. From Fig. 5.1(a) and (b) it is clear that the fragments are converted to graphene. The question arises what is the nature of the fragment peak. It has been put forward that the peak at 283 eV is due to Ni carbide [271]. Another possibility would be that a fraction of C_3H_6 is not decomposed and produces the peak at 283 eV.

Here we will show that none of the above assignments are the case for our experiments. Firstly, we deliberately made Ni carbide following the recipe in Ref. [272] and tried to convert it to graphene. In Fig. 5.1(d) we show the time-resolved photoemission signal of Nickel carbide at 700°C . Clearly, the signal stays constant over time (see inset) and no conversion to graphene takes place. Concerning the case of adsorbed C_3H_6 on Ni(111), we

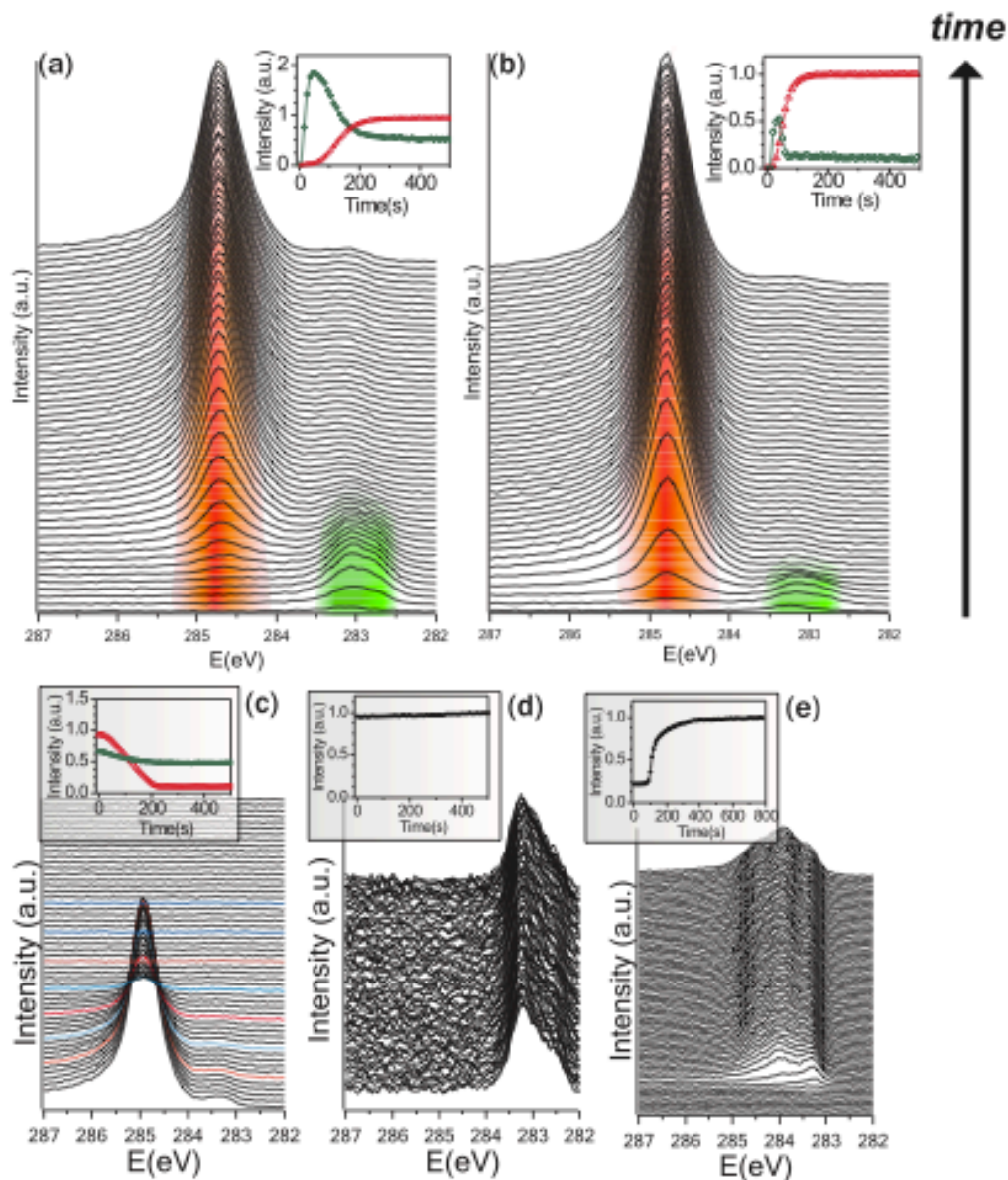


FIGURE 5.1: Time evolution of the PE intensity in the C 1s region during the graphene growth for (a) 400°C and (b) 550°C. The red (green) shaded areas denote the graphene (fragment) peaks. The insets show the graphene (Δ) and fragment (\square) intensities, respectively. Note that the fragment intensity is multiplied by a factor of 10 for visibility. (c) Desorption of a graphene layer by at T=700° C. (d) Nickel carbide is stable at T=700 °C. (e) Room temperature adsorbed C₃H₆. Courtesy of Alexander Grüneis, University of Vienna.

studied the room temperature adsorption where C_3H_6 is stable. The theoretical spectrum of C_3H_6 has been calculated by using our in-house developed code SURPRISES [62] and it is reported in Fig. 2.4 of chapter 1. The main features of this spectrum, found at $\simeq 291$ eV, rules out gase-phase propene as responsible of the lower binding energy peak of Fig. 5.1a).

Thus, the C1s signal at 284 eV in Fig. 5.1(e) can be safely attributed to C_3H_6 on Ni(111). However, the signal position in Fig. 5.1(a,b) is 1 eV lower in energy and, thus, we exclude both Nickel carbide and unfragmented C_3H_6 as origin of this peak. We rather suppose that the 283 eV bump is due to fragmented C_3H_6 chemisorbed on the nickel surface. In order to check this hypothesis we performed some model calculations of the C 1s spectrum of two different fragments/nickel surface configurations, as sketched in Fig. 5.2a) and b). These structures have been optimized by minimizing the free energy of the electrons at each nuclei position with a smooth Fermi-Dirac smearing, relaxing the atomic bond length until the forces are less than 0.001 eV/Å per atom. The ion-electron interaction has been described using Perdew-Zunger LDA pseudo-potentials, with single-particle orbitals and charge density expanded in plane waves with a cut-off of 40 a.u. With respect to the adsorbed CH_3 fragment, the CH fragment, as expected from the shorter Ni-C bond length (1.78 Å instead of 1.93 Å) and from the higher bond coordination number with the nickel atoms (3 instead of 1) results more tightly bound to the surface (see Fig. 5.2a,b)). The adsorbed propene fragments C 1s binding energies referred to the Fermi level are found at 282.931 eV and 282.999 eV for the CH_3 and CH structures, respectively. Thus in agreement with our experimental observation of the growth process, ab-initio calculations assign this peak to fragmented C_3H_6 molecules.

To assign the main peak in Fig. 5.1a,b) arising in the time-dependent spectrum at 285 eV, we performed the calculations of C 1s carbon core-level of a complete graphene monolayer adsorbed on the top of the nickel surface, as sketched in the bottom panel of Fig. 5.2. LDA calculations reproduce accurately the Ni-C bond distance for the two different topological positions of the carbon atom, directly on the top of nickel and in the hollow site of the nickel lattice, respectively. We obtain 2.08 Å (measured value 2.11 Å [247]) and 2.11 Å (measured value 2.16 Å [247]), for the former and the latter case, respectively. The graphene honeycomb results strongly chemisorbed at the surface, with a charge transfer from nickel to carbon of about $0.5 e^-$ found by Bader charge analysis, and a strong 2s/2p carbon - 3d nickel hybridization. The calculated C 1s level binding energies with respect to the Fermi level are found at 284.432 eV (carbon atom on the top) and 285.076 eV (carbon atom on the hollow site of the nickel lattice) for the two different topological positions of carbon atoms in the adsorbed graphene honeycomb. The following observation can be made from these ab-initio calculations and by analyzing the spectral lines of Fig. 5.1(a) and (b): (1) the graphene growth starts after the fragment peak has reached maximum intensity and starts decreasing. This is pointing towards graphene island nucleation from fragments. (2) The maximum intensity of the graphene peak is several time higher than the maximum in the fragments, pointing towards an additional path of carbon incorporation apart from fragments conversion. (3) The rate of graphene growth increases with temperature. (4) A small fraction of the fragments remains even after the growth of the graphene layers has terminated and this fraction decreases for higher temperatures. These fragments may sit on strongly bound defect sites of the metal surface and therefore cannot be converted to graphene easily. This accounts for the fragment intensity that is remaining after a graphene layer is completed. The above facts can be explained by a

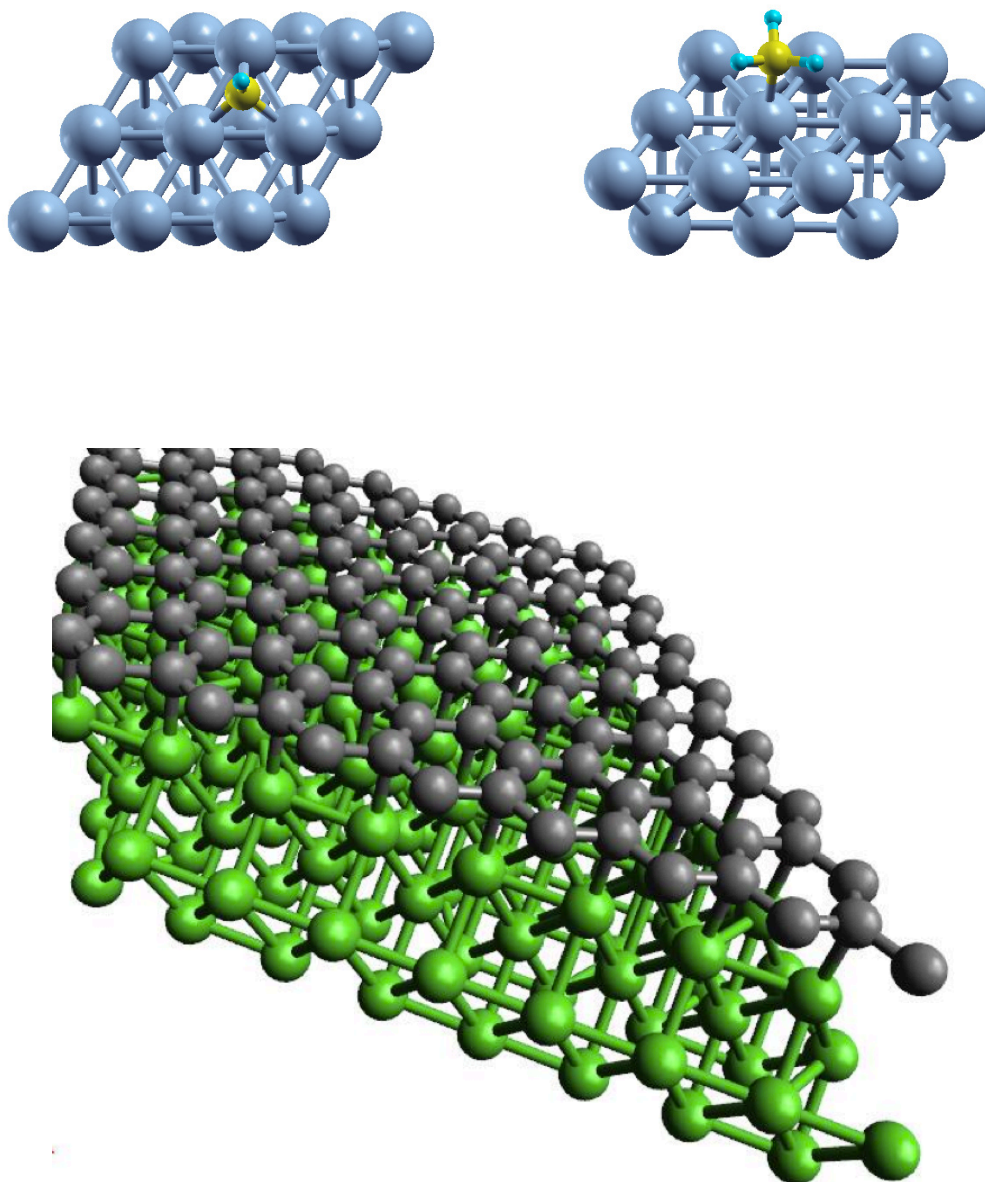


FIGURE 5.2: Sketch of the investigated propene fragments (top) adsorbed on graphene and (bottom) of the complete graphene layer chemisorbed on the Ni(111) surface.

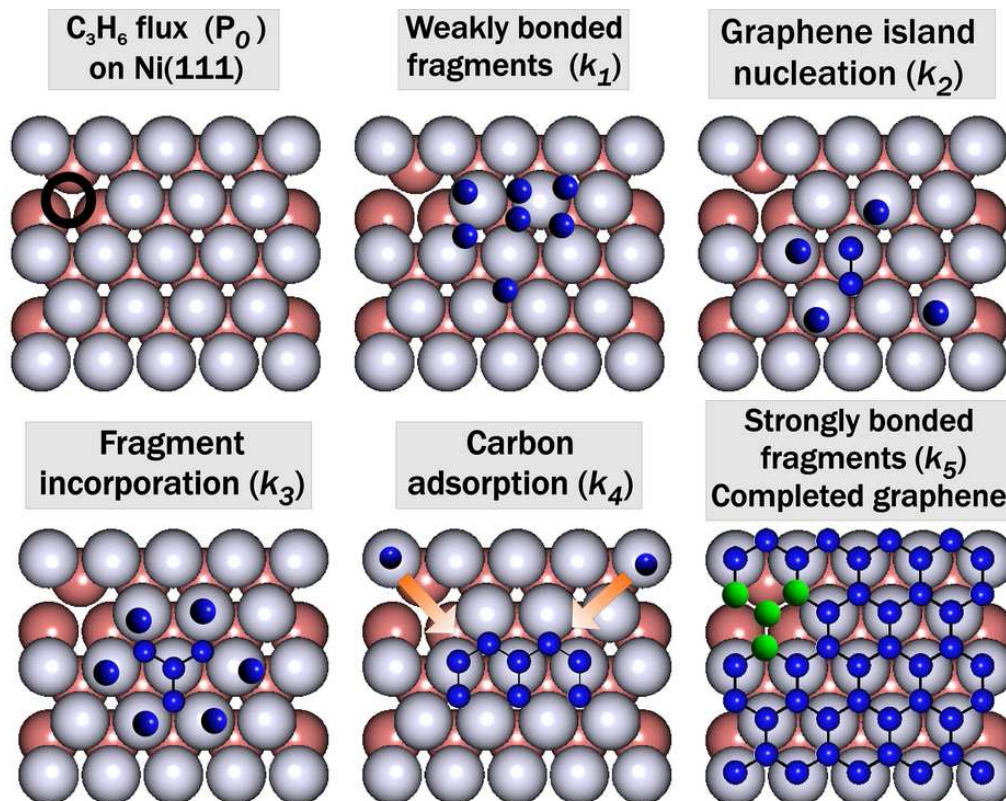


FIGURE 5.3: Elementary processes during the growth of graphene on a metal surface are described by their respective reaction constants: decomposition of C_3H_6 on Ni(111) and formation of weakly bonded fragments (k_1) and strongly bonded fragments (k_5). (The circle in the upper left figure denotes a vacancy in the Ni(111) surface.) Furthermore nucleation of graphene islands from of C_3H_6 fragments (k_2) and incorporation of fragments to graphene (k_3). These two processes lead to the growth of graphene from fragments. Graphene can also grow by adsorption of carbon atoms to the graphene layer (k_4). Courtesy of Alexander Grüneis, University of Vienna.

growth model in terms of elementary reaction steps and rate constants k_1 - k_4 . As shown in Fig. 5.3 these processes are: (1) decomposition of gas molecules on the metal surface leading to weakly bonded fragments (k_1), (2) graphene nucleation from fragments (k_2), (3) adsorption of fragments to graphene (k_3), (4) adsorption of decomposed C_3H_6 to graphene (k_4). The portion of fragments that is not converted to graphene is strongly bound to substrate defects and produced at a rate k_5 . We assume that all defects on the substrate are saturated within a critical time t_{crit} and, furthermore, that the growth of fragments is limited by the available free metal surface area. This is an important difference to the standard model of film growth, which is not self-limiting. Two mechanisms of graphene growth (k_3 and k_4) are needed in order to account for the fact that the conversion of all fragments to graphene is not sufficient to form a complete monolayer. This is obvious from the peak PE intensity of fragments that is smaller than the completed graphene PE intensity. Thus we speculate that additional processes described by k_4 incorporates carbon atoms into the graphene lattice directly. This could for example be dissociation of C_3H_6 close to the graphene edges.

With these five processes described by rate constants k_1 - k_5 we can formulate the rate equations for the concentration of weakly bonded fragments $f(t)$, graphene $c(t)$ and strongly bonded fragments that are not converted to graphene $f_r(t)$. The C_3H_6 flux onto the Ni(111) surface is equal to P_0 and the maximum fragment concentration is reached at $t = t_{crit}$. At the final stage of the experiment a fragment concentration remains which corresponds to strongly bonded fragments because the other fragments have been converted to graphene. The conversion efficiencies are assumed to be directly proportional to the abundance of each reactant.

Within this framework, one can write the following rate equations for the different species:

$$\begin{aligned} \frac{df(t)}{dt} &= P_0 k_1 \Theta(t - t_{crit}) - k_2 f(t) f(t) - k_3 f(t) c(t) \\ \frac{dc(t)}{dt} &= k_2 f(t) f(t) + k_3 f(t) c(t) + P_0 k_4 \Theta[1 - f(t) - c(t) - f_r(t)] (1 - f(t) - c(t) - f_r(t)) \\ \frac{df_r(t)}{dt} &= P_0 k_5 \Theta(t - t_{crit}) \end{aligned} \quad (5.1)$$

The first term in the top of Eqs. 5.1 describes fragmentation of C_3H_6 up to a critical time t_{crit} that corresponds to the experimentally observed maximum in fragments. The second and third term describe the growth of graphene by fragment coalescence and by adsorption to graphene, respectively. These terms appear again in the second of Eqs. 5.1 as a positive graphene growth rate $dc(t)/dt$. The third term in $dc(t)/dt$ accounts for a direct incorporation of carbon atoms from the propylene. A function $\Theta1 - f(t) - c(t) - f_r(t)$ is needed to denote the free surface area available to support the catalytic decomposition of C_3H_6 . Here $\Theta[x]$ denotes the Heaviside function. Finally, the last equation denotes the strongly substrate bonded fragments which cannot be converted to graphene. For higher temperatures graphene desorption become important which would introduce a negative term to $c(t)$. However, we do not consider this process here as the temperatures are sufficiently low. Numerical integration of the rate equation is performed with the following boundary conditions: $f(t) = c(t) = f_r(t) = 0$ for $t = 0$.

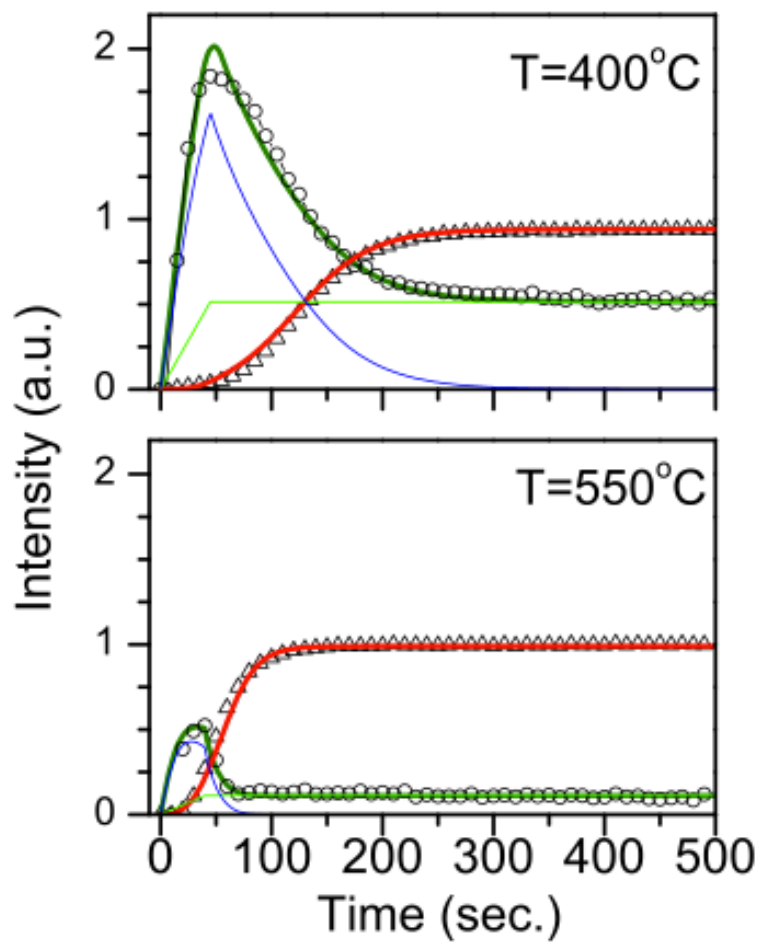


FIGURE 5.4: The experimental and calculated values of the graphene and fragment abundances as a function of time for two temperatures. The calculated curves have been produced using the set of parameters from Table 1. The fragment curves are decomposed into weakly bonded (WB) and strongly bonded (SB) fragments. Courtesy of Alexander Grüneis, University of Vienna.

T [°C]	k_1	k_2 [(MLs) ⁻¹]	k_3 [(MLs) ⁻¹]	k_4 [(ML) ⁻¹]	k_5
400	1.69	0.042	0.028	19.2	0.551
550	1.57	1.36	0.18	33.9	0.14

TABLE 1: Parameters for describing the growth according to the elementary processes from Fig. 5.3. Here k_1 denotes the production of C_3H_6 fragments, k_2 the growth of graphene islands from fragments, k_3 the incorporation of fragments to graphene, k_4 the adsorption of carbons directly to graphene and k_5 the production of strongly bound C_3H_6 fragments.

The C_3H_6 flux onto the Ni(111) surface is calculated with the Hertz-Knudsen formula and yields $P_0 = 5 \times 10^3$ monolayer (ML) per second. The parameters k_1 - k_5 are the only fit parameters that describe the whole time evolution of 100 spectra recorded in steps of 10 sec. We fitted k_1 - k_5 to the experimental data shown in Fig. 5.1. The resulting values of k_1 - k_5 are given in Table 1. In Fig. 5.4 we compare the experimentally observed to the calculated reactant concentrations. Note that the calculated concentrations were smoothed in order to account for the finite integration time of 10 s. In order to highlight the applicability of our model we perform fits to the lower and upper end of a temperature regime where high quality graphene layers are formed. It can be seen that the calculations of the fragment and graphene intensities for both synthesis temperatures are in excellent agreement to the experimentally observed abundances. This points out that graphene growth is indeed described by the set of phenomenological rate equations in Eq. 5.1.

We now discuss the implications of the graphene growth model and the relations to carbon nanotube growth. It is conceivable that some defects on the Ni(111) surface facilitate the formation of C_3H_6 fragments. A saturation of lattice sites where fragments can be efficiently produced would also explain the stop of fragment growth for $t > t_{crit}$. Graphene islands can nucleate from the fragments and grow by incorporation of further fragments and carbon atoms.

To check this hypothesis, we tried a simple free energy minimization at 600 °C, starting from random positions of carbon atoms on the nickel surface. We obtain, as found in the experiments, the initial nucleation of carbon atom couples on the nickel surface acting as a catalyst and a small-barrier diffusion, thermically overpassed at 600 K. Finally carbon atoms drift together to form the hexagonal honeycomb, which is the graphene basic building block. In Fig. 5.5 we sketch some snapshots of our DFT optimization. A small fraction of fragments always remains. These are probably strongly bounded to defect sites on the Ni(111) surface. A typical number of defects on a surface is also in reasonable agreement with the observed fragment to graphene ratios of the order of 1%. This assignment is also consistent with the observation of fewer remaining fragments with increasing temperature and can be related to healing of defects on the Ni(111) and to a higher probability of breaking the bond of the fragment to the Ni. In our model this fact is reflected by a slightly smaller k_1 and k_5 for higher temperatures.

The reaction constants k_2 , k_3 , k_4 increase with temperature which is directly related to the increased diffusivity with temperature. Concerning the growth mechanism of carbon nanotubes one reaction step is nucleation of a nanotube cap and incorporation of carbon atoms by surface diffusion. Indeed, these two processes are limited by the same constraints as graphene growth. Carbon nanotubes have also been grown from thin metal films made by electron beam evaporation [272]. The main difference is that the growth of nanotubes is

not epitaxial but unordered (spaghetti like) or perpendicular to the surface. This is a result of the fact that nanotubes nucleate from nanometer sized catalyst particles that form after the Ni film melts at high synthesis temperatures. In fact, the graphene synthesis proceeds for flat substrates while nanotubes grow exclusively from nanometer sized catalyst particles which determine the nanotube diameter.

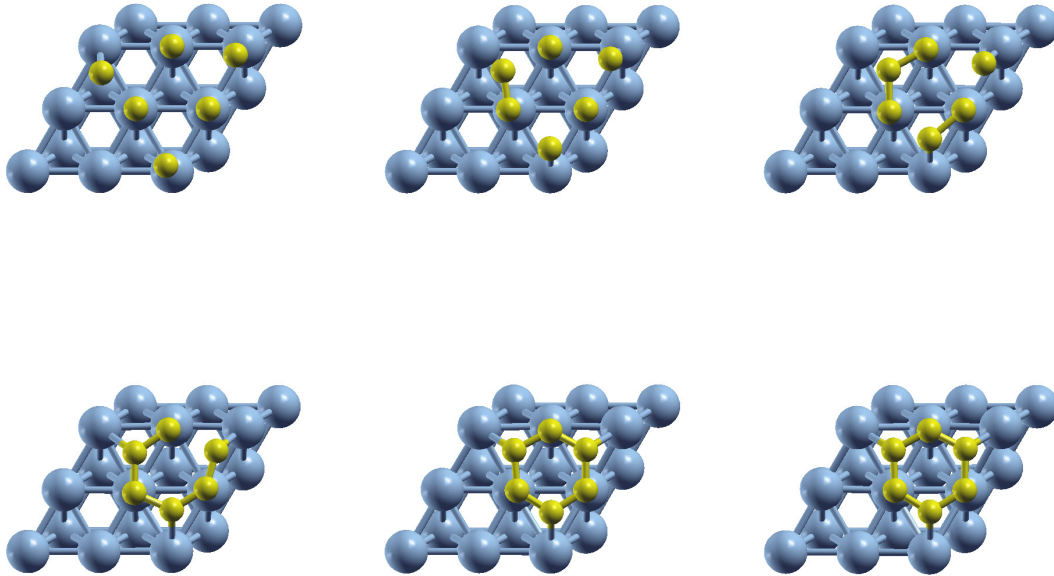


FIGURE 5.5: Ab initio molecular dynamics simulation of graphene growth on Ni(111). Snapshots of carbon atoms configurations are taken along the minimum free energy path, starting from initial random carbon atom positions (top left) to the final honeycomb structure (right bottom). Carbon atoms are depicted in yellow, while nickel atoms are in violet.

However, the nucleation of a nanotube cap on a (111) facet of a nanocrystal and the surface diffusion might be described by the same processes shown here. Also the shape of the growth curve and the time constants are similar. Thus one can conclude that a nanocrystal with (111) facets to all sides would immediately be covered by graphene and not useful for nanotube catalysis. Contrary, for carbon incorporation some lattice mismatch is good in order to keep small the diffusion barrier. However, in order to nucleate an initial nanotube cap one needs a (111) facet. This also seems the rate limiting process as the time constants are the same as in graphene.

5.3 Tunable Band Gap in Hydrogenated Quasi-Free-Standing Graphene

Doping is at the heart of modern semiconductor technology because it allows for control of the carrier density and is therefore the basis for all circuit elements. In the previous

	graphene/Ni		H-graphene/Au		
	top	hollow	C1	C2	C3
expt	284.7	284.8	284.2	283.9	284.7
calcd	284.80	284.89	284.33	283.59	284.6

TABLE 2: Experimental and theoretical C 1s Binding Energies for Graphene/Ni and Graphene/Au. For graphene/Ni, the carbon atoms are located above top and hollow Ni sites. If 1 ML of Au is intercalated between graphene and Ni, the binding energy of graphene is given by C1. The values C2 and C3 denote binding energies of extra peaks that appear upon hydrogenation and the formation of C-H bonds (see sketches in Figure 5.6a).

section we discussed a possible growth model of graphene on nickel, in this paragraph we will show how one can open a band gap upon hydrogenation in pristine quasi-free-standing graphene for microelectronic applications.

5.3.1 Core-Level Spectroscopy and X-ray Absorption

Figure 5.6a illustrates the Au intercalation and hydrogenation procedure.

Hydrogen induces a local sp^3 bonding thereby breaking double bonds to the neighboring carbon atoms. Atoms C1-C3 denote the chemical environments of unhydrogenated carbons, C atoms next to an sp^3 site, and C atoms in an sp^3 environment, respectively. In Figure 5.6b) we show the C 1s core-level spectra of graphene. The line shapes depend sensitively on the chemical bonding of the C atoms to the Ni and Au substrate and the amount of hydrogenation. The binding energies and hydrogen coverage are determined with a Doniach Sunjic line shape analysis [273].

The initial C 1s peak for graphene on Ni is gradually disappearing as Au intercalation proceeds and a second C 1s peak emerges at 500 meV lower binding energy (we call this peak C1). Both peaks are visible for intercalation of 0.5 ML Au. After intercalation of 1ML Au, only the lower binding energy peak remains, which indicates a substantially reduced bonding of graphene to the substrate.

Following the hydrogenation we observe a dramatic change in the C 1s line shape. From the line shape analysis, we obtain two new peaks with locations at $\simeq 500$ meV lower and higher (C2 and C3) binding energies than the C1 peak binding energy (which corresponds to the unhydrogenated C on Au). We assign the C2 peak to a shift in binding energy felt by a C 1s electron next to a hydrogenated carbon atom. The C3 peak can be identified with sp^3 bonded C atoms that form an out-of-plane C-H bond. This finding is in accordance with the reported results for hydrogenated SWCNTs and graphite [274, 275]. These works have shown that a shoulder at higher binding energy appears upon hydrogenation and that it can be attributed to the C 1s signal of the C-H bond. By comparing the relative peak areas of the C 1s components from the sp^2 and sp^3 carbon species, we obtain a maximum hydrogen coverage of about 25%, which is comparable to previously reported hydrogen coverages for SWNTs and graphite [274, 275, 276]. Finally, we completely removed the hydrogen stored on graphene by heating the sample to $\simeq 600$ K as is evidenced by the absence of a C-H shoulder in the C 1s spectrum (bottom panel of Figure 5.6b). This provides evidence for full reversibility of the hydrogenation and the complete removal of hydrogen.

Calculations of the C 1s binding energies are indicated by vertical lines on the energy

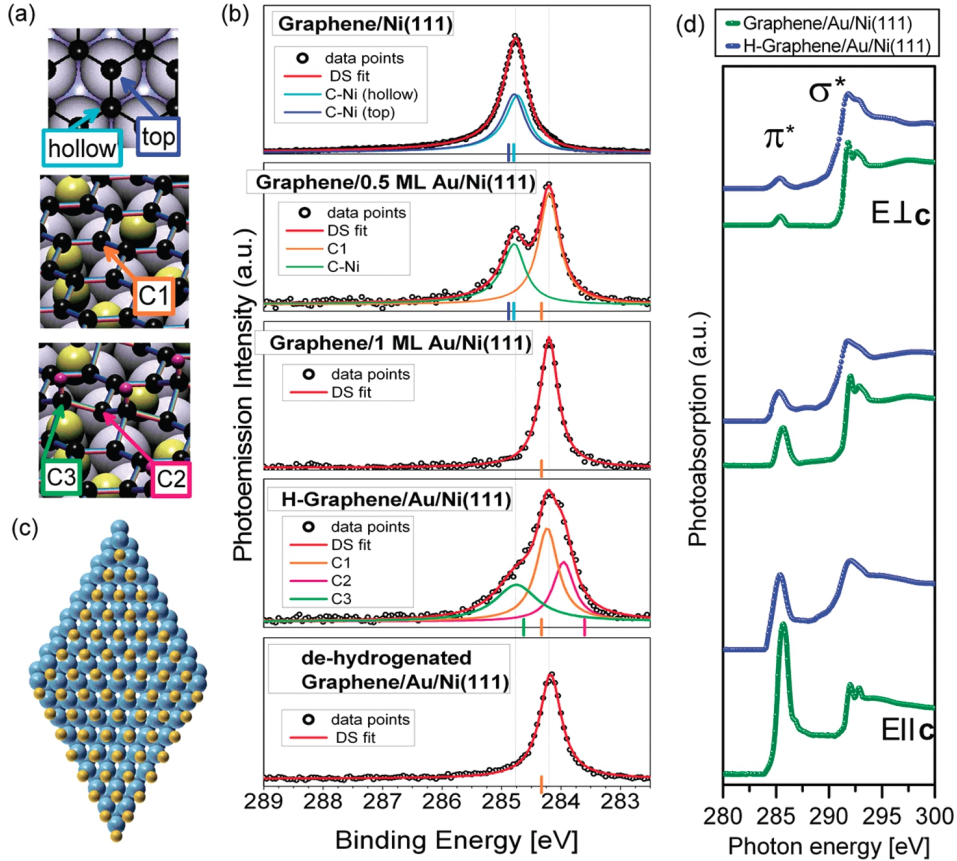


FIGURE 5.6: (a) Sketch of the functionalization procedure. From top to bottom: graphene on Ni(111), Au intercalated between the graphene/Ni interface, and hydrogenated graphene on Au. The hydrogen atoms are marked in violet. C1 and C2-C3 indicate chemical environments for graphene/Au and hydrogenated graphene, respectively. (b) C 1s core level spectra of graphene on Ni and on Au (0.5 and 1 ML of Au) and fully hydrogenated graphene. The bottom panel depicts graphene's C 1s level after dehydrogenation. All C 1s features were fitted with Doniach-Sunjić (DS) lineshapes with components for graphene/Ni (top and hollow sites), graphene/Au (C1) and hydrogenated graphene (C2-C3). The vertical lines on the energy axis correspond to the calculated C 1s energies of these components (the same color code applies). From the integrated area of the C-H component, we estimate a 25% hydrogen load. (c) The optimized superstructure of one monolayer Au (8×8) on a Ni(111) surface (9×9). (d) X-ray absorption of pristine and hydrogenated graphene on Au for grazing incidence (bottom), 45° (middle), and normal incidence (top). E and c denote the electric field vector and the sample surface normal vector, respectively.

axis of Figure 5.6b and confirm the above assignment. The experimental and calculated C 1s peak positions for the constituents of the corresponding lineshapes are summarized in Table 2.

While for pristine graphene on Ni our calculations yielded C-Ni distances of 2.08 and 2.11 Å for top and hollow Ni sites, respectively, the distance to the substrate increases to 3.15 Å for the weaker C-Au bonds which results in a significantly lowered cohesive energy of 6.60 eV/atom for C/Au (C/Ni has 7.03 eV/atom). The cohesive energy in an inhomogeneous material is given by the difference of the bulk total energy of the compound solid and the total energy of free atoms of different species, weighted by the number of atoms of each species, divided by the total number of atoms itself.

Figure 5.6c shows the optimized (8×8) on (9×9) geometry of the Au on Ni which we used for performing the calculations of the C 1s energies. We find the supercell has a length of 22.75 Å, which is in good agreement with previously reported values [277, 278]. Figure 5.6d shows the NEXAFS spectra for pristine and hydrogenated graphene on Au from close to normal to close to grazing incidence. Here grazing incidence refers to the electric field vector normal to the sample surface. The NEXAFS spectra show two prominent features at 285.5 and 293 eV which correspond to the transitions from C 1s to the π^* and σ^* bands, respectively [9]. The selection rules for the $1s \rightarrow 2p_z$ dipole transition imply a π^* intensity maximum for grazing incidence. Similarly, the $1s \rightarrow 2p_{x,y}$ dipole transitions imply a σ^* maximum for normal incidence. For grazing incidence, the NEXAFS spectrum of pristine graphene is dominated by the π^* resonance. Indeed, this behavior is remarkably similar to the NEXAFS of graphite [260].

Upon hydrogenation, we observe a strong decrease in the intensity of the π^* related peak. The attachment of atomic hydrogen to carbon atoms of graphene leads to the loss of π^* intensity and is explained by the reduced number of π -bonds due to the formation of sp^3 C-H bonds. For normal incidence (upper curves of Figure 5.6d), we observe an increase of intensity between 288 and 291 eV that can be identified as the energy position of the C-H* resonance in hydrocarbons [9]. These results nicely confirm the formation of C-H bonds which we also observe in XPS as discussed above (see Figure 5.6b). It is tempting to relate the loss of π^* intensity to an absolute H coverage. However, we find that a direct comparison is not as straightforward as in the case of the XPS because the NEXAFS spectrum is influenced by strong excitonic effects that shift the resonance peaks making the choice of the integration limits crucial. A discussion of the NEXAFS spectra was given in chapter 2 and we refer to section 2.4.6 for further details on the calculations of spectra at different incidence angles.

5.3.2 Angle-Resolved Photoemission

We now turn to an analysis of the quasi-particle dispersion and a discussion of the electronic band structure of hydrogenated graphene. This is vital for unraveling changes close to E_F that determine optical and transport properties. To this end, we perform ARPES experiments, which is the most powerful technique to study electronic energy band dispersions and gives access to graphene's spectral function [279]. A self-energy analysis allows us to estimate the hydrogen coverage independently from XPS and we find good agreement between the two methods. Figure 5.7a shows the spectral function of graphene intercalated with Au in the ΓK direction. From the momentum dispersion of the π -band, we obtain a Fermi velocity of $v_F = 1.05 \times 10^6$ m/s, identical to that of graphite [242].

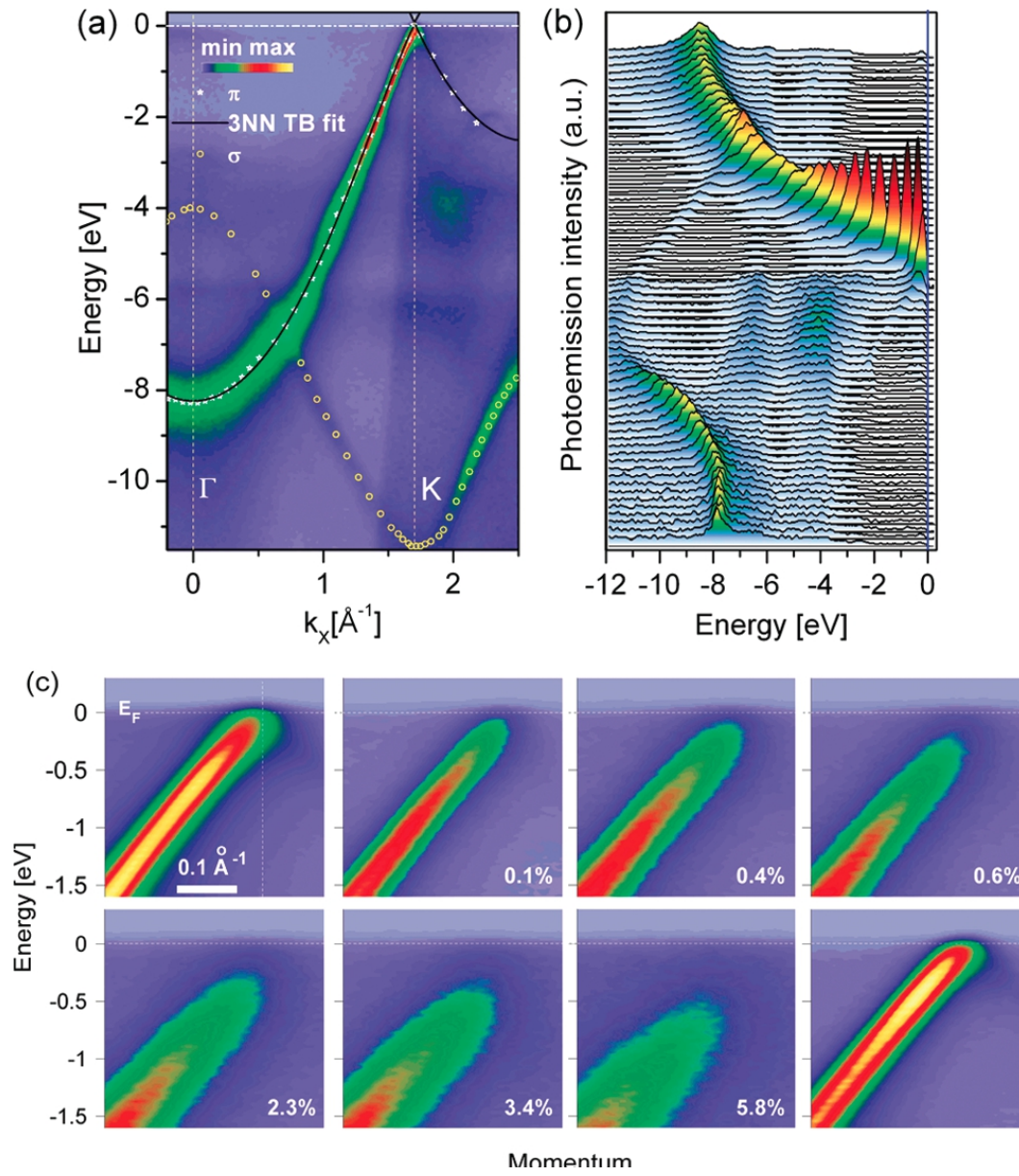


FIGURE 5.7: (a) ARPES spectrum of graphene/Au along with a 3NN TB calculation and (b) the raw photoemission data. (c) ARPES spectra around the K point of hydrogenated graphene with increasing H-coverages as denoted. The last image (bottom right) corresponds to graphene after thermal annealing.

Interestingly, the third nearest neighbor (3NN) tight-binding (TB) calculations employing the previously reported TB parameters from graphite [280] yield a band structure that is fully consistent with the measured ARPES maxima of graphene on Au. Au intercalated graphene is therefore an ideal model system to study hydrogenation. Figure 5.7c displays the spectral function of graphene at the K point after in situ exposure to a beam of atomic hydrogen. Since the spectral function provides access to the imaginary part of the self-energy, $\text{Im}(\Sigma)$, we can estimate the increase in scattering time, τ , by using the Heisenberg uncertainty principle $\text{Im}(\Sigma)\tau/\hbar \geq 1/2$, and therefore estimate the H concentration, η . To this end, we fitted constant energy cuts of the spectral function with Lorentzians in order to derive the momentum line widths Δk which are related to the imaginary part of the self-energy as $\text{Im}(\Sigma) = v_F \Delta k/2$. With the mean free path of the electrons moving in 2D graphene given by $l = 1/\eta\lambda$, where λ is the linear scattering cross section of the H impurities, and $l = v_F\tau$, we find the scattering rate, valid for low H coverage, to be $f = 1/\tau = \eta v_F \lambda$. The cross section λ measures the linear dimension of the hydrogen impurity and is expected to be on the order of a few graphene lattice parameters. An estimate based on a simple tight-binding model of H adsorption on graphene is given by $1/\tau = 2(\pi/\hbar)\eta A_c |t_0(\epsilon)|^2 \nu_0(\epsilon)$, where A_c is area per carbon atom, t_0 is a renormalized T -matrix element for scattering from a single impurity, ϵ is the electron energy, and ν_0 is the graphene electronic density of states per carbon atom [268]. Using the previously reported H-C TB parameters [281], we found for a coverage of 6% ($\eta A_c = 0.06$) and an energy of 1 eV below Fermi level, $f = 1.0 \times 10^{15} \text{ s}^{-1}$, equivalent to a scattering cross section of $\lambda = 4.4 \text{ \AA}$. Therefore, the chemisorption of one hydrogen atom results in a lattice distortion felt by electrons inside a circle of radius 4.4 \AA . This is in reasonable agreement with previous reported values [253]. Notably, we do not include effects of inhomogeneous H clustering or the effect of varying chemisorption energies for an H atom that might lead to a different and not entirely random chemisorption pattern.

Turning back to Figure 5.7c, it is clear that already at low H/C ratios of 0.5%, we observe a dramatic decrease of the photoemission (PE) intensity of the π band close to E_F accompanied by a general broadening of the π -band. The most striking effect is the opening of a gap of reduced ARPES intensity between the π -band and E_F . The π band maxima are therefore not crossing E_F anymore but appear at lower energies as hydrogenation proceeds. Finally, the last graph of Figure 5.7c shows the fully recovered π -band after annealing at 600 K, demonstrating the reversibility of this functionalization procedure. The energy dispersion curves (EDCs) through K (indicated by a vertical dashed line in the first viewgraph of Figure 5.7c) are displayed in Figure 5.8a.

The EDCs have been integrated over 2° around K. It can be seen that the maxima of the EDCs shift by $\simeq 800 \text{ meV}$ for 8.7% hydrogenation. As we will show later, this is directly related to a gap opening. The inset in Figure 5.8a depicts the momentum dispersion curves (MDCs) taken at 1 eV below E_F from which we determined the H/C ratio η as described above.

Several mechanisms responsible for the downshift of the π band are conceivable. First, the chemisorbed H might lead to graphene quantum dot formation and hence to size quantization resulting in the opening of a band gap. This effect might be especially important for a regularly chemisorbed H superstructure. The strong increase in impurity scattering rate, however, points toward randomly chemisorbed H. Furthermore, assuming single sided attachment of H to graphene on a substrate, the lowest energy configurations for two neighboring H atoms break the sublattice symmetry [282]. Symmetry breaking in turn

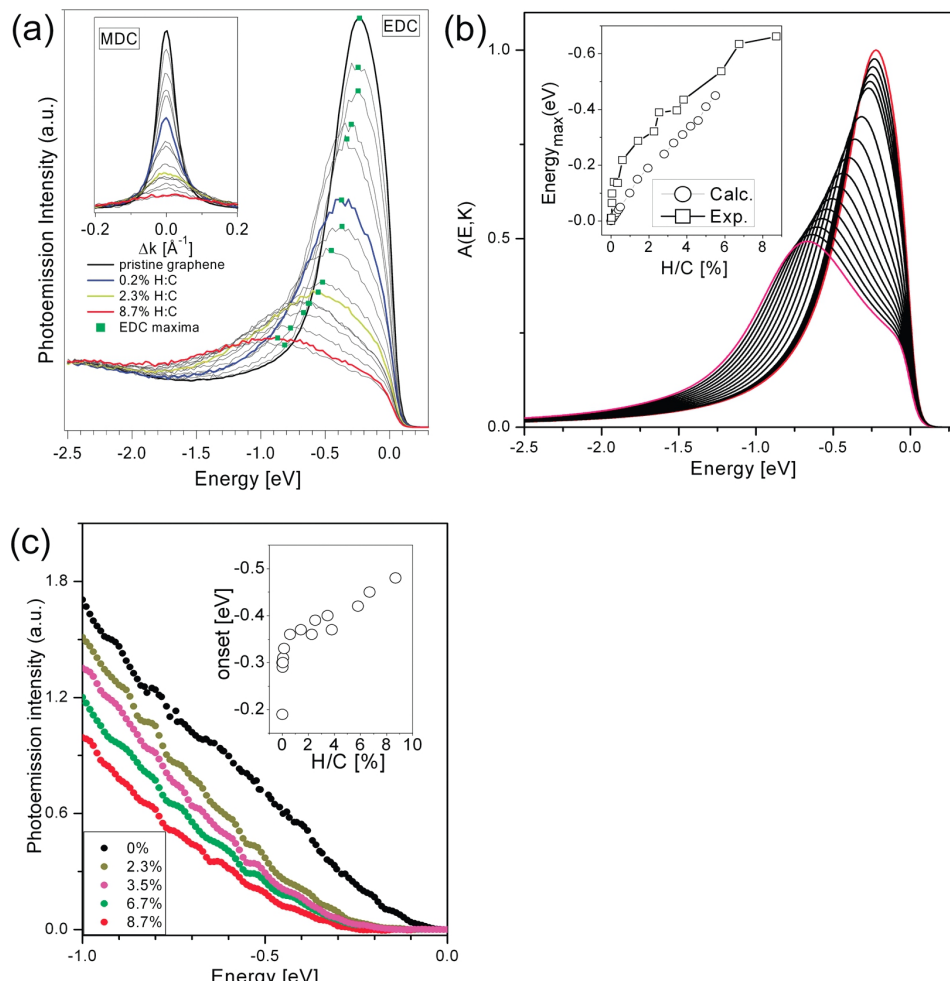


FIGURE 5.8: (a) Energy dispersion curves (EDC) and momentum dispersion curves (MDC) for 15 different hydrogenation stages as indicated. (b) Calculations of $A(E, K)$ for increasing hydrogen content between 0% and 5.5% (indicated by red color). The inset compares the calculated maxima of $A(E, K)$ to the experimental EDC maxima (relative shift to the curves for pristine graphene). (c) Angle-integrated PE intensity for different H/C ratios with the Au background intensity subtracted. The inset denotes the energy onset of the rise in intensity.

invariably leads to a gap opening which is proportional to the difference in potential energy felt by the hydrogenated and unhydrogenated carbon atoms. This would also explain the broadening of the spectral function $A(E, K)$: in this model there are sp^2 and sp^3 sites and the spectral weight is merely shifting between them.

Clearly, other chemisorption patterns which do not break the sublattice symmetry are also conceivable but their contribution is much smaller as can be inferred from the agreement of the measured spectral functions and the model calculations for symmetry breaking H chemisorption sites as discussed below. The cuts of the calculated spectral function $A(E, K)$ for single-sided hydrogenation are depicted in Figure 5.8b and are to be compared to the EDCs from Figure 5.8a. It can be seen that the shift of the maxima of $A(E, K)$ with proceeding hydrogenation, the broadening, and also the line shape are in good agreement to the experiments. The small remaining differences come from the fact that the experimental EDCs contain some intensity from the Au electronic states. Notably, we can only obtain the downshift of the maxima of $A(E, K)$ for our calculation if we impose the constraint that at most one C atom per graphene unit cell can be hydrogenated. This provides evidence that symmetry breaking is the mechanism responsible for the gap opening as seen in the ARPES spectra. The inset in Figure 5.8b compares the EDC maxima to the energy maximum of the calculated $A(E, K)$ and it is evident that they also agree well.

Looking at the downshift of the EDC maxima with hydrogenation, it is clear that this will also influence the total density of states (DOS) which is proportional to the angle integrated PE intensity. After performing the integration, we subtracted the small PE intensity of the underlying Au. The resulting integrated PE intensity of hydrogenated graphene for different $\eta = \text{H/C}$ ratios is depicted in Figure 5.8c. It is clear that for increasing η , the integrated PE intensity at a given energy is smaller which relates to the gap opening and puts our data in a wider context relevant for optical absorption experiments. This gap opening is also evident from the inset to Figure 5.8c where we depict the energy value at which the PE intensity starts to rise (we define this onset as 10% of the integrated PE intensity of pristine graphene at 1 eV). With proceeding hydrogenation, the onset energy appears at a lower energy, opening up a region of no PE intensity (i.e., a gap). Most importantly, this onset is directly related to half the band gap value since it is measured with respect to E_F if we assume electron-hole symmetry. In Figure 5.8c we have an onset energy of 0.5 eV for the maximum hydrogenation level. Therefore we expect twice this value, i.e., 1 eV for the electronic band gap between π and π^* . This is a perfect energy range for optical applications, and it is also in agreement with calculated values [264, 269].

5.4 Direct observation of a dispersionless impurity band in hydrogenated graphene

In this section we present the first experimental and theoretical evidence of a hydrogen-derived midgap state in H-graphene using ARPES and near-edge x-ray absorption fine structure (NEXAFS) measurements. The latter method provides access to unoccupied electronic states above the Fermi level by measuring the x-ray absorption which is caused by transitions from the C 1s core level to the π^* and σ^* energy bands. For undoped H-graphene the impurity band is located within the emerging gap at the Fermi level and is therefore hardly accessible with ARPES since this method probes only the occupied electronic states of the band structure.

Using potassium intercalated n -doped graphene, the hydrogen-derived state becomes available for an occupation with electrons and acts as an acceptor level for π^* electrons which can be directly observed in ARPES.

Density functional theory (DFT) calculations suggest that the midgap state is largely derived from H 1s orbitals. Calculations of the typical and average density of states (DOS) using the kernel polynomial method (KPM) with a tight-binding (TB) band structure calculation [268, 270] indicate that the new state does not localize easily despite the randomness in the H chemisorption sites.

We now discuss the electronic properties of hydrogenated graphene intercalated with Au using NEXAFS, by inducing a dipole transitions from the C 1s core levels to the empty π^* energy band as a function of hydrogenation. In Figs. 5.9(a) and 5.9(b) we show the NEXAFS spectra for pristine and H-graphene (H/C \simeq 15%), respectively. Both sets of curves depict a similar behavior with ϕ , the angle of light incidence. For grazing incidence ($\phi = 20^\circ$) we have a maximum photoabsorption referring to the π^* resonance and for normal incidence ($\phi = 90^\circ$) we have a maximum absorption identified as the σ^* resonance. This is in agreement with the NEXAFS experiments performed on graphite and previous measurements on graphene [283, 260, 284].

A closer look at the π^* resonance is shown in Fig. 5.9(c). Two observations can be made from the comparison of pristine and H-graphene: (1) the π^* resonance gets weaker in intensity upon hydrogenation and (2) the high-resolution spectra show a low-energy shoulder appearing upon hydrogenation for grazing incidence. Observation 1 can be well understood since hydrogen adsorption effectively removes bonds (sp^3 C-H bond). Concerning observation 2, the feature appears between 284.3 eV and 285.3 eV, as indicated by the arrows in Fig. 5.9(c).

In the following we argue that this extra feature can also be attributed to a midgap state that lies in between the π and π^* bands. Such a feature can contribute to a downshift of the π^* resonance.

To 0th order NEXAFS resembles the unoccupied density of states (neglecting the light polarization, excitonic, and matrix element effects). A comparison with the calculated DOS is therefore key to assign the measured feature at the π^* resonance to an electronic state. To that end we performed tight-binding (TB) calculations of the DOS of disordered H-graphene using the equation-of-motion method for various values of H coverages [285]. This method allows us to treat large systems with adjustable hydrogen coverages. In this case we chose graphene with 180.000 C atoms for the calculations. The TB parameters we used were $\gamma = 2.7$ eV for the C-C interaction energy, $\gamma_i = 5.7$ eV for the C-H hopping energy, and $\epsilon_i = -0.2$ eV for the on-site energy of the hydrogen orbital [285]. In Fig. 5.9(d) we depict the calculated density of states of C_nH for various C/H ratios in agreement with previous calculations of disordered graphene [285]. It can be seen that with increasing H/C ratio, a new electronic state appears in between the π and π^* bands at the Fermi energy. Looking at Fig. 5.9(c) the additional shoulder at the π^* resonance also appears close to the onset (the edge of the conduction band in Fig. 5.9 is located at 284.2 eV). It is therefore likely that the additional shoulder in NEXAFS is a fingerprint of a hydrogen-derived midgap state. Such midgap states have been theoretically predicted [264] but have not been observed so far in graphene. Their existence may have implications for superconductivity comparable to the case of boron-doped diamond [286, 287, 288] as well as magnetism and optical properties of H-graphene [264]. The spectral contribution of these new states can be engineered for attainable H/C ratios by exposing graphene to an H beam for a defined time.

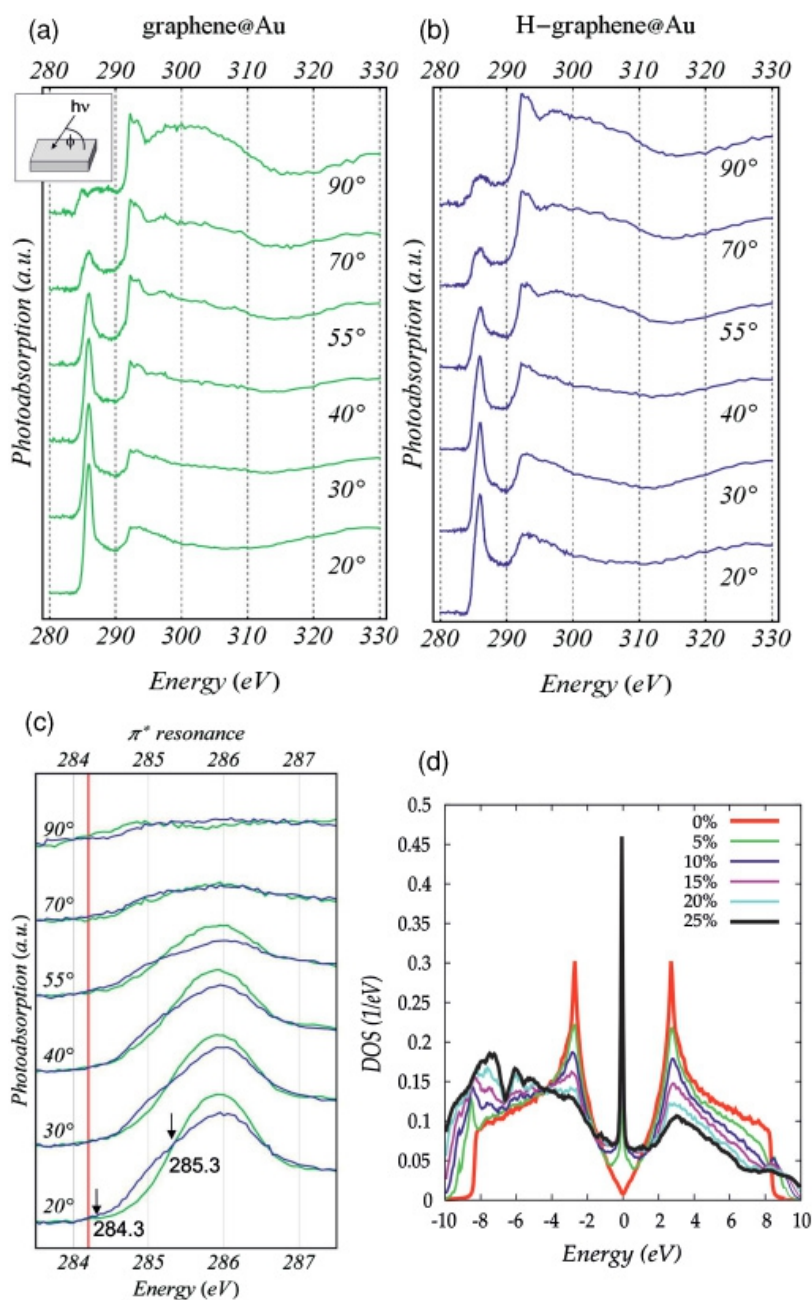


FIGURE 5.9: NEXAFS spectra of (a) pristine graphene and (b) hydrogenated graphene (H/C 15%) for various incident angles between normal (90°) and grazing incidence (20°). The inset in (a) shows the experimental geometry and ϕ , the angle of light incidence. (c) Comparison of pristine (green) and H-graphene (blue) in the region of the π^* resonance. The additional shoulder at lower photon energy denoted by two arrows is best visible for grazing incidence. The red line indicates the C 1s energy position of unhydrogenated graphene/Au. (d) Calculated density of states for hydrogenated graphene with various H/C ratios.

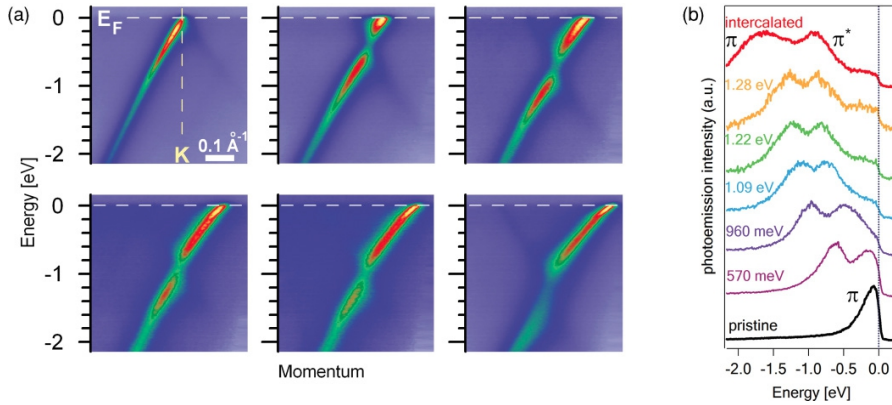


FIGURE 5.10: (a) ARPES intensities around the K point of the Brillouin zone of graphene intercalated with one monolayer Au for increasing potassium doping. The last viewgraph (bottom right) denotes the photoemission intensities of graphene intercalated with potassium in between the graphene/Au interface. (b) Energy dispersion curves taken at the K point for the six doping steps in (a) with the shift of E_F as indicated. For the doped graphene, the two peaks correspond to the π and π^* bands. Upon intercalation of potassium between graphene and Au, the value of the gap between π and π^* bands doubles.

However, it should be noted that the observed shoulder in the vicinity of the π^* resonance cannot exclusively be attributed to a hydrogen midgap state as it is also possible that changes in the carbon bond configurations at the hydrogenation sites contribute to the observed shoulder in NEXAFS [284]. Therefore, we turn to an alternative strategy which comprises the doping of graphene with additional electrons. This results in a shift of the Fermi level with respect to the Dirac point so that the hydrogen midgap state becomes populated with electrons and should be observable with ARPES. A well-known approach from graphite is the intercalation of potassium [289, 290], since alkali metals donate their electrons without forming covalent bonds which might influence the hydrogenation procedure. Figure 5.10(a) shows ARPES spectra of monolayer graphene with an increasing potassium coverage. The first viewgraph (upper left) in Fig. 5.10(a) corresponds to undoped graphene and one can see the π band touching E_F at the K point in the Brillouin zone. Clearly, the Dirac point shifts away from E_F to higher energies with increasing potassium coverage up to a final value of $\simeq 1$ eV.

It has been put forward that the small gap in the spectral function at the K point originates from the Au superstructure which breaks the AB symmetry [291]. Warming up the sample to RT and cooling to 25 K again yields a completely different picture shown in the last panel (bottom right) of Fig. 5.10(a). A much larger separation between π and π^* at the K point is observed. We attribute this to the intercalation of potassium atoms into the graphene/Au interface, consistent with the behavior of other metals (Au, Ag, Fe, Cu...) that readily intercalate in between the interface of graphene and the Ni substrate [283, 277, 292, 293]. The intercalation at RT is also consistent with the reported 100 K temperature limit above which potassium ions on a graphene sheet become mobile [294]. Upon potassium intercalation the gap between the π and π^* bands increases which could

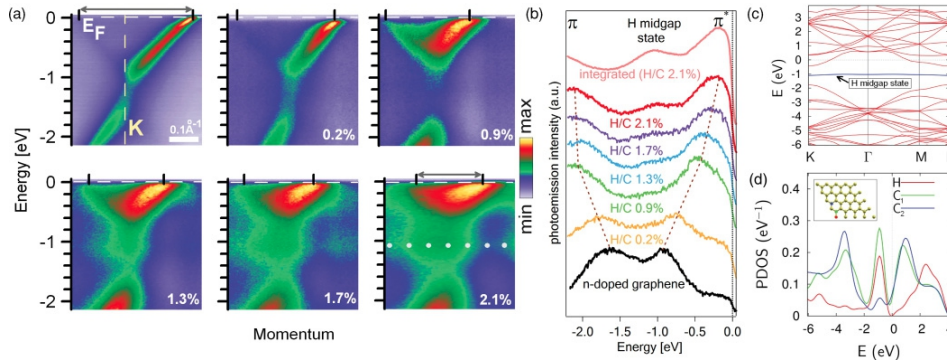


FIGURE 5.11: (a) ARPES intensities around the K point of the Brillouin zone of hydrogenated n -doped graphene with increasing H/C ratios as denoted in percent. The size of the Fermi surfaces is indicated by two black vertical ticks on top and an arrow for the H/C = 0 and H/C = 2.1% ratios. The dots in the last panel are a guide to the eye and depict the dispersionless midgap state. The photoemission intensity scale is depicted and applies to all graphs. (b) Energy dispersion curves of the ARPES intensity at the K point. (c) DFT calculation of the electronic energy bands and (d) the partial DOS of HC_{32} . A rigid band shift of 1 eV was applied in (c) to account for the potassium doping. The dispersionless band 1 eV below E_F in blue corresponds to the midgap state. The inset to (d) depicts the unit cell and the atoms (H, C1, and C2) in the graphene lattice which contribute significantly to the midgap-state DOS.

be explained by the fact that the Au lattice forces the potassium ions to positions which distort the graphene lattice and further break the AB symmetry of the carbon atoms.

The energy dispersion curves (EDCs) at the K point are shown in Fig. 5.10(b) for the potassium-doping steps. The n doping does not significantly change the separation between the π and π^* bands. However, upon potassium intercalation the energy separation increases from 400 meV to 800 meV. We purposefully induce this “gap” for a direct observation of the hydrogen acceptor level which we will discuss below.

In Fig. 5.11(a) we present ARPES spectra of a hydrogenation series that was performed on fully n -doped graphene. In the potassium intercalated graphene with the larger gap between π and π^* , the graphene layer provides a buffer between potassium ions and H atoms on top of graphene which efficiently prevents chemical bonding [295]. From the hydrogenation series in Fig. 5.11(a) we observe (i) a general broadening of the spectra, (ii) a shrinkage of the Fermi surface pointing towards hole doping, (iii) that the gap between π and π^* increases with hydrogenation, and most importantly, (iv) that a new state appears within this gap. The new state is almost dispersionless and its ARPES intensity increases as hydrogenation proceeds. The increased ARPES intensity of the midgap state and the shrinkage of the Fermi surface of the π^* band as indicated by the two black vertical ticks on top of each panel in Fig. 5.11 (a) go together and are attributed to an electron transfer from the π^* band to the midgap state. We employ the Fermi surface shrinkage to calculate the H/C ratio [266] which is depicted for each hydrogenation step in Figs. 5.11(a) and 5.11(b).

Notably, this estimation of the H/C ratio is based on the assumption that each hydrogen

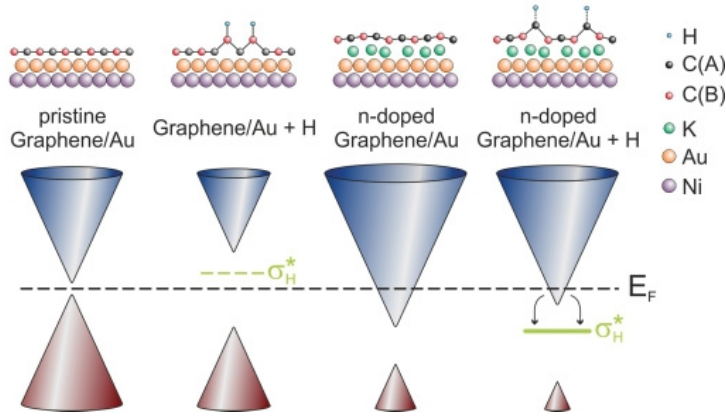


FIGURE 5.12: Sketches of symmetry-breaking, hybridization, and charge-transfer processes in pristine and n -doped H-graphene. In the case of undoped hydrogenated graphene the hydrogen-derived midgap state can be measured with absorption spectroscopies probing unoccupied states such as NEXAFS. Only if E_F is above the energetic position of the midgap state (denoted by σ_H^*) can it be directly observed in ARPES. In this case, the midgap state likely accepts electrons from the π^* band of graphene denoted by arrows (see the right panel).

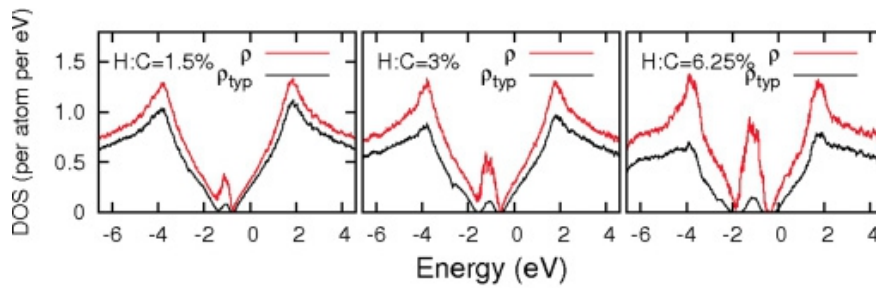


FIGURE 5.13: The calculated typical (black line) and average (red line) DOS for three different H/C ratios. The vanishing of the typical DOS at energies slightly higher or lower than the acceptor level (located at $E = 1$ eV) indicates a localization of the π -band edges. The typical DOS of the midgap state never reaches zero which indicates that it is resistant to localization. A relatively large width of the impurity band helps the states in the middle of the impurity band remain extended.

atom accepts one electron [266]. Hence a smaller charge transfer to the acceptor hydrogen level would lead to effectively higher H/C ratios. As we will show later, the acceptor level forms an impurity band which does not localize for the low H/C ratios ($\simeq 1\%$) shown here, despite the randomness in H positions.

In Fig. 5.11(b) we depict an analysis of the spectral functions from Fig. 5.11(a) of hydrogenated n -doped graphene at the K point which fortifies our findings. Already at ratios of H/C = 0.9% the energetic distance between the π and π^* bands increases from 0.8 eV to 1.6 eV, which we attribute to the partial sp^3 hybridization as discussed previously [283]. The EDCs integrated over all k values for H/C = 2.1% [from last panel of Fig. 5.11(a)] unambiguously visualizes the new electronic state between 0.7 eV and 1.6 eV [top curve of Fig. 5.11(b)]. The lack of a dispersion of this feature can be clearly seen when comparing the integrated EDC with the single EDC taken at the K point. Whereas the shape of the midgap state is nearly identical in both curves, only the intensity of this state is increased when integrating the EDCs in k space. Figure 5.11(c) shows DFT calculations of the band structure of H-graphene HC_{32} in agreement with previous calculations [264], which is comparable to that measured for the highest H/C ratio of 2.1%. To account for the n doping from potassium atoms, we applied a rigid shift by 1 eV. Clearly, there is an almost dispersionless shallow acceptor level also present in the calculation which we identify as the new electronic midgap state at $\simeq 1$ eV that we have found using ARPES.

For a complete understanding of the origin of this new state, we project the DOS on the C $2p_z$ and H1s orbitals. We consider C $2p_z$ from the hydrogenated site up to the third-nearest neighbor. Figure 5.11(d) depicts the projected DOS for the midgap state. Interestingly, the contribution of the $2p_z$ orbital of the same sublattice of the hydrogenated C atom is almost zero. From the projected DOS it is evident that the midgap state is made up largely from H 1s orbitals and the C $2p_z$ orbitals from the neighboring lattice site. In Fig. 5.11(d) these two atoms are indicated by H and C1.

A more realistic DFT calculation of hydrogenated graphene on a K/Au substrate has been performed and indicates that the midgap state is robust against substrate interactions. The geometry of the systems with (left panel) and without (right panel) hydrogen is shown in Fig. 5.14(a). The ratio K/C is 10/98 $\simeq 10\%$ while the H:C ratio is 8/98 $\simeq 8\%$, respectively. The corresponding density of states, which is projected for the carbon site (PDOS) before and after hydrogenation, is depicted in Fig. 5.14(b). It is evident, that a midgap feature appears upon hydrogenation close to the energy $E \simeq 1.0$ eV. This calculation demonstrates that the main feature of the model DFT and KPM calculations are robust against a substrate effect from K ions and Au atoms.

Our present data suggest that the midgap state always exists in hydrogenated graphene, but its position with respect to E_F determines whether it is observable by ARPES which probes only occupied states or absorption spectroscopies such as NEXAFS measuring unoccupied states above the Fermi level. A sketch of the ongoing symmetry-breaking, charge-transfer, and hybridization processes in pristine and n -doped H-graphene is shown in Fig. 5.12.

Calculations of the accumulated DOS (assuming a charge transfer of one electron per potassium) suggests that K/C $\simeq 1/50$ would be sufficient for explaining the shift of E_F of 1 eV in the π^* band. Surprisingly, the DFT calculations suggest that $\simeq 75\%$ of all electrons coming from potassium are transferred to the Au layer and therefore a higher K/C $\simeq 1:12$ stoichiometry is needed. Given the almost identical electronegativities and work functions of Au and C, this result can only be understood in terms of the much larger Fermi

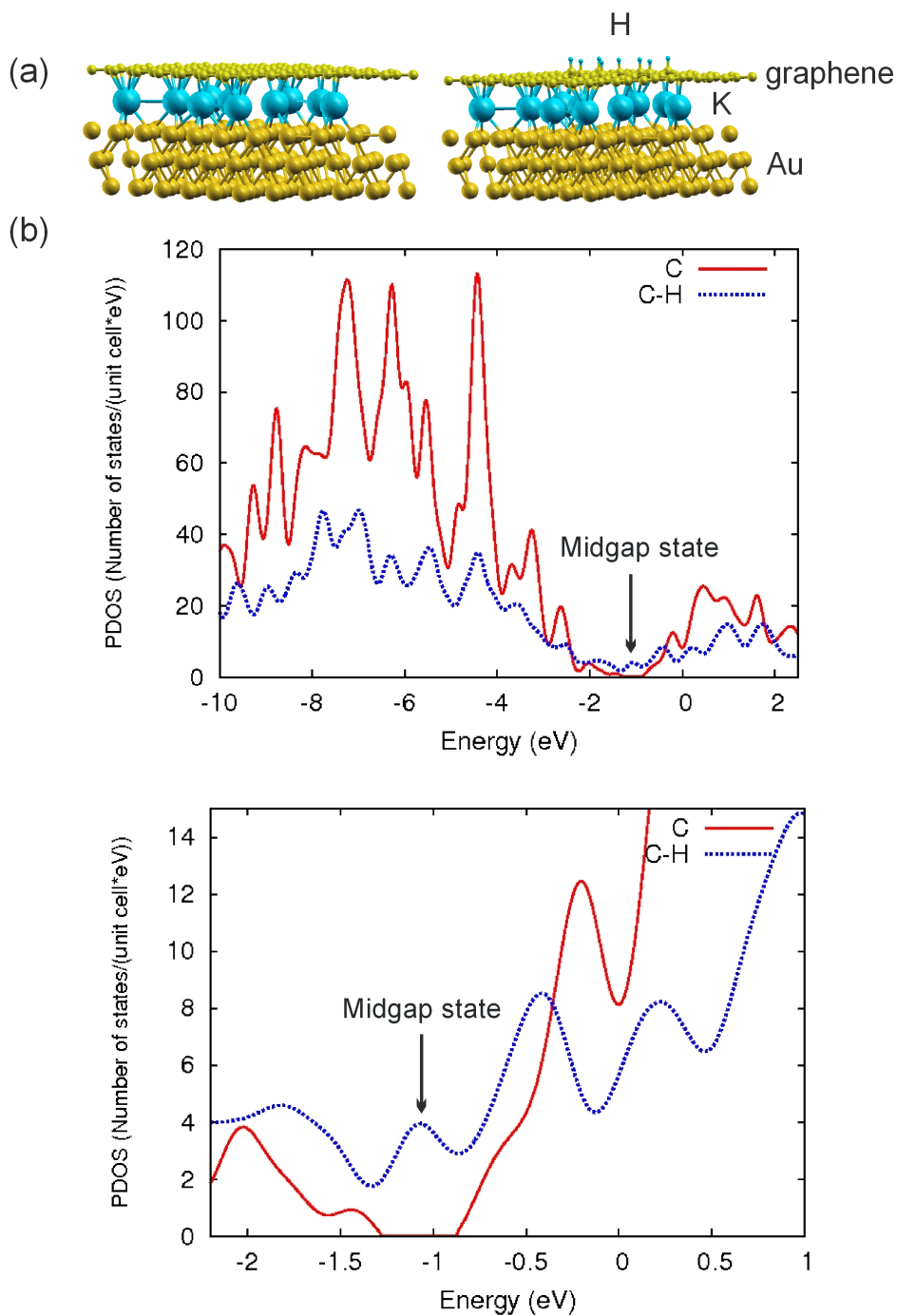


FIGURE 5.14: (a) The optimized structure of a realistic system with potassium atoms (in light blue) intercalated in between the Au and graphene interface. We use $K/C \approx 1/10$ in order to reproduce the experimentally observed charge transfer. In the left panel we show the structure before and in the right panel after hydrogenation ($H/C \approx 1/8$). (b) The projected density of states (PDOS) on the Carbon site of this system before and after hydrogenation shown in blue and red color, respectively. The upper panel shows the full energy range. In the lower panel the energy region of the midgap state is enlarged. The peak in the PDOS that corresponds to the midgap state is depicted.

surface of Au which is capable of accepting more electrons while yielding the same shift of E_F as graphene. The positively charged potassium ions underneath the graphene attract negatively charged H ions. This intuitive explanation is fortified by our DFT calculation. We have checked the chemisorption energies for H on pristine graphene/Au and H on graphene/K/Au. We found no substantial difference in energy for the chemisorption of H between any two lattice sites of pristine graphene. However, in the case of potassium intercalated underneath the graphene, the adsorption site close to the potassium ion is favored by a 1 eV higher chemisorption energy. This clearly points towards a random chemisorption of H on graphene/Au and a favored chemisorption of H close to potassium ions in the case of the electron doped graphene. Therefore, in our model calculations of the typical and average DOS, we have assumed a random chemisorption site among a subset of all C atoms that are adjacent to a potassium atom. The relevant K/C=1/12 stoichiometry that has been discussed earlier on was used for this calculation in order to be consistent with the observed doping level. For such a chemisorption pattern, we find gaps in both the DOS and the spectral function.

Finally, we investigate impurity band formation and electron localization in H-graphene which governs its transport and optical properties. On the one hand, a minimum concentration (Mott criterion) is needed for band formation, but on the other hand, too much disorder can induce electron localization in both the π electron bands and the midgap state. A very low H impurity concentration leads to midgap energy levels corresponding to bound states. The radius of such bound states is given by $a_B = e^2/(2\epsilon B)$ where ϵ is the relative dielectric constant of the host material (in this case graphene) and E_B is the binding energy of the acceptor level. The Mott criterion [296] for the formation of a metallic band from such discrete levels states that the concentration n_c of the impurities must be high enough to satisfy $n_c^{1/2} a_B \simeq 1/4$. Assuming the H/C ratio to be η , the critical concentration will be given by $\eta_c = 0.007(\epsilon B)^2$. In our case the position of the impurity band with respect to E_F is given by $E_B \simeq 1.0$ eV, and with $\epsilon \simeq 2$ the critical concentration needed for metalization is $\eta_c \simeq 1.4\%$. Therefore when the concentration of H atoms is $\simeq 1\%$, we expect the formation of an impurity band.

However, since the position of H adsorbates is random, the question of the localization of impurity band states arises. To answer this question, we use the KPM method to calculate the typical electron density of states, wherein the vanishing of this DOS indicates localization [270]. In Fig. 5.13 we have depicted the average DOS and the typical DOS for H-graphene within a TB model [268]. Such a TB model, although ignoring the effect of the substrate, is consistent with our ARPES data for the non-hydrogenated samples which show perfect Dirac cone dispersion. When the concentration of H atoms is very low, the model results in an effective Hamiltonian for C atoms only, with an energy-dependent on-site potential [268]. However, when the H impurity concentration is comparable to η_c , in addition to the energy-dependent random potential (Anderson type), the hydrogenic wave functions will have substantial overlap to give rise to an impurity band. Moreover, for moderate values of the diagonal on-site disorder $W = \gamma$, where W is the range of the on-site energies and γ is the C-C hopping energy, a mobility edge emerges in the conduction and valence bands [270].

The acceptor band survives the randomness regarding the position of the H atoms, and the states in the center of the acceptor band remain extended and a localization of these states is not expected. As can be seen in Fig. 5.13, a vanishing of the typical DOS indicates that the states close to the edges of the impurity band get localized, but due to

the substantial bandwidth, states in the middle of the band remain extended. Therefore, although the impurity band has no dispersion as indicated by the ARPES measurements of the spectral function, it nevertheless has a sufficiently large bandwidth, so as to provide enough kinetic energy to enable conduction within this band. For very low concentrations, a localization of charge carriers in this impurity state would be expected, as the right and left mobility edges of the impurity band are expected to merge when the impurity band becomes narrow enough.

5.5 Conclusion

In summary we have unraveled the processes that lead to the formation of a high quality graphene layer on metal surfaces during a CVD process. Our results provide valuable insights and guidance for CVD of graphene and also nanotubes. We have observed a strong temperature dependence that influences both the quality of the resulting graphene layer and the growth speed. The growth is modelled by a set of three coupled nonlinear differential equations which is solved numerically and in excellent agreement to the observed C1s intensities.

Furthermore, we have investigated the functionalization of quasi-free-standing graphene with atomic hydrogen. The XPS measurements of graphene have shown a C 1s core level shift of 0.5 eV toward lower binding energy upon Au intercalation in between the graphene/Ni(111) interface, resulting in a substantial reduction of the substrate interaction. This is in accordance with our calculations that predict a reduction of the cohesive energy per atom by 0.4 eV and an increase of the graphene substrate distance by 1 Å. The exposure of graphene to atomic hydrogen induces the formation of C-H bonds resulting in a local sp^3 hybridization. This is directly observed in XPS by the appearance of two additional C 1s peaks originating from the C-H bond and the C atom next to it. These two features are separated by almost 1 eV from each other, which is also in good agreement with the C 1s binding energy calculations (see the features C2 and C3 depicted in Figure 5.6b). NEXAFS measurements indicate a rehybridization from sp^2 to sp^3 and the formation of C-H bonds perpendicular to the graphene layer. Most importantly, the ARPES spectra of hydrogenated graphene clearly show the downshift of the π band's spectral function to lower energies and also a broadening. Our calculations support sublattice symmetry breaking as the reason for the observed changes in the ARPES upon hydrogenation. Since the energy difference between the onset of the integrated PE intensity (proportional to the DOS) and E_F is related to half the electronic band gap value, we expect tunable optical properties for hydrogenated graphene. Our results also unraveled an interesting connection between the hydrogenation of graphene and amorphous carbon. On the one hand, the origin for the tunable optical band gap in a-C:H [261] might also be understood in terms of sublattice symmetry breaking. On the other hand, hydrogenation might as well also lead to functional optical devices based on graphene because the electronic band gap can be tuned with hydrogen coverage and to a model system to study hydrogen storage in carbon materials. Our results are therefore also relevant to optical absorption, photoluminescence, and resonance Raman spectroscopy of graphene. First, the optical gap should be observable and possibly lead to photoluminescence, similar to the case of oxidized graphene [297]. The broad peak maximum in the spectral function would manifest itself as the so-called Urbach tails in the optical absorption spectrum, similar to the case of a-C:H. Second, it is

well-known that hydrogenated graphene shows an increase in its D band Raman spectrum which is due to the randomly chemisorbed H atoms that act as defects [265]. Little is known about the relation of the D band intensity to the absolute number of defects. We therefore propose a combined photoemission and resonance Raman study of hydrogenated graphene with a defined H coverage to determine the relation between D band Raman intensity and H/C ratio. Such a defined environment is extremely important for a quantitative understanding of the defect scattering-induced D band and also for the emerging field of graphene metrology.

Finally, we have found a new electronic state in H-graphene that is located between the π and π^* bands. For undoped H-graphene this state is energetically situated within the gap around E_F and is accessible with absorption spectroscopies such as NEXAFS. In the case of n -doped H-graphene the midgap state becomes available for electrons and directly observable with ARPES since it is then situated below E_F . Therefore, the H impurity band likely acts as an electron acceptor level which provides the possibility to control the electron concentration in H-graphene via the H/C ratio. An estimation of the Mott criterion and a calculation of the typical DOS suggests that above H/C \simeq 1% and below H/C \simeq 6%, the acceptor level can form an extended impurity band. DFT calculations of the DOS show this new band to be largely composed from H 1s orbitals. Hence the new electronic state we found is expected to give rise to metallic conduction when the chemical potential is tuned to cross the impurity band. Furthermore the questions of a spin splitting of the impurity band and the magnetic properties of H-graphene arise as has been suggested by theoretical calculations [264]. Further studies including spin-resolved methods might be necessary to address these open questions and gain more detailed insights into the nature of this new electronic state in H-graphene.

Chapter 6

Zeolitic Imidazolate Frameworks for gas separation, storage and diffusion

In this chapter we study, firstly, adsorption and dynamics of CO_2 , CH_4 , H_2 and binary mixtures thereof, in the Zeolitic Imidazolate Frameworks ZIF-2 to ZIF-10, using computer simulations. We find that the amount of gas adsorbed in these materials is smaller than what can be stored in other organic frameworks, due to the small-pore structure of these crystals.

The presence of these small pores has a favorable effect when adsorptive gas separation is considered. In particular, ZIF-9 has a CO_2/H_2 selectivity much higher than that observed in other organic frameworks. However, the narrowness of the pores has a serious effect on permeation selectivity: the diffusion of gases in ZIF-5 and ZIF-9 is severely hindered.

When both adsorption and diffusion are considered, ZIF-2, ZIF-3 and ZIF-8 are the best performing materials among those studied. Our results indicate the need for a precise characterization of the solid-fluid interaction for materials with sub-nanometric pores.

In the second part of this chapter, we investigate dynamical processes dependent on the flexibility in Metal-Organic Frameworks (MOF) by using Density-Functional Tight-Binding (DFTB). We show that one can perform DFTB simulations on systems having unit cells of several hundreds atoms at a modest computational cost. This approach is validated by calculating the barriers to diffusion for small molecules (hydrogen, carbon dioxide, and methane) crossing the windows connecting the pores of ZIF-7 and ZIF-8, two prototypical materials that have been the subject of many experimental and theoretical investigations. Additionally, we calculate the vibrational densities of states for MOF-5 and ZIF-8. These calculations are compared with simulations using the bonded and non-bonded part of the Universal Force Field (UFF). The results show that UFF's description of the bonded interactions has a quality comparable to DFTB's, at an even smaller computational cost.

6.1 Introduction

Metal-organic frameworks (MOF) are a novel class of crystalline compounds, whose microscopic structure is characterized by metal-oxide centers (acting as joints) with organic linkers (acting as struts). Since their synthesis obtained by Li *et al.* [298], MOF received a considerable attention for their promising applications to gas adsorption and storage. In fact, such properties can be tuned by varying the composition of the metal center as well

as the type of organic linker [299]. These materials have been tested for their capacity of storing methane and hydrogen, showing very good performance [300, 301].

Further improvements in the gas storage capacity were obtained by the discovery of Covalent Organic Frameworks (COF) [302, 303]: in these materials boron was used to replace the metal cluster, obtaining light rigid structures still with tailorable porosity. Among the materials of this series, COF-108 is the lightest crystalline material known to date. Hydrogen and methane storage capacity of COFs, both from a volumetric or a gravimetric point of view, is actually among the highest known for nanoporous materials [304].

Very recently a new class of nanoporous materials, called Zeolitic Imidazolate Frameworks (ZIF), has been synthesized and characterized [305, 306]. Zeolitic Imidazolate Frameworks (ZIF) have a pore size topology resembling that of zeolites, offering a larger variability by replacing the linker structure with various kind of organic molecules. These materials demonstrated a considerable affinity to carbon dioxide, and have been considered as viable substrates for CO₂ removal from a given gas flow, as discussed by [307].

Organic frameworks are currently the subject of many experimental and theoretical investigations to assess their ability to store gases and separate components from a given mixture. We refer to the recent and comprehensive reviews by Han *et al.* [308] and Li *et al.* [309] where the current state-of-the-art of these two applications is summarized.

Since an enormous number of MOF, COF and ZIF structures can be designed, the availability of reliable molecular models able to describe the interaction of gases with these organic frameworks are of paramount importance, for two main reasons.

On the one hand, a detailed atomistic description of gas interaction with these materials could suggest the optimal characteristics for any specific application, be it gas storage or gas separation. On the other hand, well validated models can be of use both in the screening of synthesized materials to select the most promising for a particular task, and to focus experimental effort into a valid direction for material testing.

Usually, the development of such numerical models starts from general force fields – mostly DREIDING [310] or UFF [311] – to calculate the interaction between the MOF and the various adsorbates [312, 313, 314, 308]. These force fields are tested and adapted to the particular materials under consideration by comparing their results with experimental data. Subsequently, these refined force fields can be safely used to obtain insight into material properties relevant to discern those worthy of further investigation. This approach is computationally very efficient, and allows to investigate both equilibrium (adsorption) and dynamical properties (diffusion and transport) in a large number of structures at a moderate computational effort. However, the accuracy of the results depends on the accuracy of the force field and its parametrization. Since the most used force fields are meant to be valid in a wide range of chemical environments, their predictions can be misleading in some cases.

A second approach is to resort to *ab initio* calculations. However, since the unit cells of many MOFs are made by hundreds of atoms, this approach is computationally very demanding. Usually, a reasonable tradeoff between computational cost and accuracy is found by using *ab initio* quantum chemical methods to parametrize the interaction between the adsorbates and relevant moieties of the adsorbent with a small set of interaction parameters, subsequently used for performing classical simulations [315, 316].

The accuracy of this approach depends of course on the accuracy of the *ab initio* calculations and the ability of the chosen parametrization to capture the main physical and

chemical properties of the system. Usually, the set of parameters so obtained cannot be transferred to other materials, and each MOF class requires to carry out again this quite time-consuming procedure.

In the first part of this chapter, we apply firstly the former, classical, theoretical framework to calculate gas adsorption and dynamics in ZIF-2 to ZIF-10, which are described in [305].

Since an efficient separation of a mixture depends on adsorption and diffusion of the gas components in the material, we deal with both of these processes. In the first case, we use grand canonical Monte Carlo simulations to generate adsorption isotherms and molecular configurations. These configurations are in turn used as starting points for molecular dynamics simulation, from which the diffusion coefficients of the gases in ZIFs are calculated.

As a further improvement to the previous classical molecular dynamics approach, in the second part of this chapter we will propose a different route to model absorption and diffusion in this type of materials, based on an *initio* approach and including framework flexibility otherwise neglected. In fact, in the vast majority of the computer simulations performed so far the rigid-framework approximation for the adsorbent has been always assumed. However, the synthesis of MOFs undergoing structural rearrangement upon adsorption of particular species has been recently achieved [317, 318, 319, 320, 321]. In this case, the widely used rigid-framework approximation clearly fails. In addition, it has been observed that some important features of gas diffusion within MOFs are determined by the interaction of the guest molecules with the vibration of the adsorbing frameworks [322, 323, 324, 325, 326, 327, 328, 329].

In modeling framework flexibility, many research groups have been resorting to the two approaches used to model dispersion interactions. On the one hand, the bonded interactions from transferable force fields have been used [327, 330]. On the other hand, a set of functional forms for the bonded interactions have been assumed, and their parameters calculated by fitting a set of quantum chemical simulations. This last approach has been used to develop force-fields for MOF-5 [331, 322, 323], ZIF-8 [329], Zn-TBIP [324, 325], and Cu-BTC [328].

At variance with this approach, to model flexibility in MOFs, we will apply an approach combining the accuracy of *ab initio* calculations with the computational efficiency typical of simulations based on classical force fields. Our approach to flexibility is based on the use of the Density Functional Tight Binding (DFTB) method. DFTB is based on the second-order expansion of the energy in Density Functional Theory (DFT) with respect to atom-centered densities [171, 173]. The resulting energy functional is characterized by a set of fixed matrix elements between atomic Kohn–Sham orbitals, which can be evaluated using high-quality DFT calculations and are highly transferable among different chemical environments.

When compared with DFT-based results, DFTB calculations have been shown to be quite accurate for static [332, 333, 334] and dynamical properties [335, 336], especially in the case of biological systems. DFTB produces reliable results with a computational cost that is significantly smaller (two to three orders of magnitude) than that of DFT. Details on the DFTB approach have been given in section 3.4.2.

Our results can be used to single out the most promising ZIFs for the gas separations discussed above.

Material	Volume (\AA^3)	Free volume (\AA^3)	Density (g cm^{-3})
ZIF-2	5707	2809 (49.2%)	0.929
ZIF-3	6024	3482 (57.8%)	0.880
ZIF-5	10590	1962 (18.5%)	1.57
ZIF-6	6940	4353 (62.7%)	0.764
ZIF-8	4905	2124 (43.3%)	0.924
ZIF-9	7179	1057 (14.7%)	1.22
ZIF-10	14211	9239 (65.0%)	0.746

TABLE 1: Unit cell parameters of the materials studied in this work. The free volume is defined in Eq. (6.8).

6.2 Zeolitic Imidazolate Frameworks for separation of binary mixtures of CO_2 , CH_4 , N_2 and H_2 : computational modeling

In this section, we will focus on the capacity of these compounds to perform gas separation, analyzing, in particular, the CO_2/H_2 , CO_2/CH_4 and CH_4/H_2 mixtures. We use a potential model that correctly reproduces the adsorption isotherms of CH_4 and CO_2 in ZIF-8, even if the experimental data are not yet conclusive in this latter case. Furthermore, we show that this model potential correctly describes the adsorption isotherm of H_2 in ZIF-8.

6.2.1 The materials studied

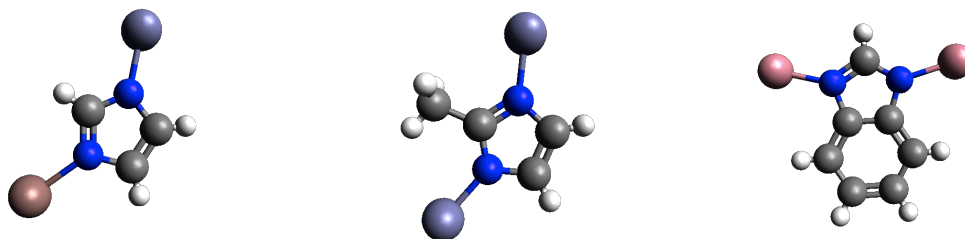


FIGURE 6.1: The imidazolate linkers used in the ZIFs studied in this section. Leftmost picture: ZIF-2, ZIF-3, ZIF-5 and ZIF-6. Central picture: ZIF-8. Rightmost picture: ZIF-9.

In this section we will investigate CO_2 , CH_4 and H_2 adsorption in materials of the ZIF family, namely ZIF-2 to ZIF-10, with the exception of the materials named ZIF-4 and ZIF-7, for which we were unable to find reliable crystal structures. These materials are formed by metal centers (cobalt, zinc or indium), connected by imidazole-based linkers which are shown in Figure 6.1.

In Table 1 we report the main geometrical features of the crystallographic unit cell for the materials studied, and we refer the reader to the original paper by Park *et al.* [305] for further details.

6.2.2 Potential models

A reliable computer model for gas adsorption in microporous materials is based on a realistic description of both gas-gas and gas-adsorbent interaction. In the first case it is customary to describe the interaction using Lennard-Jones centers suitably placed on the various atoms. When the intermolecular interactions are characterized by considerable electrostatic interactions, point charges are generally used in order to reproduce the correct moments of the charge distribution. For the gases studied in the present work, this happens only for CO₂, where the first non-zero moment is the quadrupole. Three point charges are placed on the atomic sites to reproduce its value.

In this section we will describe H₂ and CH₄ as single Lennard-Jones centers, using the parameters validated by Buch [337] and Goodbody *et al.* [338], respectively. Carbon dioxide will be modeled as a rigid linear molecule using the EPM2 potential by Harris *et al.* [339]. All of these potentials have been shown to reproduce very accurately the pure-fluid phase diagrams of the corresponding gases.

Various force fields are available in the literature to model the gas-adsorbent interactions. Among these, the DREIDING ([310]), UFF ([311]) and OPLS ([340]) potentials have been successfully used to model adsorption in a wide range of organic frameworks, such as MOFs ([312]), COFs ([313, 314]) and ZIFs ([341, 342, 343])

Although these force fields usually give a reasonable description of the gas-adsorbent interaction, they are usually augmented with framework charges in order to adapt them to a particular adsorbate. This procedure is particularly important when CO₂ is considered, due to the strong quadrupolar moment of this molecule, especially when the microscopic structure of the adsorbent is characterized by the presence of moieties with a non-negligible charge distribution (e.g. those made by highly electronegative atoms, such as oxygen or chlorine).

In fact, Liu *et al.* [342] investigated CO₂ adsorption in ZIF-68 and ZIF-69 using framework charges calculated *ab-initio* together with a non-standard CO₂-CO₂ potential, obtaining a good agreement with the experimental data [344]. This approach has been criticized by Rankin *et al.* [343], who demonstrated that the CO₂-CO₂ potential developed by Liu *et al.* is not able to properly describe the phase diagram of carbon dioxide. On the other hand, they find that the DREIDING potential with no additional framework charges is able to reproduce fairly well the available experimental data.

In the case of the ZIFs studied in this work, we will use the potential developed by Pérez-Pellitero *et al.* [345]. These authors found that a simple rescaling of the UFF potential parameters ($\varepsilon = 0.69 \varepsilon_{\text{UFF}}$ and $\sigma = 0.95 \sigma_{\text{UFF}}$) is able to reproduce satisfactorily the experimental adsorption isotherms of CH₄ and CO₂ in ZIF-8. No additional framework charges were required, due to the absence of strong electronegative atoms in the structure of ZIF-8. Since this property is shared by all the other ZIFs examined in this study we have decided to use this potential in our investigation.

We notice, however, that very recent measurements by Venna *et al.* [346] on CO₂ adsorption in ZIF-8 are in disagreement with the results reported by Pérez-Pellitero in [345]. In particular, the experimental results reported by Venna *et al.* [346] point towards a larger CO₂ uptake, as can be seen from Figure 6.2 reported below. On the other hand, the CH₄ adsorption isotherms reported by Venna *et al.* [346] agree with the results by Pérez-Pellitero [345] as well as those reported by Zhou *et al.* [347]. Moreover, our results will show that the potential developed by Pérez-Pellitero *et al.* [345] is able to reproduce

quite well the experimental adsorption isotherm of H₂ in ZIF-8 reported by Zhou *et al.* [347], thus validating the choice of our gas-adsorbent potential.

6.2.3 Simulation of pure fluid adsorption

An adsorption experiment measures the amount of gas adsorbed by a material exposed to a gas at a given temperature T . Once equilibrium is reached, the chemical potentials of the bulk and adsorbed species are the same. These experiments can be modeled in the framework of the grand canonical ensemble by fixing the volume V of the simulation cell at a constant temperature. The amount of adsorbed gas is determined by the value of the chemical potential μ of the bulk fluid in contact with the adsorbent. The chemical potential is in turn related, via an equation of state, to the gas pressure p .

The grand canonical partition function for the adsorbed fluid is given by

$$\Xi(\mu, T, V) = \sum_{N=0}^{\infty} \int d\xi_1 \dots d\xi_N \frac{e^{\beta\mu N}}{\Lambda^{3N} N!} e^{-\beta U_{\text{FF}}(\xi_1, \dots, \xi_N)} e^{-\beta U_{\text{SF}}(\xi_1, \dots, \xi_N)} \quad (6.1)$$

where $\beta = 1/k_B T$, Λ is the de Broglie thermal wavelength, $U_{\text{FF}}(\xi_1, \dots, \xi_N)$ is the potential energy due to the interactions of the N gas particles among themselves and $U_{\text{SF}}(\xi_1, \dots, \xi_N)$ is the potential energy of the interaction between the fluid particles and the substrate. We denote by ξ_k all the relevant degrees of freedom of the k -th particle. In the case of structure-less particles (H₂ and CH₄ in our models) these correspond to the three coordinates identifying the center-of-mass position, whereas in the case of rigid linear rotors (that is, CO₂) the degrees of freedom are the center-of-mass coordinates of the molecule and two angles describing its orientation.

The grand canonical Monte Carlo method is an efficient way to generate a collection of particles distributed with a probability

$$P(\xi_1, \dots, \xi_N) \propto \frac{e^{\beta\mu N}}{\Lambda^{3N} N!} \exp[-\beta U_{\text{FF}}(\xi_1, \dots, \xi_N) - \beta U_{\text{SF}}(\xi_1, \dots, \xi_N)] \quad (6.2)$$

corresponding to the partition function of Eq. (6.1). In this algorithm, the particles can be either moved within the adsorbent, added to or deleted from the simulation box.

A translation to a distance R from the initial position of a random particle is accepted with a probability

$$\pi_{\text{D}} = \min [1, e^{-\beta\Delta U}] \quad (6.3)$$

where ΔU is the variation of the energy of the system due to the particle displacement.

An insertion is made by adding the $(N+1)$ -th particle in a random position ξ uniformly within the adsorbent and accepting this move with a probability

$$\pi_{\text{I}} = \min \left[1, \frac{e^{\beta\mu}}{\Lambda^3 (N+1)} e^{-\beta\Delta U(\xi)} \right] \quad (6.4)$$

where $\Delta U(\xi)$ is the variation of the potential energy of the system due to the presence of the new particle. Particles are removed from the system with a probability

$$\pi_{\text{R}} = \min \left[1, \frac{\Lambda^3 N}{e^{\beta\mu}} e^{\beta\Delta U(\xi)} \right] \quad (6.5)$$

where $\Delta U(\xi)$ is the variation of the potential energy of the system upon removal of the particle.

It can be shown that this algorithm eventually produces a series of configurations of particles, whose position and number are distributed according to Eq. (6.2). These configurations can therefore be used to calculate grand canonical averages.

In our simulations, we have related the chemical potential μ to the actual pressure of the gas in contact with our system using the van der Waals equation of state,

$$\left(p - \frac{N^2 a}{V^2}\right)(V - Nb) = Nk_B T \quad (6.6)$$

whose parameters a and b have been chosen to reproduce the critical point of the gas under consideration. In particular, from the thermodynamic identities $dG = Vdp - SdT$ and $G = \mu(p, T)N$, one obtains

$$\mu(p, T) = \mu(p_{\text{ref}}, T) + \int_{p_{\text{ref}}}^p \frac{1}{\varrho(p, T)} dp \quad (6.7)$$

where p_{ref} is a very low pressure such that the chemical potential can be approximated with its ideal gas value and $\varrho(T, P) = N/V$ is the gas density as calculated from the equation of state.

In order to match the experimental measurements, we report the excess adsorption, defined as the quantity of gas adsorbed minus the amount of an ideal gas present within the adsorbent. This is given by

$$N_{\text{ex}} = N_{\text{tot}} - \varrho_{\text{id}} V_{\text{free}} \quad (6.8)$$

where N_{tot} is the total number of molecules in a unit cell of the crystal, ϱ_{id} is the density of an ideal gas at the pressure and temperature of the adsorbed gas and V_{free} is the free volume of the system, defined as the region within unit cell where the potential energy of interaction of the adsorbent with a Helium atom is less than 10^4 K.

6.2.4 Simulation of mixture adsorption: selectivity

When an adsorbent comes in contact with a mixture of two gases it might happen that one of the two components is preferentially adsorbed with respect to the other. This phenomenon is measured by the adsorption selectivity $S(A/B)$ of a species A with respect to a species B , defined as

$$S(A/B) = \frac{y_A/y_B}{x_A/x_B} \quad (6.9)$$

where y_A and y_B are the mole fractions of the two species in the adsorbed phase and $x_A = x$ and $x_B = 1 - x$ are the mole fractions of the two species in the bulk phase.

In the low-pressure limit the selectivity is independent of the molar composition of the bulk gas and is given by the expression

$$S_0(A/B) = \frac{\int d\xi_A e^{-\beta U_{\text{SF},A}(\xi_A)}}{\int d\xi_B e^{-\beta U_{\text{SF},B}(\xi_B)}} \times \frac{\int d\xi_B}{\int d\xi_A} \quad (6.10)$$

which gives the ratio of the single-particle partition functions of the two species in the adsorbed phase, divided by the ratio of the free-particle partition functions of the same two species.

In general, mixture adsorption is described by the multicanonical grand partition function

$$\Xi(\mu_1, \mu_2, T, V) = \sum_{N_1=0}^{\infty} \sum_{N_2=0}^{\infty} \int d\xi_1 \dots d\xi_{N_1} d\zeta_1 \dots d\zeta_{N_2} \frac{e^{\beta(\mu_1 N_1 + \mu_2 N_2)}}{\Lambda^{3N_1} N_1! \Lambda^{3N_2} N_2!} \times \\ \times e^{-\beta U_{\text{FF}}(\xi_1, \dots, \xi_{N_1}, \zeta_1, \dots, \zeta_{N_2})} e^{-\beta U_{\text{SF}}(\xi_1, \dots, \xi_{N_1}, \zeta_1, \dots, \zeta_{N_2})}. \quad (6.11)$$

where ξ_k and ζ_n denote the coordinates of the k -th particle of species 1 and the n -particle of the species 2, respectively.

Molecules distributed according to Eq. (6.11) can be generated with a Monte Carlo procedure analogous to what has been described in the pure fluid case. The two chemical potentials μ_1 and μ_2 can be related to the overall pressure p and the bulk composition of the mixture x using the van der Waals equation of state with proper combination rules (see [348]).

In particular, starting from the van der Waals parameters for the two pure species (a_1, b_1) and (a_2, b_2) one defines the combined values

$$a_{12} = \sqrt{a_1 a_2} \quad (6.12)$$

$$b_{12} = \left(\frac{b_1^{1/3} + b_2^{1/3}}{2} \right)^3. \quad (6.13)$$

The van der Waals parameters describing the mixture as a function of the molar fraction of species 1, x , are given by

$$a_M = a_1 x^2 + 2a_{12} x(1-x) + a_2 (1-x)^2 \quad (6.14)$$

$$b_M = b_1 x^2 + 2b_{12} x(1-x) + b_2 (1-x)^2. \quad (6.15)$$

From these parameters one can calculate the chemical potential $\mu_M(x, P, T)$ of the mixture with the same procedure used for a pure fluid. Finally, the expression of the chemical potentials of the two species in Eq. (6.11) can be written by (see [349])

$$\mu_1 = \mu_M - (1-x) \left. \frac{\partial \mu_M}{\partial x} \right|_{T,P} \quad (6.16)$$

$$\mu_2 = \mu_M + x \left. \frac{\partial \mu_M}{\partial x} \right|_{T,P}. \quad (6.17)$$

$$(6.18)$$

It is desirable that the amount of particles of both species in the simulation cell is of the same order. According to this, the bulk mole fraction x has been chosen such that an almost equal number of molecules for each species is found in the simulation cell. The knowledge of the zero-pressure selectivity allows one to estimate that an almost equimolar mixture in the adsorbent would be given by a bulk mole fraction

$$x \sim \frac{1}{1 + S_0}. \quad (6.19)$$

6.2.5 Permeance selectivity

The performance of separation devices based on adsorption of gas mixtures in nanoporous materials also depends on the ability of the various components of the mixture to diffuse through the material. We define the diffusion selectivity $\Pi(A/B)$ as the ratio of the self-diffusion coefficients D_A and D_B of the two species A and B in the material under consideration:

$$\Pi(A/B) = \frac{D_A}{D_B}. \quad (6.20)$$

Since in general the diffusion coefficient depends on the loading (which in turn depends to the external pressure), we have chosen to evaluate $\Pi(A/B)$ at the external pressure of $p = 10$ bar.

Although it is known that the diffusion of a gas in a membrane can be a collective phenomenon, and therefore the transport diffusion coefficient should be used to define the permeance selectivity, computer simulations show that these effects are sizable only close to saturation conditions, as discussed by Sholl [350]. Inspection of the adsorption isotherms, *vide infra*, shows that at $p = 10$ bar saturation is not reached in any of the materials under consideration. Under these conditions the transport diffusion coefficient is well approximated by the self-diffusion coefficient. This approach has been successfully used to study mixture separation in novel organic frameworks by Liu *et al.* [351].

6.2.6 Pure fluid isotherms

In Figure 6.2 we report the adsorption isotherms of carbon dioxide at $T = 298$ K in ZIF-2, ZIF-5, ZIF-8 and ZIF-9. The adsorption isotherm in ZIF-8 is in a very good agreement with the experimental data by Pérez-Pellitero *et al.* [345], according to the force field parametrization tailored to reproduce them. We also report the isotherm measured by Venna *et al.* [346], showing the degree of disagreement between these two data sets.

Inspection of the calculated isotherms shows that the results for ZIF-5 and ZIF-9 are qualitatively different from those obtained in the other cases. Adsorption on CO_2 in these materials is characterized by a significantly lower uptake than in the other ZIFs. On the other hand, the adsorption isotherms in the other materials are quite similar, with ZIF-2 and ZIF-10 having the highest and lowest uptake at any given pressure, respectively.

The highest uptake of carbon dioxide at room temperature is reached by ZIF-2, with a maximum of $\sim 180 \text{ cm}^3(\text{STP})/\text{cm}^3$ at 45 bar. This is more than twice the largest uptake observed in ZIF-5 and ZIF-9, which is of the order of $70 - 75 \text{ cm}^3(\text{STP})/\text{cm}^3$ at a slightly lower pressure of 35 bar.

Compared to other organic frameworks, the maximum volumetric uptake in these ZIFs is almost one half of what has been observed in the screening of MOFs for CO_2 adsorption performed by Babarao *et al.* [352].

Nevertheless, the amounts adsorbed are comparable to those reported in the case of CO_2 adsorption in other ZIFs. Liu *et al.* [342] and Sirjoosingh *et al.* [353] reported an amount of 2.5 mmol/g of CO_2 ($\sim 50 \text{ cm}^3(\text{STP})/\text{cm}^3$) adsorbed in ZIF-68 and ZIF-69 at a pressure of 0.8 bar, which is close to the value observed in the case of ZIF-2 and ZIF-8.

Almost the same situation is observed in methane uptake. From the adsorption isotherms reported in Figure 6.3 it can be seen that also for this gas ZIF-2 and ZIF-8 are the best performing material, with a maximum uptake of $\sim 120 \text{ }^{247}\text{Cm}$ at 50 bar. ZIF-5 and ZIF-9 have a maximum uptake of 50 and $75 \text{ }^{247}\text{Cm}$, respectively.

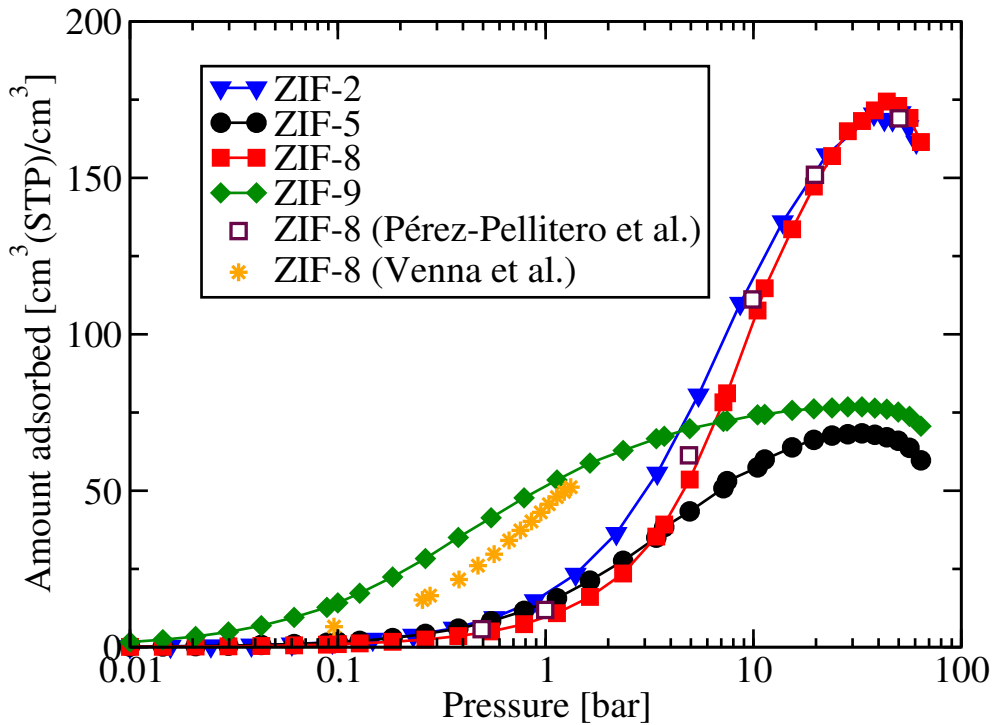


FIGURE 6.2: Adsorption isotherms of CO_2 at $T = 298$ K. Triangles: ZIF-2, circles: ZIF-5, squares: ZIF-8, diamonds: ZIF-9. The open symbols refer to the experimental data from [345] and the stars report the experimental data from [346].

Anyway, the amount of CH_4 adsorbed in ZIFs is appreciably smaller than that observed in other organic frameworks. According to the simulations by Garberoglio *et al.* [313], COFs have the largest methane uptake, most likely exceeding the Department of Energy (DoE) target of $180 \text{ cm}^3(\text{STP})/\text{cm}^3$ at 35 bar. MOFs have a slightly smaller uptake, but values as high as $150 \text{ cm}^3(\text{STP})/\text{cm}^3$ have been experimentally reported ([300]). Extensive computer simulations performed by Duren *et al.* [354] show that MOFs could be suitably tailored to meet the DoE targets.

These results suggest that the pore size and topology of these ZIFs is not large enough to accommodate substantial amounts of carbon dioxide or methane. The trend in the adsorption results for CO_2 and CH_4 can be related to the free volumes (see Table 1): the materials with the largest volume available for adsorption are also the ones having the largest uptake. ZIF-5 and ZIF-9 have a smaller free volume and, therefore, a smaller uptake.

We notice, however, that for pressures around 1 bar ZIF-9 adsorbs the largest amount of gas despite having the smallest available free volume. This is due to the favorable solid-fluid interaction: adsorption in the smaller pores is largest at low pressures due to the more favorable solid-fluid attraction. This is a very general result supported by extensive calculations performed by Frost [355].

Therefore, adsorption in small-pore materials favors smallest adsorbates, notably hydrogen. In fact, the H_2 adsorption isotherms reported in Figure 6.4 show that ZIF-9 outperforms the other two materials for hydrogen storage in the all range of pressure studied, adsorbing more than 50% of the amount adsorbed in ZIF-8 and almost 6 times as much as what can be stored in ZIF-5. Hydrogen adsorption in ZIF-9 is comparable, on a volumetric

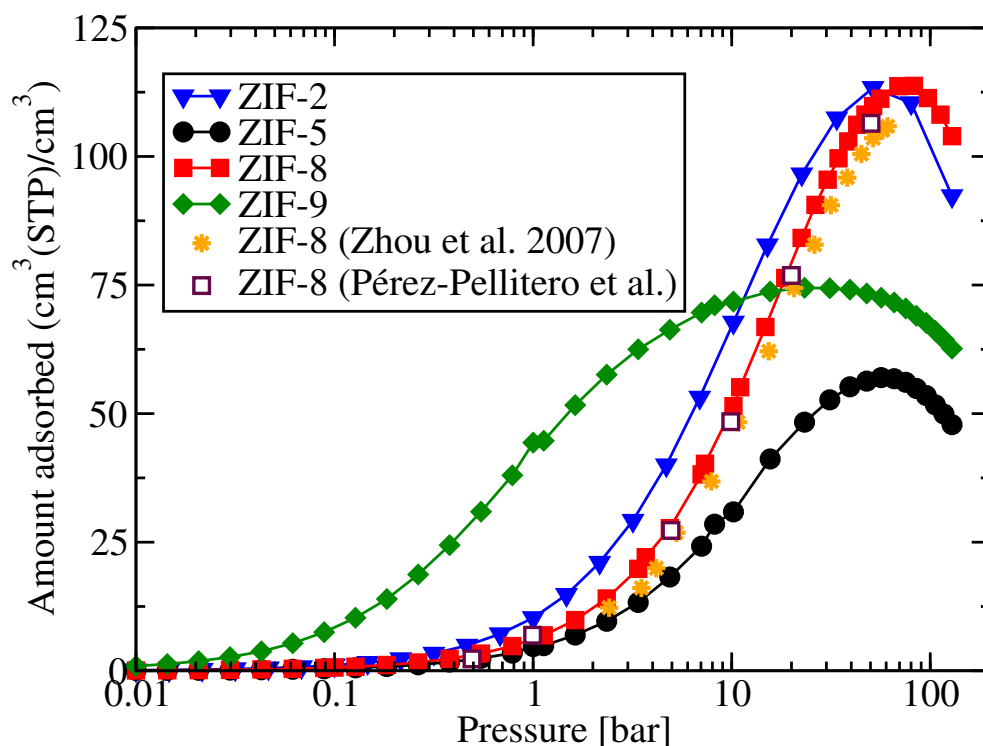


FIGURE 6.3: Adsorption isotherms of CH_4 at $T = 298$ K. Triangles: ZIF-2, circles: ZIF-5, squares: ZIF-8, diamonds: ZIF-9. The open symbols refer to the experimental data from [345].

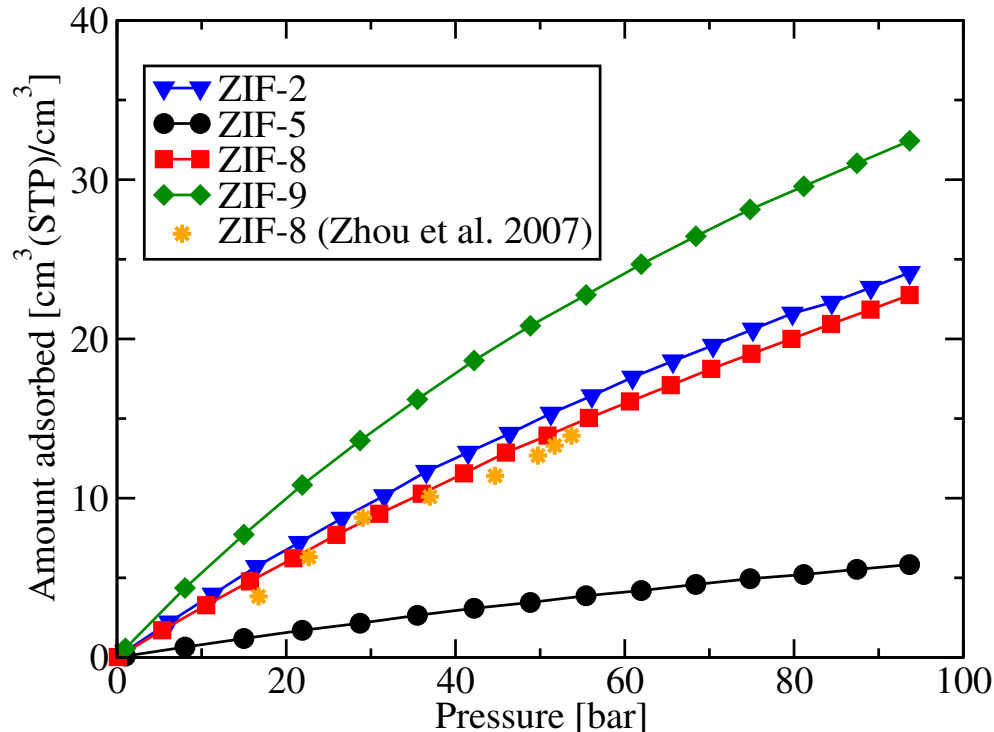


FIGURE 6.4: Adsorption isotherms of H_2 at $T = 298$ K. Triangles: ZIF-2, circles: ZIF-5, squares: ZIF-8, diamonds: ZIF-9. The stars report the adsorption data by Zhou *et al.* [347].

Mixture	ZIF-2	ZIF-3	ZIF-5	ZIF-6	ZIF-8	ZIF-9	ZIF-10
CO ₂ /H ₂	20.7	19.5	64.8	9.6	13.5	275	7.7
CH ₄ /H ₂	13.5	12.4	18.4	6.8	9.2	131	5.7
CO ₂ /CH ₄	1.5	1.6	3.5	1.4	1.5	2.1	1.4

TABLE 2: Zero-pressure adsorption selectivities in the ZIFs studied in the present work.

basis, to what is observed in the case of adsorption in IRMOF-1 ([312]) and in COF-102 ([313]) under room temperature conditions.

We notice, finally, that the results of our simulation for the adsorption of H₂ in ZIF-8 agree quite well with the experimental data reported by Zhou *et al.* [347], thus validating the choice of our force field.

6.2.7 Mixture adsorption and selectivity

We calculated the CO₂/CH₄, CO₂/H₂ and CH₄/H₂ adsorption selectivity in the zero-pressure limit as given by Eq. (6.10) for all the ZIFs considered in this study. The results are reported in Table 2.

We notice that ZIF-9 is the material having the best performance among those considered here, followed by ZIF-5. ZIF-2 and ZIF-3 have similar performance, followed by ZIF-8, ZIF-6 and ZIF-10 in this order. Given these results, we decided to study the pressure dependence of the selectivity only in the case of ZIF-2, ZIF-8, ZIF-5 and ZIF-9.

In the case of the CO₂/CH₄ mixture, the selectivity observed is not very high, ranging from the value of 1.4 in the case of ZIF-10 to the value of 3.5 in the case of ZIF-5. These values are comparable to what has been observed in other metal-organic frameworks. Yang *et al.* [356] performed extensive computer calculations of mixture selectivities, obtaining values of 2 and 6 for $S_0(\text{CO}_2/\text{CH}_4)$ in the case of adsorption in IRMOF-1 and CuBTC, respectively. Similar results have been obtained independently by Keskin *et al.* [357], Bae *et al.* [358] and Babarao *et al.* [359].

We notice, however, that our results do not agree with the findings of Venna *et al.* [346], who quote a selectivity in the range 5 – 7 for CO₂/CH₄ mixtures in ZIF-8. The reason of the discrepancy can be traced back to the different amounts of CO₂ adsorption in ZIF-8 observed by Venna *et al.* [346] and by Pérez-Pellitero [345]. Our model reproduces the isotherm of Pérez-Pellitero [345] and it is not able to reproduce the experimental value of the CO₂/CH₄ selectivity observed by Venna *et al.* [346].

In Figure 6.5 we report the values of $S(\text{CO}_2/\text{CH}_4)$ at finite pressures. We notice that the selectivity remains almost constant up to 1 bar for ZIF-2, ZIF-8 and ZIF-9, and up to 10 bar for ZIF-5. At high pressures, however, the qualitative behavior of the selectivity depends on the adsorbent. It increases in ZIF-2 and ZIF-8 and decreases in the other two cases. This is a consequence of the different pore dimension in the various systems, and the interplay between entropic and enthalpic factors.

In materials with large pores, notably ZIF-2 and ZIF-8, the collective attraction of CO₂ molecules favors them with respect to CH₄, resulting in a higher selectivity. On the other hand, when adsorption occurs in small-pore materials, such as ZIF-5 and ZIF-9, methane is slightly favored with respect to carbon dioxide, since the latter molecule usually has

an unfavorable entropy reduction (i.e. orientational localization) upon adsorption. As a consequence the CO_2/CH_4 selectivity is reduced at high pressure, as one may observe in Figure 6.5.

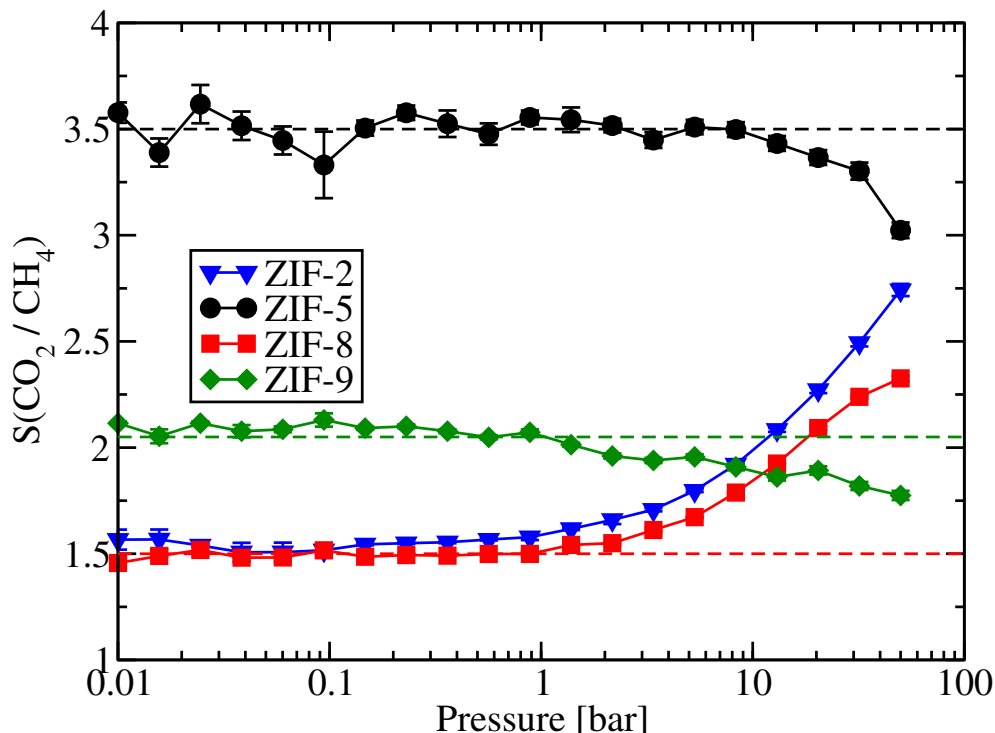


FIGURE 6.5: CO_2/CH_4 selectivity at $T = 298$ K. Triangles: ZIF-2, circles: ZIF-5, squares: ZIF-8, diamonds: ZIF-9.

Finally, dealing with CO_2/H_2 mixtures, we observe that the zero-pressure adsorption selectivity is quite high for ZIF-9, where the value of 275 has been found. This is a consequence of the small-pore nature of this material, which favors adsorption of small species with respect to large ones, as discussed by Keffer *et al.* [360].

The values of $S_0(\text{CO}_2/\text{H}_2)$ obtained for the ZIFs should be compared to the corresponding values observed in other organic frameworks. Yang *et al.* [356] report a value of ~ 100 for the $S_0(\text{CO}_2/\text{H}_2)$ selectivity in CuBTC, and a smaller value ($S_0(\text{CO}_2/\text{H}_2) \sim 12$) in the case of the organic framework MOF-5 (also known as IRMOF-1).

The pressure dependence of the CO_2/H_2 selectivity, reported in Figure 6.6, shows the same behavior already discussed in the case of the CO_2/CH_4 mixture. The selectivity in the small-pore materials tends to decrease with increasing pressure, whereas it tends to increase for large-pore materials.

6.2.8 Dynamics of adsorbed molecules and permeation selectivity

The dynamics of the molecules adsorbed in ZIFs has been studied by molecular dynamics (MD) simulations. We have used the GROMACS 4 package [361], starting from representative configurations of pure gas adsorption at the pressure of $p = 10$ bar.

We have considered the frameworks as fixed, consistently with the assumption made in performing the GCMC calculations. The gas molecules, kept at $T = 298$ K by a Berendsen

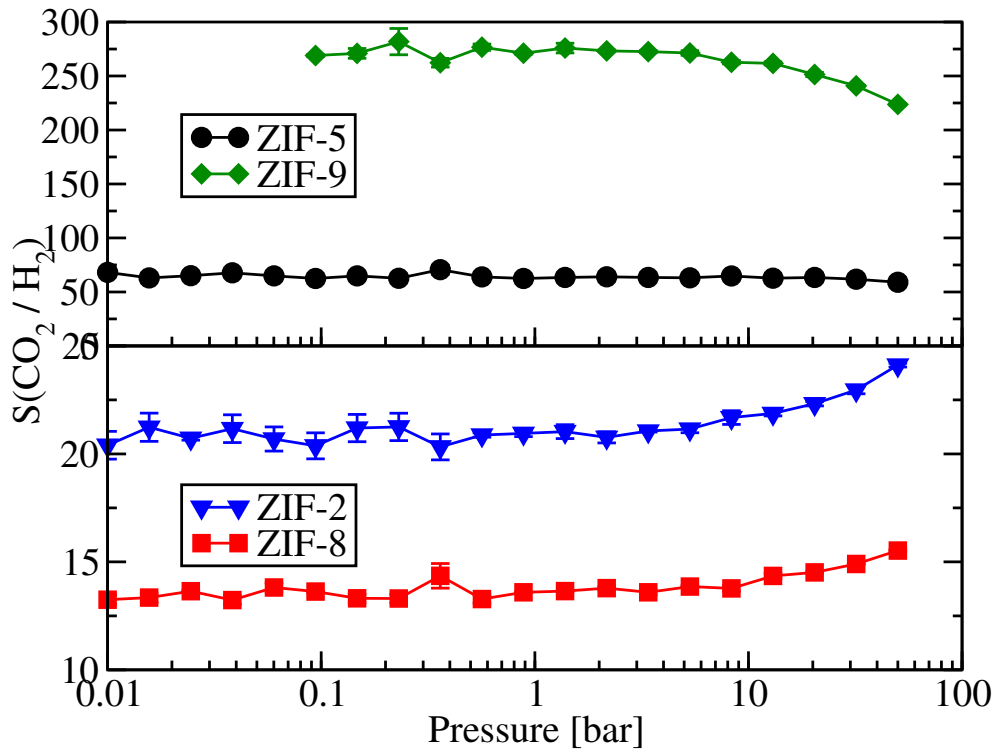


FIGURE 6.6: CO_2/H_2 selectivity at $T = 298$ K. Triangles: ZIF-2, circles: ZIF-5, squares: ZIF-8, diamonds: ZIF-9.

Adsorbate	ZIF-2			ZIF-5			ZIF-8			ZIF-9		
	D_x	D_y	D_z	D_x	D_y	D_z	D_x	D_y	D_z	D_x	D_y	D_z
H_2	12	1.3	14	0	0	0	1.7	2.2	1.5	0	0	0
CH_4	1.3	0	1.1	0	0	0	$< 10^{-3}$	$< 10^{-3}$	$< 10^{-3}$	0	0	0
CO_2	0.6	0.0	0.5	0	0	0	0.13	0.11	0.11	0	0	0

TABLE 3: Diffusion coefficients (in units of $10^{-8} \text{ m}^2 \text{ s}^{-1}$) for representative ZIFs among those studied in the present work.

thermostat with a time constant $\tau = 1$ ps, have been equilibrated for 500 ps. Subsequently, we generated a 5 ns trajectory, reducing the coupling to the heat bath to $\tau = 50$ ps. This trajectory was used to calculate the mean-squared displacement along the x , y and z directions, from which the corresponding diffusion coefficient D_x along the x direction has been obtained from the relation

$$D_x = \lim_{t \rightarrow \infty} \frac{1}{2} \frac{d\Delta x^2(t)}{dt}. \quad (6.21)$$

Similar expressions were used to calculate diffusion along the y and z directions. We define the total diffusion coefficient D as the average of the diffusion coefficients along the three Cartesian directions,

$$D = \frac{1}{3} (D_x + D_y + D_z) \quad (6.22)$$

The results for the diffusion coefficient are reported in Table 3. We notice that the gases do not diffuse appreciably in ZIF-5 and ZIF-9, at least within the time interval of our

Mixture	ZIF-2	ZIF-5	ZIF-8	ZIF-9
CO ₂ /H ₂	0.040	N.A.	0.065	N.A.
CH ₄ /H ₂	0.088	N.A.	< 10 ⁻³	N.A.
CO ₂ /CH ₄	0.460	N.A.	> 115	N.A.

TABLE 4: Permeation selectivities Π (see Eq. (6.20)) for the ZIFs studied in the present work. N.A. means that we were unable to measure any gas diffusion for ZIF-5 and ZIF-9.

calculations. Indeed, visual inspection of the computer generated configurations shows that molecules fit well within the nanoscopic cages present in these materials, but the windows connecting the cages are too narrow to let the molecules pass.

In ZIF-2 and ZIF-8 we observed a non-zero diffusion in all cases, except for methane in ZIF-8. In the latter case we could only establish an upper bound to D of about 10^{-11} m² s⁻¹, which is at least two orders of magnitude less than the all the other non-zero diffusion coefficients.

As a general trend, we notice that, for a given material, hydrogen presents the highest diffusion, with a diffusion coefficient almost one order of magnitude larger than either methane or carbon dioxide.

In the case of ZIF-2 methane diffuses faster than carbon dioxide, but in the case of ZIF-8 carbon dioxide is able to move within the framework, whereas the motion of methane is severely hindered. These results are summarized in Table 6.2.8, where we report the permeation selectivities for three mixtures in ZIF-2, 5, 8 and 9. Due to the absence of diffusion for any gas in ZIF-5 and ZIF-9 we could not report any value for these materials. In the case of the CO₂/H₂ mixture, ZIF-2 and ZIF-8 show a very similar behavior. However, ZIF-2 seems to be more suitable to perform CH₄/H₂ separations. ZIF-8 has a very high CO₂/CH₄ permeation selectivity, due mostly to the fact that diffusion of CH₄ seems to be highly hindered in this material.

As a measure of the overall performance of these materials to perform gas separations, we consider the product $\Sigma = S \Pi$ between the adsorption and permeation selectivities. In the case of CO₂/H₂ mixtures ZIF-2 and ZIF-8 have a very similar performance, with Σ in the range 0.8 – 0.9. In the case of the CH₄/H₂ mixture ZIF-2 turns out to be the most promising material with $\Sigma = 1.2$. ZIF-2 has a value of Σ , close to 0.7, for the CO₂/CH₄ mixture, while, for the same mixture, ZIF-8 has $\Sigma \sim 175$. This last result is of course a consequence of the considerably hindered motion of CH₄ in ZIF-8.

6.3 Modeling flexibility in Metal-Organic Frameworks: comparison between Density-Functional Tight-Binding and Universal Force Field approaches for bonded interactions

6.3.1 Overview of the problem

Due to the large number of existing and potential structures, a systematic experimental screening of MOFs aimed at identifying those more promising for a specific application (be

it storage or separation) is a highly impractical task. Therefore, computer simulations have been systematically used to short-list the most suitable candidates [352, 362, 353, 330] and even to design new materials [354].

Very recently, DFTB has been applied to the calculation of static properties of MOFs [363], COFs [364, 365] and ZIFs [366], showing how this method can be used to successfully reproduce the principal structural properties of these materials, as well as to provide information about the energetics of gas adsorption.

In the following section, we demonstrate the effectiveness of the DFTB approach to study the dynamics of MOFs. We will show how the DFTB method within the Born–Oppenheimer (BO) approximation, can be used to investigate dynamical properties of MOFs, such as their vibrational density of states (vDOS), and to study the diffusion mechanisms of light gases (such as H₂, CO₂ and CH₄) in small-pore MOFs at a computational cost that does not require the use of large-scale computing clusters.

Moreover, we compare the results on dynamical properties obtained by using DFTB and the Universal Force Field (UFF) [311], which is one of the most used classical force fields. UFF dispersion parameters have been widely used to investigate adsorption and diffusion of gases in MOFs when adopting the rigid-framework approximation. Here we show that UFF compares favourably with DFTB in the description of MOF flexibility, and can therefore be considered as an acceptable trade-off between accuracy and speed for large-scale screening of MOFs.

The DFTB and UFF approaches are validated by concentrating on the compounds known as MOF-5, ZIF-7, and ZIF-8. MOF-5 (also known as IRMOF-1) is one of the prototypical metal-organic frameworks, and its properties have been studied with a lot of experimental and theoretical techniques, whereas ZIF-7 and ZIF-8 are among of the most studied representatives of the ZIF class of MOFs [367, 368, 369, 370, 371, 372, 373, 321, 327, 329].

In particular, we will present results on the vibrational density of states in MOF-5 and ZIF-8, comparing the outcome of DFTB and UFF simulations. Framework flexibility in ZIF-7 and ZIF-8 will be further investigated by calculating energy profiles for the crossing of hydrogen, carbon dioxide and methane through the windows connecting the pores present in these materials. These energy profiles probe the flexibility of the framework, and therefore provide a good benchmark for comparing the outcome of the DFTB technique and the classical UFF approach.

6.3.2 Computational approaches

Density functional tight-binding

Theoretical details and computational approaches used to perform DFTB calculations can be found in section 3.4.2. The simulations of periodic systems have been performed using only the Γ point, including van der Waals dispersion interactions. The unit cells MOF-5 and ZIF-8 are cubic, with side lengths of 25.7 Å and 17.0 Å, respectively. ZIF-7 has an hexagonal unit cell, with crystallographic axis lengths of $a = b = 23.0$ Å and $c = 15.8$ Å. The number of atoms per unit cell of MOF-5, ZIF-8, and ZIF-7 are 424, 276, and 522, respectively.

Universal Force Field

The UFF calculations have been performed using the implementation developed for the Open Babel package (version 2.3.1) [374]. In this program, the UFF atom typing is performed using Daylight SMARTS [375] pattern matching of the atomic environments. This approach is very versatile, and can be extended to chemical environment not yet implemented in the standard distribution. We have exploited this possibility by adding the description of the tetrahedrally coordinated oxygen in the zinc-oxide cluster of MOF-5, and by assigning UFF's N_R atom type to the imidazole nitrogens in ZIF-8 which were not correctly identified.

The current Open Babel distribution is not capable to describe periodic systems and thus we extended it to include periodicity.

In addition, we have also written a program, called `obgmx`¹, capable to translate Open Babel's internal representation of the UFF force field into input files for the GROMACS package (version 4.5.4) [376]. In this way we had access to both the efficiency of GROMACS for performing MD simulations and to GROMACS' analysis tools for the MD trajectories. Since not all the functional forms for the bonded interactions used in UFF are available in the GROMACS package, we have approximated the structural and energetical parameters so that the GROMACS representation of UFF resulted in the same position of the minima and in the same second derivatives for the bonded interactions as the original UFF parametrization.

6.3.3 Vibrational densities of states

As a first comparison between the DFTB and UFF approaches to describe framework flexibility, we present the results for the vibrational DOS calculated with both methods. The vibrational DOS for MOF-5 has already been calculated with a mixed classical-*ab-initio* potential and related to the heat transfer characteristics of this material [377].

We performed MD runs of 25 ps, with an integration time step of 0.5 fs, using the BO approximation to calculate the forces on the nuclei. The temperature has been fixed to $T = 300$ K using the Berendsen thermostat. The first 10 ps of the trajectory were used for equilibration and therefore discarded from the analysis.

The atomic velocities were saved every 4 fs, and used to calculate the velocity autocorrelation functions averaged on the atoms of each element. The Fourier transform of these quantities are the vDOS, and they are shown in Figures 6.7 and 6.8, for MOF-5 and ZIF-8, respectively using both the DFTB and the UFF forces.

The results show that the densities of states predicted by UFF and DFTB are in fairly good agreement. Starting our analysis from the carbon vDOS of MOF-5, we notice that the excitations in the low-frequency region (< 1500 cm^{-1}) are in a good agreement. However, the frequencies predicted by UFF in the $1500 - 2200$ cm^{-1} range are significantly blue-shifted with respect to those obtained by DFTB. Comparison with the hydrogen vDOS shows that this region is related to the stretching of the H-C bond. The very-high frequency oscillations at 3000 cm^{-1} are very well reproduced by both methods.

A similar behaviour is observed in the oxygen and zinc vDOS. In the latter case, the UFF vDOS is again blue shifted with respect to the DFTB result, and inspection of the oxygen vDOS shows that the UFF vDOS has a larger intensity than the DFTB vDOS at

¹A web interface with `obgmx` is available at the website <http://software-lisc.fbk.eu/obgmx/>

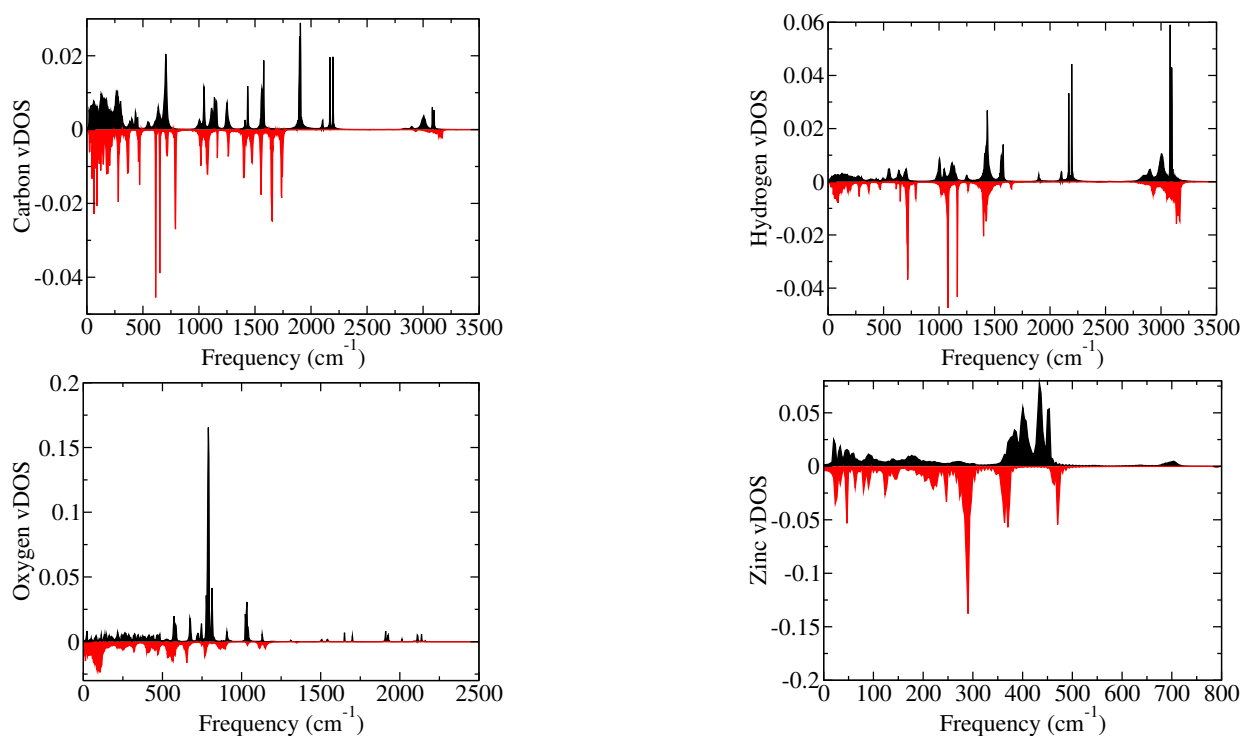


FIGURE 6.7: The vibrational densities of states in the case of MOF-5. From left to right and top to bottom: carbon, hydrogen, oxygen, and zinc. The positive values correspond to UFF calculations, the negative ones to DFTB calculations.

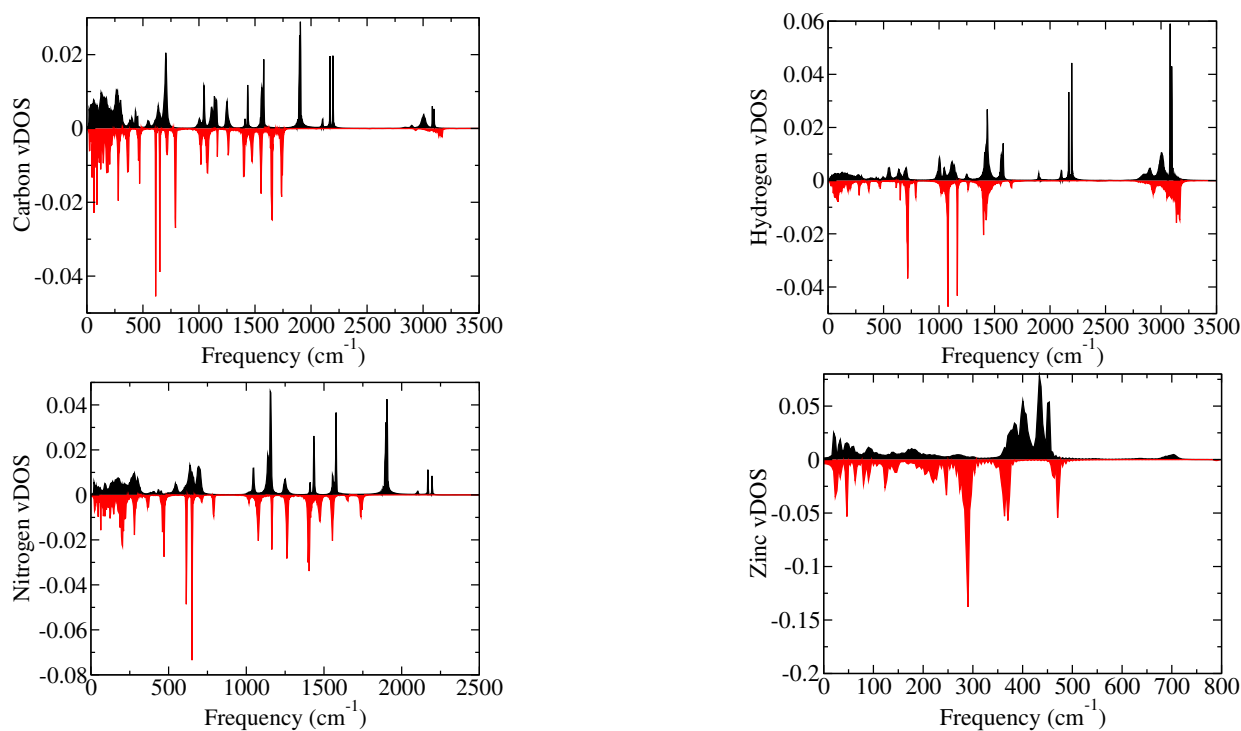


FIGURE 6.8: The vibrational densities of states in the case of ZIF-8. From left to right and top to bottom: carbon, hydrogen, nitrogen, and zinc. The positive values correspond to UFF calculations, the negative ones to DFTB calculations.

larger frequencies. This result is not completely unexpected, considering that the peculiar zinc-oxide moiety of MOF-5 contains a 4-coordinated oxygen which is not part of the original UFF parametrization.

The analysis of the ZIF-8 vDOS, reported in Fig. 6.8, leads to a picture very similar to that observed in the case of MOF-5. Starting again from the carbon vDOS, one observes a good agreement in the frequency region $< 1500 \text{ cm}^{-1}$, followed by a blue shift of the peaks in the $1500 - 2200 \text{ cm}^{-1}$ region. Similarly to what has been observed for MOF-5, comparison with the hydrogen vDOS shows that these frequencies are related to the stretching of the H-C bond, but that the very-high oscillation frequencies at 3000 cm^{-1} are consistently identified by both the UFF and the DFTB method.

Also the vDOS of nitrogen in ZIF-8 shows that UFF tends to blue-shift the highest frequency oscillations with respect to UFF. However, below 1500 cm^{-1} , the agreement between UFF and DFTB is quite good. One notices again a large disagreement between the two approaches in the case of zinc, as already pointed out in the case of MOF-5. However, we would like to point out that both approaches agree in the prediction that the vDOS of zinc does not extend above 500 cm^{-1} .

Finally, a comment on the computational resources needed for these calculations. UFF calculations can be performed on any modern desktop computer, and take roughly 10 minutes with 2.0 GHz processors. The DFTB calculations are more demanding, requiring 12 and 48 hours on an 8-core machine with the same 2.0 GHz frequency, for ZIF-8 and MOF-5, respectively. These results show that framework dynamics be efficiently investigated using DFTB. However, simulations lasting nanoseconds – such as those required to investigate gas diffusion within microporous materials – would require a significant computational effort. Nevertheless, as we will show in the next section, barriers to diffusion can be estimated using UFF and DFTB with only a modest investment in computational resources.

6.3.4 Barriers to diffusion of small molecules: CO_2 and CH_4 in ZIF-8

In this section we show that a DFTB-based approach can be successfully used to calculate barriers to diffusion. Since we are mostly concerned with assessing the reliability of UFF to describe flexibility in MOFs, we consider first the crossing of two guest molecules through the small windows in ZIF-8. These windows are framed by four methyl groups attached to the imidazole linker as shown in Fig. 6.9. We would like to point out that gas diffusion in ZIF-8 does not proceed by crossing these windows, because larger ones are present which provide a significantly smaller barrier to diffusion. The larger windows are also shown in Fig. 6.9.

The crossing of the small windows requires a significant local rearrangement of the ZIF-8 structure and is therefore ideal to investigate how the DFTB and the UFF approaches compare for describing framework flexibility.

To carry out this study, we calculated the minimum energy path for both carbon dioxide and methane crossing the small window. The minimum energy path is calculated using the Nudged Elastic Band (NEB) method [378, 379, 380] using an in-house developed code [381, 382] interfaced with both Open Babel and DFTB+.

We report in Fig. 6.10 the energy profile for a CO_2 molecule crossing the small window of ZIF-8, calculated using both UFF and DFTB. In the case of UFF, both the framework and the CO_2 molecule were modeled according to the UFF prescription. The NEB path was

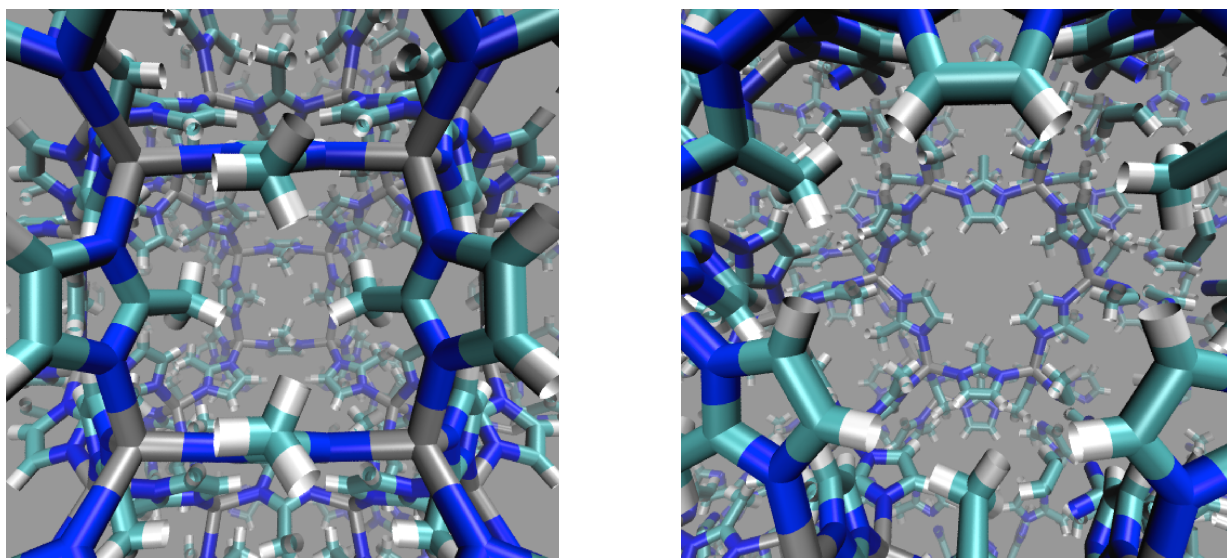


FIGURE 6.9: The small (left) and large (right) windows connecting the cages in ZIF-8

discretized using 64 slices, and optimized using a modified velocity Verlet algorithm [378].

First of all we notice that this path requires a considerable activation energy, almost 25 times higher than the thermal energy ($k_B T$) at room temperature. Inspection of the NEB trajectories shows a considerable rearrangement of the framework during the transition, making this path ideal to study the effect of framework flexibility and to compare approaches at different level of theory.

The energy profile shows that the UFF and DFTB description of this process are remarkably similar: initially, the CO_2 molecule is attracted towards the window. Subsequently, the methyl groups open up to let carbon dioxide pass, and this requires a considerable activation energy of almost 0.7 eV. The second half of the trajectory is symmetrical with the first half, as expected.

The more accurate SCC version of DFTB shows a similar curve, with a transition-state energy smaller than 0.1 eV. This result points out that the non-SCC version of DFTB is already a good description of MOF flexibility, and is able to capture the greatest part of the interaction.

Regarding the computational cost of these calculations, the optimization of the NEB path in the case of non-SCC DFTB method required 5 hours using 64 modern processors running with a frequency of 2.0 GHz, whereas the SCC-DFTB method required 19 hours using the same number of nodes. The UFF optimization of the NEB path was performed in roughly half an hour on a quad-core desktop computer.

The same conclusions can be drawn from the analysis of the energy along the reaction coordinate for the crossing of a CH_4 molecule through the small window of ZIF-8. The results, reported in Fig. 6.11, show that the UFF and non-SCC DFTB method give quite similar results. The CH_4 molecule is initially attracted towards the window, whose opening requires an activation energy of ~ 0.7 eV. During the crossing, the orientational rearrangement of the CH_4 molecule results in a slightly rugged energy profile.

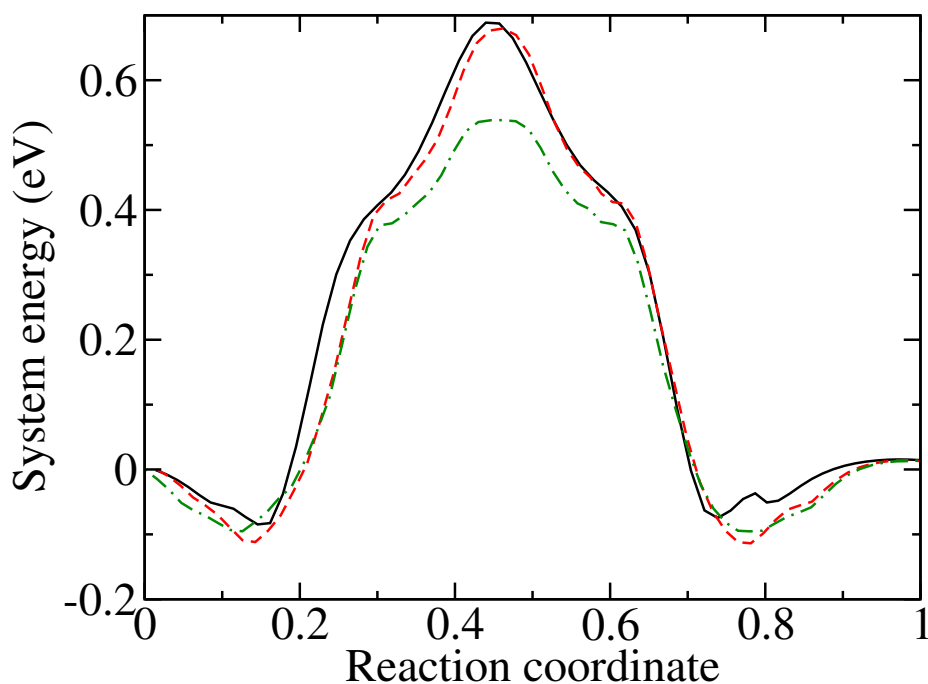


FIGURE 6.10: The energy profile for a CO_2 molecule crossing the small window of ZIF-8. Full line: UFF method, dashed line: DFTB method (non-SCC), dot-dashed line: SCC-DFTB method. In all cases, the reaction coordinate is the normalized path length. The values of zero and one of the reaction coordinate correspond to the molecule on either side of the window.

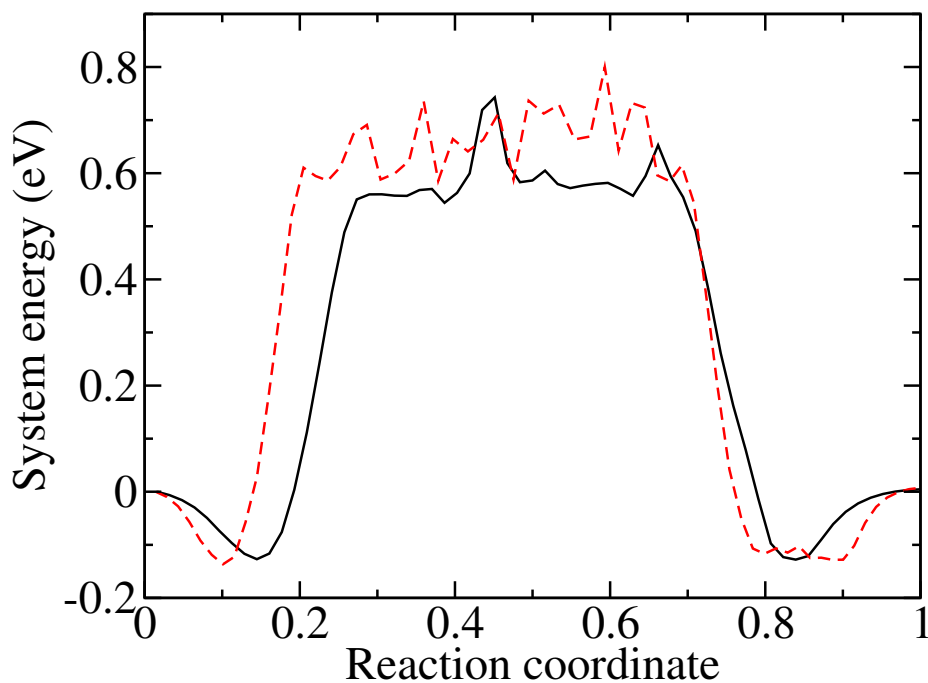


FIGURE 6.11: The energy profile for a CH_4 molecule crossing the small window of ZIF-8. Full line: UFF method, dashed line: DFTB method (non-SCC). In all cases, the reaction coordinate is the normalized path length. The values of zero and one of the reaction coordinate correspond to the molecule on either side of the window.

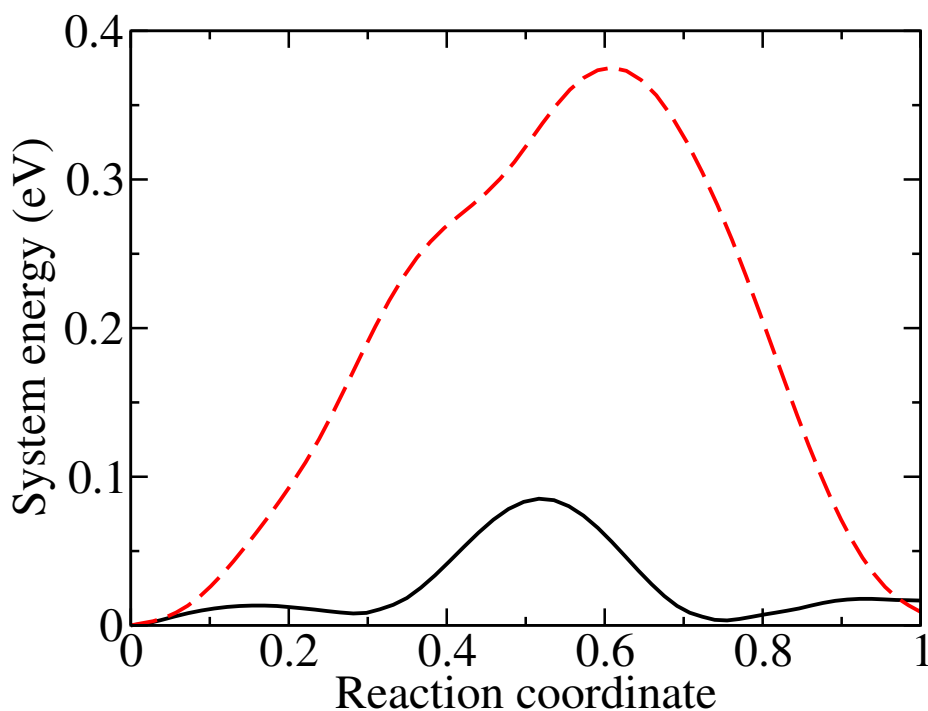


FIGURE 6.12: The energy profile for a H₂ (solid line) and a CO₂ (dashed line) molecule crossing the windows of ZIF-7 obtained using the NEB algorithm and a DFTB-SCC description of the system. The values of zero and one of the reaction coordinate correspond to the molecule on either side of the window.

6.3.5 Barriers to diffusion of small molecules: H₂ and CO₂ in ZIF-7

ZIF-7 has been recently shown to exhibit molecular sieving for the separation of H₂ from other small gases, both experimentally [368, 369] and using computer simulations [383, 330, 370], making it an interesting material for hydrogen purification and extraction. The structure of ZIF-7 is quite similar to that of ZIF-8, and is characterized by relatively small cages connected by relatively narrow windows.

We show in Fig. 6.12 the energy profile for hydrogen and carbon dioxide diffusing through the windows in ZIF-7. The curves have been calculated using the NEB algorithm at the DFTB-SCC level of theory. These results show that the energy barriers for diffusion in ZIF-7 for the two molecules are markedly different. H₂ has to overcome a barrier of 0.085 eV, which is 2.5 times higher than the average translational kinetic energy at room temperature, and thus easily overcome. On the other hand, the barrier for diffusion of CO₂ molecules in the same material is 0.375 eV, which is 10 times higher than the kinetic energy at room temperature.

This finding alone shows that one can expect diffusion of CO₂ in ZIF-7 to be severely hindered with respect to that of H₂: this material can therefore act as an efficient molecular sieve to separate a H₂-CO₂ mixture. This is indeed what is observed in actual experiments [368, 369].

6.4 Conclusions

In this chapter we have presented the results of computer simulations of gas adsorption and dynamics in novel Zeolitic Imidazolate Frameworks. We have investigated the performance of ZIFs to perform gas separation, considering binary mixtures made by CO₂, CH₄ and H₂. Our results point out that in these kind of studies, both adsorption and dynamics have to be considered to evaluate the performance of materials for mixture separation. We found a very high performance of ZIF-5 and ZIF-9 for gas separation when only selective adsorption is considered, due to the presence of highly selective small cages in the crystalline structure of these materials. However, molecular dynamics investigations of gas diffusion in ZIF-5 and ZIF-9 showed that the windows between the cages where adsorption occurs are so narrow that gas diffusion is severely hindered. We conclude that diffusion in these materials would be too slow, thus preventing their use for these applications.

The porous structure of the other ZIFs is made by larger cages. They can adsorb larger quantities of gas than ZIF-5 and ZIF-9, but from the point of view of adsorptive separation, their performance is significantly smaller. Nevertheless, it is comparable to the results obtained by similar studies in the case of other organic framework materials. We found, in particular, that CH₄ diffusion in ZIF-8 is significantly smaller than in other organic frameworks, and, as a consequence, we obtained a very high value of the separation efficiency of this material in the case of CO₂/CH₄ mixtures.

The significance of our results is of course very much dependent on the details of the force field used in our calculations. We used an interaction potential which has been shown to be able to reproduce the experimentally measured adsorption isotherms of all the gases in the case of ZIF-8, obtained independently by three research groups. However, we noticed that in the case of CO₂, the results in the literature are scattered.

Furthermore, in the second part of this chapter, we demonstrated that DFTB can be successfully used to model framework flexibility and to characterize the vibrational dynamics in materials with several hundreds of atoms per unit cell, such as MOFs, at only a moderate computational effort. Moreover, the DFTB approach can be used to investigate the barriers to diffusion of small molecules adsorbed within MOFs without requiring the use of large computational facilities.

In addition, we have also compared the predictions of a DFTB based approach to MOF flexibility with the results obtained using UFF, a classical and transferable potential model spanning the whole periodic table. We showed that results obtained with the UFF description of MOF flexibility is quantitatively comparable with the DFTB predictions. In particular, we analyzed the vibrational density of states of pure MOF-5 and ZIF-8 – two prototypical MOFs – as well as the crossing of small molecules (H₂, CO₂, and CH₄) to the windows connecting the pores in ZIF-7 and ZIF-8. In the former case, the main difference between UFF and DFTB concerns the dynamics of the H–C bond in the intermediate frequency range ($1500 < \omega < 2200 \text{ cm}^{-1}$). In the latter case, the DFTB and UFF approach give a strikingly similar result.

These results suggest that the bonded interactions described by the Universal Force Field are a reliable and computationally very efficient description of the flexibility of MOFs, which can be considered for large-scale screening of MOFs. More accurate results are obtained using the DFTB approach, at the expense of a larger computational cost than UFF. However, we showed that DFTB can be used to simulate cells with hundreds of atoms, with affordable computational resources.

Chapter 7

Infrared spectroscopy of copper-resveratrol complexes: a joint experimental and theoretical study

Infra-red multiple-photon dissociation spectroscopy has been used to record vibrational spectra of charged copper-resveratrol complexes in the 3500-3700 cm^{-1} and 1100-1900 cm^{-1} regions. Minimum energy structures have been determined by density functional theory calculations using plane-waves and pseudopotentials. In particular, the copper(I)-resveratrol complex presents a tetra-coordinated metal bound with two carbon atoms of the alkenyl moiety and two closest carbons of the adjoining resorcinol ring. For these geometries vibrational spectra have been calculated by using linear response theory. The good agreement between experimental and calculated IR spectra for the selected species confirms the overall reliability of the proposed geometries.

7.1 Introduction

Resveratrol ((E)-5-[2-(4-hydroxyphenyl) ethenyl] benzene-1, 3-diol) is a hydroxylated stilbene present in grapes, nuts, peanuts, and some plants used in traditional pharmacopoeia like *Polygonum cuspidatum*, from which it is extracted to prepare nutritional supplements. Being a minor component of red wines (0.1 - 8 mg/L) it is considered responsible for the beneficial health effects attributed to moderate wine consumption. In fact many valuable properties are attributed to resveratrol [384], in particular antioxidant, anticarcinogenic, and antiinflammatory activities. Most interestingly, resveratrol has been demonstrated to regulate various proteins and in particular it directly inactivates phosphodiesterase enzymes (PDEs), leading to a signaling cascade that activates SIRT1 [385]. Because the expression of SIRT1 is linked to calorie restriction effects on life-span extension, resveratrol has been suggested as a mimetic of calorie restriction, a well known way to prevent aging [386]. This implication has increasingly attracted the interest of both the scientific community as well as the parapharmaceutical industry [387].

However, it should not be forgotten that molecules normally acting as antioxidants can also exert prooxidant properties by reducing metal ions, which can then produce reactive oxygen species. The prooxidant mechanism of resveratrol is based on the acidity of the phenol group, involving a proton loss from the OH in para position, to give a phenoxide an-

ion which reacts with Cu(II) ion producing Cu(I). This latter ion is then involved in redox reactions with oxygen species, whose final products are Cu(II) and oxygen radicals [388]. It is therefore important to investigate the interaction between metal ions and resveratrol. A recent paper reported for the first time the detection of resveratrol-copper complexes by electrospray ionization (ESI) mass spectrometry [389]. The structure of these complexes can be investigated by vibrational spectroscopy. In the present work we used infra-red multiple-photon dissociation (IRMPD) spectroscopy to perform such a task. IRMPD spectroscopy is an action spectroscopy in which the response of the molecule to photon absorption is recorded rather than the direct absorption of the incident light [390]. It is based on the use of IR laser radiation of high fluence and broad tunability. When the energy of the photon flux is resonant with an active vibrational mode of the sample, a multiple sequence of events comprising photon absorption by the investigated mode and fast energy redistribution increases the vibrational energy reaching a fragmentation threshold. The dependence of the fragmentation yield on the photon wavenumber generates an IRMPD spectrum revealing the IR absorption features of the assayed species. Action spectroscopy is a viable spectroscopic probe for gaseous ions whose typically low density number does not allow performing direct absorption spectroscopy. In this way, IRMPD spectroscopy has provided valuable contributions in the past decade in elucidating the structural and electronic features of organometallic complexes or metal ion cationized organic molecules [391, 392, 393, 394].

IRMPD spectroscopy is used in this work to investigate the 1:1 and 1:2 copper (I) complexes with resveratrol, henceforth denoted $[\text{Cu}(\text{Resv})]^+$ and $[\text{Cu}(\text{Resv})_2]^+$, respectively. In addition, the investigation has included ionized resveratrol $(\text{Resv})^{+\bullet}$ and the copper(I) complex with dihydroresveratrol (5-(4-hydroxyphenethyl)benzene-1, 3-diol, henceforth referred to as DHResv). In the latter complex, $[\text{Cu}(\text{DHResv})]^+$, also comprised in the previous report, the flexible $-\text{CH}_2-\text{CH}_2$ chain connecting the two aryl rings allows a folded structure whereby the metal ion can interact with the two aromatic rings, embedded between them. The scope of the present investigation, besides providing IR signatures for the selected species in an isolated state, aims at linking the experimental IRMPD spectra with the plausible structures of the sampled ions.

To this end calculations of the IR spectra have been performed within the framework of density functional theory (DFT). This approach, along with the plane-wave (PW) expansion of the molecular orbitals, allows us treating the different complexes investigated in this work at the same level of accuracy, and to include the dispersion forces. On this respect, molecular vibrational properties can be calculated using two different approaches: by diagonalizing the dynamical matrix or by applying linear response theory. In the former approach, the energy gradient with respect to atomic displacements is usually computed analytically by using the Hellmann–Feynman theorem, while second derivatives are computed as numerical derivatives of energy gradients using the central difference formula. Therefore, within this method one has to test the size of the displacement to be used in the calculation of the force constant matrix, which is given by:

$$D_{\alpha,\beta}(i,j) = -\frac{1}{\sqrt{(m_i \times m_j)}} \phi_{\alpha\beta}(i,j) \quad (7.1)$$

where i, j identifies the atoms i and j , $\phi_{\alpha\beta}(i, j)$ is the force constant matrix and m_i, m_j are the masses of atoms i and j . The displacement has to be small in order to be in the validity range of the harmonic approximation, but also big enough so that the forces in-

duced in the molecular complex are not too small compared to the numerical noise in the calculations. Finally, one calculates eigenvalues and eigenvectors of the dynamical matrix to be directly compared with experimental spectra available from infrared absorption spectroscopy. Intensities are finally found by applying dipole approximation. To obtain good quality spectra, extremely accurate total energies must be found and extensive checks on the size of the atomic displacement have to be performed. Therefore, in order to calculate the second derivatives to obtain vibrational frequencies and intensities of resveratrol-based molecular complexes we preferred to use density functional perturbation theory (DFPT) [179], also referred to as linear response (LR) theory. In this case, tests on the resveratrol molecule showed that frequencies and intensities do not depend critically on the value of the displacement.

7.2 Experimental methods

The ions of interest are generated by electrospray ionization (ESI) of an approximately 1:1 Resveratrol(DHResveratrol)/CuSO₄ solution (10⁻⁴ M) in a 50/50 mixture of methanol and water using direct infusion by a syringe pump. Resveratrol and CuSO₄ were supplied by Sigma Aldrich Co. (St. Louis, USA). Dihydroresveratrol was prepared by hydrogenation of resveratrol [389]. Typical ESI parameters are an infusion flow rate of 180 μ L/h, a spray voltage of 4500 V and a capillary temperature of 300 °C.

IRMPD experiments on the sampled species are performed using two experimental platforms with different laser systems. The 1100-1900 cm⁻¹ region has been explored using the free electron laser (FEL) beamline at the CLIO (Centre Laser InfraRouge, Orsay) center. The FEL system is based on a 16-48 MeV linear electron accelerator where bunches of electrons are injected in the alternating magnetic field placed in the optical cavity. Wavelength tunability of this laser system is achieved at fixed electron energy by changing the gap between magnets. For the experiments in the 1100-1800 cm⁻¹ spectral region, the electron energy was fixed at 45 MeV and a stable average power of 1 Watt was observed. The IR FEL delivers 8 μ s long trains of macropulses at a repetition rate of 25 Hz. Each macropulse conveys typical energies of 40 mJ. The laser-wavelength profile was monitored while recording the spectra with a monochromator associated to a pyroelectric detector array. The band width of IR-FEL is 0.4-0.5% of the central wavelength.

The FEL based experiment was performed using a modified Bruker Esquire 3000 Paul-trap type mass spectrometer with a conical hole in the ring electrode allowing the optical access to the center of the trap [395]. The commercial Bruker Esquire software was used in the experiment. The ions of interest were mass-selected in the MS1 step and the control of the irradiation time (typically 1s) was obtained using the MS2 step. In the case of [Cu(Resv)]⁺, the species was obtained in the MS2 step by dissociation of [Cu(Resv)₂]⁺, and was then submitted to irradiation in the MS3 step for 2 sec. Mass spectra were averaged over 10 accumulations and the sequence repeated for 6 times at each recorded frequency.

An Optical Parametric Oscillator/Amplifier (OPO/OPA) (LaserVision) coupled to a Paul ion trap tandem mass spectrometer Esquire 6000+, (Bruker Inc) is employed to explore the 3500-3700 cm⁻¹ spectral region of the different species under study [396]. This parametric converter is pumped by a non seeded Nd:YAG laser (Continuum Surelite II) operating at 10Hz repetition rate. The typical pulse width of this pump laser is 4-6 ns

with output pulse energy of 600 mJ at 1064 nm. Tunability is achieved by angle tuning of OPO and OPA crystals simultaneously using software controlled stepping motors. The typical output energy from the OPO/OPA laser was 22 mJ/pulse in the spectral range of investigation with 3-4 cm^{-1} bandwidth. The mid IR output from OPO/OPA is steered in the ion trap using a gold coated plane mirror and is focused loosely using an MgF_2 lens of focal length 37 cm. The IR beam focusing is performed to achieve better overlap with the trapped ion cloud. In the trap, ions were accumulated for 10 msec prior to IR irradiation which was allowed to last 0.5-2 sec. Once again, multistage mass spectrometry is performed using the standard Bruker Esquire Control (v5.2) software.

IRMPD spectra are obtained by plotting the photofragmentation yield R ($R = -\ln(I_{\text{parent}}/[I_{\text{parent}} + \sum I_{\text{fragment}}])$), where I_{parent} is the intensity of the parent ion and $\sum I_{\text{fragment}}$ is the sum of the intensities of fragment ions as a function of the IR radiation wavenumber.

7.3 Theoretical and computational methods

Calculations have been performed within the framework of DFPT using the ab initio total-energy and molecular dynamics program VASP [159, 160, 161]. The ion-electron interaction has been described using the projector augmented wave (PAW) [162, 163, 165] technique, in which the explicit treatment of core electrons is replaced by atom-centered augmentation spheres within a given ionic radius and by envelope functions outside such spheres. Single-particle orbitals are expanded in plane waves (PW). In principle, electron orbitals may be expanded in term of any convenient basis set, be it Gaussians (GTO) or PW. While Gaussian functions have been used in a large number of code suites, such as Gaussian [397] or GAMESS, [398] for the simulation of molecular properties, notably the vibrational frequencies, in this work we decided to use the latter for three reasons.

Firstly, we study a variety of resveratrol-copper complexes at different levels of aggregation. On this respect, while Gaussian basis sets need to be tailored for any specific application and may suffer basis set superposition errors (BSSE), the use of PW ensures the same level of accuracy irrespectively of the dimensionality of the system as accuracy depends only on the energy cutoff.

Secondly, we use LR theory to calculate both the normal mode eigenvectors and the Born effective charge tensors for the assessment of the vibrational intensities. The use of PW on this respect presents the advantage of simplifying the calculation of the Hellmann-Feynman forces as Pulay forces are zero by construction.

Thirdly, we show that dispersion forces, resulting from dynamical correlations between fluctuating charge distributions, play an important role in the stability and conformation of resveratrol-copper complexes. The wrong asymptotic behavior of GTO basis-sets can have significant impact on the accurate determination of such long-range properties, forcing to enlarge the basis set to include diffuse or polarized functions. This would rapidly make unfeasible the assessment of the van der Waals contribution to the energy, at least for the size of the molecules investigated in this work. PW-DFT approach rather uses a semi-empirical dispersion potential, usually not present in standard implementation of DFT, added to the total energy to work around this problem.

Finally, a principal difference between all-electron GTO implementations of DFT and PW approaches is the use of pseudo-potential, which acts as an effective interaction between

valence electrons and ions, while core-electrons are frozen in the core. Tosoni et al. [399] showed that the use of PW in connection with PBE [165] and PW91 [400] pseudo-potentials compares very well with GTO-based approaches for calculating structures, binding energies, and harmonic vibrational spectra of the formic acid molecule in the free-gas phase. Furthermore, PW performs much better in the molecular crystal phase to assess binding energies likely due to larger BSSE in this phase. In particular, the results of the frequency calculation involving the O-H stretching mode at around 3600 cm^{-1} , which is of interest in our work, are improved in accuracy by increasing from one side the energy cut-off of the PBE pseudo-potential from 110 to 130 Ry and from the other side by enlarging the GTO basis set from 6-311G(d,p) to TZP. Harmonic frequencies are quite poor with small size GTO basis set, with discrepancies higher than 100 cm^{-1} in comparison to TZP basis set. Counterpoise corrections prove to be crucial to obtain well converged results for molecular crystals containing hydrogen and first-row elements. For frequencies involving intramolecular normal modes the agreement is better.

Karhánek et al. [401] performed the vibrational analysis of methane-thiol (CH_3SH) and methyl thiolate (CH_3S^-) in the gas phase by using both PW91 and B3LYP [402] exchange-correlation functional in connection with 6-311G(d) GTO basis set as implemented in GAUSSIAN. These results were compared with PW-DFPT calculations using PW91 pseudo-potential for 400 eV energy cut-off. In this case, even larger discrepancies are found between the two approaches. For both molecules, the PW approach shows much better agreement than GTO based methods with available experimental data for the stretching, deforming and rocking modes and the C-S stretching mode. In particular, for the two almost degenerate asymmetric C-H stretching modes, which are of importance even in our work, the frequencies calculated by using GAUSSIAN are as high as 100 cm^{-1} on respect to the values obtained by using LR theory, a difference too high to be attributed to anharmonic effects only. Furthermore, large discrepancies have been found in the relative intensity of the modes between PW and GTO based approaches. A comparison between the spectra of the complexes investigated in this work obtained at this level of theory with those obtained by using more standard GTO-based DFT calculations, using B3LYP exchange-correlation potentials, shows that the main source of discrepancies between GTO and PW approaches for calculating IR spectra on resveratrol-Cu complexes is mainly the need of rescaling the frequencies in the former case.

In order to test PW-based approach for our system, we decided to apply LR theory for simulating the structures and relative stabilities of a phenol-copper cation for different copper binding sites, on the aromatic ring and on the oxygen atom respectively. In this case-study we tested different exchange-correlation functionals and various PAW pseudo-potentials. These calculations aim at the assessment of the DFT parameters to be used in the study of the binding of copper on more complex systems, notably copper-resveratrol complexes.

The kinetic energy cutoff is set to 500 eV, which ensures convergence of the structural parameters of phenol complexes to better than 0.05% with respect to available experimental data. Spin-orbit and fully non-collinear magnetic effects have also been tested without finding appreciable difference in the structural parameters, notably binding site and bond length, with respect to the case in which they are not included. Calculations have been performed at Γ point. The simulation cell is cubic with a linear dimension of 12 \AA .

The resulting configurations obtained for different binding sites of the copper atom are plotted in Fig. 7.1) in order of increasing energy from a) to e). The figure clearly shows

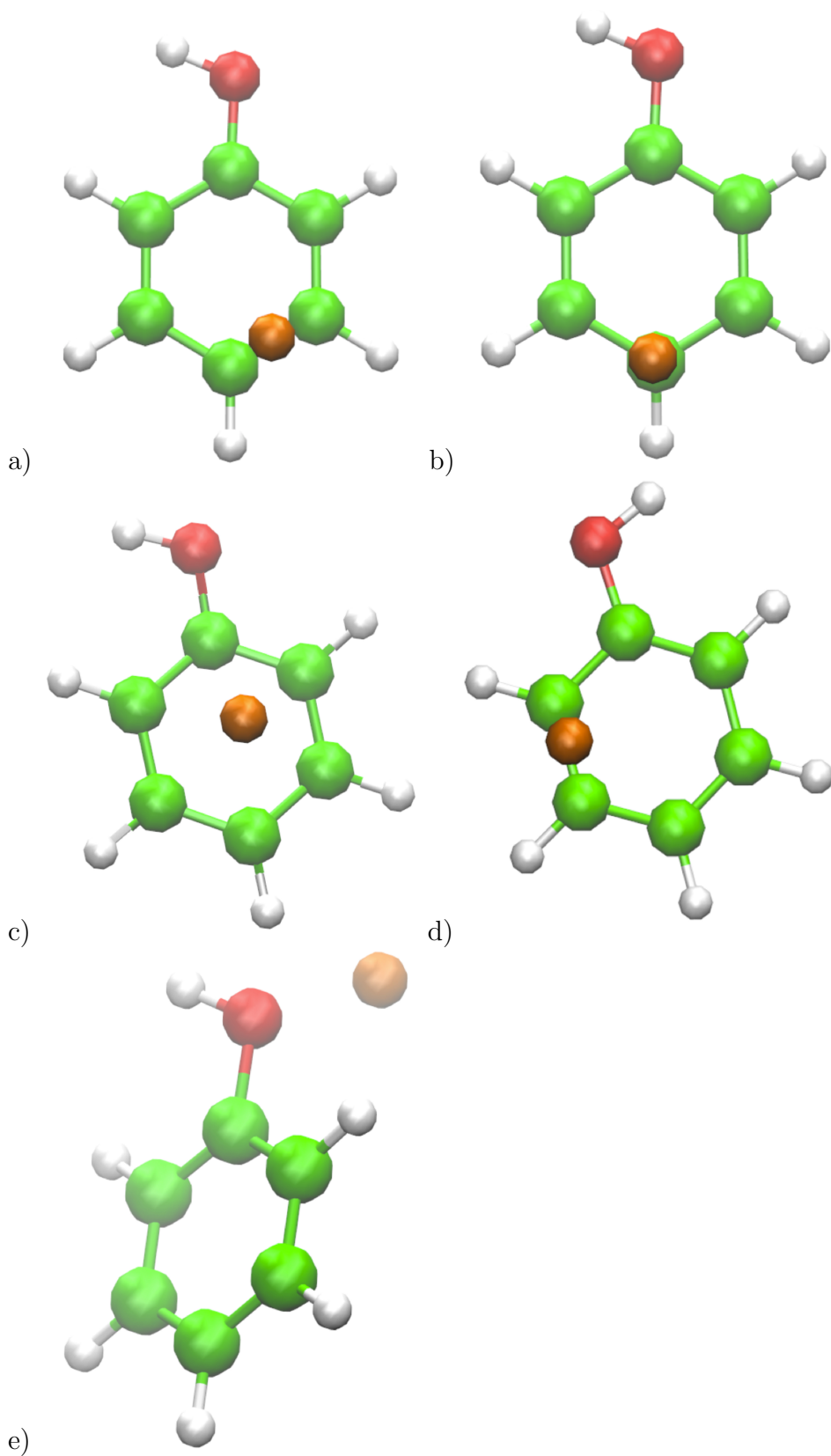


FIGURE 7.1: Optimized structures of phenol complexes for different binding sites of the copper(I) atom. Carbon is in green, hydrogen in gray, copper in orange, oxygen in red.

that the copper ion preferentially sits on the top of the ring, while unfavorably it binds with the oxygen lone pairs, as one could rather expect from chemical analysis. The differences in energy among the most stable configuration (see Fig. 7.1a)) and the other structures are 0.018, 0.025, 0.054 and 0.083 eV, respectively. The first two structures are therefore almost degenerate within chemical accuracy, with the copper-to-carbon bond length equal to 2.11 Å in the most stable configuration. These preliminary results have been obtained by using PBE-GGA [165] pseudo-potential. Within Local Density Approximation (LDA) [164] we obtain a slight decrease of about 0.3 % of the carbon to copper bond distance, as expected since PBE usually overestimates the bond length, particularly for hydrogen bonds [403]. We also tested these PAW potentials with the 3p either frozen in the core, or explicitly included in valence, along with the 3d and 4s electrons. After these tests, we decided to use the PBE-GGA [165] functional in all further calculations, the PAW potential without 3p electrons in valence, and to neglect spin-orbit interactions. Our prediction on the copper ion binding site above the aromatic ring is in good agreement with simulations performed by Milko et al. [404] on the same system using coupled cluster (CCSD(T)) extrapolated to the basis set limit. A second goal of this work is the vibrational analysis of resveratrol-copper molecular complexes to be compared with our IRMPD spectra. To perform these calculations, we used linear response DFPT(LR-DFPT), whose detailed description is reported in the Appendix A for the sake of completeness.

7.4 Results

7.4.1 IRMPD spectroscopy

Fig. 7.2a) shows the IRMPD spectrum of the radical cation (Resv)^{+•}, obtained by plotting the photofragmentation yield versus the IR radiation wavenumber in the 1100-1800 cm⁻¹ spectral region. The radical cation of resveratrol has been obtained by electrospray ionization from a 1:1 resveratrol/CuSO₄ solution 10⁻⁴ M in methanol/water (1:1). (Resv)^{+•} ions at $m/z = 228$ (where m/z for an ion is the ratio between its mass in atomic mass unit (a.m.u.) and its charge expressed as the number of elementary charges) yield fragment ions at $m/z = 211, m/z = 199$ and $m/z = 182$ when irradiated with the FEL beam tuned in resonance with an active vibrational mode of the parent ion. The same fragmentation products are observed in the electron ionization mass spectrum of *trans*-resveratrol [405]. The major features in the IRMPD spectrum in the mid IR region are observed at 1156, 1323-1343 and 1573 cm⁻¹. The IRMPD spectrum in the 3500-3700 cm⁻¹ region shows two distinct bands at 3601 and 3643 cm⁻¹ (see Fig. 7.3a)).

In the IR spectrum of the neutral molecule in KBr pellet the ν OH bands yield a broad and intense absorption with the ν OH of the hydroxyl group in para position assigned at 3380 cm⁻¹ and the in-phase and anti-phase coupled ν OH of the dihydroxyphenyl group assigned at 3397 and 3405 cm⁻¹, respectively [406]. However, given the possible pronounced intermolecular interactions in the solid sample, any relationship between the IR spectrum of the neutral and the one of the radical cation is subject to several factors, not easy to predict.

Fig. 7.2b) shows significant features of the IRMPD spectrum of the copper(I) complex of resveratrol, [Cu(Resv)]⁺, recorded in the 1100-1300 and 1500-1600 cm⁻¹ wavenumber ranges. The photofragmentation process proceeds mainly by formal loss of Cu and water

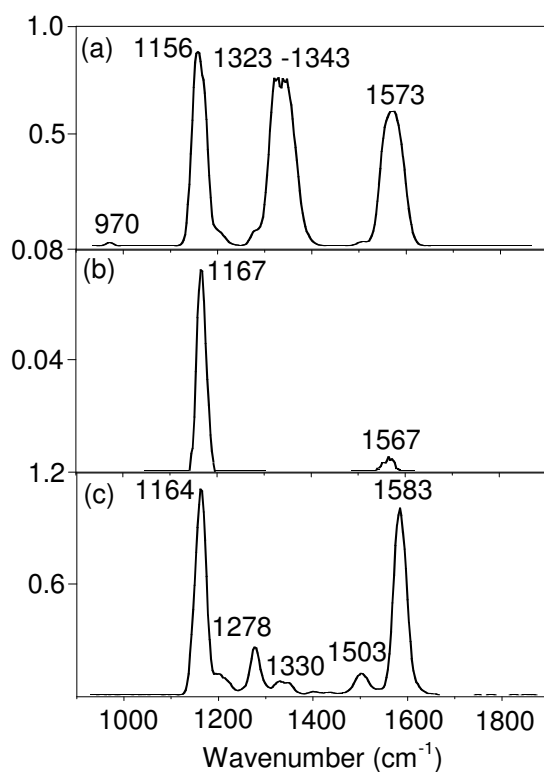


FIGURE 7.2: IRMPD spectrum of $(\text{Resv})^{+\bullet}$ (a), $[\text{Cu}(\text{Resv})]^+$ (b), and $[\text{Cu}(\text{Resv})_2]^+$ (c) in the $1000\text{-}1800\text{ cm}^{-1}$ wavenumber range.

as neutral fragments giving $\text{C}_{14}\text{H}_{10}\text{O}_2^+$ product ion. The $[\text{Cu}(\text{Resv})]^+$ complex is obtained by collision induced dissociation of the Cu(I) complex with two *trans*-resveratrol ligands and is remarkably stable against photodissociation, when compared with $(\text{Resv})^{+\bullet}$ ions for example, and required an exceptionally long irradiation time (2 sec.) in order to observe any IRMPD activity. However, the bands at 1167 and 1567 cm^{-1} , searched in a region where pronounced activity was expected, are clearly characteristic features for this species. In the νOH region a sharp band at 3628 cm^{-1} can be observed, midway between the two absorptions displayed by $(\text{Resv})^{+\bullet}$ ions (Fig. 7.3b)). The copper(I) complex with two resveratrol ligands yields $[\text{Cu}(\text{Resv})]^+$ and $[\text{Cu}(\text{Resv})(\text{H}_2\text{O})]^+$ as photofragmentation products and displays the IRMPD spectrum reported in Fig. 7.2c). The most active modes at 1164 and 1583 cm^{-1} share similar resonances with likely corresponding modes of the $[\text{Cu}(\text{Resv})]^+$ complex. In between these two pronounced bands the IRMPD spectrum in the fingerprint region shows a complex structure with several features of significant intensity. The OH stretching region is characterized by a sharp band at 3643 cm^{-1} (see Fig. 7.3c)). On its red side a very weak (less than 5% relative intensity) motif at 3628 cm^{-1} is visible as well.

The IRMPD spectroscopic investigation of the 1:1 complex of Cu(I) with dihydroresveratrol, examined in the $3500\text{-}3700\text{ cm}^{-1}$ range, presents a composite feature with a sharp maximum at 3627 cm^{-1} and an unresolved shoulder at 3618 cm^{-1} . Three weak features appearing from $3530\text{-}3590\text{ cm}^{-1}$ are mere artifacts and should be attributed no real meaning.

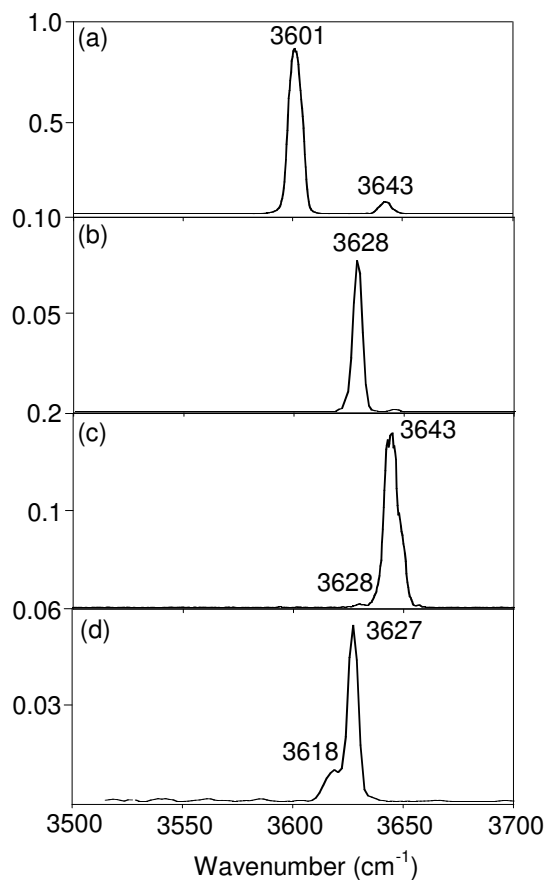


FIGURE 7.3: IRMPD spectrum of $(\text{Resv})^{+\bullet}$ (a), $[\text{Cu}(\text{Resv})]^+$ (b), $[\text{Cu}(\text{Resv})_2]^+$ (c), and $[\text{Cu}(\text{DHResv})]^+$ (d) in the $3500\text{-}3700\text{ cm}^{-1}$ wavenumber range.

7.4.2 Theoretical results and comparison with experiments

The parameters used in the calculation of the ground-state structures and of the optical properties of resveratrol and resveratrol-copper complexes have been fixed to those found from the previous test on the phenol-copper complex. After convergence tests, the atomic displacement has been finally chosen equal to 0.05 \AA . The kinetic energy cut-off is 500 eV , ensuring convergence of the structural parameters of resveratrol and resveratrol complexes to better than 0.05% with respect to available experimental data [389]. The structures have been relaxed to obtain forces below 10^{-3} eV/\AA , an accuracy needed for the rigorous assessment of the vibrational frequencies and intensities. The linear dimension of the simulation cubic cell was increased from 12 \AA for the pristine resveratrol molecule to 20 \AA for the largest complexes to avoid spurious interactions among periodic images.

The resveratrol-copper topological analysis starts from our previous finding that the copper adsorption position on phenol is not close to the oxygen as one could argue by relying only on chemical intuition. Rather copper sits on the top of the carbon atoms. The same conclusion has been drawn for resveratrol and, thus, we placed the copper atom

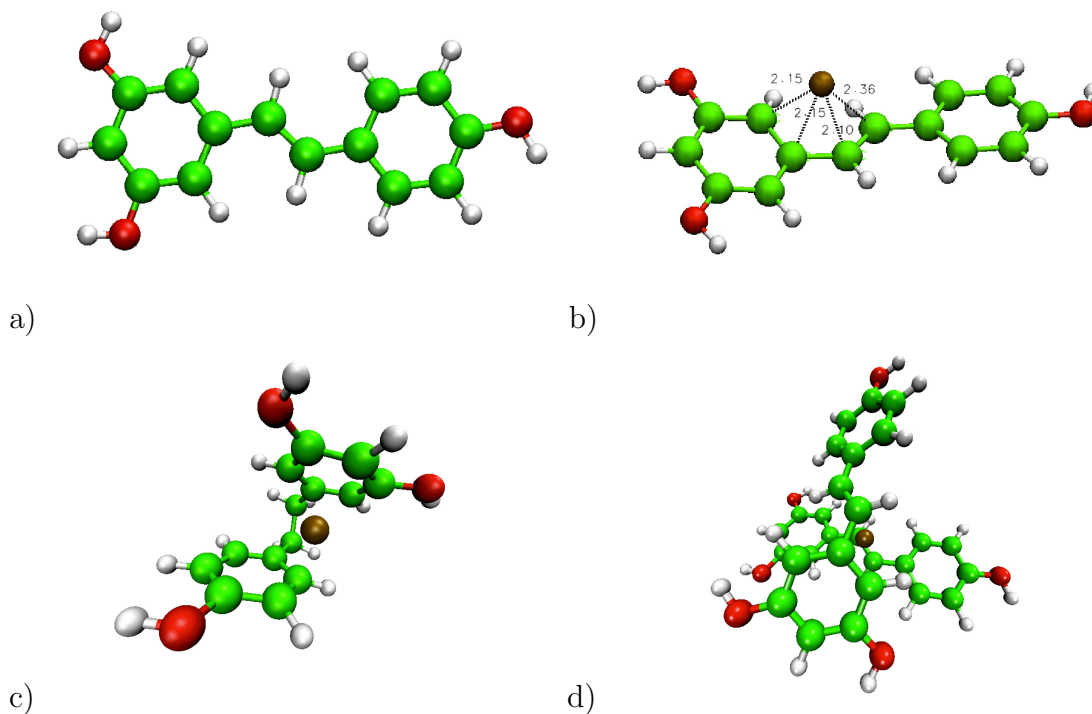


FIGURE 7.4: Optimized structures of resveratrol (a) , resveratrol complexes (b) and d)) and $[\text{Cu}(\text{DHResv})^+$ (c)). Carbon is in green, hydrogen in gray, copper in orange, oxygen in red.

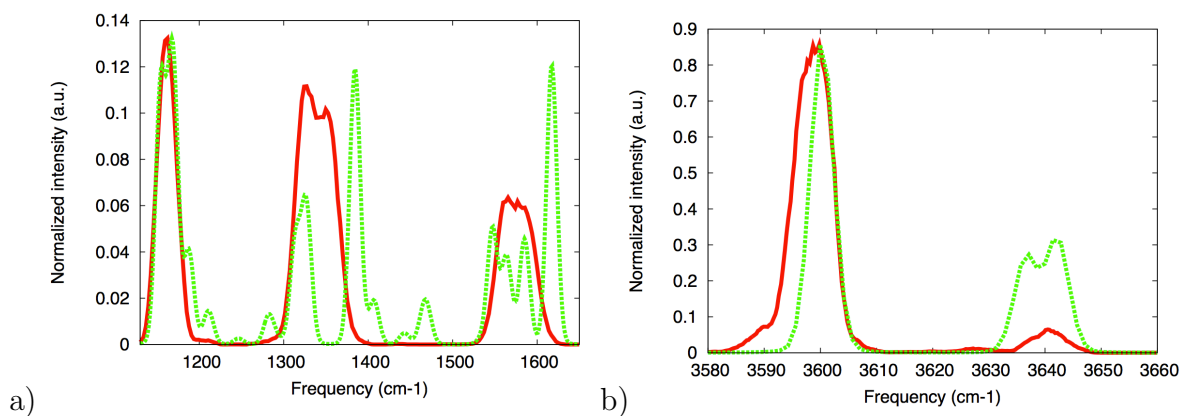


FIGURE 7.5: Calculated (green-dashed line) infrared spectra of $(\text{Resv})^{+\bullet}$ depicted in Fig. 4a) for low (a) and high (b) vibrational frequencies compared to our experimental measurements (red line). Intensity values, normalized to the maximum experimental peak, are in arbitrary units.

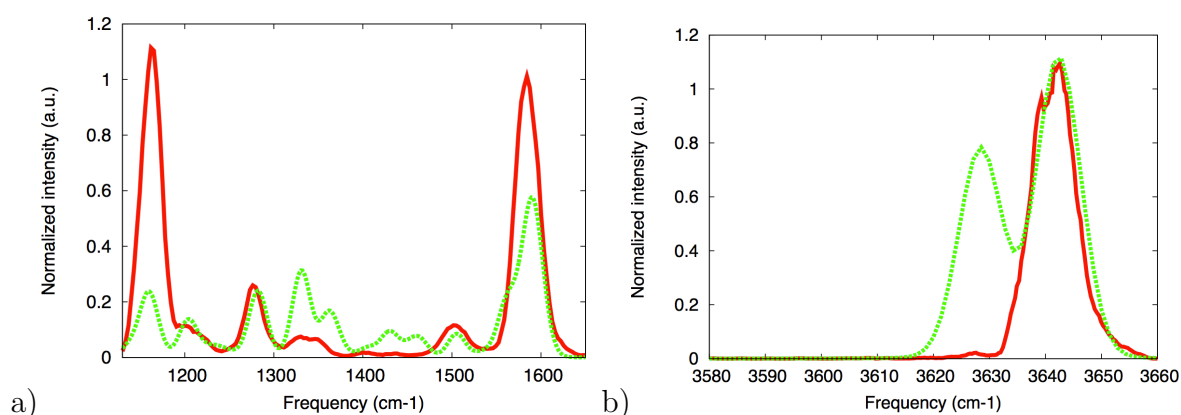


FIGURE 7.6: Calculated (green-dashed line) infrared spectra of $[\text{Cu}(\text{Resv})_2]^+$ depicted in Fig. 4d) for low (a) and high (b) vibrational frequencies compared to our experimental measurements (red line). Intensity values, normalized to the maximum experimental peak, are in arbitrary units.

on several adsorption sites coordinating with carbon atoms, for example in the middle-top of the phenol ring, on the top of a single carbon atom and bound with two carbon atoms of the alkenyl moiety and two closest carbons of the adjoining resorcinol ring. DFT structural optimization procedures were based initially on a temperature-constrained ab-initio molecular dynamics in order to find a reasonable starting guess for a quasi-Newton (variable metric) algorithm used to relax the ions into their instantaneous ground state (which is known to fail very far from the minimum). The forces and the stress tensor are used to determine the search directions for finding the equilibrium positions (the total energy is not taken into account). The minimum energy configuration by adopting this approach is found when the copper(I)-resveratrol complex presents a tetra-coordinated metal bound with two carbon atoms of the alkenyl moiety and two closest carbons of the adjoining resorcinol ring, as sketched in Fig. 7.4b). To further check this conclusion, we performed a Bader charge analysis [407, 408, 409] of the $[\text{Cu}(\text{Resv})]^+$ complex. This analysis uses zero flux surfaces to divide atoms, on which the charge density is a minimum perpendicular to the surface. Usually, the charge enclosed within the Bader volume is a good approximation to the total electronic charge of an atom. The calculation starts from a uniform positive charged cell, and at the end of the self-consistent procedure all four carbon atoms bound to copper gain about 0.15 e^- each, while copper loses about 0.6 e^- . This is a signature of the tetra-coordination between copper and the carbon atoms of resveratrol. The most stable complexes found are sketched in Fig. 7.4). One may note that the most stable structure for the $[\text{Cu}(\text{Resv})]^+$ complex is slightly different from the one reported by Tamboli *et al.* [389], though maintaining the basic binding features, possibly due to the upgraded computational approach presently adopted. In all the investigated structures, the copper atom is tightly bound to resveratrol, with binding energy decreasing from 4.931 eV in the $[\text{Cu}(\text{Resv})]^+$ complex to 4.05 eV in the $[\text{Cu}(\text{Resv})_2]^+$ complex. The binding energy calculations are referred to charged $(\text{Resv})^{+\bullet}$ and neutral metal (Cu or $(\text{Resv})+\text{Cu}$) fragments. In other words we guessed that the positive charge remains on the departing ligand as this is the lowest dissociation limit. This is due to the fact that resveratrol first ionization energy is lower than copper ionization energy. We performed the calculations of these first ionization energies finding that resveratrol has an ionization energy of 4.28 eV, while for copper is 7.73 eV, thus confirming our working hypothesis.

DFPT, as described in Sec. III, has been applied to the calculation of the vibrational spectrum of the resveratrol complexes previously shown. Since first-principles methods necessarily involve approximations, the most important of which, in the vibrational analysis of molecules and solids, is the approximate form of the exchange-correlation interaction, it is important to validate the calculations against experimental data. To compare the theoretical spectrum with the experimental measurements, the calculated vibrational eigenvalues have been broadened with a Gaussian function with FWHM equal to 35 cm^{-1} . The theoretical spectra are normalized to the height of the experimental maximum peak in both cases. It is worthy to note that no shift of the frequency has been used, differently from what is usually done when comparing experimental data with vibrational spectra calculated by using Gaussians basis sets, which overestimate the frequencies. For the sake of comparison GTO based DFT calculations have been performed as well. The calculated IR spectra were indeed found to require scaling factors to provide matching with the positions of the experimental IRMPD bands.

The comparison between theory and experiment in Figs. 7.5 and 7.6 shows fair agreement at both low ($1100\text{--}1800\text{ cm}^{-1}$) and high ($3500\text{--}3700\text{ cm}^{-1}$) frequencies, corresponding to the so-called fingerprint and OH stretching region. However, particularly in the fingerprint region, several somewhat weak bands are predicted that are not represented in the experimental spectrum. It is possible that the intensity of these bands is predicted too high by theory. One should in fact consider that band intensities, as obtained by the described theoretical calculations, reflect the coupling with the electromagnetic field by means of Born charges. These charges represent an approximation rendering the interaction between the IR field and the vibrational normal modes, which is not exactly a model for the IRMPD process. Indeed, it is not uncommon that small absorptions may be missing in IRMPD spectra due to the multiphotonic nature of the process and the requirement of an efficient intramolecular vibrational relaxation [396].

On the basis of the simulated IR spectra the major features of the experimental spectra of $(\text{Resv})^{+\bullet}$ and $[\text{Cu}(\text{Resv})_2]^+$ can be compared. The pronounced IRMPD feature at 1164 cm^{-1} in the spectrum of $[\text{Cu}(\text{Resv})_2]^+$ finds a counterpart in the most active band of $(\text{Resv})^{+\bullet}$ at 1156 cm^{-1} . At nearly the same frequency, 1167 cm^{-1} , an IRMPD band is also detected for $[\text{Cu}(\text{Resv})]^+$. In all cases this feature encompasses in plane OH and CH bending vibrations. The wide feature in the IRMPD spectrum of $(\text{Resv})^{+\bullet}$ at $1323\text{--}1343\text{ cm}^{-1}$ is associated to ring deformation and νCO modes. The corresponding bands in the IRMPD spectrum of $[\text{Cu}(\text{Resv})_2]^+$ are noticeably less active. At higher frequency a strong, wide band of $(\text{Resv})^{+\bullet}$ at 1573 cm^{-1} is matched by the feature at 1583 cm^{-1} in the IRMPD spectrum of $[\text{Cu}(\text{Resv})_2]^+$. A noticeable feature for $(\text{Resv})^+$ at 1567 cm^{-1} is also recorded in this range. As also observed by the animation of the calculated IR modes, the active vibrations here involve local modes with major νCC character. Interestingly, two marked features at 1278 and 1503 cm^{-1} appear in the IRMPD spectrum of $[\text{Cu}(\text{Resv})_2]^+$ that are not seen in the spectrum of $(\text{Resv})^{+\bullet}$. The first one at 1278 cm^{-1} contains a major contribution of νCO vibrations of the two para-hydroxyphenyl units coupled with in plane CH bending. The corresponding mode in $(\text{Resv})^{+\bullet}$ is calculated at 1310 cm^{-1} , experimentally active within the wide feature at $1323\text{--}1343\text{ cm}^{-1}$. This shift to higher frequency is likely a consequence of increased double bond character of the CO bond of the para-hydroxyphenyl group in $(\text{Resv})^{+\bullet}$, an effect of resonance charge and spin delocalization. From the comparison with the matching band in calculated IR spectrum the band at 1503 cm^{-1} is attached to one of several modes of ring deformation and νCC . These highly qualitative observations

may be extended to the νOH features. The computed IR spectrum of $(\text{Resv})^{+\bullet}$ allows us to assign the IRMPD band at 3601 cm^{-1} to the νOH mode of the para-hydroxyphenyl group while νOH of the dihydroxyphenyl group absorbs at 3643 cm^{-1} . The lower activity of the latter modes is also predicted by the calculations. Moving to the $[\text{Cu}(\text{Resv})_2]^+$, once again only modest changes are observed with νOH appearing at 3643 cm^{-1} . With regard to the $[\text{Cu}(\text{Resv})]^+$ complex, the corresponding figure reporting the calculated IR spectra together with the experimental IRMPD spectrum is not included in this text because, as explained earlier, the complete experimental spectrum was not available due to the meager photodissociation activity of this complex. Overall, the matching observed between the experimental IRMPD spectra and the calculated IR spectra for the optimized structures of $(\text{Resv})^{+\bullet}$ and $[\text{Cu}(\text{Resv})_2]^+$ complex supports the structural assignment provided by the computational method. Noteworthy, the OH-stretching frequencies in the region $3580\text{-}3660\text{ cm}^{-1}$ clearly distinguishable in Fig. 7.5b) (see Fig. 7.3a) for experiments) for the pristine resveratrol molecule become almost degenerate and move to higher vibrational frequencies in the case of copper binding (see Fig. 7.6b)). The very small shift toward higher frequency of the OH-stretching modes upon adsorption of copper (less than 1%), more evident in Fig. 7.3b)-c), can be attributed to the charge redistribution in the resveratrol molecule. Nevertheless, a Bader analysis of the charge density [409] shows that the charge on the spatially far three hydroxyl groups are left unchanged. The small frequency shift found in the OH vibrational frequencies cannot thus be due to a direct change in the OH charge density, rather to a slight stiffening of this bond due to long-range electrostatic interactions caused by the localized charge transfer.

7.5 Conclusions

Copper(I) complexes with resveratrol ligands have been found amenable to IRMPD spectroscopy. The experimental IRMPD spectra have yielded the IR signatures of the selected species isolated in the gas phase. In parallel, the geometric features of the sampled ions have been examined by DFT calculations and the optimized structures have been obtained. Energy gradient calculations with respect to atomic displacements and ensuing analysis have provided reference IR spectra validating the structural assignment and aiding the interpretation of the observed vibrational features. The combined experimental evidence and computational results point to copper(I) complexes engaging the π -electron frame of the resveratrol skeleton rather than the oxygen lone pairs in the coordination to the transition metal ion.

The IRMPD features of both $[\text{Cu}(\text{Resv})]^+$ and $[\text{Cu}(\text{Resv})_2]^+$ complexes display significant analogies with the IRMPD spectrum of ionized resveratrol which presents three pronounced bands at 1156 , $1323\text{-}1343$ and 1573 cm^{-1} in the mid IR region and active modes at 3601 and 3643 cm^{-1} in the OH stretching region. The dominant contribution of resveratrol modes in the inspected spectral regions is expected. At the same time the observed analogies seem to suggest a comparable perturbation of neutral resveratrol upon binding of $[\text{Cu}(\text{Resv})]^+$ as well as upon ionization by electron loss. The present investigation may open the way to a systematic investigation of charged complexes of transition metals with bioactive molecules in an isolated state, hopefully contributing to elucidate the factors governing their biological function.

7.6 Appendix A: Theoretical and Computational Methods

In this Appendix we provide more details on the implementation of Density Functional Perturbation theory (DFPT) [179], used for the calculation of the resveratrol-copper complexes harmonic frequencies investigated in this work. Within DFPT, the second derivative of the total energy E can be calculated by using the Hellmann–Feynman theorem as:

$$\frac{\partial^2 E}{\partial \mathbf{R}_i \partial \mathbf{R}_j} = \int \frac{\partial \rho_{\mathbf{R}}(\mathbf{r})}{\partial \mathbf{R}_j} \frac{\partial V_{\mathbf{R}}(\mathbf{r})}{\partial \mathbf{R}_i} d\mathbf{r} + \int \rho_{\mathbf{R}}(\mathbf{r}) \frac{\partial^2 V_{\mathbf{R}}(\mathbf{r})}{\partial \mathbf{R}_i \partial \mathbf{R}_j} d\mathbf{r} + \frac{\partial^2 E_{ion}(\mathbf{R})}{\partial \mathbf{R}_i \partial \mathbf{R}_j} \quad (7.2)$$

where $V_{\mathbf{R}}(\mathbf{r})$ and $E_{ion}(\mathbf{R})$ are the ion-electron and ion-ion interactions, respectively, and $\partial \rho_{\mathbf{R}}(\mathbf{r})/\partial \mathbf{R}_i$ is the derivative of the ground-state charge density with respect to the ion displacement. Within LR-DFPT, the response function $\partial \rho_{\mathbf{R}}(\mathbf{r})/\partial \mathbf{R}_i$, can be linearized by first-order perturbation of the Kohn–Sham density [410]:

$$\Delta \rho(\mathbf{r}) = 4Re \sum_{n=1}^{N/2} \psi_n^*(\mathbf{r}) \Delta \psi_n(\mathbf{r}) \quad (7.3)$$

The Hamiltonian in this approximation reads:

$$(H_{KS} - \epsilon_n) |\Delta \psi_n\rangle = -(\Delta V_{KS} - \Delta \epsilon_n) |\psi_n\rangle \quad (7.4)$$

In Eq. (7.4) H_{KS} is the unperturbed Kohn–Sham Hamiltonian, and ΔV_{KS} is the first-order correction to the Kohn–Sham potential

$$V_{KS}(\mathbf{r}) = V(\mathbf{r}) + \int \frac{\rho(\mathbf{r}')}{|\mathbf{r} - \mathbf{r}'|} d(\mathbf{r}') + v_{xc} \quad (7.5)$$

where v_{xc} is the exchange-correlation potential and $\Delta \epsilon_n = \langle \psi_n | \Delta V_{KS} | \psi_n \rangle$ is the first order perturbation of the Kohn–Sham eigenvalue. Eqs. (7.2), (7.3), and (7.4) form a set of linear equations which can be solved self-consistently as in the case of the unperturbed Kohn–Sham equations. Noteworthy, at variance with standard perturbative approaches the sum on Eq. (7.3) is only on the occupied states. This feature decreases substantially the computational cost of the calculation. Given the ground-state density and the linear response function, from Eq. (7.2) one can calculate by diagonalization the vibrational eigenmodes and eigenvalues as well as the intensity of the infrared active modes (see ref. [179] for further details). The latter can be obtained by calculating the Born effective charges $Z_{\alpha\beta}^*(i)$, measuring the coupling between the atomic displacement and the electric perturbation field, as:

$$I(\omega) = \sum_{\alpha=1}^3 \left| \sum_{i=1}^M \sum_{\beta=1}^3 Z_{\alpha\beta}^*(i) e_{\beta}(i) \right|^2 \quad (7.6)$$

where $e_{\beta}(i)$ is the vibrational eigenmode of atom i along the Cartesian coordinate β . In particular, the tensor $Z_{\alpha\beta}^*(i)$ accounts for the change in the system polarization and is calculated via DFPT as the second derivative of the energy with respect to the the atomic

displacement and the total (induced and external) electric field [411, 179, 401]. It contains thus important information on the electronic properties of the system and on the coupling between external fields and vibrational motion.

Finally, we would like to comment on the computational cost of performing these *ab-initio* simulations. The plane-wave DFT calculations of the IR spectra and of the optimization procedure to find the most stable structures according to our level of theory presented above required roughly 10^5 CPU hours on modern 2.3 GHz processors of a high-end computing terascale resource, which is a lot more expensive than the computational cost of GTO-based DFT calculations.

Chapter 8

Ultra-cold Fermi gases

We develop a theoretical method going beyond the contact-interaction approximation frequently used in mean-field theories of many-fermion systems, based on the low-energy T -matrix of the pair potential to rigorously define the effective radius of the interaction. One of the main consequences of our approach is the possibility to investigate finite-density effects, which are outside the range of validity of approximations based on Fermi-contact potentials. We apply our method to the calculation of density dependent properties of an ultracold gas of ${}^6\text{Li}$ atoms at unitarity, and out of resonance ${}^{40}\text{K}$, whose two-body interaction potential is calculated using ab initio quantum chemistry methods. We find that density effects are significant in ultracold gases with densities one order of magnitude higher than those attained in current experiments.

8.1 BEC-BCS crossover with contact interaction

Following the experimental realisation of a trapped Bose condensed gas of alkali atoms in 1995 [412, 413], the understanding of dilute matter in the deep quantum regime has made impressive progresses [414, 415, 416, 417].

Broadly speaking, these systems are characterised by very low densities and very low temperatures, in such a way that the average (thermal) size of the wavefunctions associated to each particle is so large that they substantially overlap. Denoting by $\Lambda = h/\sqrt{2\pi mk_B T}$ the thermal de Broglie wavelength of the system, this condition can be expressed as $\rho\Lambda^3 \gg 1$, where ρ is the density. In this regime, quantum statistical effects dominate the behaviour of the system.

Moreover, the diluteness condition implies that the interaction between the particles can be very well described in many circumstances using the Fermi Contact Interaction (FCI), depending only on the s -wave scattering length a of the actual interatomic potential:

$$V_{\text{FCI}}(\mathbf{x}, \mathbf{x}') = \frac{4\pi\hbar^2 a}{m} \delta(\mathbf{x} - \mathbf{x}'), \quad (8.1)$$

which is a very good approximation as long as $\rho|a|^3 \ll 1$. The scattering length can have either sign, positive or negative, denoting a repulsive or attractive effective interaction between the particles, respectively. The use of FCI has also the important theoretical advantage that the mean-field equation describing Bose–Einstein condensates (BEC) – that is, the Gross–Pitaevskii (GP) equation – can be solved relatively easily and turns out to describe very well many of the properties of these systems [416, 417].

Recently, it has become possible to tune the scattering length of fermionic alkali gases using the Fano–Feshbach resonances. By changing the value of an external magnetic field, the scattering length can be varied both in sign and magnitude, the latter of which can also be made to diverge. This possibility corresponds to the so called “unitary limit” where ultracold gases display an universal behaviour, that is independent of the details of the two-body interaction.

By crossing the magnetic field value corresponding to the unitary limit, one can pass from a gas of paired fermions ($a < 0$ and $\rho|a|^3 \ll 1$) to a gas of repulsively interacting bosonic dimers ($a > 0$ and $\rho|a|^3 \ll 1$). In the first case, the quantum gas is well described by the Bardeen–Cooper–Schrieffer (BCS) mean-field theory of superconductivity, whereas in the second case the mean-field theory of BEC, based on the GP equation, applies.

There are two main aspects of this problem in which theoretical techniques borrowed from many-body scattering theory might help in the analysis of the properties of ultracold gases, and they will be discussed in the following two subsections.

The first is, quite obviously, the calculation of the scattering length a as a function of the external magnetic field. This quantity depends on the potential between two alkali atoms, which can be calculated directly using *ab-initio* electronic structure techniques. We will use multichannel scattering theory to rationalise the details of the interactions, and to complement measurements of the scattering length in fermionic alkali atoms [418, 419].

The second contribution of multichannel scattering theory techniques to the understanding of ultracold dilute fermion gases consists in a rigorous analysis of the unitary limit. Since in this case the scattering length diverges, particular care has to be taken to extract meaningful quantities from the equations. Rigorous renormalisation schemes have been developed to this end [420, 421], but they all assume an infinite dilution limit (or, which is the same the Fermi-contact interaction) and, therefore, their prediction for the relevant quantities in the unitary regime are independent on the density of the atomic gas.

Many groups have recently treated the effect of non-universal behaviour in the unitary regime, by calculating how the relevant quantities characterising an ultracold gas – such as the chemical potential, the pairing gap or the degeneracy temperature – depend on the details of the interaction potential, which are generally summarised in a single parameter, the “effective range” [422, 423]. In the following sections, we will present an alternative but equivalent derivation of the results obtained so far. Our approach is based on a solution of the mean-field theory in the dilute regime which relies heavily on a multichannel description of the many-body interaction between the atoms.

In particular, we will present a new point of view on the FCI, which is seen as the proper limit of a separable potential, with the scattering length of the system kept constant through the limiting procedure. In this way, we will be able to show that the Hartree–Fock (HF) term of the mean field equations is identically zero. In the naive approach based on the FCI, the HF term is a constant which diverges in the unitary regime and is usually neglected. Secondly, we will write the gap equation for a system of dilute fermions as a function of the T matrix of the interaction. In this way we will be able to investigate how the properties of a gas of dilute fermions depend not only on the scattering length, but also on the effective range of the potential. In the unitary limit this correspond to a non-universal behaviour of the system. We will show that our results are in very good agreement with those obtained with other theoretical approaches.

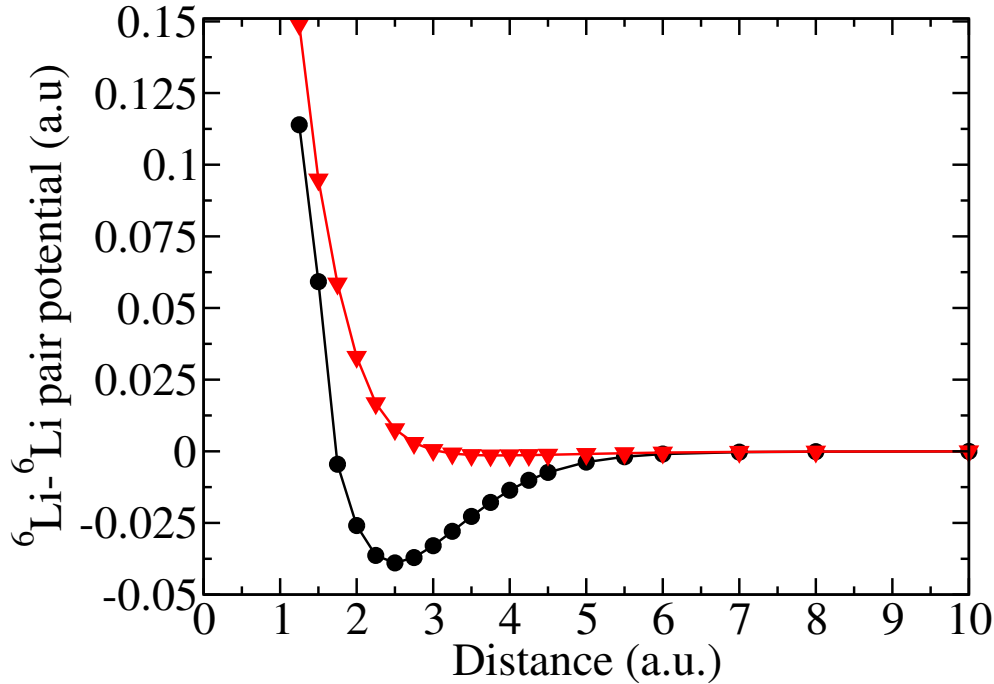


FIGURE 8.1: The potential energy of interaction between two Lithium atoms in the singlet (dots) and triplet (triangles) configurations.

8.1.1 *Ab-initio* calculation of the scattering length of alkali metals

In order to calculate the dependence of the scattering length on the magnetic field, one has to first calculate the interaction potential between two alkali atoms as a function of the global spin of the pair. We will consider the case of two ${}^6\text{Li}$ atoms, where the relevant subspaces correspond to a singlet and a triplet state.

We used configuration interaction theory (CI), with single and double excitations from a reference Hartree–Fock state, expanding the Slater determinants using molecular orbitals taken from the cc-pVQZ basis set [10]. The electronic singlet and triplet potential energy surfaces are reported in Fig. 8.1 using dots and triangles, respectively.

In the calculations of the pair potential, we neglected relativistic and hyperfine corrections to the total energy of the system, and we have accounted for this approximation by multiplying the potential by two constant factors, for the singlet and triplet respectively, so that they could reproduce the scattering length at a given point [419].

In general, we write the pair potential as:

$$\hat{V}(r) = \xi_s V_s(r) \left(1 - \frac{\mathbf{S}^2}{2}\right) + \xi_t V_t(r) \frac{\mathbf{S}^2}{2} \quad (8.2)$$

where $\hat{V}_s(r)$ and $\hat{V}_t(r)$ are the spin-singlet and spin-triplet contributions (including van der Waals dispersion) and \mathbf{S} is the total spin operator. The weights ξ_s and ξ_t appearing in Eq. (8.2) are empirical parameters adjusted to reproduce the position of the Feshbach resonance(s). The values of all the parameters appearing in Eq. (8.2) for ${}^6\text{Li}$ and ${}^{40}\text{K}$ are reported in Table 1. The fact that the ξ 's are close to 1 confirms the good quality of the pair potentials used as input in the calculation.

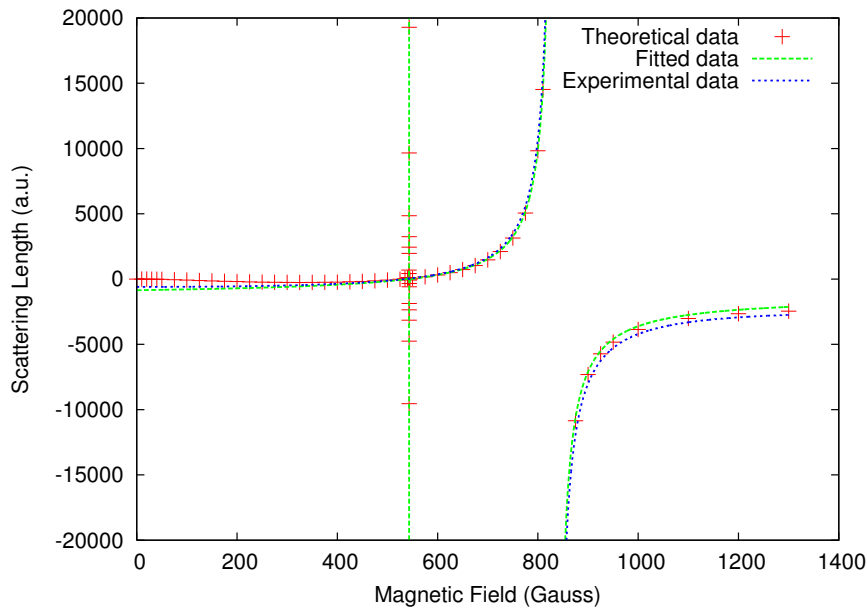


FIGURE 8.2: S-wave scattering length vs applied magnetic field for the hyperfine states $(f, m_f) = (1/2, -1/2)$ and $(1/2, 1/2)$ in ${}^6\text{Li}$ - ${}^6\text{Li}$ scattering.

Parameter	${}^6\text{Li}$	${}^{40}\text{K}$
ξ_s	0.98619	1.00312
ξ_t	0.98153	1.00312
g_N	0.822	-0.3245
A	152.14 MHz	285.73 MHz

TABLE 1: Values of the parameters used in Eq. (8.2) to calculate the interaction between pairs of ${}^6\text{Li}$ and ${}^{40}\text{K}$.

Using these potentials, we have calculated the scattering length of ${}^6\text{Li}$ (and ${}^{40}\text{K}$) atoms by adding the hyperfine interaction as well as an energy term dependent on the external magnetic field B . The atom-atom collisions are then described by an Hamiltonian of the form

$$H = T + V + V_{\text{hf}} + V_B, \quad (8.3)$$

where T is the kinetic energy of the nuclei and V is the electron Hamiltonian of Eq. 8.2 (including electronic kinetic energy, Coulomb potential and spin-orbit coupling). V_{hf} and V_B describe the hyperfine interaction and the interaction of the atoms with an external magnetic field, respectively. In formulae:

$$V_{\text{hf}} = \mathbf{A} \mathbf{I} \cdot \mathbf{S} \quad (8.4)$$

$$V_B = g_S \mu_B \mathbf{S} \cdot \mathbf{B} - g_N \mu_N \mathbf{I} \cdot \mathbf{B} \quad (8.5)$$

where \mathbf{S} is the spin operator, \mathbf{I} the nuclear spin operator, and g_S and g_N are the electronic and nuclear gyromagnetic factors, respectively. In the usual Born–Oppenheimer approximation, the wave equation for the relative motion of a pair of ultracold atoms at zero

angular momentum can be written as

$$-\frac{\hbar^2}{2m}\nabla^2\phi_\alpha(r) + V_\alpha(r)\phi_\alpha(r) + \sum_\beta V_{I,\alpha\beta}(r)\phi_\beta(r) = E\phi_\alpha(r) \quad (8.6)$$

where the label α denotes the total electron and nuclear spin states of the colliding atoms. $V_\alpha(r)$ is the internuclear potential obtained using the ground-state electronic wavefunction for the given value of α (see Fig. 8.1), $V_{I,\alpha\beta}(r)$ describes the coupling induced by the hyperfine interaction term V_{hf} , and the interaction with the magnetic field V_B .

From the solution of Eq. (8.6) in the $E \rightarrow 0$ limit, one can obtain the s-wave scattering length a of the system from the asymptotic values of the wavefunction, that is

$$\phi_\alpha(r) = A_0 \left(1 - \frac{a}{r}\right). \quad (8.7)$$

In Fig. 8.2 we plot the calculated s-wave scattering length vs magnetic field for the lowest energy hyperspin doublet open channel. The positions of the narrow (543.25 G) and broad (834 G) resonances are in good agreement with the experimental data [424].

In the case of ^{40}K after checking the correctness with our results, we finally used the pair potential for singlet and triplet states obtained in Ref. [431] from the Rydberg-Klein-Rees (RKR) theory [432, 433, 434], together with the dispersion parameters calculated in Refs. [435, 436].

8.1.2 Application of scattering theory to the solution of the Bogoliubov–de Gennes equations

Let us consider a system of quantum particles interacting via a two-body potential described by the operator \hat{V} and in a given external field $U(x)$. The Hamiltonian of the system in the second quantised formalism is

$$H = \sum_{ij} (T_{ij} + U_{ij}) a_i^\dagger a_j + \frac{1}{2} \sum_{il,jm} V_{il,jm} a_i^\dagger a_l^\dagger a_m a_j \quad (8.8)$$

where a_i^\dagger and a_i are the creation and annihilation operators for a complete set of single particle states, subject to the usual (anti)commutation relations. The indices of these operators describe all the relevant quantum numbers. Given the wavefunctions $\phi_i(x)$ of the state i , the matrix elements appearing in equation (8.8) are given by

$$T_{ij} = -\frac{\hbar^2}{2m} \int dx \phi_i^*(x) \nabla^2 \phi_j(x) \quad (8.9)$$

$$U_{ij} = \int dx \phi_i^*(x) U(x) \phi_j(x) \quad (8.10)$$

$$V_{il,jm} = \int dx dy \phi_i^*(x) \phi_l^*(y) \hat{V} \phi_j(x) \phi_m^*(y). \quad (8.11)$$

A mean-field solution of the ground state of the Hamiltonian (8.8) can be obtained by introducing an effective Hamiltonian H_{eff} , where the two-body potential V in equation (8.8) is substituted by an effective one-body potential

$$V_{\text{eff}} = \sum_{ij} \left(W_{ij} a_i^\dagger a_j + \frac{1}{2} \Delta_{ij}^* a_i a_j + \frac{1}{2} \Delta_{ij} a_i^\dagger a_j^\dagger \right), \quad (8.12)$$

where the as-yet unspecified matrices W_{ij} and Δ_{ij} are determined by requiring that the average values of H and $H_{\text{eff}} - \mu\hat{N}$ are as close as possible to each other. In the evaluation of the average value of H , one uses the Hartree–Fock–Gorkov (HFG) factorisation of the two-body density matrix which, in the case of fermions, is [425]

$$\langle a_i^\dagger a_l^\dagger a_m a_j \rangle = \langle a_i^\dagger a_j \rangle \langle a_l^\dagger a_m \rangle - \langle a_i^\dagger a_m \rangle \langle a_l^\dagger a_j \rangle + \langle a_i^\dagger a_l^\dagger \rangle \langle a_j a_m \rangle. \quad (8.13)$$

The HFG factorisation divides the total density in a Hartree–Fock-like density term plus a separable term that represents the contribution to the density of a correlated ‘anomalous’ density, which represents a Cooper pair-type correlation and thus it is connected to the gap in the BdG equations. As an example of application of the HGF factorization and to understand its physical meaning, we may try to apply it to a many-electron atom. To do that, we performed full CI calculation using a 6-31G Gaussian basis set of the two-particle charge density for the ground ($^3P, E = -37.762$ a.u.) and the first two excited states ($^1S, E = -37.654$ a.u., $^1D, E = -37.707$ a.u.) of an isolated carbon atom. Therefore, in the ground state the spin of the two p-electrons is the same (triplet), while in the excited states is the opposite (singlet), as in a Cooper pair. Since in the Hartree–Fock method only fermions with the same spin correlate, the difference between the full CI density and the antisymmetrized product of the single-particle HF wavefunctions should result in a ‘anomalous’ density, which is close to zero for the ground state and writable as a separable form, or as a projector into a mono-dimensional space, for the two excited states. By diagonalising such density difference, the maximum eigenvalues found are 0.18, 0.9769 and 0.7355 for the 3P , 1S and 1D , respectively, demonstrating that for the triplet no ‘anomalous’ density is found, while for the two singlets it is almost in a separable form. Furthermore, by analyzing the expansion coefficients of such main eigenvectors on the Gaussian basis set, one may argue that there is a tendency at level of the excited states of the two outer electrons to stay close, like in a Cooper pair, even in the case of a repulsive potential as the Coulomb interaction. Therefore, while it is known that the Hartree–Fock–Gorkov factorisation is valid for a canonical ensemble in the thermodynamic limit, nevertheless, already for one single carbon atom such a representation of the density seems appropriate.

In this way, the self-consistent equations for W_{ij} and Δ_{ij} turn out to be:

$$W_{ij} = \sum_{l,m} (V_{il,jm} - V_{il,mj}) \langle a_l^\dagger a_m \rangle, \quad (8.14)$$

$$\Delta_{ij} = - \sum_{l,m} V_{ij,lm} \langle a_l a_m \rangle \quad (8.15)$$

and one is left with a two-body effective Hamiltonian, which can be put in the form

$$H_{\text{eff}} = \sum_k \epsilon_k b_k^\dagger b_k + E_0 \quad (8.16)$$

where E_0 is the ground state energy. The sum over k is restricted to those states where $\epsilon_k \geq 0$. The new set of fermionic operators b_k and b_k^\dagger are given by the Bogoliubov transform

$$\begin{aligned} a_i &= \sum_j (u_{ij} b_j + v_{ij}^* b_j^\dagger) \\ a_i^\dagger &= \sum_j (u_{ij}^* b_j^\dagger + v_{ij} b_j). \end{aligned} \quad (8.17)$$

Notice that in writing the HFG factorisation (8.13) we have assumed that, in general, the ground state of the system does not have a fixed number of particles. Although this assumption is formally questionable, mostly because the ground state would not satisfy the mass superselection rule [417, 426], it is nevertheless very useful because in many relevant cases the results obtained with this approach are quite similar to those obtained in a more rigorous number-conserving formalism. In the non-conserving-number approach, the effective Hamiltonian includes a Lagrange multiplier μ , used to constrain the solution of the problem in the subspace of a given average number of particles N .

The equations determining the coefficients u_{ij} and v_{ij} appearing in equation (8.17) are the well known Bogoliubov–de Gennes equations [427]:

$$\begin{aligned} \sum_k [(T_{ik} + U_{ik} + W_{ik} - \mu\delta_{ik}) u_{kj} + \Delta_{ik}v_{kj}] &= \epsilon_j u_{ij}, \\ \sum_k [(T_{ik} + U_{ik} + W_{ik} + \mu\delta_{ik})^* v_{kj} + \Delta_{ik}^* u_{kj}] &= -\epsilon_j v_{ij}, \end{aligned} \quad (8.18)$$

which have to be solved self-consistently with the definitions of W_{ij} and Δ_{ij} given in equations (8.14) and (8.15), respectively, together with the condition that the commutation relations of the operators b_k describe fermionic particles. Since the effective Hamiltonian (8.16) describes independent degrees of freedom, the occupation numbers in the ground state are distributed according to the Fermi function, that is

$$\langle b_i^\dagger b_j \rangle = \frac{\delta_{ij}}{\exp\left(\frac{\epsilon_i}{k_B T}\right) + 1}, \quad (8.19)$$

although in the following we will be concerned, for the sake of conciseness, with the $T \rightarrow 0$ limit.

The Bogoliubov–de Gennes equations are routinely used to investigate, at the mean-field level, the BEC-BCS crossover in dilute quantum Fermi gases [2]. In these low-temperature and low-density systems, the two-body interaction V is usually substituted by the contact interaction of equation (8.1). However, in this case the matrix W_{ij} of equation (8.14), also known as the Hartree–Fock (HF) term, is divergent in the “unitary” limit $a \rightarrow \infty$, and the mean-field approach is not directly applicable as it stands.

One possible way to overcome this problem, is to consider the FCI as the limit of a non-local potential. The limit has to be done in such a way that the scattering length a of the limiting potential corresponds to that of the actual interatomic potential. In the coordinate representation, the matrix elements (8.11) of a separable potential $V_f = |f_\lambda\rangle V \langle f_\lambda|$ can be written as

$$\begin{aligned} V_f(\alpha, \mathbf{r}_1, \beta, \mathbf{r}_2; \gamma, \mathbf{r}'_1, \eta, \mathbf{r}'_2) &= \delta_{\alpha\gamma} \delta_{\beta\eta} \lim_{\lambda \rightarrow 0} V_\lambda f_\lambda(\mathbf{r}_1 - \mathbf{r}_2) f_\lambda(\mathbf{r}'_1 - \mathbf{r}'_2) \times \\ &\delta \left[\left(\frac{\mathbf{r}_1 + \mathbf{r}_2}{2} \right) - \left(\frac{\mathbf{r}'_1 + \mathbf{r}'_2}{2} \right) \right] \end{aligned} \quad (8.20)$$

where the δ function on the right-hand side of the previous equation expressed the fact that the potential V_f conserves the momentum, and we have introduced spin labels denoted by greek letters.

In the previous equation, the function $f_\lambda(\mathbf{r})$ tends to zero everywhere except in the origin and satisfies the scaling equation $f_\lambda(\mathbf{r}) = \lambda^{3/2} f(\lambda\mathbf{r})$. In this case, the matrix elements of

equation (8.20) tend to the proper value expected for a FCI potential, since $\lim_{\lambda \rightarrow 0} f_\lambda(\mathbf{r}) = \delta(\mathbf{r})$. In particular, the limit form of the term $f_\lambda(\mathbf{r}'_1 - \mathbf{r}'_2)$ in equation (8.20) indicates that the potential is local, whereas the first term tends to the value expected for the FCI, given by equation (8.1).

The scattering length of the potential (8.20) is given by

$$a = \frac{m}{4\pi} \frac{1}{V_\lambda^{-1} - Q_\lambda} |\langle \phi_0 | f_\lambda \rangle|^2 \quad (8.21)$$

where $Q_\lambda = \lim_{E \rightarrow 0} \frac{1}{2} \langle f_\lambda | G_0(E) | f_\lambda \rangle$ and $G_0(E)$ is the resolvent of the free-particle Hamiltonian. We have denoted with $|\phi_0\rangle$ the eigenfunction of energy E of the free Hamiltonian in the limit $E \rightarrow 0$. Therefore, the value of V_λ is equation (8.20) which gives the correct FCI limit is

$$V_\lambda^{-1} = Q_\lambda + \frac{m}{4\pi a} |\langle \phi_0 | f_\lambda \rangle|^2. \quad (8.22)$$

Finally, since one has $\lim_{\lambda \rightarrow 0} Q_\lambda = \infty$ and $\lim_{\lambda \rightarrow 0} |\langle \phi_0 | f_\lambda \rangle|^2 = 1$, one obtains that $\lim_{\lambda \rightarrow 0} V_\lambda = 0$.

The Hartree–Fock term W .

Using expression (8.20) for the effective potential, and the limiting values just discussed, the the HF term W of equation (8.14), turns out to be

$$\begin{aligned} W_{\alpha\beta}(\mathbf{r}_1, \mathbf{r}'_1) &= \lim_{\lambda \rightarrow 0} \int d\mathbf{r}_2 d\mathbf{r}'_2 V_\lambda f_\lambda(\mathbf{r}_1 - \mathbf{r}_2) f_\lambda(\mathbf{r}'_1 - \mathbf{r}'_2) \\ &\quad \delta \left[\left(\frac{\mathbf{r}_1 + \mathbf{r}_2}{2} \right) - \left(\frac{\mathbf{r}'_1 + \mathbf{r}'_2}{2} \right) \right] \times \\ &\quad \left[\delta_{\alpha\beta} \sum_{\gamma,k} v_{\gamma k}(\mathbf{r}_1) v_{\gamma,k}^*(\mathbf{r}'_1) - \sum_k v_{\beta k}(\mathbf{r}_1) v_{\alpha k}^*(\mathbf{r}'_1) \right] \end{aligned} \quad (8.23)$$

$$\begin{aligned} &= 0 \times \delta(\mathbf{r}_1 - \mathbf{r}'_1) \times \\ &\quad \left[\delta_{\alpha\beta} \sum_{\gamma,k} v_{\gamma k}(\mathbf{r}_1) v_{\gamma,k}^*(\mathbf{r}'_1) - \sum_k v_{\beta k}(\mathbf{r}_1) v_{\alpha k}^*(\mathbf{r}'_1) \right] \end{aligned} \quad (8.24)$$

$$= 0. \quad (8.25)$$

This result shows that, at the mean-field level, the HF term of a dilute Fermi gas is identically zero. Assuming from the outset an FCI interaction potential of the form (8.1) would have led to the conclusion that the HF term should be proportional to the FCI potential itself.

In fact, this cannot be so, especially in the limit of unitarity, where the scattering length diverges, leading to a divergence of the would-be HF term. In usual mean-field treatments of this limit, the HF term is neglected without any apparent justification [2]. This derivation shows that this is indeed a correct choice.

The equation for the pairing function Δ .

The equation for the pairing function Δ defined in equation (8.15) is readily seen to be

$$\begin{aligned}\Delta_{\alpha\beta}(\mathbf{r}_1, \mathbf{r}'_1) &= - \int d\mathbf{r}_2 d\mathbf{r}'_2 V(\alpha\mathbf{r}_1, \beta\mathbf{r}'_1; \alpha\mathbf{r}_2, \beta\mathbf{r}'_2) \sum_k u_{\alpha k}(\mathbf{r}_2) v_{\beta k}^*(\mathbf{r}'_2) \\ &\equiv -V\mathcal{Q}\end{aligned}\quad (8.26)$$

where in the last equality we have formally written the double integral as a “matrix product” between the matrix elements of the pair potential and the function $\mathcal{Q} = \sum_k u_{\alpha k}(\mathbf{r}_2) v_{\beta k}^*(\mathbf{r}'_2)$. In the case of the FCI potential, the equation is plagued by a ultraviolet divergence.

Equation (8.26) can be rewritten using the Lippmann–Schwinger equation (2.35), so that the pairing function is determined by the normalised interaction (embodied in the T matrix) instead of the “bare” interaction described by the potential V [428].

The LS equation is given by $T = V + VG_0T$, where G_0 denotes the free-particle propagator. Rewriting the LS equation as $V = (1 - VG_0)T$, let us consider the quantity $\Delta - VG_0\Delta$. Using equation (8.26), we have the equalities

$$\Delta - VG_0\Delta = -V\mathcal{Q} - VG_0\Delta \quad (8.27)$$

$$= -V(\mathcal{Q} + G_0\Delta) \quad (8.28)$$

$$= -(1 - VG_0)T(\mathcal{Q} + G_0\Delta) \quad (8.29)$$

from which, assuming that $(1 - VG_0)$ is invertible, we get

$$\Delta = -T(\mathcal{Q} + G_0\Delta) \quad (8.30)$$

which is an equation for the pairing function involving the T matrix instead of the “bare potential” V . The solution of equation (8.30) has of course to be determined self-consistently with the solution of the BdG equations (8.18).

Introducing the indices α and β , denoting internal degrees of freedom of the atoms, Eq. (8.30) reads:

$$\begin{aligned}\Delta_{\alpha\beta, \mathbf{p}} &= - \int \frac{d\mathbf{p}'}{(2\pi)^3} T_{+; \alpha\beta, \alpha'\beta'}(E; \mathbf{p}, \mathbf{p}') \times \\ &\left(\sum_q u_{\alpha'q, \mathbf{p}'} v_{\beta'q, \mathbf{p}'}^* + \frac{1}{E - E_{\alpha'} - E_{\beta'} - \frac{p'^2}{m}} \Delta_{\alpha'\beta', \mathbf{p}'} \right).\end{aligned}\quad (8.31)$$

In the previous expression the value of the parameter E can be chosen arbitrarily and we have used this freedom to have a better convergence of the self-consistent solution.

Indeed, the T matrix is formally dependent on the value of the energy at which scattering takes place, as well as the directions of the momenta of the incoming and outgoing particles. In the limit of contact interaction, the T matrix tends to a constant value, proportional to the scattering length.

The use of the T matrix in the gap equation (8.30) enables one to go beyond the widely used contact-potential approximation, which is characterized by a constant value of T as a function of the wavevector.

Furthermore we suggest to define as effective range of the interaction the quantity r_0 appearing in the off-shell expansion of T at low energy:

$$\langle k | T(E=0) | k \rangle = \frac{4\pi a}{m} + \frac{2\pi |a| r_0^2}{m} k^2, \quad (8.32)$$

where m is the mass of the atoms and a the scattering length. We note that the usual definition of the potential range, r_1 , based on the on-shell expansion of the T matrix [190], is:

$$\left\langle k \left| T \left(E = \frac{\hbar^2 k^2}{2m} \right) \right| k \right\rangle = \frac{4\pi}{m} \left(\frac{1}{a} - ik - \frac{r_1 k^2}{2} \right)^{-1}, \quad (8.33)$$

As we will see below, the latter definition of the effective range implies a strong dependence on the applied magnetic field with possible divergences. At variance with this, using our definitions, Eq. 8.32, the quantity r_0 in the case of ${}^6\text{Li}$ and ${}^{40}\text{K}$ is almost constant and positive in the whole range of magnetic field covering the BEC–BCS crossover in both the narrow and wide resonances of this system [429], as we will show in this chapter. It is for this reason that we decided to use r_0 as an indication of the effective range of the interaction.

8.2 Numerical approach to the solution of the Bogoliubov–de Gennes equations

8.2.1 Calculation of the T matrix

Our numerical implementation begins with the calculation of the T matrix describing the scattering of alkali atoms as a function of the externally applied magnetic field. Due to the ultracold nature of the system investigated here, the most relevant scattering channels have zero orbital angular momentum (s -wave scattering). The fermionic nature of the interacting particles can then be taken into consideration by restricting oneself to the exterior product, defined as the antisymmetric combinations of products of single-particle hyperspin states. The exterior product of an n -dimensional Hilbert space with itself has dimensionality $[n(n-1)/2]$.

In the case of ${}^6\text{Li}$, which has nuclear spin $I = 1$ and electronic spin $S = 1/2$ the single-particle hyperspin space has dimension $n = 6$, and the exterior product space is 15-dimensional. In the case of ${}^{40}\text{K}$, having $I = 4$ and $S = 1/2$ one has $n = 18$ and the exterior product space is 153-dimensional. To reduce the computational cost, and without appreciable loss of accuracy, we further project all the operators onto the lowest-energy subspace of the exterior-product space, which is characterized by $(I + S)_z = 0$. We will denote the dimensionality of this space as d , where $d = 5$ for ${}^6\text{Li}$, $d = 2$ for ${}^{40}\text{K}$.

In order to calculate T , we rewrite Eq. (2.35) in the following way:

$$\begin{aligned} \hat{T} &= (E - \hat{H})\hat{G}(E)\hat{V} + \hat{V}\hat{G}(E)\hat{V} \\ &= (E - \hat{H} + \hat{V})\hat{G}(E)\hat{V} \\ &= (E - \hat{H}_0)\hat{G}(E)\hat{V}, \end{aligned} \quad (8.34)$$

and the calculation of $G(E)$ (that is, the inversion of the operator $(E - \hat{H} + i\varepsilon)$) is conveniently performed in the relative-coordinate representation, introducing a suitable discretization interval δr for the radial coordinate, up to a cutoff distance $R_{\text{cut}} = \delta r \times N$, where N is the number of discretization points. We assume that the r -dependent part of the pair potential is negligible for $r > R_{\text{cut}}$.

Considering the reduced wavefunctions $\chi(r) = r\psi(r)$, the kinetic energy \hat{K} becomes a tridiagonal operator, and the potential energy matrix is made by $d \times d$ blocks along the main diagonal, one such block for each value of δr .

In this case, one should formally invert an infinite square matrix (due to the fact that the coordinate r is unbounded). However, as we will now show, this is not necessary, and we present an algorithm that provides directly the first $Nd \times Nd$ block of the (infinite) inverse matrix. With these definitions, we can represent the operator $E - \hat{H}$ with an infinite matrix in the form:

$$E - \hat{K} - \hat{V} = \begin{pmatrix} \mathbf{A} & \mathbf{B} \\ {}^t\mathbf{B} & \mathbf{C} \end{pmatrix}, \quad (8.35)$$

where \mathbf{A} is a $Nd \times Nd$ matrix. \mathbf{C} is an infinite tridiagonal matrix corresponding to the region where the r -dependent part of V is neglected (beyond the cutoff distance). It can be written recursively as

$$\mathbf{C} = \begin{pmatrix} \mathbf{c} & \mathbf{a} \\ {}^t\mathbf{a} & \mathbf{C} \end{pmatrix} \quad (8.36)$$

where \mathbf{a} is a $d \times \infty$ matrix whose first $d \times d$ block is the identity matrix multiplied by $\alpha = \hbar^2/(2\mu \delta r^2)$, where $\mu = m/2$ is the reduced mass of the atom pair. The $(d \times d)$ -matrix \mathbf{c} is diagonal with entries $(E - 2\alpha - E_k)$ ($k = 1, \dots, d$), where E_k are the eigenvalues of the r -independent sum of the hyperfine and magnetic interactions, $\hat{V}_{\text{hf}} + \hat{V}_{\text{B}}$.

Finally, \mathbf{B} is a $Nd \times \infty$ matrix whose only non-zero element is the lower left $d \times d$ block, having α along the diagonal.

The inverse of a matrix in the form (8.35) can be formally written as:

$$\hat{G}(E) = \begin{pmatrix} \mathbf{X} & -\mathbf{A}^{-1}\mathbf{B}\mathbf{Y} \\ -\mathbf{C}^{-1} {}^t\mathbf{B}\mathbf{X} & \mathbf{Y} \end{pmatrix} \quad (8.37)$$

$$\mathbf{X} = (\mathbf{A} - \mathbf{B}\mathbf{C}^{-1} {}^t\mathbf{B})^{-1} \quad (8.38)$$

$$\mathbf{Y} = (\mathbf{C} - {}^t\mathbf{B}\mathbf{A}^{-1}\mathbf{B})^{-1} \quad (8.39)$$

and we are interested in the first $Nd \times Nd$ block of $\hat{G}(E)$, identified in Eq. (8.37) by the matrix \mathbf{X} .

In order to calculate \mathbf{X} , we first notice that

$$\mathbf{B}\mathbf{C}^{-1} {}^t\mathbf{B} = \begin{pmatrix} 0 & \cdots & 0 \\ \vdots & \ddots & \vdots \\ 0 & \cdots & \alpha\mathbf{C}^{-1}_{(d \times d)}\alpha \end{pmatrix}, \quad (8.40)$$

where $\mathbf{C}^{-1}_{(d \times d)}$ is the first $d \times d$ block of the \mathbf{C}^{-1} matrix. This is the only ingredient required to calculate \mathbf{X} by direct inversion of the $Nd \times Nd$ matrix $\mathbf{A} - \mathbf{B}\mathbf{C}^{-1} {}^t\mathbf{B}$, as shown in Eq. (8.38). The matrix $\mathbf{C}^{-1}_{(d \times d)}$ can be calculated by noticing that one can formally write the inverse in a manner analogous to Eq. (8.37), that is:

$$\mathbf{C}^{-1} = \begin{pmatrix} \mathbf{x} & -\mathbf{c}^{-1}\mathbf{a}\mathbf{x} \\ -\mathbf{C}^{-1} {}^t\mathbf{a}\mathbf{y} & \mathbf{y} \end{pmatrix} \quad (8.41)$$

$$\mathbf{x} = (\mathbf{c} - \mathbf{a}\mathbf{C}^{-1} {}^t\mathbf{a})^{-1} \quad (8.42)$$

$$\mathbf{y} = (\mathbf{C} - {}^t\mathbf{a}\mathbf{c}^{-1}\mathbf{a})^{-1} \quad (8.43)$$

Taking the first $d \times d$ block of the left and right hand side of Eq. (8.43) gives

$$\mathbf{C}^{-1}_{(d \times d)} = \left(\mathbf{c} + \alpha^2\mathbf{C}^{-1}_{(d \times d)} \right)^{-1} \quad (8.44)$$

from which we conclude that, since \mathbf{c} is diagonal, $\mathbf{C}_{(d \times d)}^{-1}$ must be diagonal. Its diagonal entries x_k ($k = 1, \dots, d$) satisfy the equations:

$$x_k = \frac{1}{(\Delta E_k - 2\alpha) + \alpha^2 x_k} \quad (8.45)$$

where $\Delta E_k = E - E_k$, and whose solutions are

$$x_k = \frac{\Delta E_k - 2\alpha \pm \sqrt{\Delta E_k(\Delta E_k - 2\alpha)}}{2\alpha^2}. \quad (8.46)$$

Notice that x_k is real for $\Delta E_k \leq 0$, is complex for $0 < \Delta E_k < 2\alpha$, and real again from $\Delta E_k \geq 2\alpha$. These two possible solutions for the resolvent correspond to the possible solutions of the scattering problem in the finite space. For $\Delta E_k \leq 0$ we have one scattering solution which decays exponentially at long distances (beyond the cutoff R_{cut}) and one unphysical solution with exponential growth in the same region. For $0 < \Delta E_k < 2\alpha$ the two solutions correspond to considering the scattering matrices \hat{T}^+ and \hat{T}^- . The remaining energy range ($\Delta E_k \geq 2\alpha$) is unphysical from the point of view of the original scattering problem, because one would have energies larger than those available in the discretized lattice.

8.2.2 Achieving self-consistency in the Bogoliubov–de Gennes equations

After the calculation of the matrix \mathbf{X} , we can use Eq. (8.34) to calculate the matrix elements of $\langle \mathbf{k}|T|\mathbf{k}' \rangle$ which are needed in the gap equation (8.31).

From a numerical point of view, one needs only a finite number of elements of \mathbf{X} in Eq. (8.37), that is those related to the wavevectors used to perform the integral in Eq. (8.31). Therefore, one might use the efficient LAPACK [437] routines to perform an LU factorization of \mathbf{X} and evaluate the matrix elements of T from this decomposition.¹ We found that calculating 200 points in reciprocal space was enough to reach convergence.

At this point we can use Eqs. (8.32) and (8.33) to calculate the values of the effective range of the potential.

The matrix elements of T are finally used in the self-consistent gap equation (8.31), which we solve in the subspace $\alpha = \alpha'$ corresponding to the lowest-energy open channel only, and for various values of the density (linked to the Fermi momentum k_F).

In summary, our numerical approach proceeds according to the following procedure:

Initialization

- Generate elements of the exterior-product space
- Create the projections on the $F_z = 0$ subspace
- Load the potentials for the spin-singlet and triplet

Loop over the values of the B field

- Calculate the T -matrix elements using Eq. (8.34)
 - Calculate $G(E) = (E - \mathbf{H} + \mathbf{R})^{-1}$ and add the reaction
 - LU factorization of $G(E)$
 - calculate $G(E)V|k \rangle$

¹The LU factorization is performed with the `zgbtrf` routine, whereas the calculation of the matrix element of the inverse is obtained by a subsequent call to the `zgbtrs` routine.

```

    multiply the result by  $\langle k|(E - H_0)$ 
  Calculate  $a$ ,  $r_0$ , and  $r_1$ 
Loop over the values of  $\mu$ 
    Solve the self-consistent BdG equation
    Calculate  $\mu$  and  $\Delta$ 
end loop
end loop

```

This logic flow is sketched in Fig.8.3. A Python/FORTRAN program implementing this theory is made available at <http://software-lisc.fbk.eu/>.

8.3 Ab-initio calculation of the multichannel T -matrix

We have used equations (8.30) and (8.18), to calculate – at the mean-field level – the density dependence of various quantities characterising an ultracold Fermi gas in the unitary regime, such as the pairing function Δ , the chemical potential μ and the transition temperature T_c [423, 422]. The dependence of these quantities on the effective range r_e at unitarity is the hallmark of non-universal behaviour of quantum gases.

The T -matrix elements appearing in Eq. (8.31) have been computed by means of multichannel scattering theory [439]. To perform this calculation we have included relativistic terms (of the order of 2×10^{-6} a.u.), which mix the singlet and triplet states, and we have multiplied each of the *ab-initio* curves of the potential by a single parameter fixed to reproduce the values of the Feshbach resonances.

Since the open and closed channels are coupled via the hyperfine interaction, the problem is very complex if one takes into account the full on-shell multichannel T -matrix in the gap equation (8.31). Therefore, while the calculation of $T_+(0)$ has been performed in the multichannel space, we projected the T -matrix on the lowest hyperspin-doublet open channel to solve the BdG gap equation. This assumption is less drastic than using the interaction potential projected onto the open channel. In fact, the projected multichannel $T_+(0)$ matrix retains short range interactions with the closed channels and this is the reason why we prefer to use $T_+(0)$ rather than V in the self-consistent equation (8.31).

The on-shell $T_+(0)$ is represented over 10^5 equally spaced grid points, while a grid of 200×200 k -points according to a Gauss–Chebyshev quadrature over the interval $[0,1]$ has been used in the momentum space, to obtain a convergence below 10^{-5} a.u.

Our methodology provides directly the values of the relevant quantities characterizing an ultra-cold Fermi gas – such as the gap, the chemical potential or the transition temperature – as a function of the effective range r_0 . Their behavior is discussed in the following section.

8.4 Finite-range effects in the unitary limit for ${}^6\text{Li}$

The results are reported in figure (8.4) and expressed as a function of the product of the Fermi momentum k_F and r_0 . First of all we notice that our results in the low-density unitary regime compare very well with analogous calculations reported in the literature, and using a different renormalisation scheme to overcome the divergence of the scattering length.

The value that we obtain for the pairing gap is $\Delta_{\text{BdG}}/E_F = 0.69$, which is in very good agreement with the result obtained by Randeria [428]. The same level of agreement is found

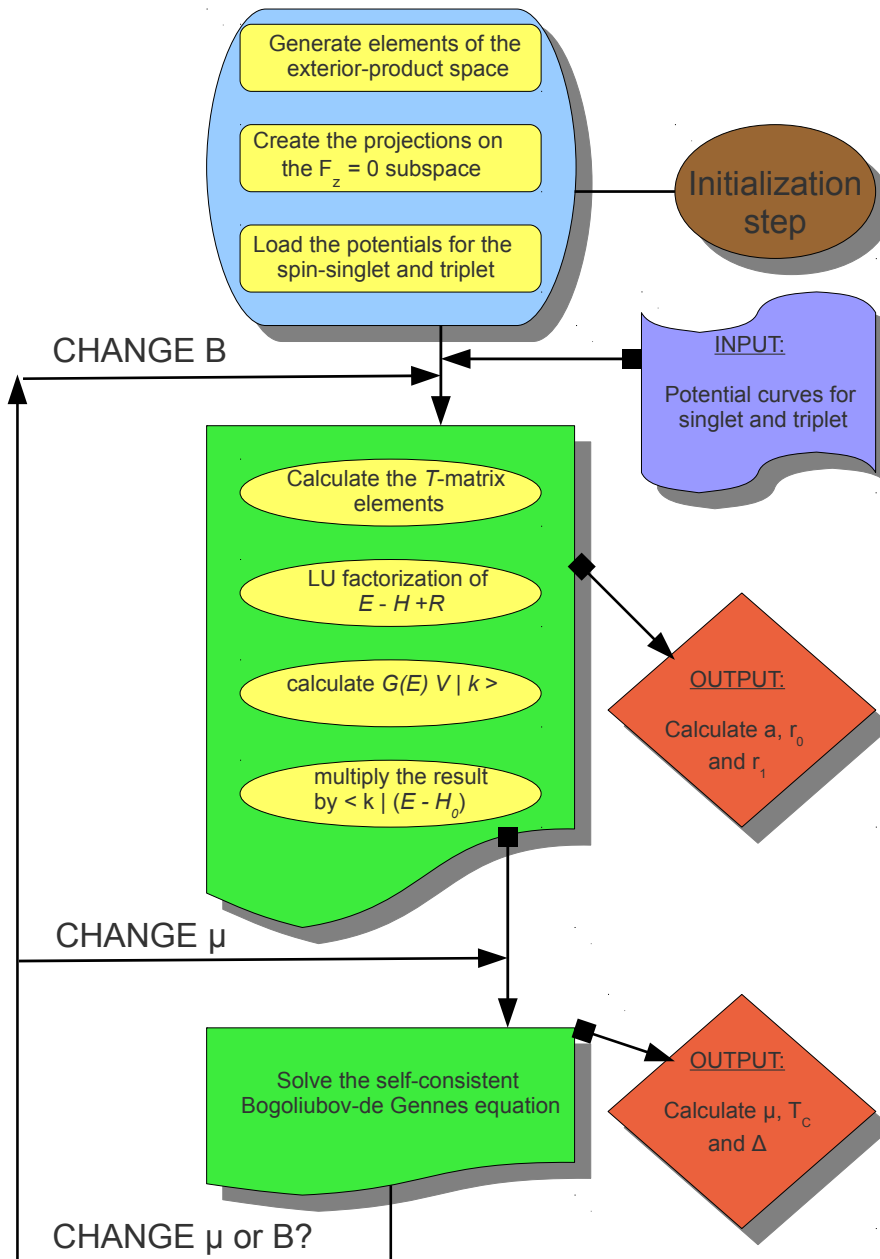


FIGURE 8.3: Flowchart for the solution of the Bogoliubov–de Gennes gap equation (8.31).

for the value of the chemical potential at unitarity, where our value $\mu_{\text{BdG}}/E_{\text{F}} = 0.6$ is the same as the one reported in the literature [440]. Finally, the value that we found for the critical temperature, $T_{\text{BdG}}/T_{\text{F}} = 0.49$, is also in good agreement with previous calculations at the same level of theory [441].

However, the mean-field approach only provides approximate values for these important quantities. More precise and almost exact results have been obtained using Monte Carlo (MC) calculations, which explicitly include two-body correlation effects. The MC value for the pairing gap of a dilute gas at unitarity is $\Delta_{\text{MC}}/E_{\text{F}} = 0.45$ [442], the chemical potential is $\mu_{\text{MC}}/E_{\text{F}} = 0.42$ [443, 444], and the transition temperature turns out to be $T_{\text{MC}}/T_{\text{F}} = 0.16$ [445].

Our methodology, based on multichannel scattering theory, allows us to investigate the behaviour of the aforementioned quantities as a function of the density, that is to investigate deviation from universality in the unitary regime. Figure 8.4 reports the value of the pairing gap, the chemical potential and the critical temperature as a function of the density, as measured by the adimensional quantity $k_{\text{F}}r_0$. We observe that the pairing gap is a decreasing function of the density, whereas the chemical potential is an increasing function. According to these mean-field calculations, the effect of a finite interaction range (or, equivalently, an increased density) is to reduce the tendency of the system to form pairs. As a consequence the chemical potential increases, tending to the value corresponding to the normal phase of the system.

Note that our theory predicts the same transition temperature at unitarity for both resonances, and it deviates up to 30 % of the corresponding FCI value by increasing the density of the system.

Our results show a significant density dependence for Δ , μ and T_c , in contrast with the predictions obtained using FCI for which a constant value is obtained for all these quantities. We estimate that the largest density that we have investigated (corresponding to $k_{\text{F}}r_0 = 0.6$) is about one order of magnitude larger than that achievable in modern harmonic traps [446]. Nevertheless, this value is likely reachable by experimental apparatus in a nearest future. At this high density, one might expect that three-body recombination could lead significant atom losses. However, we estimate that at equilibrium and for near threshold conditions 3-body recombination will play a little role even at such increased density regime, since the kinetic energy gain in the recombination process (10^{-17} a.u.) is very small compared to the Fermi energy (8×10^{-8} a.u.) [447].

The values that we obtain and their dependence on $k_{\text{F}}r_0$ are in very good agreement with results already presented in the literature, and that have been obtained with different methodologies. Calculations performed using quantum field theory also predicts a decreasing critical temperature for increasing potential range [423]. An approach based on non-local BCS equations with a finite size potential shows that the pairing gap is a decreasing function of the density [422], which agrees with our results.

In Fig. 8.5 we also plot the values of the potential radii obtained according to the standard definition of Eq. (8.33) (r_1), and with our definition reported in Eq. (8.32) (r_0). We notice that the potential radius defined in Eq. (8.32) is almost constant as a function of the externally applied magnetic field, with a value $r_0 \sim 26.6 a_0$ for both resonances, where a_0 is the Bohr radius. On the contrary, the standard definition of Eq. (8.33) results in values of the potential range which vary considerably in the physically accessible region of external fields. Moreover, r_1 turns out to be negative (-600 a.u) for some values of B .

The dependence on the resonance position and the large negative value in the narrow

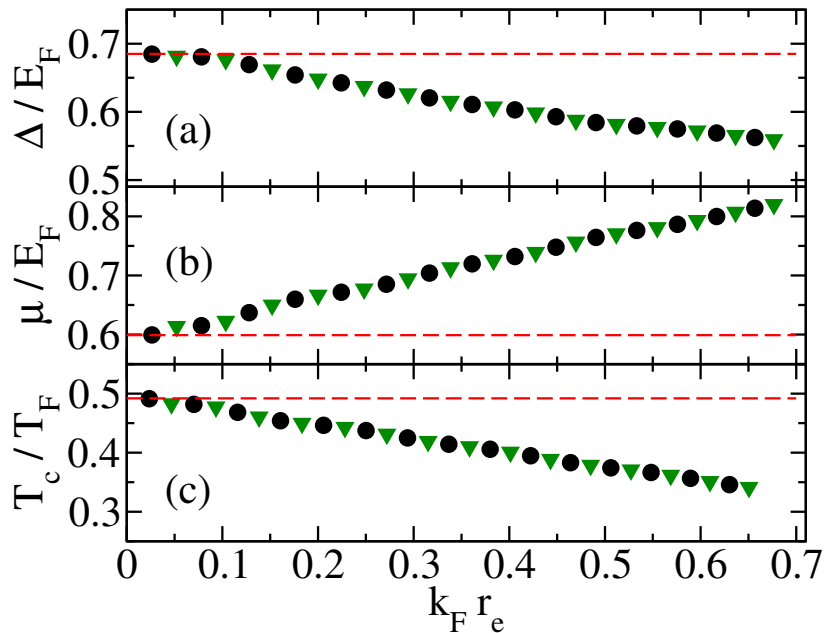


FIGURE 8.4: Plot of the pairing function Δ (a), the chemical potential μ (b) and the phase transition temperature T_c (c) for an ultracold Fermi gas of ${}^6\text{Li}$ atoms at unitarity as a function of the Fermi momentum k_F times the effective range r_0 , defined in equation (8.32). Dots and triangles refer to the narrow and broad resonances, respectively. The dashed horizontal lines report the same quantities calculated using the FCI potential.

resonance rule out, in our opinion, r_1 as a measure of the effective range of the screened potential at unitarity. By using Eq. (8.32) as a definition of the effective radius, we obtain very close values for the narrow and broad resonances, with a difference of less than 0.02 %. We consider this result as a further indication that the definition of the effective range based on the small-momentum expansion of the T -matrix is reasonable and gives consistent results.

8.5 Finite-range effects along the BEC–BCS crossover for ${}^{40}\text{K}$

Out of the unitary conditions, the solution of the Bogoliubov–de Gennes equations for fermions interacting via contact potential depends on the quantity $x = (k_F a)^{-1}$ which can be tuned by changing the magnetic field [2].

When $x < 0$ the system is in the BCS state, characterized by correlated, loosely-bound dimers, whereas for $x > 0$ tightly-bound dimers are formed, undergoing Bose–Einstein condensation (BEC regime).

The behaviour of the chemical potential μ and the gap function Δ in the case of pure contact interaction for a gas of ${}^{40}\text{K}$ atoms is reported in Fig. 8.6. The chemical potential is a decreasing function of x which is positive in the BCS and unitary regime, and becomes

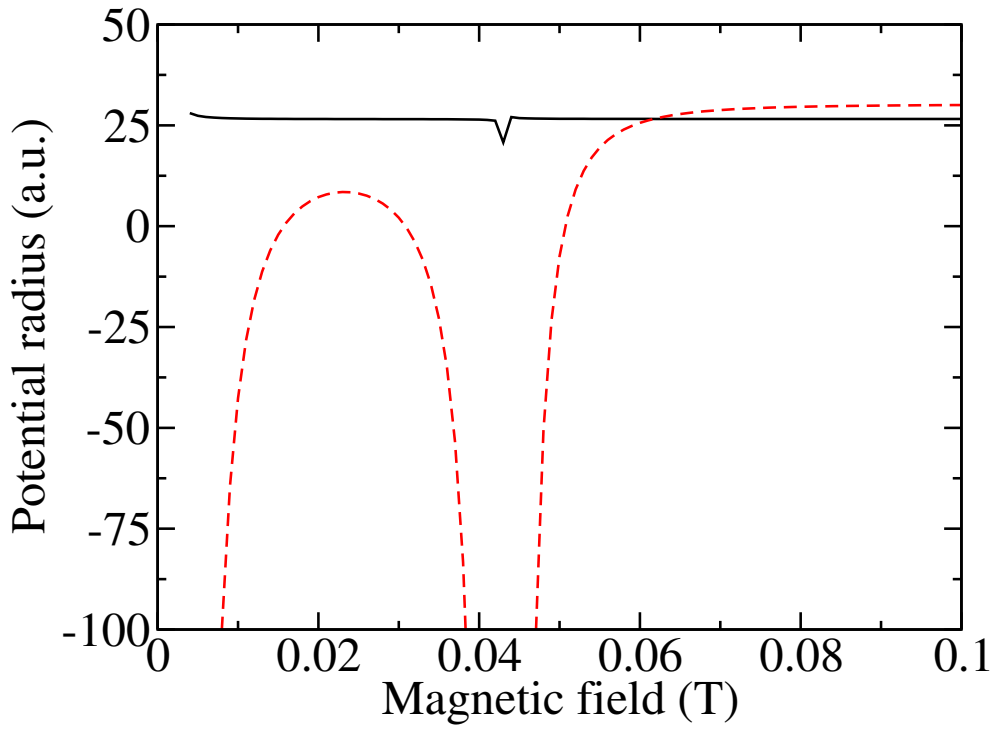


FIGURE 8.5: Potential radius r_1 defined in Eq. (8.33) (dashed line) and the potential radius r_0 defined in Eq. (8.32) (solid line) as a function of the applied magnetic field for a gas of ${}^6\text{Li}$ atoms.

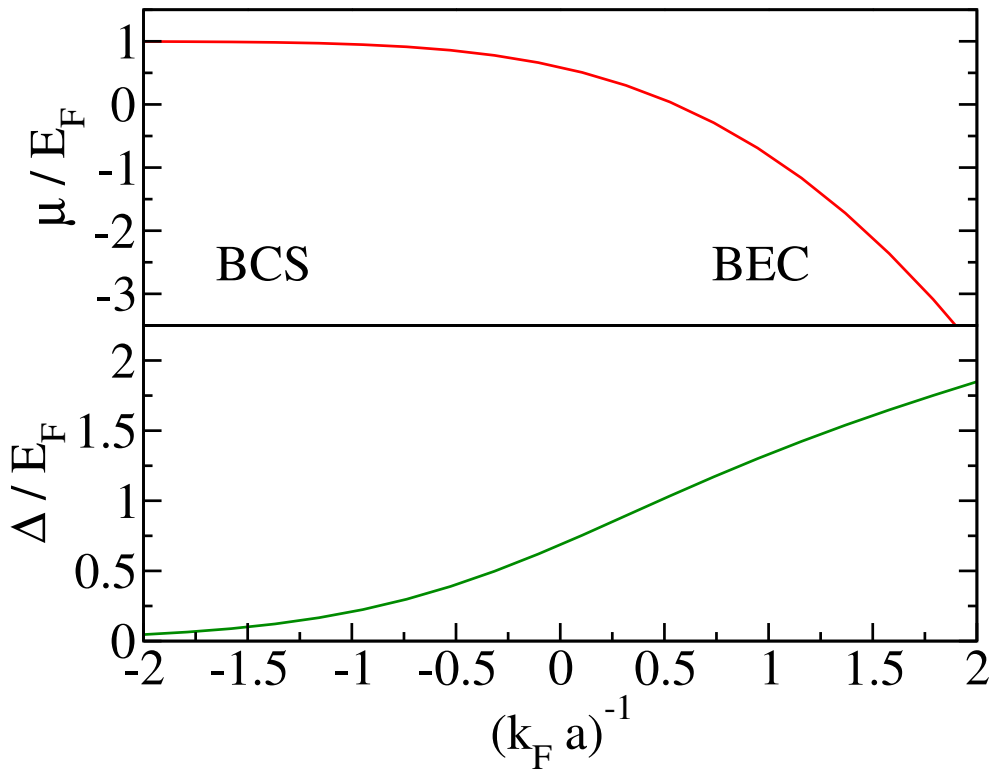


FIGURE 8.6: Value of the chemical potential (top) and the gap function (bottom) for the Bogoliubov–de Gennes solution of a gas of atoms interacting with contact interaction.

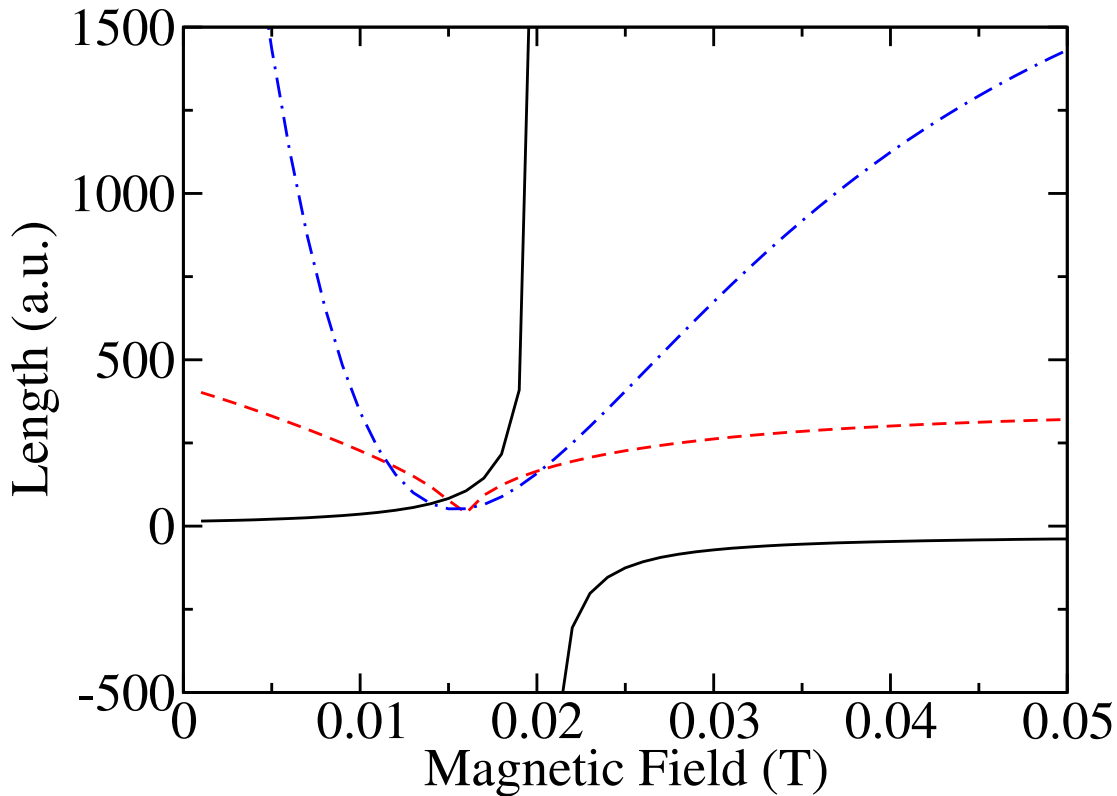


FIGURE 8.7: Value of the scattering length (thick line), of the effective range r_0 from Eq. (8.32) (dashed line) and of the effective range r_1 from Eq. (8.33) (dot-dashed line) for two interacting ^{40}K atoms.

negative in the BEC region crossing zero at the value $x_0 = 0.5531$. On the other hand, the gap function is very small in the BCS regime, and increases steadily as a function of x .

Figure 8.6 shows that the principal features characterizing the BCS and BEC regimes are already attained for $x = -1$ and $x = 1$, respectively. Thus, in our investigations, we will focus on these two values of $(k_F a)^{-1}$.

Similarly to what has been done in the case of the unitary regime for ^6Li , we will calculate the dependence of the chemical potential and the gap as a function of $k_F r_0$ in the BCS and BEC case for ^{40}K .

8.5.1 The case of ^{40}K

As a second test case, we apply the theoretical and computational method developed above to an interacting ^{40}K ultracold Fermi gas and we compare the results with those obtained for ^6Li .

We report in Fig. 8.7 the values of the scattering length a and the two effective ranges r_0 and r_1 – defined in Eqs. (8.32) and (8.33) respectively – for the case of ^{40}K . The Feshbach resonance in this system is found at $B = 0.02021$ T.

From Fig. 8.7 we observe that the B-field dependence of r_0 is stronger in the case of ^{40}K than in the case of ^6Li [429] and, secondly, that – independently on the definition used – the effective ranges r_0 (see Eq. (8.32)) and r_1 (see Eq. (8.33)) have a minimum for $B_0 = 0.016$ T.

The dependence of μ/E_F and Δ/E_F on $k_F r_0$ in the BCS regime is reported in Fig. 8.8

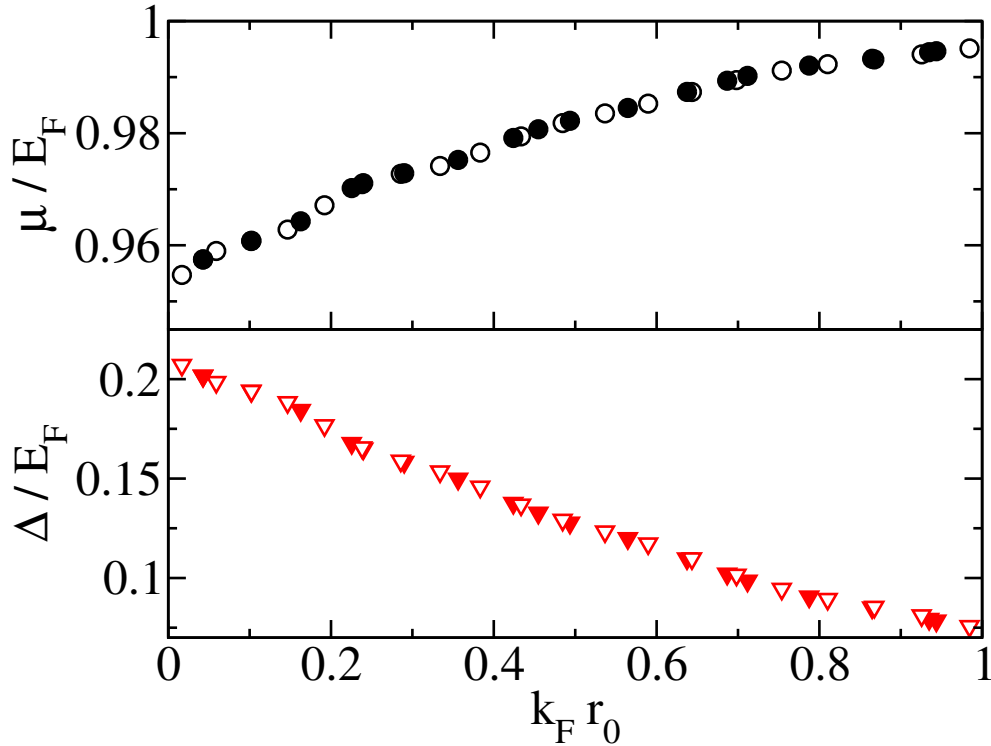


FIGURE 8.8: The dependence of the chemical potential (upper panel) and the gap function (lower panel) on the density for an ultracold gas of ^{40}K in the BCS regime ($k_{\text{F}}a = -1$).

for both ^{40}K and ^6Li . This plot has been obtained by progressively increasing the value of the Fermi momentum k_{F} , that is, the density of the system. For each value of k_{F} we found the value of the magnetic field fulfilling the condition $k_{\text{F}}a(B) = -1$, from which we calculated r_0 (cfr. Fig. 8.7). In the case of ^6Li we found it more convenient to work around the narrow Feshbach resonance.

The behaviour of the curves reported in Fig. 8.8 is very similar to the one observed in the unitary regime: [430] when the density is increased, the chemical potential increases and the gap function decreases. This result is in agreement with the outcome of a quantum field-theory based model in the same regime [423].

The similarity between the BCS and unitary regime is not completely unexpected, in the light of the fact that in both cases one has positive chemical potential, meaning that the gas is formed by loosely bound, yet strongly correlated dimers.

Finally, we notice that the density dependence of μ and Δ on the density as measured by the parameter $k_{\text{F}}r_0$ is the same for both ^{40}K and ^6Li , despite the very different interaction potentials used to perform the two calculations, as well as the different values of the r_0 parameter in the two systems. In the case of ^6Li we found a remarkably constant value of $r_0 \sim 26$ a.u. for any value of B [429], whereas in the case of ^{40}K we found r_0 to span the range 170 – 240 a.u. This result confirms the usefulness of the parameter r_0 in describing the contribution of the effective potential range to various gas properties.

A very similar picture is observed in the BEC regime, at the point characterized by $k_{\text{F}}a = 1$. Even in this case the dependence of the chemical potential and the gap on the parameter $k_{\text{F}}r_0$ is the same for both ^{40}K and ^6Li . Interestingly, we find that the r_1 parameter for ^6Li in this regime is very large and negative, spanning a considerably

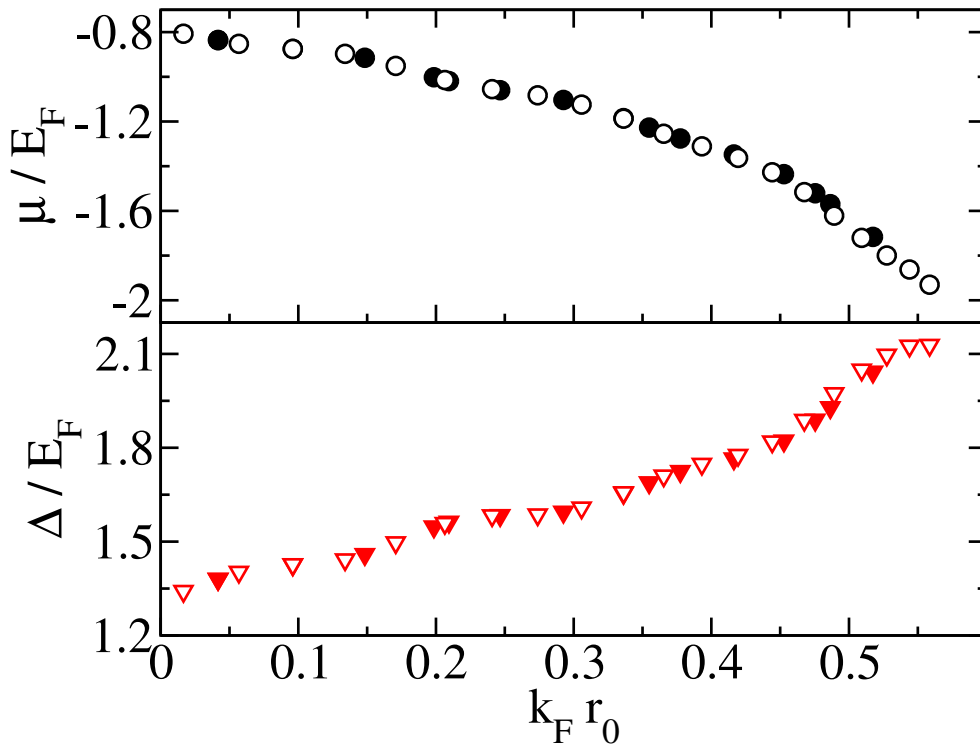


FIGURE 8.9: The dependence of the chemical potential (upper panel) and the gap function (lower panel) on the density for an ultracold gas of ^{40}K in the BEC regime ($k_{\text{F}}a = 1$).

large range from -22500 to -6500 a.u., in contrast to the almost constant behaviour of r_0 . [429] This observation further supports the validity of our suggestion to use r_0 as a useful indicator of the importance of finite-range effects in a dilute ultracold Fermi gas.

Differently to what has been observed in the case of the BCS case, we found that in the BEC regime μ and Δ decrease and increase from their contact-potential value, respectively, as a function of $k_{\text{F}}r_0$.

However, in both regimes, the chemical potential and the gap function have opposite trends as a function of $k_{\text{F}}r_0$: when the one of the quantities increases (decreases), the other decreases (increases). This “anticorrelated” behaviour between μ and Δ is also apparent in the case of pure contact potential, as is evident from the inspection of Fig. 8.6.

The origin of this opposite trend can be traced back to the physical meaning of both quantities: the gap function measures the energy required to break a correlated pair, whereas the chemical potential measures the change in the system’s energy when another particle is added. Since a newly added particle will develop strong correlations with all the others in both the BEC and BCS regimes it is clear that a stronger pairing (as measured by Δ) will be correlated with a higher energy gain upon insertion and a lower chemical potential (μ).

8.6 Conclusions

To summarize, we have proposed a new definition of contact potential based on the off-shell T -matrix radius at zero energy. This analysis underpins a short range, rather than a δ -like, model of the screened fermion-fermion interaction and rules out the scattering length and

the usually defined effective radius as relevant parameters to describe dilute quantum gases at unitarity and at the BEC-BCS cross-over regime. Furthermore, we have shown the ability of our approach to cancel out naturally the divergences arising with the use of the contact potential. Finally, the application of this new theoretical approach to the self-consistent solution of the BdG equations for ultracold ${}^6\text{Li}$ and ${}^{40}\text{K}$ homogeneous gases across the BEC-BCS cross-over has been discussed. Despite the significant differences in the interaction pair potential for the two systems, we found that the deviations of the chemical potential and the gap from the contact-potential approximation were almost indistinguishable in the two systems, confirming the usefulness of r_0 .

Chapter 9

Theoretical Estimates of Stellar e^- Captures. The half-life of ${}^7\text{Be}$ in Evolved Stars

The enrichment of Li in the Universe is still unexplained, presenting various puzzles to astrophysics. One open issue is that of obtaining reliable estimates for the rate of e^- -captures on ${}^7\text{Be}$, for T and ρ conditions different from the solar ones. This is of crucial importance to model the Galactic nucleosynthesis of Li. In this framework, we present here a new theoretical method for calculating the e^- -capture rate in conditions typical of evolved stars. Furthermore, we show how our approach compares with state-of-the-art techniques for solar conditions, where various estimates are available. Our computations include: i) “traditional” calculations of the electronic density at the nucleus, to which the e^- -capture rate for ${}^7\text{Be}$ is proportional, for different theoretical approaches including the Thomas–Fermi, Poisson–Boltzmann and Debye–Hückel (DH) models of screening, ii) a new computation, based on a formalism that goes beyond the previous ones, adopting a mean-field “adiabatic” approximation to the scattering process. The results obtained with the traditional as well as with the new approach and their differences are discussed in some detail, starting from solar conditions, where our approach and the DH model essentially converge to the same solution. We then analyze the applicability of both our method and the DH model to a rather broad range of T and ρ values, embracing those typical of red giant stars, where both bound and continuum states contribute to the capture. We find that, over a wide region of the parameter space explored, the DH approximation does not really stand, so that the more general method we suggest should be preferred. As a first application, we briefly reanalyze the ${}^7\text{Li}$ abundances in RGB and AGB stars of the Galactic Disk in the light of a revision in the Be-decay only; we however underline that the changes we find in the electron density at the nucleus would induce effects also on the electron screening (for p -captures on Li itself, as well as for other nuclei) so that our new approach might have rather wide astrophysical consequences.

9.1 Introduction

Serious problems affect our understanding of the Li evolution in the Galaxy. Big Bang Nucleosynthesis (BBN) [448] predicts a Li abundance higher than observed in extremely

metal-poor objects [449] and in low-metallicity Main Sequence (MS) stars [450]. On the other hand, in the present interstellar medium (ISM) the ${}^7\text{Li}$ abundance is higher even than that expected by BBN [451]. As Galactic Cosmic Rays do not produce much ${}^7\text{Li}$ [452, 453] we should rely on stellar nucleosynthesis for explaining this increase.

${}^7\text{Li}$ is however a very fragile nucleus, so that its photospheric concentration in stars is easily destroyed when convective processes can carry it to moderately high temperatures (a few millions K), where it undergoes proton captures [454]. Special conditions are therefore required for Li production, which are limited to a few astrophysical scenarios. These mainly include novae and intermediate mass stars (IMS) undergoing H burning at the base of their envelope through the so-called Hot Bottom Burning process [455]. In current stellar models for low mass star (LMS: those with masses below about $2 - 3 M_{\odot}$) Li is instead predicted to be destroyed already in the early phases of evolution, preceding the MS [456, 457]. In stars of mass lower than solar, whose convective envelopes remain large even during the MS, Li destruction continues in this stage; for higher masses, instead, it is predicted that external convection shrinks and does not include any more zones hot enough to affect Li. Contrary to these model expectations, observations of the Sun and of solar-like stars reveal that they undergo extensive Li-depleting processes during central hydrogen burning. One of the consequences is that the solar photosphere is about 100 times less Li-rich than meteorites [458]. Li-destruction processes are known to occur also at intermediate effective temperatures, in MS stars of the Galactic disc, generating the so-called *Li-dip* [459, 460, 461].

The above phenomena, unexpected from canonical stellar models, have been interpreted (sometimes only qualitatively) in terms of mixing episodes of a nature different from pure convection [462, 463], often attributed to rotationally-induced effects [464], atomic diffusion, or magnetic dynamo processes [465], like those observed in active stars [466]. However, the very large Li destruction in the Sun and in other main sequence stars is still not accounted for in detail, being too small in the models. In more advanced stages, i.e. along the Red Giant Branch (hereafter RGB) and along the Asymptotic Giant Branch (hereafter AGB) similar phenomena must be active [467, 468], perhaps again related to magnetic effects [469, 470, 471]. The consequence is that, in most evolved stars, Li is further depleted as compared to MS stages [472].

At odds with our need for finding sites where Li is produced in stars, only few red giants ($\sim 2\%$) show Li enhancement at their photosphere [473, 474, 475, 476, 477]. Their abundances might in principle be produced by coupled mixing and nucleosynthesis episodes, in which the depletion of Li by downward diffusion is over-compensated by an upward transport of ${}^7\text{Be}$ from burning regions, at a fast enough pace that it survives destruction by p and e^- captures, reaches the stellar envelope and finally decays there, reproducing Li. The situation is however far from being clear [464, 472]. Quantitative modeling is in particular hampered by a poor knowledge of how the rate of Be decay changes in the rapidly varying conditions below the envelopes of red giants. In fact, extrapolations of this rate from the works done for the Sun [478, 479, 480] are extremely insecure, due the ambient conditions of H burning in evolved stars, which are very different from solar. Indeed, in the layers above the H-burning shell of a red giant the temperature (T) spans a range from 70-80 MK down to a few MK, while the density (ρ) is lower than in the solar center from one to five orders of magnitudes.

In general, the pioneering works of the sixties for the Sun were performed considering the ionization degree of Be through the Saha equation, and including the contribution of

free electrons on the assumption that inside a Debye radius around a Be nucleus they behave as a Maxwellian gas, thus following a treatment of the Coulomb screening in the plasma originally due to Debye and Hückel [481]. Although more recent and general approaches do exist [482, 483, 484] sometimes demonstrating the limits of the Debye–Hückel (hereafter DH) approximation [485], they maintain a treatment similar to the Born-Oppenheimer approach, where the electronic response is considered to be much faster than the ionic one. These works almost invariably find for the Sun results very similar to those of the classical studies cited above, but they do not consider the physical conditions prevailing in evolved stars.

It has to be further noted that, at the high temperatures of shell H-burning in red giants, recombination might occur in states that are highly excited and very close to each other. In such conditions, the Born-Oppenheimer approach is questionable; moreover, the conditions for the classical DH approximation often do not actually hold (see next sections) and one does not know whether this introduces small or large deviations in the capture rate.

We decided therefore to explore the problem of e^- captures on ${}^7\text{Be}$ for the typical T and ρ values of H-burning layers in evolved stars, both following the traditional DH approach and introducing a new treatment, in which the assumption that electrons follow a Maxwell-Boltzmann energy distribution is relaxed (considering them, more generally, as a Fermi gas) and in which a mean-field adiabatic approximation to the scattering process is used. The primary scope is to provide the missing weak-interaction input data for Li nucleosynthesis calculations, clarifying whether such data can be deduced in the traditional way or not. Subsequently, we also plan to apply our results to a re-evaluation of the problem of electron screening in stellar plasmas (see some comments on that issue in sections 3.1 and 5).

We remind that other cases exist, involving nuclei heavier than Li, in which the predictions of nucleosynthesis are still unreliable for the lack of knowledge about the dependence of electron captures on the ambient conditions, during the transport of newly produced nuclei to the stellar surface. Crucial isotopes subject to these uncertainties are, e.g., ${}^{41}\text{Ca}$ and ${}^{205}\text{Pb}$, which are important clocks for dating the latest nucleosynthesis processes before the contraction of the Solar Nebula [486, 487]. If one considers also β decays, then it turns out that several reaction branchings along the s -process path are still affected by our poor knowledge of weak interactions in stars, in contrast with the high accuracy of the competing neutron-capture processes.

In general, a better knowledge of radioactive decays would be relevant for a large number of physical problems, well beyond the borders of stellar astrophysics. Accurate decay rates are e.g. of paramount importance in Earth and Planetary sciences, in order to date geological and astronomical processes by estimating the amount of a given long-lived species remaining in a sample (a rock or a stellar photosphere). Furthermore, nuclear decay provides an impressive source of heat in any planetary body, including the Earth. It is believed that as much as half the heat measured at the Earth surface, corresponding to approximately 21 TW, be due to radioactive processes involving ${}^{40}\text{K}$, ${}^{232}\text{Th}$, ${}^{235}\text{U}$ and ${}^{238}\text{U}$, occurring both in the crust and in the core [488, 489, 490]. Heating from shorter-lived radioactivities like ${}^{26}\text{Al}$ is then believed to provide the energy for melting and differentiating the early solid bodies around the Sun [487].

9.2 The electron captures on ${}^7\text{Be}$: state-of-the-art.

The driving force responsible for the electron capture decay is the weak nuclear interaction, a process of very short range that was therefore long believed to be insensitive to extra-nuclear factors, notably the chemical environment, the ionization degree, the pressure and temperature conditions. Contrary to this simple view, many authors reported evidence of changes in nuclear decay rates with temperature [491, 492], pressure [490], and the chemical environment [493, 494, 495], which are believed to be connected to the modification of the electron density at the nucleus, $\rho_e(0)$, induced by the change of these parameters. The rate indeed depends on the s-type atomic-orbital wavefunctions, the only ones with finite density at the nucleus. Therefore, factors affecting this density can appreciably modify the decay rate. Besides T and ρ values, also the pressure, the level of ionization, and the presence of other charged particles, screening the interaction, might in principle be of relevance. On the other side, *ab-initio* calculations of the radioactive decay rate at room temperature for ${}^7\text{Be}$ (and several other isotopes) performed by [490] showed a very small dependence (within $\sim 0.1 - 0.2\%$) on the chemical environment and on the pressure, up to 25 GPa.

Furthermore, very little is still known about decay events that occur at very high T in ionized media for changing ρ , such as those found in stellar interiors, and similar studies are still challenging for theory and intensively debated. The recent recommendations by [496] are mainly based on the work by [480] and [479]. In these works a partial ionization of ${}^7\text{Be}$ in the Sun was assumed, thus the rate now currently used includes contributions from both bound and continuum states and the total-to-continuum capture ratio is 1.217. Different results were presented by [497], who assumed that ${}^7\text{Be}$ is fully ionized in the solar plasma; this implied an increase of the ${}^7\text{Be}$ lifetime by ~ 20 to 30% as compared to previous recommendations. An even more complicated situation is depicted by [498], who recently found a ${}^7\text{Be}$ lifetime shorter by about 10% , using a modified DH screening potential. The present situation is therefore quite unsatisfactory and the uncertainties affecting Li abundances in stars have to cope also with this poor understanding of the basic nuclear input data.

This is actually the main motivation of our present attempt, as essentially no one of the existing reaction rate compilations for stellar physics can be safely extrapolated from the Sun to other situations. For example, the rate by [496] is derived from a simple fit over a very small domain of the parameter space, while the formula by [499] imposes a specific choice for the density.

In this context, our goal is to lay the foundations of a theoretical and computational method for studying the electron capture and decay rates at high temperature in a density-varying medium, to go beyond the existing treatments. We shall probe its validity through a comparison with more classical approaches, and shall use the results to reconsider briefly the problem of Li production and destruction in red giant stars.

9.3 Dynamics of electron capture from *ab-initio* calculations: our model

In this section we describe our first-principle approach for computing electron captures over a much wider range of T and ρ than so far possible. These two parameters alter considerably

the balance between bound and free electronic states contributing to the capture.

While we believe that our formalism is totally general and can be applied even to other systems, as a test case of our method we will estimate the decay rate of ${}^7\text{Be}$ by electron captures:



${}^7\text{Be}$ may decay into ${}^7\text{Li}$ through different decay channels. In particular the decay from the ground state of ${}^7\text{Be}$ may occur to both the ground and the first excited state of ${}^7\text{Li}$. Of course the phase space and the kinetic energy of the neutrino will be different for these two decay paths. At ambient conditions, that is for negligible kinetic energy of the impinging electron, ${}^7\text{Be}$ decays in 53 days into the ground state of ${}^7\text{Li}$ (3/2-) in the 89.7% of cases, while in the remaining 10.3% it decays into the first excited state (1/2-) [500]. The latter is found at an energy of 477.4 KeV higher than that one of the ground state. The weak branching ratio (BR) at room temperature is thus 8.709.

By defining Q_0 and Q_1 as the kinetic energies of the neutrino, escaping respectively from the ${}^7\text{Li}$ nucleus in its ground and first excited state, we have $Q_0 = 861.6$ keV and $Q_1 = Q_0 - 477.4 = 384.2$ keV [501]. Being the kinetic energy higher in the first case, larger will be the available phase space. Roughly, we can estimate that at temperature $T=107$ K, we have $\text{BR} = 89.7/10.3 \times (Q_0 + kT)^2 / (Q_1 + kT)^2 / (Q_0^2/Q_1^2) = 8.684$. The percentage variation of the BR due to an increase of the temperature of five order of magnitude is thus only 0.3%. Of course, even the weak matrix elements will be different for these two channels and this should be in principle taken into account. However, our main goal is to estimate accurately the total electron capture decay rate, as this is the data we need for assessing the astrophysical consequences of these new data. Thus, in the following discussion we will assume that the decay occurs only to the ground state of ${}^7\text{Li}$.

The framework within which we shall calculate the decay rate is given by the theory of scattering under two potentials: V , representing the screened, short-range Coulomb potential and W , which represents the weak interaction coupling the Coulomb distorted initial state and the final channels. We define $\phi_{i,\mathbf{p}}$ as a free plane-wave, $\phi_{i,\mathbf{k}}^+$ the perturbed ‘in-state’, described by a Coulomb-distorted plus an outgoing spherical wave, $\phi_{f,\mathbf{k}}^-$ and $\psi_{f,\mathbf{k}}^-$ the perturbed ‘out-states’, which describe asymptotically the emission of a neutrino with relative momentum \mathbf{k} , released into the final channel f of the target, respectively without and with the weak coupling. Then we can write the cross section of the electron capture process as:

$$\begin{aligned} \sigma_{i \rightarrow f} &= \int \frac{d^3k}{(2\pi)^3} \frac{2\pi}{v} \left| \langle \psi_{f,\mathbf{k}}^- | W | \phi_{i,\mathbf{p}}^+ \rangle + \langle \phi_{f,\mathbf{k}}^- | V | \phi_{i,\mathbf{p}} \rangle \right|^2 \delta \left(\frac{p^2}{2m_e} + E_i - E_f - ck \right) \\ &= \int \frac{d^3k}{(2\pi)^3} \frac{2\pi}{v} \left| \langle \phi_{f,\mathbf{k}}^- | T_w | \phi_{i,\mathbf{p}}^+ \rangle \right|^2 \delta \left(\frac{p^2}{2m_e} + E_i - E_f - ck \right) \end{aligned} \quad (9.2)$$

E_i, E_f represent the internal energies of the target (${}^7\text{Be}$) and of the final decay product (${}^7\text{Li}$), $\mathbf{p} = m_e v$ and \mathbf{k} are the relative electron and neutrino momenta in the initial and final channels, and v is the electron velocity in the initial channel, relative to ${}^7\text{Be}$. In Eq. (9.2) the matrix element $\langle \phi_{f,\mathbf{k}}^- | V | \phi_{i,\mathbf{p}} \rangle$ must vanish, as the Coulomb interaction does not couple the initial and final decay channels ($\langle \phi_{f,\mathbf{k}}^- | V | \phi_{i,\mathbf{p}} \rangle = 0$). Thus we can define the T -matrix of the weak interaction as

$$\langle \psi_{f,\mathbf{k}}^- | W | \phi_{i,\mathbf{k}}^+ \rangle = \langle \phi_{f,\mathbf{k}}^- | T_w | \phi_{i,\mathbf{k}}^+ \rangle \quad (9.3)$$

From Eq. (9.2) one can obtain the electron capture rate by multiplying the cross section for the electron current:

$$\Gamma_{i \rightarrow f} = \int 2\pi \frac{d^3k}{(2\pi)^3} |\langle \phi_{f,\mathbf{k}}^- | T_w | \phi_{i,\mathbf{p}}^+ \rangle|^2 \delta \left(\frac{p^2}{2m_e} + E_i - E_f - ck \right) \quad (9.4)$$

The calculation of the nuclear T -matrix elements, particularly with the inclusion of the $p^2/2m_e$ dependence, is very difficult from first-principles and is out of the scope of this thesis. Indeed $p^2/2m_e$ depends on the temperature of the system. However, the full calculation is not needed in our case, and two approximations will enable us to simplify the equations without sacrificing accuracy. Firstly, we will neglect the dependence on the temperature of this matrix element, and consider only one initial state. This approximation is motivated by the fact that the first nuclear excited state of ${}^7\text{Be}$ is at 429.2 keV above the ground state [501], corresponding to a temperature of 5×10^9 K, larger by factors of 50 to 100 with respect to the maximum values found during H-shell burning in the RGB or AGB phases.

The second approximation is to model the weak interaction, owing to its very short-range nature, by a Fermi contact interaction $T_W \propto \delta(\mathbf{r})$, independent of the neutrino momentum \mathbf{k} . By integrating out in \mathbf{k} using the latter assumption:

$$\begin{aligned} \Gamma_{i \rightarrow f} &= \frac{\bar{k}^2}{\pi c} |t_{f,i} \langle i, 0 | \phi_{i,\mathbf{p}}^+(0) \rangle|^2 = \frac{1}{\pi c^3} |t_{f,i}|^2 \langle i, 0 | \phi_{i,\mathbf{p}}^+ \rangle \left(\frac{p^2}{2m_e} + E_i - E_f \right)^2 \langle \phi_{i,\mathbf{p}}^+ | i, 0 \rangle \\ &= \frac{1}{\pi c^3} |t_{f,i}|^2 \langle i, 0 | \phi_{i,\mathbf{p}}^+ \rangle (H_0 + V + E_i - E_f)^2 \langle \phi_{i,\mathbf{p}}^+ | i, 0 \rangle \end{aligned} \quad (9.5)$$

where $\bar{k} = \frac{1}{c} \left(\frac{p^2}{2m_e} + E_i - E_f \right)$ and $\langle \phi_{i,\mathbf{p}}^+ | i, 0 \rangle$ is the electron wavefunction representation at the Be nucleus. We will assume that the nuclear T -matrix elements $t_{f,i}$ are known and equal to those measured on the Earth. The assumptions of Eq. (9.5) imply that the electron capture can be modeled as a ${}^7\text{Be}-e^-$ two-body scattering process at a given relative electron momentum p , and that the rate is proportional to the electron density at the nucleus $\rho_e(0)$, which is screened and modified by the presence of the surrounding particles.

Our model system of the hot plasma, for different conditions of T and ρ , is represented by a homogeneous Fermi gas composed by ${}^7\text{Be}$ atoms surrounded by N_p protons (hydrogen nuclei) and N_e electrons. The presence of other particles, such as helium, will be neglected in the following discussion and in the stellar decay rate calculation, unless otherwise stated. However, the generalization of our method to include several species is straightforward.

An *exact, ab-initio* calculation of the electron capture rate would be extremely complex, due to the many-body nature of the scattering, and one needs to introduce some further approximations. The first step of our method is thus the formal reduction of this complicated many-body problem to a screened two-body scattering problem, by using an ‘‘adiabatic’’ factorization of the eigenfunctions, resembling the widely known Born-Oppenheimer (BO) approximation adopted in standard electronic structure methods. This goal is reached by fixing the reference frame into the ${}^7\text{Be}$ nucleus and by writing the different parts of the Hamiltonian in this non-inertial frame (we remember that the ${}^7\text{Be}$ nucleus is in principle free to move around). In every sense this is only a coordinate transformation. However, as in classical mechanics, the consequence of using a non-inertial frame will bring about some complicacy (apparent forces), e.g. in this case we will have a two-body kinetic energy operator. In the Appendix A we describe the mathematical details of this derivation,

from which we obtain that the many-body scattering Hamiltonian in the coordinate system relative to the ${}^7\text{Be}$ nucleus can be written as:

$$\begin{aligned}
H = & \sum_{j=1}^{N_e} \left(-\frac{1}{2m_e} - \frac{1}{2M_{\text{Be}}} \right) \nabla_{e,j}'^2 + \sum_{J=1}^{N_p} \left(-\frac{1}{2m_p} - \frac{1}{2M_{\text{Be}}} \right) \nabla_{p,J}'^2 - \sum_{j=1}^{N_e} \frac{Z_{\text{Be}}}{|\mathbf{r}'_{e,j}|} + \sum_{J=1}^{N_p} \frac{Z_{\text{Be}}}{|\mathbf{R}'_{p,J}|} \\
& - \sum_{j=1}^{N_e} \sum_{J=1}^{N_p} \frac{1}{|\mathbf{r}'_{e,j} - \mathbf{R}'_{p,J}|} + \sum_{j=1}^{N_e} \sum_{k=j+1}^{N_e} \frac{1}{|\mathbf{r}'_{e,j} - \mathbf{r}'_{e,k}|} + \sum_{J=1}^{N_p} \sum_{K=J+1}^{N_p} \frac{1}{|\mathbf{R}'_{p,J} - \mathbf{R}'_{p,K}|} - \frac{1}{2M_{\text{Be}}} \nabla_{\text{Be}}'^2 \\
& - \sum_{\substack{J,J'=1 \\ J \neq J'}}^{N_p} \left(\frac{1}{M_{\text{Be}}} \nabla'_{p,J} \cdot \nabla'_{p,J'} \right) - \sum_{\substack{j,j'=1 \\ j \neq j'}}^{N_e} \left(\frac{1}{M_{\text{Be}}} \nabla'_{e,j} \cdot \nabla'_{e,j'} \right) - \frac{1}{M_{\text{Be}}} \sum_{j=1}^{N_e} \sum_{J=1}^{N_p} \nabla'_{p,J} \cdot \nabla'_{e,j} \\
& + \sum_{j=1}^{N_e} \left(\frac{1}{M_{\text{Be}}} \nabla'_{e,j} \cdot \nabla'_{\text{Be}} \right) + \sum_{J=1}^{N_p} \left(\frac{1}{M_{\text{Be}}} \nabla'_{p,J} \cdot \nabla'_{\text{Be}} \right)
\end{aligned} \tag{9.6}$$

where, in order of appearance, one has the electron and proton kinetic energies, the electron-Be and proton-Be potential energies, the electron-proton, electron-electron, proton-proton interaction, the Be kinetic energy and, finally, terms coupling the different particle species. In the inter-particle coupling terms, resulting from our coordinate transformation, $\{\mathbf{r}'_{e,j}, \mathbf{R}'_{p,J}\}$ identify the coordinates of the j -electron and J -proton relative to the ${}^7\text{Be}$ coordinate, $\mathbf{R}_{\text{Be}} = \mathbf{R}'_{\text{Be}}$.

We then look for separable eigensolutions of the form:

$$\Psi(\mathbf{R}'_{\text{Be}}, \{\mathbf{r}'_e\}, \{\mathbf{R}'_p\}) = \chi(\mathbf{R}'_{\text{Be}}) \Phi(\{\mathbf{r}'_e\}, \{\mathbf{R}'_p\}) \tag{9.7}$$

$$\nabla'_{\text{Be}} \chi(\mathbf{R}'_{\text{Be}}) = \mathbf{k} \chi(\mathbf{R}'_{\text{Be}}) \tag{9.8}$$

This wavefunction factorization differs from the usual formulation of the BO approximation in two ways. At variance with the BO approximation, the function $\Phi(\{\mathbf{r}'_e\}, \{\mathbf{R}'_p\})$ in Eq. (9.7), written in the ${}^7\text{Be}$ reference system, does not depend parametrically on the ${}^7\text{Be}$ coordinates and thus needs to be calculated only once. Furthermore, the BO approximation is applicable only when the electronic potential energy surfaces are well separated. These are not our conditions, as the electrons, for T and ρ values pertinent to the burning regions of stars, occupy either highly excited states of the ${}^7\text{Be}$ atom or continuum orbits. Thus, we are out of reach of the BO scheme, which cannot be rigorously applied.

However, it can be shown that the last two coupling terms in Eq. (9.6), which are crucial for the application of our mean-field treatment of the many-body interaction, can be neglected. In Appendix A we provide a detailed explanation of the conditions where this approximation can be used.

We notice that, by introducing the two-body framework and the relative coordinate system, we can achieve two important results. The first one is that in our approach the ${}^7\text{Be}$ nucleus is in principle free to move around (thus overcoming the limitations of the Born-Oppenheimer scheme), even though in general its motion is strongly limited by the presence of other particles; the second one is that, by neglecting the two last terms of Eq. (9.6), the two-body electron- ${}^7\text{Be}$ density-matrix can be factorized as the product of two one-body density-matrices and thus it is possible to introduce different schemes of approximations to the many-body interaction, including the Hartree-Fock's one (hereafter HF). Therefore, the

screening brought about by all the interacting fermions of the surrounding environment, which modifies the two-body electron- ${}^7\text{Be}$ scattering and thus the electron-capture rate, can be now taken into account, using standard many-body techniques.

9.3.1 Screening at different levels of accuracy: Thomas–Fermi, Poisson–Boltzmann and Debye–Hückel

While the importance of the screening for the assessment of the electron-capture rate is well understood, the approaches used so far are all based on the DH approximation; thus, their reliability is not a priori guaranteed in every situation. Within this approximation [479], for example, realized that, in solar conditions, the electron density at the nucleus is reduced by the electronic screening for both bound and continuum electrons. [482] further improved this model by integrating the density-matrix equation to treat on similar grounds the bound and continuum electrons, and by including via a Monte-Carlo approach non-spherical charge fluctuations induced by the small number of ions within the radius λ_D of a Debye sphere.

Despite these improvements, the conclusions drawn by these works rely on the assumption that the hot plasma can be modeled as a classical non-interacting electron gas, screened by using the DH model, in thermodynamic equilibrium with a heat bath at absolute temperature T . The range of applicability of this approximation is based on both classical and statistical considerations: for the former ones, we need a large number of electrons and a high temperature; for the latter ones, we require a smooth change of the potential over a characteristic distance (λ_D), which is large as compared to the thermal De-Broglie wave-length of the electrons (λ_{DB}). However, in the solar case, where $T \simeq 16 \times 10^6 K$, $\rho = 150 g/cm^3$, we have, for the electrons, $\lambda_D = 0.407$, $\lambda_{DB} = 0.352$ a.u.. The conditions are therefore, already for our Sun, at the limits of validity of the classical (Maxwell-Boltzmann) gas approximation. Over the more extended range of parameters characterizing the radiative layers above the H-shell in a red giant (down to $T \simeq 2.0 \times 10^6 K$) the application of the Maxwell–Boltzmann distribution might no longer be justified.

We underline that the simple DH approach, commonly used in the literature so far, can actually be derived as a two-step approximation of the more general Thomas–Fermi (hereafter TF) model, by using the linearized Maxwell-Boltzmann distribution. (In Appendix B we provide a detailed discussion of the DH treatment).

Hence we can compute the crucial parameter, i.e. the electron density at the Be nucleus $\rho_e(0)$, at different levels of approximation, in order to disentangle the differences introduced in the results by the various approaches. In Table 1 we report the results of such calculations, adopting as an example the solar conditions. We underline that $\rho_e(0)$ is directly related to the electron-capture rate.

In the above calculations, the plasma was modelled by a ${}^7\text{Be}$ nucleus surrounded by a Fermi gas occupying an infinite volume and helium was explicitly included. One can see that both the classical Poisson–Boltzmann approach (PB) and the DH approximation give sizeable different results (of the order of 38% and 6% respectively) with respect to the TF approximation, already for solar conditions. The change becomes even larger when we use our more general method, based on the HF approximation, which we will discuss in the next section. (Surprisingly, the DH approximation is closer to the HF and TF results than the PB case, from which it is derived by linearization).

Table 1

$\rho_{HF}(0)$	$\rho_{TF}(0)$	$\rho_{PB}(0)$	$\rho_{DH}(0)$
16.320 ± 0.020	16.135 ± 0.025	14.870 ± 0.020	16.085 ± 0.025

TABLE 1: Values (in atomic units) of the electron density at the Be nucleus $\rho_e(0)$ for different levels of the theory (HF=Hartree-Fock, TF=Thomas-Fermi, PB=Poisson-Boltzmann, DH=Debye-Hückel) for solar conditions ($T = 16\text{MK}$). The conditions at which we performed the calculations are $T = 15.67\text{MK}$, $\rho=152.9 \text{ g/cm}^3$, $X_{\text{H}} = 0.34608$, $X_{\text{He}} = 0.63368$.

Even more important, one must underline that the PB and DH approximations do not hold outside the conditions of the solar nucleus. This is true, in particular, at lower temperatures and densities, where a large part of the Li production occurs (because the competing p-captures on ${}^7\text{Be}$ become ineffective). In order to check this point, we performed the calculations of the the electron density at the Be nucleus for all the previously discussed approaches over a wide range of T and ρ conditions. The results are reported in Table 9.7, where T is in units of 10^6K and ρ in g/cm^3 . Values at the left of the obelus (\div) represent the electron density at the nucleus $\rho_e(0)$, while those at the right represent $\rho_e(0)$ multiplied by $(1 + p^2/2m)/(E_i - E_f)$ (see Eq. 9.5), to which the capture rate is proportional. The Debye radius λ_D and the De-Broglie wavelength λ_{DB} for electrons (e^-) and protons (p) are given in atomic units.

From the analysis of the electron density at the nucleus $\rho_e(0)$ for the different approximations, it is clear that, when we are out of reach of the DH approximation ($\lambda_D \leq \lambda_{DB}$), the values calculated using this model may differ by more than 30% from the HF values. In particular, we underline that, except for very high temperatures, the PB approximation is extremely unreliable, while over the whole considered range of T and ρ values, the TF model systematically underestimates the density at the nucleus $\rho_e(0)$. At variance with this, the DH model, except for low temperatures ($T \leq 10^6 \text{ K}$), seems to partially correct the wrong behaviour of the PB approximation, but not in a systematic way. This is due to the fact that the electron density at the nucleus $\rho_e(0)$ is finite for the DH model, while it is infinite for the Boltzmann approximation (in the HF method the density is always finite, due to the fact that in this case the electronic wavefunction is finite at the nucleus). It is thus evident that the DH model fails in capturing the electron screening properties over a portion of the parameter space that is very important for Li nucleosynthesis and, if one is to assess accurately the electron-capture rate of ${}^7\text{Be}$ in that region, it is necessary to go beyond this approach.

We notice that the issue at stake here is not only a better estimate of weak interactions. If the traditional methods underestimate the electron density over a considerable part of the conditions typical of H-burning in Red Giants, as it seems to be the case, then this implies that they also underestimate the effect of electrons in screening strong interactions. In the case we discuss here (Li production and destruction) our next step will therefore be a re-evaluation of electron screening for proton captures on ${}^7\text{Li}$, which occur down to very low temperatures (few 10^6K). It is well known that the huge destruction of Li in the Sun is still unaccounted for quantitatively, being too small in the models, so that a more effective process of proton captures on Li, induced by an increased estimate of the electron density and of its screening of the Coulomb barrier, might have important consequences on solar physics and on our understanding of nucleosynthesis in general.

At high temperature and high density ($T \geq 10^7 \text{ K}$, $\rho \geq 100 \text{ g/cm}^3$) the approaches

discussed so far (with the exception of the purely classic PB treatment) become essentially equivalent to one another, as shown in Table 1; in particular, the values of the electron density at the Be nucleus produced by our new method and the one from the DH approximation differ by less than 1.5% (see Table 1, column 1 and 4).

9.3.2 Calculations of an accurate decay rate from first principles

In order to apply our model Hamiltonian, Eq. (9.6), to the calculation of the capture rate over a wider range of T and ρ values than so far possible, we need to develop new tools, suitable to go beyond the DH approximation and capable of treating accurately the electronic screening for both bound and continuum electrons. We will then use the new estimates for interpreting the observational data.

In our approach, the Coulomb screening is calculated using a temperature-dependent HF method, within the canonical ensemble, by populating both the ground-state and excited-state atomic orbitals via a Fermi-Dirac distribution. In our treatment, we will neglect the electron-proton pair-formation at low temperature ($T < 10^6$ K). Our method can be outlined as follows. i) We assume that the decay rate is proportional to $\rho_e(0)$ calculated by solving self-consistently a system of coupled HF equations for protons and electrons in the electrostatic field of a ${}^7\text{Be}$ nucleus at the origin of the coordinate system. ii) The coupling is given by the self-consistent Hartree term, describing the Coulomb interaction between the two fermionic species. iii) The chemical potentials of protons and electrons are chosen in such a way that the system is neutral far from the ${}^7\text{Be}$ atom. iv) Within this framework, the scattering of ${}^7\text{Be}$ with protons and electrons is a two-body interaction, with the remaining particles acting as a mean-field.

The first step in the above list consists in solving self-consistently the equations for the electron charge density ρ and the potential V to calculate the electron-capture rate. The HF equations for this problem read:

$$-\frac{1}{2m_j}\nabla^2\psi_{j,\alpha\sigma_e\tau_{Be}n}(\mathbf{r}) + V_j^{ext}(\mathbf{r})\psi_{j,\alpha\sigma_e\tau_{Be}n}(\mathbf{r}) - \mu_j\psi_{j,\alpha\sigma_e\tau_{Be}n}(\mathbf{r}) \quad (9.9)$$

$$+ \sum_{\beta\sigma'_e\tau'_{Be}} \int d\mathbf{r}' V_{j,\alpha\sigma_e\tau_{Be}\beta\sigma'_e\tau'_{Be}}^{HF}(\mathbf{r},\mathbf{r}')\psi_{j,\beta\sigma'_e\tau'_{Be}n}(\mathbf{r}') = \epsilon_{j,n}\psi_{j,\alpha\sigma_e\tau_{Be}n}(\mathbf{r})$$

$$\rho_{j,\alpha\sigma_e\tau_{Be}\alpha'\sigma'_e\tau'_{Be}}(\mathbf{r},\mathbf{r}') = \sum_n \frac{1}{e^{\frac{\epsilon_{j,n}}{kT}} + 1} \psi_{j,\alpha\sigma_e\tau_{Be}n}(\mathbf{r})\psi_{j,\alpha'\sigma'_e\tau'_{Be}n}(\mathbf{r}') \quad (9.10)$$

$$V_{j,\alpha\sigma_e\tau_{Be}\alpha'\sigma'_e\tau'_{Be}}^{HF}(\mathbf{r},\mathbf{r}') = \delta(\mathbf{r}-\mathbf{r}') \sum_{j'\beta\beta'} \int d\mathbf{s} \frac{Z_j Z_{j'}}{|\mathbf{r}-\mathbf{s}|} \delta_{\sigma_e\sigma'_e} \delta_{\tau_{Be}\tau'_{Be}} \rho_{j',\beta\sigma'_e\tau'_{Be}\beta\sigma''_e\tau''_{Be}}(\mathbf{s},\mathbf{s}) \quad (9.11)$$

$$- \frac{Z_j^2}{|\mathbf{r}-\mathbf{r}'|} \delta_{\alpha\alpha'} \delta_{\sigma_e\sigma'_e} \delta_{\tau_{Be}\tau'_{Be}} \rho_{j,\alpha\sigma_e\tau_{Be}\alpha'\sigma'_e\tau'_{Be}}(\mathbf{r},\mathbf{r}')$$

In Eqs. (9.9, 9.10, 9.11), σ_e ($\frac{1}{2}$) and τ_{Be} ($\frac{3}{2}$) are the electronic and nuclear spins, while α and β represent all the other quantum numbers. The index j runs over all the fermionic particle types. The self-consistent HF potential is used in Eq. (9.5), along with the external potential, $V = V_{HF} + V_{ext}$, to calculate the (static exchange) electron-capture decay rate.

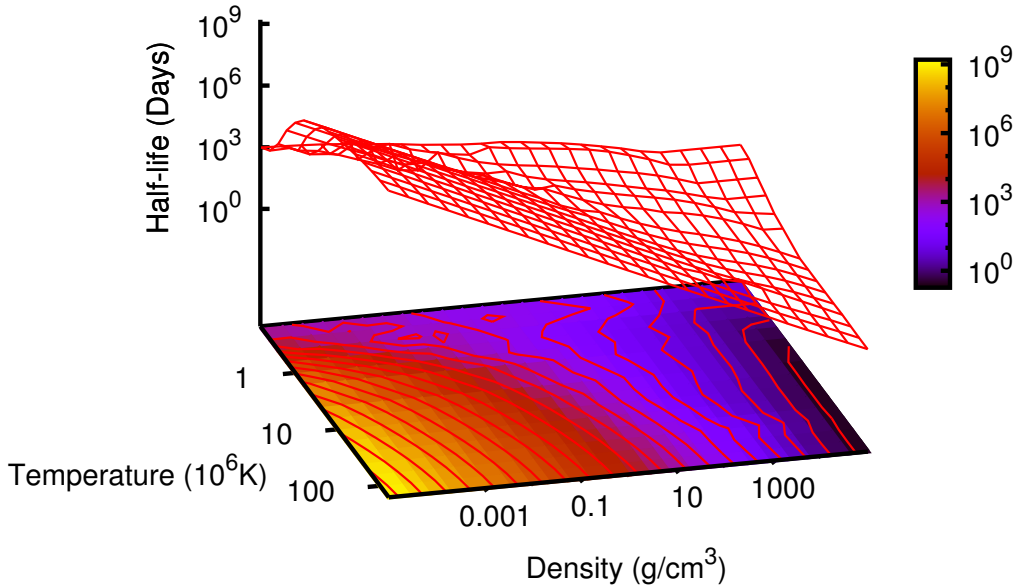


FIGURE 9.1: Electron-capture decay rate in days for ${}^7\text{Be}$ as a function of ρ and T .

In order to be complete, the above treatment of the many-body interaction needs to include the electron and proton continuum states, as the capture can occur from the continuum orbitals and, at high T , the plasma is from partially to totally ionized. To include the continuum states in the HF equations, we used the theory of projected potentials, developed for the calculation of the electronic emission spectra from solids [502, 503, 93]. Within this theory, while the Coulomb interaction among the particles (see Eq. 9.6) is projected onto the Hilbert space spanned by a basis set, giving rise to the discrete part of the spectrum, the kinetic terms are left unprojected. In this way, as the eigenfunctions of the kinetic energy operator are plane waves at a given energy, one can “recover” the energy continuum. Furthermore, the sums over the discrete states n in Eq. (9.10) should be thought of as integrals over the continuum. In our case a $cc - pVDZ$ Gaussian basis set (GBS), centered on the ${}^7\text{Be}$ nucleus, has been optimized for the calculation of the bound states. We underline that the addition of the continuum states to the projected Coulomb interaction can have significant enhancement effects on the decay rate over a wide portion of the parameter space spanned. This however does not include the solar case, where our estimates are essentially indistinguishable from those reported by [496]. We notice in any case that, when applicable, our changes point to the opposite direction with respect to the suggestions by [497] for the Sun.

Our two-body scattering framework allows us to go beyond even the HF treatment of the screening; therefore, we estimated the importance of correlations by computing $\rho_e(0)$ for an isolated ${}^7\text{Be}$ atom using the Full Configuration Interaction approach (FCI) for the previously used $cc - pVDZ$ GBS. We however did not find appreciable differences between the $\rho_e(0)$ estimates calculated by the HF and the FCI methods up to the third digit (see Table 2), thus justifying our mean-field approach, which neglects dynamical correlations.

	Energy	$\rho_{e\uparrow}(0)$
Hartree-Fock	-14.573	17.68521
Full-CI	-14.660	17.68060

TABLE 2: Energy of the isolated beryllium atom in atomic units and spin-up density at the nucleus obtained by HF and CI calculations.

The calculation of the decay rate, performed at different T and ρ values using our approach is reported in Figure 9.1. We recall once again that the above treatment of the many-body interaction goes beyond the DH approximation previously used to estimate the electron-capture decay rate in the Sun [479, 478]. The field of applicability of the HF screening effects can in fact be extended rigorously, to cover the whole range of parameters found in the layers between the H-burning region and the envelope base in evolved stars.

9.4 An application to the Li production and destruction in evolved stars

As an example of application of our new rate estimates to practical nucleosynthesis problems in stars, we briefly illustrate here the situation for rather low mass stars ($M \lesssim 2M_{\odot}$) of solar metallicity, undergoing the RGB and AGB evolutionary phases in presence of deep-mixing processes. They were recently discussed by [467, 472] within the framework of reaction rates offered by [496].

We consider here only the impact on the above astrophysical scenario of our "best choice" for the reaction rate (our new method), without analyzing the individual behavior of all the four estimates presented.

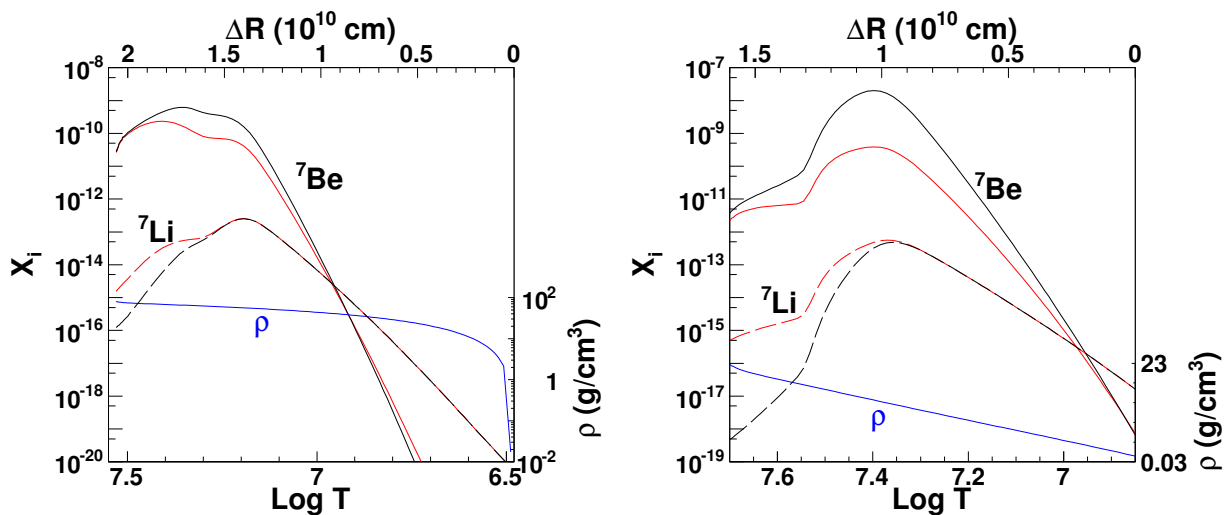


FIGURE 9.2: A comparison between the equilibrium abundances of ${}^7\text{Be}$ and ${}^7\text{Li}$ achieved in the layers above the H-burning shell, adopting our ${}^7\text{Be}$ lifetime (red line) and the one extrapolated by [496] (black line), in a $2 M_{\odot}$ evolved star of solar metallicity. Panel a) refers to typical RGB conditions, panel b) to AGB stages. The matter density is also shown (blue line), and is referred to the scale on the right axis.

Figure 9.2 (a,b) shows the abundances of ${}^7\text{Be}$ and of its daughter ${}^7\text{Li}$ in the layers below

the convective envelope bottom and above the H-burning shell. They are plotted shortly after the bump of the Luminosity Function on the RGB (panel a) and in between two thermal pulses, during quiet H-burning, on the AGB (panel b). The stellar models are the same discussed in [472]. The red lines illustrate the situation obtained with our new rate (the case previously labelled HF), while the black line shows the previous findings, obtained with extrapolations from [496], hence based on the DH approximation. The right-end limit of the plot, at the position $\Delta r = 0$, characterized by temperatures below 10^7 K, represents the base of the envelope; the left-end limit is the region where the maximum energy is released from H-burning. As is shown, the matter density of the layers considered never achieves the high values typical of the solar core: this is the most critical reason why the DH approximation is inadequate for evolved stars. In our more general approach both higher and lower values of the electron density near the ${}^7\text{Be}$ nucleus can be found, depending on the conditions; however, over a major part of the region of interest, where the density is not far from one tenth solar and the temperature remains high enough ($T \gtrsim 10^7$ K) the values of $\rho_e(0)$ we find are higher than in the DH model; the electron captures are therefore faster than in [472], and a lower equilibrium abundance of ${}^7\text{Be}$ is established.

Notice that in our present example neither the ${}^3\text{He}+{}^4\text{He}$ rate, nor the ${}^7\text{Be}+p$ or the ${}^7\text{Li}+p$ rate have been modified, so that the variations shown in Figure 9.2 are entirely due to the new approach adopted in computing electron captures on ${}^7\text{Be}$. As discussed before, further effects are actually to be expected on proton captures, as the changes in the electron density will affect the screening of the Coulomb barrier for charged-particle interactions.

As discussed in the Section 1, it is known that interpreting the observed isotopic abundances of light and intermediate elements in evolved stars does not require only the use of the proper reaction rates, but also needs the assumption that deep mixing phenomena occur, both destroying fragile nuclei of the envelope (like Li), by exposing them to high temperatures, and carrying to the surface products of H-burning nucleosynthesis. These mixing mechanisms are generally parameterized and depend on two main parameters; in the approach by [467, 472] these parameters are the mass circulation rate (in units of $10^{-6} M_\odot/\text{yr}$) induced by the transport processes (\dot{M}_6) and the depth in the structure they achieve. This last is expressed in terms of the (logarithmic) temperature difference between the deepest mixed layers and those where the maximum energy is released in the H-shell ($\Delta = \log T_H - \log T_P$). Recently, an analysis devised specifically for fixing such extra-mixing parameters, adopting bright RGB stars as constraints, was carried out by confirming the indications by Palmerini et al. on the need of a rather shallow and slow mixing on the RGB [504].

With reference to Panel a) in Figure 9.3, the points labeled BLF indicate the position in temperature of the Bump of the Luminosity Function, for two representative Li abundances, inside the wide spread allowed both by observations and models of the previous evolutionary stages ($-0.3 \lesssim A(\text{Li}) \lesssim 1.5$); crosses indicate observations.

From each one of the two luminosity functions (BLF), the two black curves show the Li destruction induced by adopting, for the extra-mixing parameters, $\Delta = 0.22$ and $\dot{M}_6 = 0.01$ (upper curve) or 0.1 (lower curve). The effects of deep mixing are considered up to the moment when the RGB tip is reached. Subsequently, the temperature increases at constant values of $A(\text{Li})$ (dashed lines) up to the start of core He-burning (in the CLUMP region in the plot), after which Li would decrease again during the early-AGB stages; see also for details [472]. The curves showing the evolution of Li are completely insensitive to the adoption of the new or of the old rate for e^- -captures. Panel b) of Figure 9.3 shows instead

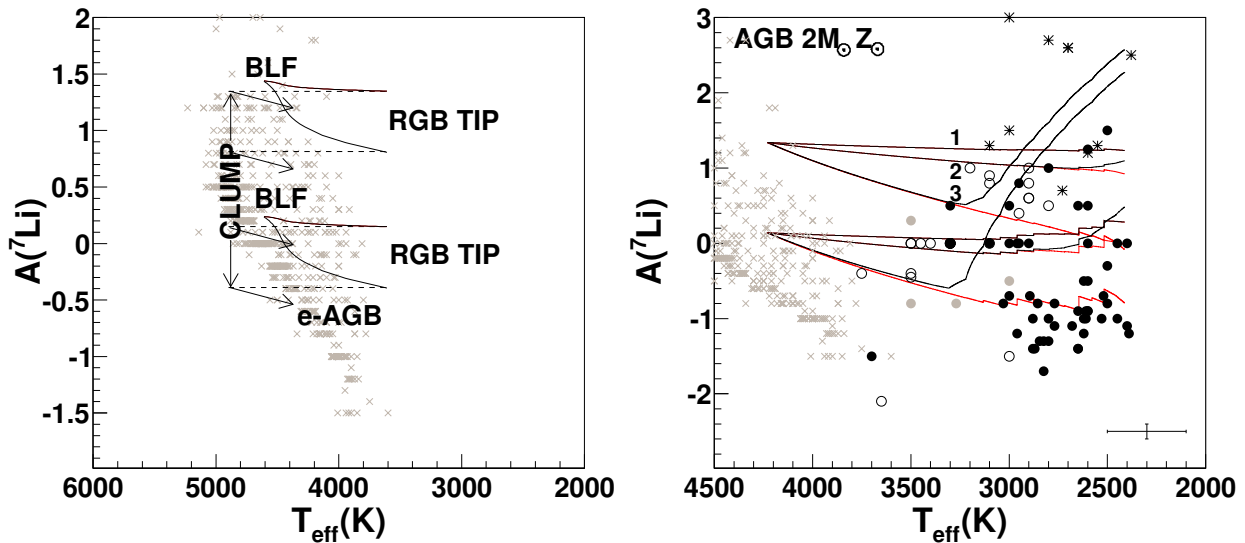


FIGURE 9.3: Panel a) The Li destruction induced by extra-mixing on the RGB. Panel b) The same effects for AGB stages (see text for explanations, and [472] for the details of the observational points and their references)

that a different situation emerges during the subsequent AGB evolution. Here we started the computations from three initial values of the Li abundance, inside the observed spread left by RGB stages. Open and solid dots in the Figure represent observations of M-MS-S and of C(N) stars, respectively. Asterisks show the high Li abundances of CJ stars. The curves refer to stellar models with $\Delta = 0.22$ and $M_6 = 0.1, 0.3, 1$ (cases labelled 1, 2, 3, respectively). The black curves are obtained using the ${}^7\text{Be} + e^-$ rate extrapolated by [496], while the red ones refer to our best choice from the present analysis (HF). It is clear that large changes emerge (in particular, with the new rate, Li production becomes impossible).

The reasons for the above dichotomy between RGB and AGB stages can be understood with reference to the time scales for ${}^7\text{Be}$ mixing and decay in the two cases. They are shown in Figure 9.4. As the figure shows, for the range of mixing rates required to explain the other RGB chemical anomalies (panel a) both the new and old choice for the ${}^7\text{Be}$ decay provide a short enough lifetime for ${}^7\text{Be}$, to allow its decay to Li before being saved to the envelope. In other words, conditions suitable for Be destruction are in any case met, both with the older and with the newer choice of the rate. This explains why the new estimate for the rate, which has evident effects in the stellar structure shown in panel a) of Fig 9.2, does not modify the envelope abundances produced by the mixing process. The opposite occurs for AGB stages (panel b). Here, the reduction in the lifetime of ${}^7\text{Be}$ obtained with our new rate is strong enough that even with relatively fast mixing processes the destruction of Li in the envelope is not compensated, and the highest observed Li abundances (typical of CJ stars) cannot be reached. Essentially, with our rate Li behaves, on the AGB, in a way similar to what occurs on the RGB: destruction always prevails.

We notice that, far from creating a new problem, this finding is now in agreement with the indications provided by other chemical anomalies of the very peculiar CJ stars. Let's comment on this in some more detail. In [472] it was surprisingly shown that, adopting the extrapolation to AGB conditions of the ${}^7\text{Be}$ lifetime from [496], the high Li abundances observed in CJ-type carbon stars could be explained in the framework of the evolution of

single stellar structures experiencing rather fast extra-mixing see in particular Fig. 10 in [472]. This result was in itself quite strange, as many peculiarities in such objects suggested instead, since a long time, that they do not follow the “normal” evolutionary sequence for LMS. This is in particular demonstrated by their luminosity, on average lower than for other C stars, by their lack of enrichment in s-process elements and by the fact that a remarkable fraction of CJ stars have O-rich shells. Among the hypotheses presented in the literature for explaining the anomalous CJ evolutionary path, binarity is probably the most commonly-invoked scenario [505, 506], especially if leading to coalescence into a single peculiar object [507]. In this case, obviously, the high Li abundances of the peculiar descendants of such a stellar merging are not expected to be explained by single-star nucleosynthesis. We actually predict that Li destruction, with our new rate, be even more facilitated than what emerges from the first simple example of Figure 9.3. In fact a further effect is expected by an increase in the electron screening, due to the now higher (on average) electron densities near the nuclei, making proton captures on Li more effective.

In general, the Li-rich red giants (even outside the peculiar CJ class) need really exceptionally fast transport rates to explain the net Li production. Their small number says that these phenomena must be very rare, or concentrated in extremely short evolutionary stages.

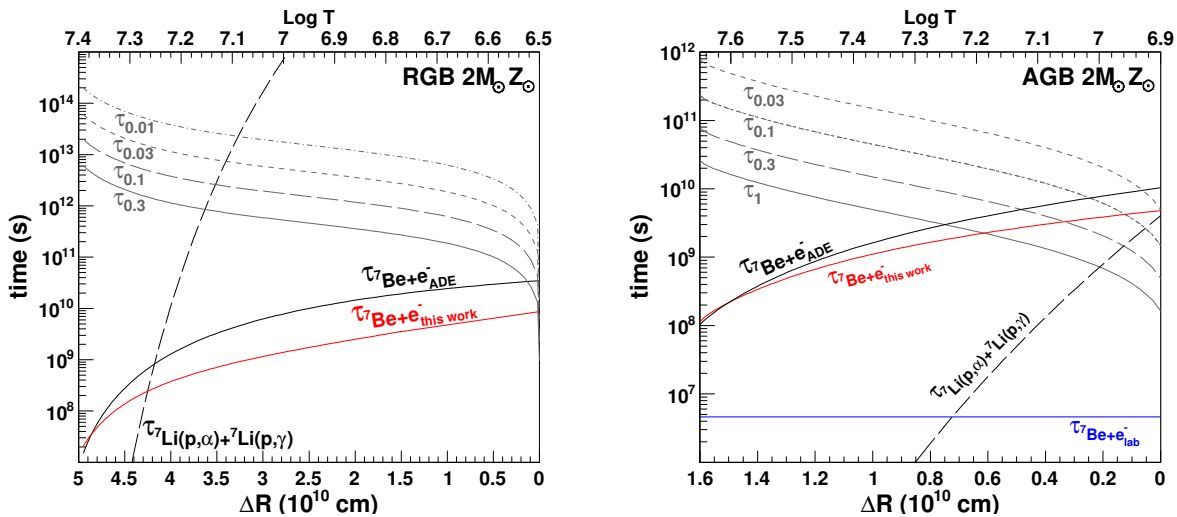


FIGURE 9.4: A comparison between our life-time for ${}^7\text{Be}$, $\tau_{\text{Be}e}$ (red line) and the one extrapolated from [496] (black line) with the time scales of non-convective mixing at various rates (labelled by the mixing rate in units of $10^{-6} M_{\odot}/\text{yr}$) in the radiative layers between the H-burning shell and the base of the convective envelope, for a star with $2 M_{\odot}$ and solar metallicity. Panel a) presents a typical situation for the RGB phase, while panel b) is instead typical of AGB conditions.

9.5 Conclusions

In this chapter we have presented a revision of the methods normally employed for estimating electron captures and, more in general, the electron density near a nucleus in a stellar plasma. For this scope we have devised an *ab-initio* technique, based on a formalism that goes beyond the previously-adopted ones. In our method, we firstly reduced the

complicated many-body problem by a screened two-body scattering model, by using an “adiabatic” factorization of the eigenfunctions, resembling the Born-Oppenheimer (BO) approximation. We did that by fixing the reference frame into the ${}^7\text{Be}$ nucleus and then writing the different parts of the Hamiltonian in this frame. The frame itself was considered as non-inertial, to account for the possibility that ${}^7\text{Be}$ be in motion in a rather complex way. In this coordinate transformation, the non-inertiality translated into some technical complicacy, with the need of considering the ensuing apparent forces. The mathematical details of this procedure were presented in Appendix A. In our Hamiltonian we then had to include the electron kinetic and the electron-Be potential energies, the proton kinetic and proton-Be potential energies, the Be kinetic energy, the electron-proton, electron-electron, proton-proton interactions. Furthermore, we also had to consider two-particle kinetic terms, which identify the coordinates of the j -electron and J -proton relative to the ${}^7\text{Be}$ coordinate. In particular, the conditions under which the two terms coupling the Be and plasma momenta must be considered carefully, as this is crucial for the application of our mean-field treatment. We then looked for separable eigensolutions and wrote the wavefunction factorization in a way different from the usual formulation of the BO approximation. Indeed, at variance with that approach, in our method there is neither the need that the electronic potential energy surfaces be widely separated, nor that there is a mass scale difference among the particles. By introducing the two-body framework and the relative coordinate system, we achieved two main results. The first one is that in our approach the ${}^7\text{Be}$ nucleus is free to move around (thus overcoming the limitations of the Born-Oppenheimer scheme); the second one is that the two-body electron- ${}^7\text{Be}$ density-matrix can be factorized as the product of two one-body density-matrices and thus it is possible to introduce different schemes of approximations to the many-body interaction, including the Hartree-Fock’s one. Then, the screening effects due to all the fermions of the environment, which modify the electron- ${}^7\text{Be}$ scattering, were taken into account, using standard many-body techniques.

By comparing our results with those obtained at various levels of simplification of the theory we showed that, while the traditional DH approximation yields reliable results for the solar core, where both high temperature and high density conditions exist, such simplified methods do not always hold in stellar evolution. In particular, in the low density and temperature environments characterizing partial H-burning above the H-shell in Red Giants, where lithium undergoes important depletion, we showed that our general method should be used and that extrapolations from existing e^- -capture rates on ${}^7\text{Be}$ in the Sun are not applicable.

As an example of the astrophysical consequences of our new method we recomputed, for a star of $M = 2M_{\odot}$ and solar metallicity, the evolution of the surface Li abundance in presence of deep mixing mechanisms. While, for RGB phases, with the new technique we re-obtain previously known results, on the AGB (where the density drops more remarkably) a stronger Li depletion was obtained and it was shown that high Li abundances (as observed e.g. in CJ-type carbon-rich giants) cannot be the result of extra-mixing occurring in single stars, but need more intricate evolutionary paths, as already speculated in the past from other chemical peculiarities of these objects.

Apart from the limited example presented in this chapter, our method yields, in the regions characterized by temperatures of one to a few 10^7K and moderate densities (from 1 to $30\text{-}40\text{ g/cm}^3$) higher values of the electron density at the nucleus than the DH approach. These conditions are not relevant for the solar core, but are important in red giant stars

and in sub-envelope layers of MS stars. This should have the effect of enhancing, in those astrophysical environments, the electron screening, thus favoring thermonuclear fusion. Such a possibility may be especially important for light nuclei (like Li, or ^3He), burning at relatively low temperature and that are related to crucial cosmological problems, like the explanation of the gradual ^3He consumption in the Universe and of the huge Li destruction below the surface of main sequence stars, including our Sun.

9.6 Appendix A: Transformation to relative coordinates

The calculation of the electron-capture decay rate in a many-body system is a difficult task, thus we propose to use an “adiabatic” approximation of the Hamiltonian, which resembles the widely used Born-Oppenheimer approach.

In order to derive the equation of motion for the fermions in the coordinate system relative to the ^7Be nucleus, we will consider a model system composed by a single ^7Be atom surrounded by N_p protons and N_e electrons. The Hamiltonian of such system in the laboratory frame can be written:

$$\begin{aligned}
H = & -\frac{1}{2M_{Be}}\nabla_{Be}^2 + \sum_{j=1}^{N_e} \left(-\frac{1}{2m_e}\nabla_{e,j}^2 \right) + \sum_{J=1}^{N_p} \left(-\frac{1}{2m_p}\nabla_{p,J}^2 \right) - \sum_{j=1}^{N_e} \frac{Z_{Be}}{|\mathbf{R}_{Be} - \mathbf{r}_{e,j}|} \\
& + \sum_{J=1}^{N_p} \frac{Z_{Be}}{|\mathbf{R}_{Be} - \mathbf{R}_{p,J}|} - \sum_{j=1}^{N_e} \sum_{J=1}^{N_p} \frac{1}{|\mathbf{r}_{e,j} - \mathbf{R}_{p,J}|} + \sum_{j=1}^{N_e} \sum_{k=j+1}^{N_e} \frac{1}{|\mathbf{r}_{e,j} - \mathbf{r}_{e,k}|} \\
& + \sum_{J=1}^{N_p} \sum_{K=J+1}^{N_p} \frac{1}{|\mathbf{R}_{p,J} - \mathbf{R}_{p,K}|} \tag{9.12}
\end{aligned}$$

By performing the following transformation to the ($^7\text{Be}-e^-$ and $^7\text{Be}-p^+$) relative coordinates

$$\begin{aligned}
\mathbf{R}'_{Be} &= \mathbf{R}_{Be}, & \mathbf{r}'_{e,j} &= \mathbf{r}_{e,j} - \mathbf{R}_{Be}, & \mathbf{R}'_{p,J} &= \mathbf{R}_{p,J} - \mathbf{R}_{Be} \\
\nabla_{Be} &= \nabla'_{Be} - \sum_{J=1}^{N_p} \nabla'_{p,J} - \sum_{j=1}^{N_e} \nabla'_{e,j}, & \nabla'_{e,j} &= \nabla_{e,j}, & \nabla'_{p,J} &= \nabla_{p,J} \tag{9.13}
\end{aligned}$$

one obtains:

$$\begin{aligned}
H = & \sum_{j=1}^{N_e} \left(-\frac{1}{2m_e} - \frac{1}{2M_{Be}} \right) \nabla_{e,j}^{\prime 2} + \sum_{J=1}^{N_p} \left(-\frac{1}{2m_p} - \frac{1}{2M_{Be}} \right) \nabla_{p,J}^{\prime 2} - \sum_{j=1}^{N_e} \frac{Z_{Be}}{|\mathbf{r}'_{e,j}|} + \sum_{J=1}^{N_p} \frac{Z_{Be}}{|\mathbf{R}'_{p,J}|} \\
& - \sum_{j=1}^{N_e} \sum_{J=1}^{N_p} \frac{1}{|\mathbf{r}'_{e,j} - \mathbf{R}'_{p,J}|} + \sum_{j=1}^{N_e} \sum_{k=j+1}^{N_e} \frac{1}{|\mathbf{r}'_{e,j} - \mathbf{r}'_{e,k}|} + \sum_{J=1}^{N_p} \sum_{K=J+1}^{N_p} \frac{1}{|\mathbf{R}'_{p,J} - \mathbf{R}'_{p,K}|} - \frac{1}{2M_{Be}} \nabla_{Be}^{\prime 2} \\
& - \sum_{\substack{J,J'=1 \\ J \neq J'}}^{N_p} \left(\frac{1}{M_{Be}} \nabla'_{p,J} \cdot \nabla'_{p,J'} \right) - \sum_{\substack{j,j'=1 \\ j \neq j'}}^{N_e} \left(\frac{1}{M_{Be}} \nabla'_{e,j} \cdot \nabla'_{e,j'} \right) - \frac{1}{M_{Be}} \sum_{j=1}^{N_e} \sum_{J=1}^{N_p} \nabla'_{p,J} \cdot \nabla'_{e,j} \\
& + \sum_{j=1}^{N_e} \left(\frac{1}{M_{Be}} \nabla'_{e,j} \cdot \nabla'_{Be} \right) + \sum_{J=1}^{N_p} \left(\frac{1}{M_{Be}} \nabla'_{p,J} \cdot \nabla'_{Be} \right)
\end{aligned} \tag{9.14}$$

Within this model the ${}^7\text{Be}$ nucleus plays the role of the heavy nucleus in the BO approximation, moving more slowly than the light particles (electrons and protons).

Eq. (9.14) can be simplified by neglecting all the inter-particle coupling terms, which are divided by the Be mass (M_{Be}). However, the last two terms in Eq. (9.14) are special as they couple the Be nucleus and plasma momenta. Thus, we need to find the conditions under which these two coupling terms can be neglected as this is crucial for the application of our mean-field treatment. To determine when this is possible, one can notice that the two-body density-matrix of the system in relative coordinates at temperature T is given by:

$$\mathcal{Z} = \frac{1}{Z} \sum_{\alpha} \int \frac{d\mathbf{k}}{(2\pi)^3} e^{-\frac{E_{r,\alpha\mathbf{k}}}{k_B T}} e^{-\frac{1}{2M_{Be}} \frac{k^2}{k_B T}} |\Phi_{\alpha,\mathbf{k}} \rangle \langle \Phi_{\alpha,\mathbf{k}}| \otimes |\chi_{\mathbf{k}} \rangle \langle \chi_{\mathbf{k}}| \tag{9.15}$$

where α identifies the electronic quantum numbers, $E_{r,\alpha\mathbf{k}}$ are the eigenvalues of the secular problem for Φ , and Z is the canonical partition function. The exponential term in Eq. (9.15) kills the integral, unless:

$$k \sim \sqrt{2M_{Be}k_B T} \tag{9.16}$$

Using Eq. (9.16), the two coupling terms in Eq. (9.6) are of the order of $|\frac{1}{M_{Be}} \mathbf{k} \cdot \nabla'_{e,j}| \simeq 2\sqrt{k_B T K_e m_e / M_{Be}}$ and $|\frac{1}{M_{Be}} \mathbf{k} \cdot \nabla'_{p,j}| \simeq 2\sqrt{k_B T K_p m_p / M_{Be}}$, where K_e and K_p are the electron and proton kinetic energies, respectively. Therefore, if the two conditions

$$4k_B T m_e / M_{Be} \ll K_e, \quad 4k_B T m_p / M_{Be} \ll K_p \tag{9.17}$$

hold, then $\left(-\frac{i}{m_e} \mathbf{k} \cdot \nabla'_{e,j} \right)$ and $\left(-\frac{i}{m_p} \mathbf{k} \cdot \nabla'_{p,j} \right)$ are negligible. These conditions are generally satisfied, due the presence of the Be mass in the denominator and to the fact that the scalar products $\left(-\frac{i}{m_e} \mathbf{k} \cdot \nabla'_{e,j} \right)$ and $\left(-\frac{i}{m_p} \mathbf{k} \cdot \nabla'_{p,j} \right)$ contain the cosine of the reciprocal direction of the two multiplying vectors, which, on average, is very small. Finally, the last three terms of the Hamiltonian (9.14) can be safely neglected as they contain a multiplying factor proportional to the inverse of the Be mass.

9.7 Appendix B: The Thomas–Fermi and Debye–Hückel models

The widely used DH model can be obtained via a two-step approximation starting from the TF theory of the electron gas. The TF model is a simplified HF theory, in which the electron gas is treated within the local density approximation (LDA), so that a large number of electrons is needed in a region where the potential is nearly constant. In this theory the density is thus diagonal in the electron coordinates:

$$\rho_{j,\alpha\alpha'}(\mathbf{r}, \mathbf{r}') = \rho_{j,\alpha\alpha'}(\mathbf{r})\delta(\mathbf{r} - \mathbf{r}') \quad (9.18)$$

$$\rho_{j,\alpha\alpha'}(\mathbf{r}) = \int \frac{d\mathbf{p}}{(2\pi)^3} \frac{\psi_{j,\alpha\mathbf{p}}\psi_{j,\alpha'\mathbf{p}}}{e^{\epsilon_{j,\mathbf{p}}} + 1} \quad (9.19)$$

and can be obtained by the self-consistent solution of the TF equation:

$$-\frac{p_j^2}{2m_j}\psi_{j,\alpha\mathbf{p}} + V_{j,\mathbf{p}}^{ext}(\mathbf{r})\psi_{j,\alpha\mathbf{p}} - \mu_j\psi_{j,\alpha\mathbf{p}} + \sum_{\beta} V_{j,\alpha\mathbf{p}\beta\mathbf{p}}^{HF}\psi_{j,\beta\mathbf{p}} = \epsilon_{j,\mathbf{p}}\psi_{j,\alpha\mathbf{p}} \quad (9.20)$$

where $V_{j,\mathbf{p}}^{ext}(\mathbf{r})$ is the electron-nucleus interaction, μ is the chemical potential, α, α' identify the electron quantum numbers and

$$V_{j,\alpha\alpha'}^{HF}(\mathbf{r}, \mathbf{r}') = \delta(\mathbf{r} - \mathbf{r}') \sum_{j'\beta\beta'} \int d\mathbf{s} g_{j\alpha\beta,j'\alpha'\beta'}(\mathbf{r} - \mathbf{s}) \rho_{j',\beta\beta'}(\mathbf{s}, \mathbf{s}) - \sum_{\beta\beta'} g_{j\alpha\beta,,j\beta'\alpha'}(\mathbf{r} - \mathbf{r}') \rho_{j,\beta\beta'}(\mathbf{r}, \mathbf{r}') \quad (9.21)$$

. Here g is the bare Coulomb potential.

In order to obtain the DH approximation, in the first step one substitutes the quantum-mechanical Fermi-Dirac statistics with the classical Boltzmann distribution, while, in a second step, the high-temperature (weak coupling) limit is obtained by Taylor expanding at the first order the exponential distribution:

$$\rho_j(\mathbf{r}) = \int \frac{d\mathbf{p}}{(2\pi)^3} e^{-\beta \left[\frac{p_j^2}{2m_j} + q_j\Phi(\mathbf{r}) - \mu_j \right]} \quad (9.22)$$

In this way one obtains the DH equation for a neutral plasma as follows:

$$\nabla^2\Phi = \lambda_D\Phi \quad (9.23)$$

where

$$\Phi(\mathbf{r}) = \sum_{j'} \int d\mathbf{r}' \frac{q_{j'}\rho_j(\mathbf{r}')}{|\mathbf{r} - \mathbf{r}'|}$$

In Eq. (9.23), the DH length is defined by $\lambda_D = (\epsilon_r\epsilon_0k_B T / \sum_{j=1}^N \rho_j^0 q_j^2)^{\frac{1}{2}}$, where k_B is the Boltzmann constant, ρ_j^0 is the mean charge density of the species j , ϵ_r and ϵ_0 are the relative and vacuum dielectric constants. In this framework, λ_D sets the characteristic length scale for the variation of the potential and of the charge concentration.

Table 2

ρ (g/cm^3)	T ($10^6 K$)	λ_{Debye} a.u.	$\lambda_{DeBroglie}$ ($e-p$)	$\rho_{HF}(0)$ a.u.	$\rho_{TF}(0)$	$\rho_B(0)$	$\rho_{DH}(0)$
1000.		0.038		71.87 \div 71.97	68.99 \div 69.11	42.61 \div 42.74	47.46 \div 47.55
100.		0.119		33.52 \div 33.53	29.53 \div 29.55	4.027 \div 4.031	19.13 \div 19.14
10.		0.377		17.37 \div 17.37	13.83 \div 13.83	0.945 \div 0.945	13.33 \div 13.33
1.	1.	1.193	1.409 - 0.0329	7.839 \div 7.837	5.708 \div 5.707	0.184 \div 0.184	8.151 \div 8.149
0.1		3.771		1.940 \div 1.940	1.415 \div 1.415	0.044 \div 0.044	2.059 \div 2.058
0.01		11.93		0.278 \div 0.278	0.220 \div 0.220	0.0075 \div 0.0075	0.279 \div 0.279
0.001		37.71		0.0308 \div 0.0308	0.0264 \div 0.0264	0.0012 \div 0.0012	0.0303 \div 0.0303
1000.		0.119		122.43 \div 122.89	116.21 \div 116.68	51.77 \div 52.05	108.56 \div 109.01
100.		0.377		20.23 \div 20.27	19.53 \div 19.57	10.36 \div 10.39	19.54 \div 19.58
10.		1.193		2.578 \div 2.581	2.554 \div 2.558	2.515 \div 2.519	2.570 \div 2.573
1.	10.	3.771	0.445 - 0.0103	0.274 \div 0.275	0.274 \div 0.275	0.274 \div 0.274	0.274 \div 0.275
0.1		11.93		0.0281 \div 0.0282	0.0281 \div 0.0282	0.0281 \div 0.0282	0.0281 \div 0.0281
0.01		37.71		(2.84 \div 2.84) $\cdot 10^{-3}$	(2.84 \div 2.84) $\cdot 10^{-3}$	(2.84 \div 2.84) $\cdot 10^{-3}$	(2.83 \div 2.83) $\cdot 10^{-3}$
0.001		119.3		(2.84 \div 2.84) $\cdot 10^{-4}$			
1000.		0.377		78.31 \div 80.39	78.24 \div 80.32	76.57 \div 78.64	78.22 \div 80.30
100.		1.193		9.051 \div 9.289	9.051 \div 9.288	9.031 \div 9.268	9.051 \div 9.288
10.		3.771		0.773 \div 0.787	0.773 \div 0.787	0.773 \div 0.787	0.773 \div 0.787
1.	100.	11.93	0.141 - 0.0033	0.0775 \div 0.0789	0.0775 \div 0.0789	0.0775 \div 0.0789	0.0775 \div 0.0789
0.1		37.71		(7.75 \div 7.90) $\cdot 10^{-3}$			
0.01		119.3		(7.75 \div 7.90) $\cdot 10^{-4}$			
0.001		377.1		(7.75 \div 7.90) $\cdot 10^{-5}$			

Values of the electron density $\rho_e(0)$ (in atomic units) at the Be nucleus, for different theoretical approaches (see text for explanations)

Chapter 10

Final conclusions and future developments

10.1 Bird's eye view on the achieved results

The first and foremost goal of the present work was to develop novel theoretical and computational methods and use state-of-the-art techniques in electronic structure theory to interpret a specific set of physical problems mainly related, but not limited to, materials science. Our guiding principle was to relate information obtained from scattering experiments with the numerical solution of the multichannel dynamics of many-body systems, shedding light on the origin of electronic and optical properties of a variety of systems. The general approach adopted in this thesis, which should be clear to the reader, was not to present separate chapters for theory, rather we introduced methods along with the experiments.

In particular, we focused on the modeling of both ground and excited states of materials, on vibrational, core and valence electron spectroscopy of condensed matter systems using computational methods at different level of accuracy and complexity to interpret a number of experimental data. While these methods have been devised for this scope, their applicability, notably the treatment of the continuum states through multichannel scattering formalism, is totally general and can be applied to describe several different experiments, performed with a variety of apparently distant techniques. In particular, the Fano–Feshbach discrete-continuum interaction provides a common framework suitable to this task.

Within this scheme, thus, the calculation of the spectral lineshapes measured by XPS, Auger, NEXAFS, and EEL spectroscopy can be reconciled on the same theoretical grounds with the investigation of the properties of ultra-cold Fermi gases at unitarity, or of the electronic capture and decay rate in ultra-hot plasma found in stellar environments or, finally, with the study of the epitaxial growth of nanostructured materials.

Crossing the borders between several computational, theoretical and experimental techniques, this thesis should be of interest to a broad community, including those interested in aspects of atomic and molecular physics, electronic structure calculations, experimental and theoretical spectroscopy, astrophysics and scattering theorists in a broad sense.

Finally, during the PhD course I visited abroad two leading Institutions for about a year on personal awarded grants. In the following final sections I will outline the motivation of these visiting periods at University College London (London, UK) and Université Pierre et Marie Curie (Paris, FR) and the achieved results.

10.2 Visiting London for solving the puzzle of SiC growth by SuMBE

This visit was made it possible through the joint economical support of the Provincia Autonoma di Trento and the ‘People Programme’ of the 7th FP, under the Marie-Curie Action ‘Trentino programme of research, training and mobility of post-doctoral researchers – Outgoing Researcher’ (2Superb project).

This project aimed to lay the foundation of a comparative theoretical method for studying the epitaxy and electronic properties of carbon-based materials on inorganic surfaces from first principle calculations. In particular, the goal was to investigate two specific case studies of high scientific interest. Firstly, to lay the foundation of a growth model of graphene grown by Chemical Vapour Deposition (CVD) on Ni(111) and to study the electronic properties of pristine and doped graphene on Ni(111). Secondly, to study the epitaxy of silicon carbide (SiC) grown via Supermolecular Beam Deposition (SuMBD) technique on a 7×7 reconstructed Si(111) surface.

In the former case, linear dispersion close to Fermi level, reduced dimensionality and ballistic transport at room temperature are a few properties imposing graphene as a paradigm of a conceptually new class of materials, having large spillover effects within high-frequency electronics and spintronics. Experimental results on the epitaxy of graphene on Ni(111) using propene (C_3H_6), point towards a catalytic self-limiting growth model, ending up as soon as the Ni surface is completely filled by the graphene monolayer. While LEED and TEM experiments agree well with this growth model, real-time ARPES results are not well understood in peak position and intensity of the carbon core-level. Therefore, the first goal of our project was to shed some light on the growth of graphene by means of the theoretical interpretation of electron spectra recorded on these system and to investigate the possibility of tuning such properties by hydrogenation. The study of graphene doping by hydrogen, while not planned at the early stage of the project, has been the subject of an intense investigation during my staying at UCL, after the observation of a dispersionless impurity band in hydrogenated graphene.

As a second case study, the growth of SiC by SuMBE technique has been investigated. SiC is one of the most promising and versatile large gap semiconductors, characterized by electronic properties attractive for micro-electronic and sensor device applications in alternative to Si.

Kinetically driven synthesis of SiC obtained by supersonic beams implanted with C_{60} is a very promising technique, able to reduce drastically the growth temperature and increase structural order. Experiments of deposition at high kinetic energy ($\simeq 30\text{-}35$ eV) on Si gave evidence of SiC islands formation at room temperature. Computer simulation performed on these systems are in complete disagreement with experiments. It appears that Si structural order is kept, with no evidence of C_{60} cage breaking, the main effect being superficial permeation up to an energy per atom three times that occurred in experiments.

To interpret this specific set of experimental data, the 7 month visiting period resulted finally in three specific work plans.

- Simulation of the growth of graphene on Ni(111) from ab-initio calculations to find recognizable growth stages. This analysis was aimed to determine the dynamics of chemical bonds, whereas the theoretical analysis of electron spectroscopy measurements has been used to investigate the effect of the substrate on the growth.

- Simulation from first principles of the covalent doping of graphene with hydrogen to investigate the effect of the impurities, impurity band formation and magnetic properties of H-doped graphene.
- Simulation of the epitaxy of SiC on Si(111) from ab-initio calculations at different levels of theory until a reliable description of the C_{60} -silicon surface impact was obtained in agreement with our experiments. Calculations of the electronic properties of fullerene and of the silicon substrate during the experimentally recognizable growth stages were performed in order to gain insight on the growth mechanism.

In the third chapter of this thesis I extensively described our new model of SiC growth, including experiments and theory, to show how the SiC epitaxy on silicon is possible at room temperature and why the C_{60} cage break occurs. The accomplishment of this part occupied the entire visiting period and, due to the complexity of this problem, a further year after that.

In chapter 5 a new model of graphene growth is proposed, along with the calculations of core-level spectra of functionalized graphene. The accomplishment of this part occupied the first three months of my visit to London.

10.3 Ongoing work: the superconductivity puzzle of $C_{60}K_3$

The discovery of superconductivity in alkali-doped organic systems, notably K_3 -doped fullerene [508, 509] and picene [510] paved the way to a new research area owing to the richness of the organic chemistry and the potential exploitation of their chemical functionalization. The study of the superconducting properties of K_3 -doped fullerene, which belongs to the broader area of strongly correlated systems, has been the subject of the investigation during my double visit to the Institut de Minéralogie et de Physique des Milieux condensés (IMPMC), Paris. This visit was made possible through a grant provided by the European Science Foundation through the INTELBIOMAT program.

10.3.1 Purpose of the visit to Université Pierre et Marie Curie

This project was aimed at the investigation of the superconductivity in alkali-metal-doped fullerides with the principal goal of introducing me to the existing technology developed at IMPMC for calculating electronic structure, phonons, and electron-phonon coupling in BCS-type superconductors. This goal was reached by revisiting, under the guidance of recognized world-leading experts in this field, the previous work done on the fullerides, carrying out a state-of-the-art DFT study of the electron-phonon coupling in the potassium-doped fullerene solid. Thanks to this work, it will be possible to compute ab-initio the total coupling, for the first time converged in both the electron and phonon momenta.

IMPMC carried out a pioneering theoretical study of the superconductivity in the potassium-doped picene based on the electron-phonon coupling, computed at the density functional theory (DFT) level with Wannier interpolation [511]. There is substantial experimental evidence [510] that the mechanism inducing superconductivity in K-doped picene is phonon-driven with superconductivity appearing at a critical temperature T_c of

18 K. The properties of electron-phonon couplings in K-doped picene were analyzed by exploiting a molecular orbital representation derived in the maximally localized Wannier function formalism. This allows one to separate both the intra- and inter-molecular phonon contributions but also the local and non-local electronic states in the electron-phonon matrix elements. Despite the molecular nature of the crystal, they found out that the purely molecular coupling of the local deformation potential with intra-molecular phonons in K_3 -picene accounts only for 20% of the total electron-phonon interaction λ . The local phonons are indeed strongly screened by the metallic bands of the doped crystal. At variance with previous hypothesis, thus, in K_3 -picene superconductivity comes from non-local couplings due to phonon modulated hoppings. These findings rule out the use of molecular electron-phonon calculations to estimate the total electron-phonon coupling in metallic picene, and possibly in other doped molecular crystals, notably K_3 -fullerene, completely modifying the actual explanation of superconductivity in these compounds.

The purpose of this visit was to investigate the above-mentioned scenario, put forward in the case of K-doped picene, about the possible nature of the phonon-mediated superconductivity in K-doped C_{60} , which offers the advantage to have a much more well-established and clean geometrical structure than hydrocarbon-based materials. Some experimental measurements on K-doped C_{60} powder suggest that the superconductivity in alkali-doped fullerenes can be understood in terms of the electron-phonon interaction for both K- and Rb-doped fullerene, having a T_c of 19.3 K and 28 K, respectively [512], although other experiments in Cs-doped fullerene reveal the proximity of a correlated Mott phase, signaling that strong correlation effects could be important also in the superconducting state [513]. On the theoretical side the situation is less advanced, even though quite a few model calculations were performed on the structural and electronic properties of this system [514], and on the electron-phonon coupling [515]. These studies showed that the observed superconductivity could be mediated or driven by the the strong electron-phonon coupling between the low-energy t_{1u} electronic bands with the highest frequency intra-molecular modes A_g and H_g of fullerene. In the molecular approximation, the electron-phonon coupling λ is factorized into the electronic interball part, setting the density of states, and local intraball phonon quantities. Other theoretical studies supported the idea that electronic correlation is the fundamental ingredient which stabilizes the superconducting state, with the electron-phonon coupling in the molecular approximation providing the attractive channel as an effective exchange term [516].

The molecular approximation picture seems reasonable in light of the molecular nature of the loosely bound fullerenes within the fcc crystal and could be shared among all the molecular crystals presenting superconductivity. However, a full DFT calculation of the electron-phonon coupling in alkali-doped fullerenes with a detailed analysis of the different local and non-local contribution is still missing to date. In particular, the validity of the molecular approximation has never been tested against a full phonon momentum integrated electron-phonon coupling calculation from first-principles. This study, which undoubtedly represents a very interesting theoretical challenge, would allow one to make more strict conclusions on the impact of the total electron-phonon coupling, and specifically on the importance of intermolecular modes. Furthermore, it is of paramount importance in order to devise new types of carbon-based superconducting materials. This problem can be nowadays tackled by using the very recent theoretical development of the Wannier interpolation scheme, implemented in the IMPMC laboratory [517], and with the help of the outstanding HPC French facilities.

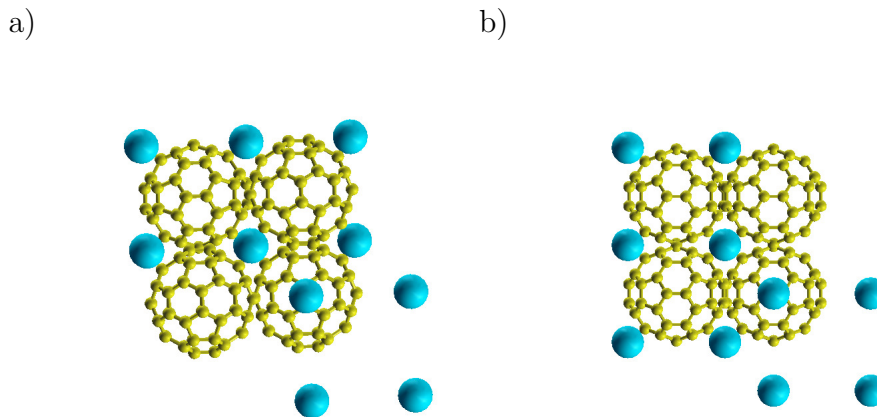


FIGURE 10.1: The equilibrium crystal structure of K_3 -fullerene in the merohedral disordered (left) and in the ordered (right) phases.

10.3.2 Description of the work carried out during the visit and of the results

The first step in any ab-initio calculation of a real material is the assessment of the equilibrium structure. Thus, initially, we performed the structural optimization of K_3C_{60} . It is known from XRD experiment [509] that in K_3C_{60} the fullerenes occupy the sites of a fcc lattice in which two possible orientations of the C_{60} balls can occur, with the bonds shared among hexagons and pentagons oriented along the x or y axis. These two configurations are randomly oriented, giving rise to a merohedral disorder, with the crystal belonging to the $Fm\bar{3}m$ space group. This structure is represented in Fig. 10.1a. In our calculations we neglected this orientational disorder, and considered the fullerenes with the same orientation (x or y) with the structure thus belonging to the $Fm\bar{3}$ space group. The relaxed structure used in all the following calculations is represented in Fig. 10.1b and were obtained by plane-wave calculations using the Quantum Espresso package. This assumption actually allows us to use a smaller simulation cell, containing 63 (60 C and 3 K) instead of 252 atoms. This approximation, other than mandatory for lowering the computational cost of the phonon band calculation, should not have a sizeable impact on the electron-phonon coupling except for slightly changing the hopping between the fullerenes.

However, in order to make sure that the latter approximation does not change the electronic properties, at least at the Fermi level, we performed the DOS calculations for both ordered and merohedral disordered phases. The resulting DOS confirm the validity of our assumption (Fermi energy is shifted at 0 eV) and are plotted in Fig. 10.2. From now onwards, thus we will refer to the orientationally ordered phase only.

In the K_3 -doped fullerene crystal, potassium atoms are incorporated in two distorted tetrahedral and one octahedral interstitial sites, and play only the role of donating electrons to fullerene and increasing the lattice spacing from 14.12 to 14.24 Å with respect to the pristine fullerene crystal. Surprisingly, we discovered that the potassium atom intercalated in the highest symmetric position of the octahedral site, is not stable and a lower-energy structure exists with this potassium moved away. This has been confirmed by our phonon calculation, where we find three negative frequencies corresponding to such potassium instability in this configuration. Test calculations rule out a Jahn-Teller distor-

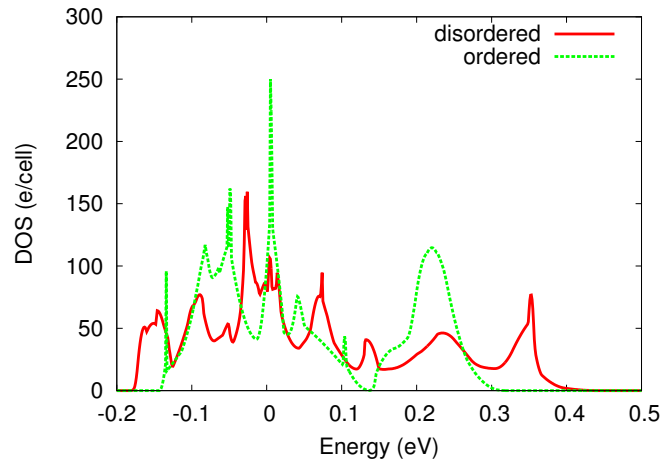


FIGURE 10.2: Density of states of the K_3 -fullerene crystal for the ordered (green dashed line) and merohedral disordered (red line) phases.

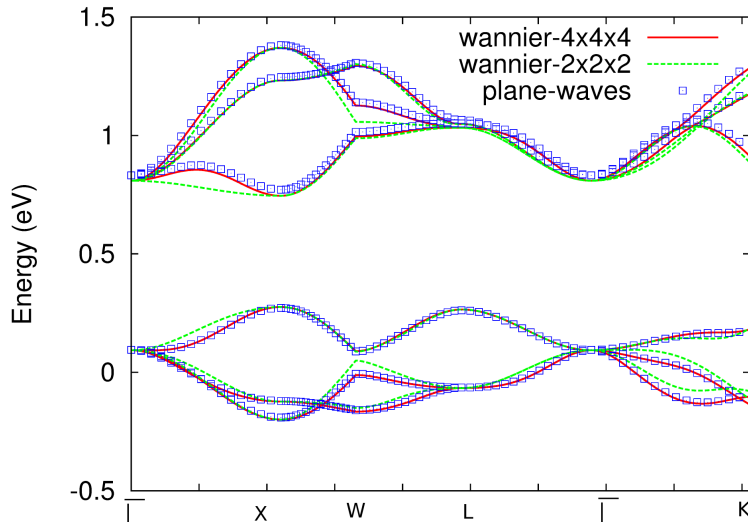


FIGURE 10.3: Band structure of K_3 -fullerene crystal at and above the Fermi level obtained from a plane-wave calculation (empty squares) and derived by Fourier-transforming a MLWF basis set (red line) including 6 states at and above the Fermi level, plotted along the Γ -X-W-L- Γ -K k-space path.

tion mechanism as a reason of this saddle point, and the electron-phonon coupling related to these modes is negligible.

Convergence tests have been performed on both electron (see Fig. 10.3) and phonon bands (see Fig. 10.4). Finally, we decided to use the Local Density Approximation (LDA) for treating the exchange-correlation, norm-conserving pseudo-potentials for C and K to avoid convergence issues with the charge density in the phonon calculation, a kinetic energy cut-off equal to 50 Ry, and a 4x4x4 k-point grid centered at the Gamma point (reduced to 8 points by symmetry) with a Gaussian smearing of 0.003 Ry, which ensure converged results within chemical accuracy and an optimal grid for the Wannier function calculation. The number of valence bands have been reduced to 138 (4 empty bands) to save computational time and improve convergence of the phonon branches.

In Fig. 10.3 we report the band structure calculation for K_3C_{60} along the high-symmetry

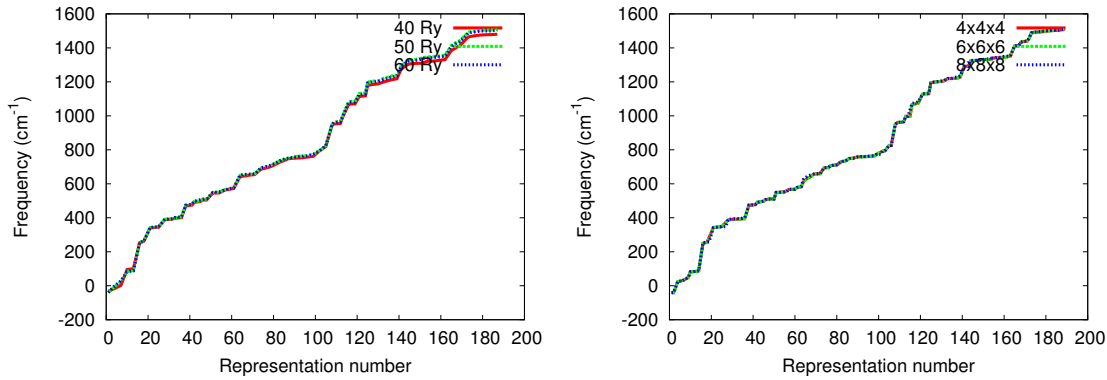


FIGURE 10.4: Phonon frequencies as a function of the kinetic energy cut-off (left) and of the k-point grid for 50 Ry kinetic energy cut-off (right).

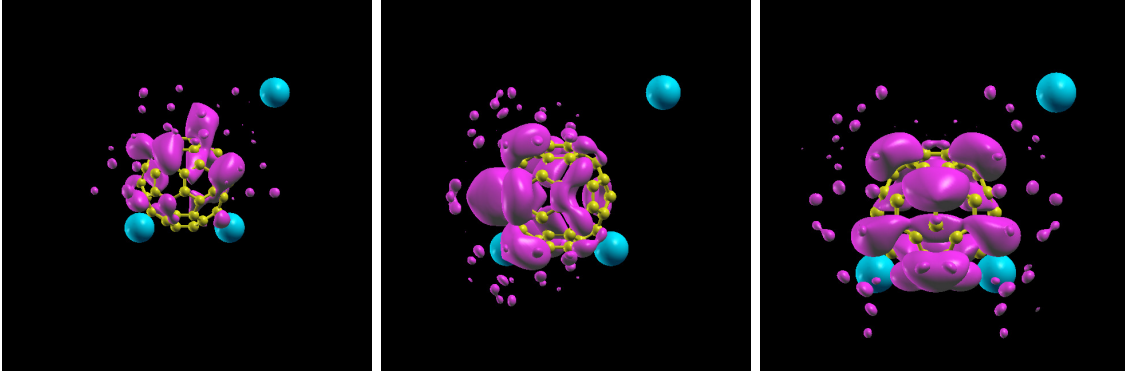
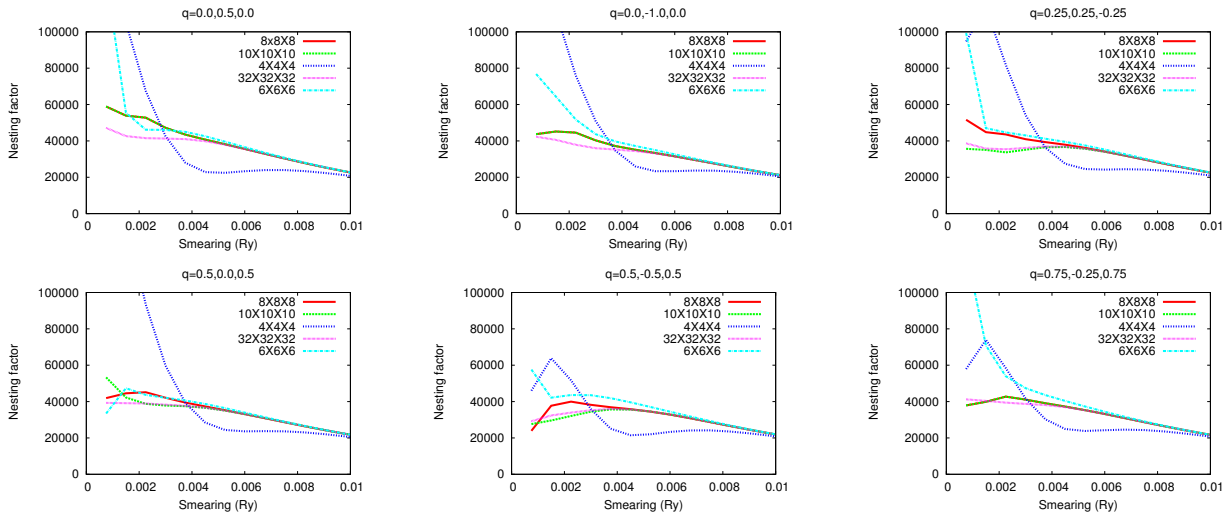


FIGURE 10.5: Molecular maximally localized Wannier functions in real space for the K_3 -fullerene crystal at the Fermi level centered on the fullerene.

points of the fcc crystal group. As by Fig. 10.3 these molecular crystals, once doped, have very narrow bands of about 0.5 eV crossing the Fermi level.

To better understand the interplay between the K_3 -fullerene crystal geometry and the band structure, and to accurately computing the electron-phonon coupling by k-point interpolation, we want to derive a tight-binding model constructed on a Wannier basis set. Therefore, a key step is the Wannierization of the three t_{1u} bands crossing the Fermi level, which has been performed by following the procedure of Marzari and Vanderbilt [215], implemented in the Wannier90 code [518]. The usefulness of this step is twofold: firstly, it allows performing a very dense sampling in the k-integration of the coupling λ , owing to the Wannier interpolation; secondly, it leads to a physical interpretation of the band structure, in terms of hoppings among the localized molecular orbitals. This information can be used to derive a tight-binding Hamiltonian, which will be used in the second part of the project. In order to calculate the maximally localized Wannier functions (MLWF) we had to include both the t_{1u} bands and three higher energy bands due to the a not-so-weak entanglement of the latter with the upper bands and to use a $4 \times 4 \times 4$ k-point grid. Therefore a preliminary disentanglement procedure has been performed, before the Wannier transformation matrix can be obtained. Plots of the Wannier functions in real space and of the band dispersion at the Fermi level, obtained by Fourier-transforming back the Wannier functions to the momentum space, are reported in Figs. 10.3 and 10.5.

FIGURE 10.6: Nesting factors for different q-points as a function of the Gaussian smearing (Ry) and k-point grid.



The second step of our work plan was the assessment of the phonon dispersion on the same $4 \times 4 \times 4$ grid of k-points used in the previous electronic structure calculation. This is needed for the electron-phonon coupling calculation. To make sure that a fairly accurate screening in the phonon calculation is included, we have preliminarily checked the nesting factor, a quantity closely resembling the electron-phonon coupling λ , and related to the bare susceptibility χ_0 , for each point in the q-grid. This calculation, reported in Fig. 10.6, shows that a $8 \times 8 \times 8$ k-point grid with a Gaussian smearing of 0.003 Ry is needed if one is to take into account accurately the electronic screening in the electron-phonon coupling interaction. The result of the phonon calculation, performed within the linear response density functional perturbation theory framework (DFPT) [179], is reported in Fig. 10.7. On the left-hand side the Fourier-interpolated phonon branches from a $2 \times 2 \times 2$ q-point grid are reported in all the frequency range, from low-energy libration modes to high-energy intra-molecular C-C modes. The lowest three frequencies are found to be negative and correspond to the previously mentioned instability of potassium in the interstitial site. On the right-hand side a more insightful comparison between the vibrational DOS and the available inelastic neutron scattering data [519] is presented.

In order to complete the electron-phonon coupling two post-processing steps are still needed: the estimate of the full electron-phonon coupling of the molecular crystal, and the derivation of a low-energy model for correlated many-body calculations in fullerenes with local and non-local electron-phonon couplings (hopping). These two last steps are still the subject of further investigation.

Finally, we would like to comment on the computational cost of performing these calculations. While the ab-initio calculation of λ in molecular crystals are now feasible thanks to the increased computational power of the HPC facilities and to the continuous improving of the algorithms, performed even during the visit, still the computational load for the assessment of the electron-phonon coupling in a large simulation cell is very expensive in terms of both memory resources and computing time. In the specific case of K_3C_{60} , the calculation of the electronic bands - including strict convergence tests - costed around 20.000 CPU hours in a modern super-computer, while the phonon calculation costed four

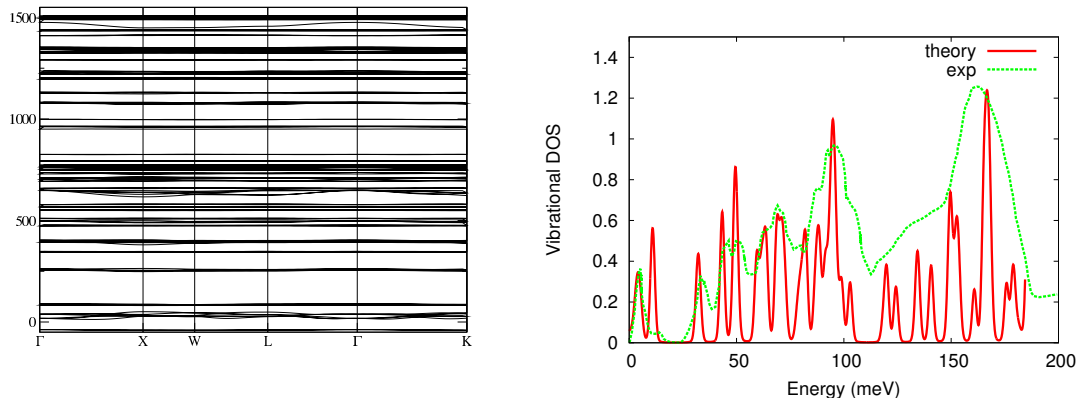


FIGURE 10.7: Left: Phonon branches. Right: vibrational density of states of the K_3 -fullerene crystal as compared to inelastic neutron scattering experiments [519] in a $2X2X2$ grid of q-points for a $8X8X8$ grid of k-points at 0.003 Ry Gaussian smearing.

times as much.

10.3.3 Future collaboration with host institution

This research project has been hosted by IMPMC, where scientists interested in computational modelling of various physical phenomena routinely exchange ideas and develop novel and mutual collaborations, exploiting the methodologies used in different areas of computational science to perform state-of-the-art research in condensed matter physics, notably electron-phonon interaction and many-body theories. Furthermore, the present project overlaps with many research activities in fundamental materials science currently ongoing at the Interdisciplinary Laboratory for Computational Science in Trento, where the applicant moved from. Therefore, while the applicant spent a period of 13 weeks, just necessary to gain knowledge and to develop expertise in electron-phonon coupling calculations from first principles, the accomplishment of the outstanding tasks will certainly require further intense collaboration for the success of this project.

The first task will be to accomplish the calculation of the the electron-phonon coupling by using the Wannier interpolation procedure. On this respect, the opportunity to work in close collaboration with a group that is one of the main contributors to the Quantum-espresso total energy DFT code suite is necessary for reaching the final goal of this investigation. This was one of the particularly appealing aspects of this project, and represented a new opportunity for me, gaining experience in performing large-scale calculations on phonons using linear response rather than the frozen-phonon approach I was used to.

As a second step, which will be part of a further collaborative effort among the two institutions, an effective low-energy model for the fullerenes that includes the one-body part, and the screened couplings of the problem (local Coulomb interaction, and local and non-local electron-phonon coupling) will be derived. In perspective, this will pave the way to further studies, where correlation could be treated by many-body methods, such as dynamical mean field theory or quantum Monte Carlo, applied to the low-energy Hamiltonian. The role of the correlation in screening the phonons using different approaches

is indeed a completely new task, still unclear and debated. This further study is aimed at shedding some light on this point.

10.3.4 Projected publications resulting or to result from the grant

The complexity of the electron-phonon coupling calculation in systems with large simulation cell, the required computational cost, and the post-processing of the obtained results are such that the relatively short period of time spent in Paris was just enough to set-up the working plan, perform the electronic structure DFT calculations, calculate the Wannier basis set and the phonon spectra on a 4X4X4 grid, and, finally, check it with respect to the existing experimental and theoretical data. The actual problem of the assessment of the electron-phonon coupling matrix elements has been just tackled and will be the subject of intense investigation in the nearest future. We plan to release our results as soon as possible after the accomplishment of the *ab-initio* DFT estimate of the full electron-phonon coupling of the molecular crystal and of the derivation of a low-energy model for correlated many-body calculations in fullerenes with local and non-local electron-phonon couplings. This work will of course include information on all the tests performed and the results obtained on electronic structure, Wannier bands, dynamical matrix and vibrational density of states above discussed. A second work will deal with the derivation of the tight-binding model for correlated many-body calculations to assess the role of screening in the electron-phonon coupling.

Chapter 11

Paper published during the PhD course and concerning this thesis

1. **“Mixed ab initio quantum mechanical and Monte Carlo calculations of secondary emission from SiO₂ nanoclusters”**
Taioli S. & Simonucci S. & Calliari L. & Filippi M. & Dapor M.
Phys. Rev. B: Cond. Mat. 79:085432. (2009)
2. **“SURPRISES: When ab-initio meets statistics in extended systems”**
Taioli S. & Simonucci S. & Dapor M.
Comp. Sci. Disc. 2:015002 (2009)
3. **“Electronic properties of carbon based nanostructures from GW calculations”**
Taioli S. & Umari P. & De Souza M.M.
Phys. Stat. Sol. 246:1 (2009)
4. **“Tunable bandgap in hydrogenated quasi-free-standing graphene”**
Haberer D. & Vyalikh D.V. & Taioli S. & Dora B. & Farjam M. & Fink J. & Marchenko D. & Pichler T. & Ziegler K. & Simonucci S. & Dresselhaus M. S. & Knupfer M. & Büchner B. & Grüneis A.
NanoLett. 10:3360 (2010)
5. **“Electron spectroscopies and inelastic processes in nanoclusters and solids: theory and experiment”**
Taioli S. & Simonucci S. & Calliari L. & Dapor M.
Phys. Rep. 493:237 (2010)
6. **“Zeolitic Imidazolate Frameworks for CO₂/CH₄ and CO₂/H₂ separation: a computer simulation investigation”**
Garberoglio G. & Battisti A. & Taioli S.
Microporous and Mesoporous Materials 143:46 (2011)

7. **“Direct observation of a dispersionless impurity band in hydrogenated graphene”**
Haberer D. & Petaccia L. & Farjam M. & **Taioli S.** & Jafari S. A. & Nefedov A. & Zhang W. & Calliari L. & Scarduelli G. & Dora B. & Vyalikh D.V. & Pichler T. & Woll Ch. & Alfè D. & Simonucci S. & Dresselhaus M. S. & Knupfer M. & Buchner B. & A. Grüneis A.
Phys. Rev. B 83:165433 (2011)
8. **“Finite-range effects in dilute Fermi gases at unitarity”**
Simonucci S. & Garberoglio G. & **Taioli S.**
Phys. Rev. A 84:043639 (2011)
9. **“Electronic band gaps of semiconductor zig-zag carbon nanotubes from GW calculations”**
Umari P. & Petrenko O. & **Taioli S.** & De Souza M.M.
COMMUNICATIONS: J. Chem. Phys. 136:181101 (2012)
This manuscript was the most downloaded article in May 2012 from JCP.
10. **“Infrared spectroscopy of copper-resveratrol complexes: a joint experimental and theoretical study”**
Chiavarino B. & Crestoni M.E. & Fornarini S. & **Taioli S.** & Mancini I. & Tosi P.
J. Chem. Phys. 137:024307 (2012)
11. **“Epitaxy of Nanocrystalline Silicon Carbide on Si(111) at Room Temperature”**
Verucchi R. & Aversa L. & Nardi M.V. & **Taioli S.** & a Beccara S. & Alfè D. & Nasi L. & Rossi F. & Salviati G. & Nasi L. & Iannotta S.
J. Am. Chem. Soc. 134:17400 (2012)
(2012)
12. **“A scattering view of the Bogoliubov-de Gennes equations”**
Simonucci S. & G. Garberoglio & **Taioli S.**
AIP Conf. Proc. 1485:312 (2012)
13. **“Modeling flexibility in Metal-Organic Frameworks: comparison between Density-Functiona Tight-Binding and Universal Force Field approaches for bonded interactions”**
Garberoglio G. & **Taioli S.**
Microporous and Mesoporous Materials 163:215 (2012)
14. **“Non-adiabatic ab-initio molecular dynamics of Supersonic Beam epitaxy of Silicon Carbide at room temperature”**
Taioli S. & Garberoglio G. & Simonucci S. & a Beccara S. & Aversa L. & Nardi M. & Verucchi R. & Iannotta S. & Dapor M. & Alfè D.
The Journal of Chemical Physics, 138:044701.
This article gained the Journal COVER featured in Volume 138 Issue 4 on 28 January 2013.
15. **“Theoretical Estimates of stellar e^- captures. I. The half-life of ${}^7\text{Be}$ in evolved stars”**

Simonucci S. & **Taioli S.** & Palmer-ini S. & Busso M.
The Astrophysical Journal 764:118 (2013)

16. **“The BEC–BCS crossover in ultracold Fermi gases beyond the contact-potential approximation”**
Garberoglio G. & **Taioli S.** & Simonucci S.
Submitted to European Physical Journal D (2013)
17. **“Electron-phonon driven Superconductivity in K_3C_{60} from first-principles calculations”**
Taioli S. & Casula M. & Calandra M & Mauri F.
Submitted to Phys. Rev. Lett. (2013)

Bibliography

- [1] A. K. Geim and K. S. Novoselov. *Nat. Mater.*, 6:183, 2007.
- [2] S. Giorgini, L.P. Pitaevskii, and S. Stringari. *Rev. Mod. Phys.*, 80(4):1215, 2008.
- [3] G. Margaritondo. *Elements of Synchrotron Light: For Biology, Chemistry, and Medical Research*. Oxford University Press, USA, 2002.
- [4] K. Horiba, H. Ohguchi, H. Kumigashira, M. Oshima, K. Ono, N. Nakagawa, M. Lippmaa, M. Kawasaki, and H. Koinuma. *Rev. Sci. Instrum.*, 74:3406, 2003.
- [5] S. Aksela. *J. Electron. Spectrosc. Rel. Phenom.*, 79:247, 1996.
- [6] S. Aksela, A. Kivimäki, A. Naves de Brito, O.P. Sairanen, S. Svensson, , and J. Väyrynen. *Rev. Sci. Instrum.*, 65:831, 1994.
- [7] R.G. Newton. *Scattering theory of wave and particle*. Springer Verlag, New York, 1982.
- [8] J.R. Taylor. *Scattering theory: the quantum theory of nonrelativistic collisions*. Wiley, 1972.
- [9] J. Stöhr. *NEXAFS Spectroscopy*. Springer-Verlag: Berlin, 1996.
- [10] A. Szabo and N.S. Ostlund. *Modern quantum chemistry*. Dover Publications, New York, 1996.
- [11] R.M. Martin. *Electronic Structure Basic Theory and Practical Methods*. Cambridge University Press, 2004.
- [12] P. García-González and RW Godby. *Physical Review B*, 63(7):075112, 2001.
- [13] A. Schindlmayr, T.J. Pollehn, and R.W. Godby. *Physical Review B*, 58(19):12684, 1998.
- [14] H.A. Bethe and E.E. Salpeter. *Phys. Rev.*, 84:1232, 1951.
- [15] E. Runge and E.K.U. Gross. *Physical Review Letters*, 52(12):997–1000, 1984.
- [16] U. Fano. *Phys. Rev.*, 124(6):1866, 1961.
- [17] D.E. Ramaker. *Critical Reviews in Solid State and Materials Sciences*, 17:211, 1991.
- [18] H. Beutler. *Z. Physik*, 93:177, 1935.

- [19] P. Auger, P. Ehrenfest, R. Maze, J. Daudin, and R. Frèon. *Rev. Mod. Phys.*, 11:288, 1939.
- [20] N. Balakrishnan, C. Kalyanaram, and N. Sathyamurthy. *Phys. Rep.*, 79:280, 1997.
- [21] S. Taioli and J. Tennyson. *J. Phys. B*, 39:4379, 2006.
- [22] R. Colle, D. Embriaco, M. Massini, S. Simonucci, and S. Taioli. *Nuc. Inst. Meth. Phys. Res. B*, 213:65, 2004.
- [23] M. De Crescenzi and M.N. Piancastelli. *Electron scattering and related spectroscopies*. World Scientific, Singapore, 1996.
- [24] P. Defazio, C. Petrongolo, B. Bussery-Honvault, and P. Honvault. *J. Chem. Phys.*, 131:114303, 2009.
- [25] S.C. Althorpe and D.C. Clary. *Ann. rev. phys. chem.*, 54(1):493–529, 2003.
- [26] JD Gorfinkiel, A. Faure, S. Taioli, C. Piccarreta, G. Halmova, and J. Tennyson. *The European Physical Journal D-Atomic, Molecular, Optical and Plasma Physics*, 35(2):231–237, 2005.
- [27] B.A. Lippmann and J. Schwinger. *Phys. Rev.*, 79(3):469, 1950.
- [28] S. Huzinaga and C. Arnau. *Phys. Rev. A*, 1:1285, 1970.
- [29] H.J. Silverstone and M.L. Yin. *J. Chem. Phys.*, 49:2026, 1968.
- [30] D.P. Craig and T. Thirunamachandran. *Molecular Quantum Electro-dynamics*. Academic Press, London, 1984.
- [31] A.F. Starace. *Theory of Atomic Photoionization, Handbuch der Physik*. W. Mehlhorn, Ed. Springer, Berlin, 1980.
- [32] J.D. Jackson. *Classical Electrodynamics*. Wiley, 3 edition, 1998.
- [33] T. Åberg and G. Howat. *Theory of the Auger Effect*, volume 31. S. Fluège and W. Melhorn, Eds., Handbuch der Physik, Springer, Berlin, 1982.
- [34] T. Åberg. *Physica Scripta*, 21:495, 1980.
- [35] G. Howat, T. Åberg, and O. Goscinski. *J. Phys. B*, 11:575, 1978.
- [36] T. Åberg. *Phys. Scr.*, 41:71, 1992.
- [37] G. Breit and E.P. Wigner. *Phys. Rev.*, 49:519, 1936.
- [38] R. Colle and S. Simonucci. *Recent Research Developments in Quantum Chemistry, vol. 2*. S.G.Pandalai (Transworld Research Network), 2001.
- [39] JV Lill, GA Parker, and JC Light. *Chemical Physics Letters*, 89(6):483–489, 1982.
- [40] JC Light, IP Hamilton, JV Lill, et al. *The Journal of chemical physics*, 82:1400, 1985.

- [41] Z. Bacic and J.C. Light. *Annual Review of Physical Chemistry*, 40(1):469–498, 1989.
- [42] MD Feit, JA Fleck Jr, and A. Steiger. *Journal of Computational Physics*, 47(3):412–433, 1982.
- [43] MD Feit and JA Fleck Jr. *The Journal of Chemical Physics*, 78:301, 1983.
- [44] MD Feit and JA Fleck Jr. *The Journal of chemical physics*, 80:2578, 1984.
- [45] D. Kosloff and R. Kosloff. *Journal of Computational Physics*, 52(1):35–53, 1983.
- [46] A. Askar and A.S. Cakmak. *The Journal of Chemical Physics*, 68:2794, 1978.
- [47] MD Feit and JA Fleck Jr. *Applied Optics*, 17(24):3990–3998, 1978.
- [48] MD Feit and JA Fleck Jr. *Applied Optics*, 19:3140, 1980.
- [49] H. Tal-Ezer and R. Kosloff. *The Journal of chemical physics*, 81:3967, 1984.
- [50] C. Lanczos. *J. Res. Nat. Bur. Standards*, 45(4):255–282, 1950.
- [51] H.D. Meyer and G.A. Worth. *Theoretical Chemistry Accounts: Theory, Computation, and Modeling (Theoretica Chimica Acta)*, 109(5):251–267, 2003.
- [52] R.D. Coalson and J.L. Kinsey. *The Journal of chemical physics*, 85:4322, 1986.
- [53] S. Taioli and J. Tennyson. *Computer physics communications*, 175(1):41–51, 2006.
- [54] M.A.L. Marques and E.K.U. Gross. *Annu. Rev. Phys. Chem.*, 55:427–455, 2004.
- [55] S.R. White. *Physical Review Letters*, 69(19):2863–2866, 1992.
- [56] S.R. White. *Physical Review B*, 48(14):10345, 1993.
- [57] G.K.L. Chan and M. Head-Gordon. *The Journal of chemical physics*, 116:4462, 2002.
- [58] MA Martin-Delgado, J. Rodriguez-Laguna, and G. Sierra. *Physical Review B*, 65(15):155116, 2002.
- [59] G.K.L. Chan and M. Head-Gordon. *The Journal of chemical physics*, 118:8551, 2003.
- [60] J. Dukelsky and S. Pittel. *Rep. Prog. Phys.*, 67:513, 2004.
- [61] K.A. Hallberg. *Advances in Physics*, 55(5):477–526, 2006.
- [62] S. Taioli, S. Simonucci, and M. Dapor. *Comput. Sci. Discov.*, 2:015002, 2009.
- [63] R. Colle, D. Embriaco, M. Massini, S. Simonucci, and S. Taioli. *Phys. Rev. A*, 70:042708, 2004.
- [64] S. Taioli, S. Simonucci, L. Calliari, M. Filippi, and M. Dapor. *Phys. Rev. B*, 79:085432, 2009.
- [65] L. Hedin. *Phys. Rev.*, 139:A796, 1965.

- [66] P.Umari, G. Stenuit, and S. Baroni. *Phys. Rev. B*, 79:201104(R), 2009.
- [67] R. McWeeny and B.T. Sutcliffe. *Methods of Molecular Quantum Mechanics*. Academic Press, London, 1969.
- [68] H.P. Kelly. *Phys. Rev. A*, 11:556, 1975.
- [69] H. Körber and W. Mehlhorn. *Z. Phys.*, 191:217, 1966.
- [70] V. Carravetta and H. Ågren. *Phys. Rev. A*, 35:1022, 1987.
- [71] H. Ågren, S. Svensson, and U.I. Wahlgren. *Chem. Phys. Lett.*, 35:336, 1975.
- [72] H. Siegbahn, L. Asplund, and P. Kelfve. *Chem. Phys. Lett.*, 35:330, 1975.
- [73] A. Damascelli, Z. Hussain, and Z.-X. Shen. *Rev. Mod. Phys.*, 75:473, 2003.
- [74] D.A. Shirley. *Phys. Rev. B*, 5:4709, 1972.
- [75] S. Tougaard. *Surf. Sci.*, 139:208, 1984.
- [76] M. Cini. *Solid State Comm.*, 24:681, 1977.
- [77] G.A. Sawatzky. *Phys. Rev. Lett.*, 39:504, 1977.
- [78] J.J. Lander. *Phys. Rev.*, 91:1382, 1953.
- [79] A. Golebiewski and J. Mrozek. *Int. J. Quantum Chem.*, 7:1021, 1973.
- [80] R. Colle, A. Fortunelli, and S. Simonucci. *Nuovo Cimento*, 9:969, 1987.
- [81] L. Eisenbud and E.P. Wigner. *Phys. Rev.*, 72:29, 1947.
- [82] J.C. Phillips and L. Kleimann. *Phys. Rev.*, 116:287, 1959.
- [83] F.P. Larkins. *Appl. Surf. Sci.*, 13:4, 1982.
- [84] E. Antonides, E.C. Janse, and G.A. Sawatzky. *Phys. Rev. B*, 15:1669, 1977.
- [85] M. Cini. *Phys. Rev. B*, 17:2788, 1978.
- [86] G. Trèglia, M. C. Desjonquères, F. Ducastelle, and D. Spanjaard. *J. Phys. C: Solid State Phys.*, 14:4347, 1981.
- [87] M. Kotrla and V. Drchal. *J. Phys.: Condens. Matter*, 1:4783, 1989.
- [88] M. Cini. *Phys. Scr.*, T41:59, 1992.
- [89] W. Nolting, G. Geipel, and K. Ertl. *Phys. Rev. B*, 45:5790, 1992.
- [90] N.D Lang and A.R. Williams. *Phys. Rev. B*, 20:1369, 1979.
- [91] J.E. Houston, J.W. Rogers, Jr., R.R. Rye, F.L. Hutson, and D.E. Ramaker. *Phys. Rev. B*, 34:1215, 1986.

- [92] D.E. Ramaker. *Crit. Rev. Solid State*, 17:211, 1992.
- [93] S. Taioli, S. Simonucci, L. Calliari, and M. Dapor. *Phys. Rep.*, 493:237, 2010.
- [94] L. Calliari, G. Speranza, J.C. Lascovich, and A. Santoni. *Surf. Sci.*, 501(3):253, 2002.
- [95] D. Haberer, DV Vyalikh, S. Taioli, B. Dora, M. Farjam, J. Fink, D. Marchenko, T. Pichler, K. Ziegler, S. Simonucci, et al. *Nano letters*, 10:3360–3366, 2010.
- [96] LJ Saethre, O. Svaeren, S. Svensson, S. Osborne, TD Thomas, J. Jauhiainen, and S. S. Aksela. *Phys. Rev. A*, 55(4):2748, 1997.
- [97] D. Haberer, L. Petaccia, M. Farjam, S. Taioli, SA Jafari, A. Nefedov, W. Zhang, L. Calliari, G. Scarduelli, B. Dora, et al. *Physical Review B*, 83(16):165433, 2011.
- [98] M. L. Ng, R. Balog, L. Hornekær, A. B. Preobrajenski, N. A. Vinogradov, N. Mårtensson, and K. Schulte. *J. Phys. Chem. C*, 114(43):18559–18565, 2010.
- [99] R. Shimizu and Z.J. Ding. *Rep. Prog. Phys.*, 55:487, 1992.
- [100] N.F. Mott. *Proc. R. Soc. London Ser.*, 124:425, 1929.
- [101] M. Dapor. *J. Appl. Phys.*, 79:8406, 1996.
- [102] M. Dapor. *Electron-Beam Interactions with Solids: Applications of the Monte Carlo Method to Electron Scattering Problems*. Springer Tracts in Modern Physics 186, Springer, Berlin, 2003.
- [103] A. Jablonski, F. Salvat, and C.J. Powell. *J. Phys. Chem. Ref. Data*, 33:409, 2004.
- [104] N.F. Mott and H.S.W. Massey. *The Theory of Atomic Collisions*. Oxford University Press, Oxford, 1965.
- [105] G. Holtkamp, K. Jost, F.J. Peitzmann, and J. Kessler. *J. Phys. B*, 20:4543, 1987.
- [106] S.-R. Lin, N. Sherman, and J.K. Percus. *Nucl. Phys.*, 45:492, 1963.
- [107] P.J. Bunyan and J.L. Schönfelder. *Proc. Phys. Soc.*, 85:455, 1965.
- [108] R.H. Ritchie. *Phys. Rev.*, 106:874, 1957.
- [109] R.H. Ritchie and A. Howie. *Phil. Mag.*, 36:463, 1977.
- [110] D.R. Penn. *Phys. Rev. B*, 35:482, 1987.
- [111] J.C. Ashley. *J. Electrons Spectrosc. Relat. Phenom.*, 46:199, 1988.
- [112] F. Yubero and S. Tougaard. *Phys. Rev. B*, 46:2486, 1992.
- [113] A. Cohen-Simonsen, F. Yubero, and S. Tougaard. *Phys. Rev. B*, 56:1612, 1997.
- [114] M. Filippi, L. Calliari, and M. Dapor. *Phys. Rev. B*, 75:125406, 2007.
- [115] B.L. Henke, E.M. Gullikson, and J.C. Davis. *At. Data Nucl. Data Tables*, 54:181, 1993.

- [116] U. Buechner. *J. Phys. C: Sol. State Phys.*, 8:2781, 1975.
- [117] Y. Baba, K. Yamamoto, and T.A. Sasaki. *Surface Science*, 307:896, 1994.
- [118] T. Kashiwakura, H. Araib, N. Kozuka, K. Odagawa, T. Yokohama, A. Kamata, and S. Nakai. *J. Electron Spectrosc. Relat. Phenom.*, 7:207, 1996.
- [119] G.A. van Riessen, S.M. Thurgate, and D.E. Ramaker. *J. Electron. Spectrosc. Relat. Phenom.*, 161:150, 2007.
- [120] D.E. Ramaker. *Phys. Rev. B*, 21:4608, 1980.
- [121] D.E. Ramaker, J.S. Murday, N.H. Turner, G. Moore, M.G. Lagally, and J. Houston. *Phys. Rev. B*, 19:5375, 1979.
- [122] G.L. Harrys. *Properties of Silicon Carbide*. Ed. INSPEC: London, 1995.
- [123] C.R.-Jr. Eddy and D.K. Gaskill. *Science*, 324:1398, 2009.
- [124] S.E. Sadow. *Silicon Carbide Biotechnology*. Elsevier: Amsterdam, 2012.
- [125] P. Ramesh, M.E. Itkis, E. Bekyarova, F. Wang, S. Niyogi, X. Chi, C. Berger, W. de Heer, and R.C. Haddon. *J. Am. Chem. Soc.*, 132:14429, 2010.
- [126] P. Masri. *Surf. Sci. Rep.*, 48:1, 2002.
- [127] G. Scoles. Oxford University Press: Oxford, U.K., 1988.
- [128] P. Milani and S. Iannotta. *Cluster Beam Synthesis of Nano-structured Materials*. Springer-Verlag, Berlin, 1999.
- [129] L. Aversa, R. Verucchi, G. Ciullo, P. Moras, M. Pedio, L. Ferrari, A. Pesci, and S. Iannotta. *Appl. Surf. Science*, 184:350, 2001.
- [130] R. Verucchi, L. Aversa, G. Ciullo, A. Podestà, P. Milani, and S. Iannotta. *Eur. Phys. J. B*, 26:50, 2002.
- [131] G. N. Makarov. *Physics-Uspokhi*, 49:2, 2006.
- [132] A. Wucher and N. Winograd. *Analytical and Bioanalytical Chemistry*, 396:105, 2010.
- [133] G. Fuchs, M. Treilleux, F. Santos Aires, B. Cabaud, P. Melinon, and A. Hoareau. *Phys. Rev. A*, 40:6128, 1989.
- [134] F. Rohmund, E. E. B Campbell, O. Knospe, G. Seifert, and R. Schmidt. *Phys. Rev. Lett.*, 76:3289, 1996.
- [135] T. Raz and R.D. Levine. *Chem. Phys. Lett.*, 226:47, 1994.
- [136] R. J. Beuhler, G. Friedlander, and L Friedman. *Phys. Rev. Lett.*, 63:1292, 1989.
- [137] J. Jakowski, S. Irle, and K. Morokuma. *Phys. Rev. B*, 82:125443, 2010.

- [138] L. Aversa, R. Verucchi, A. Boschetti, A. Podestà, P. Milani, and S. Iannotta. *Eur. Phys. J. B*, 26:509, 2002.
- [139] X. Hu, K. Albe, and R.S. Averback. *J. Appl. Phys.*, 88:49, 2000.
- [140] G. Galli and F. Mauri. *Phys. Rev. Lett.*, 73:3471, 1994.
- [141] John C. Tully. *J. Chem. Phys.*, 137(22):22A301, 2012.
- [142] Jörg Behler, Karsten Reuter, and Matthias Scheffler. *Phys. Rev. B*, 77:115421, Mar 2008.
- [143] Daniel Matsiev, Zhisheng Li, Russell Cooper, Igor Rahinov, Christof Bartels, Daniel J. Auerbach, and Alec M. Wodtke. *Phys. Chem. Chem. Phys.*, 13:8153–8162, 2011.
- [144] Igor Rahinov, Russell Cooper, Daniel Matsiev, Christof Bartels, Daniel J. Auerbach, and Alec M. Wodtke. *Phys. Chem. Chem. Phys.*, 13:12680–12692, 2011.
- [145] K. Sakamoto, D. Kondo, Y. Ushimi, M. Harada, A. Kimura, A. Kakizaki, and S. Suto. *Phys. Rev. B*, 60:2579, 1999.
- [146] M.A.K. Zilani, H. Xu, Y.Y. Sun, X.-S. Wang, and A.T.S. Wee. *Appl. Surf. Sci.*, 253:4554, 2007.
- [147] P. Mèlinon, P. Kéghélian, A. Perez, C. Ray, J. Lermé, M. Pellarin, M. Broyer, M. Boudeulle, B. Champagnon, and J.L. Rousset. *Phys. Rev. B*, 58:16481, 1998.
- [148] C.-C. Liu, C. Lee, K.-L. Cheng, H.-C. Cheng, and T.-R. Yew. *Appl. Phys. Lett.*, 66:168, 1995.
- [149] A. Santoni, J. Lancok, V.R. Dhanak, S. Loreti, G. Miller, and C. Minarini. *Appl. Phys. A*, 81:991, 2005.
- [150] M. De Seta, N. Tomozeiu, D. Sanvitto, and F. Evangelisti. *Surf. Sci.*, 460:203, 2000.
- [151] C. Cepek, P. Schiavuta, M. Sancrotti, and M. Pedio. *Phys. Rev. B*, 60:2068, 1999.
- [152] K. Sakamoto, M. Harada, D. Kondo, A. Kimura, A. Kakizaki, and S. Suto. *Phys. Rev. B*, 58:13951, 1998.
- [153] K. Sakamoto, T. Suzuki, M. Harada, T. Wakita, and S. Suto. *Phys. Rev. B*, 57:9003, 1998.
- [154] P. Moriarty, M.D. Upward, A.W. Dunn, Y.-R. Ma, P.H. Beton, and D. Teehan. *Phys. Rev. B*, 57:362, 1998.
- [155] J. G. Hou, J. Yang, H. Wang, Q. Li, C. Zeng, H. Lin, W. Bing, D. M. Chen, and Q. Zhu. *Phys. Rev. Lett.*, 83:3001, 1999.
- [156] D. Turner and H.J. Shanks. *J. Appl. Phys.*, 70:5385, 1991.

- [157] S. Suto, K. Sakamoto, T. Wakita, C.-W. Hu, and A. Kasuya. *Phys. Rev. B*, 56:7439, 1997.
- [158] U. Starke, J.B. Pendry, and K. Heinz. *Prog. Surf. Sci.*, 52:53, 1996.
- [159] G. Kresse and J. Hafner. *Phys. Rev. B*, 47:558, 1993.
- [160] G. Kresse and J. Hafner. *Phys. Rev. B*, 49:14251, 1994.
- [161] G. Kresse and J. Furthmüller. *Comput. Mater. Sci.*, 6:15, 1996.
- [162] G. Kresse and D. Joubert. *Phys. Rev. B*, 59:1758, 1999.
- [163] P. E. Blochl. *Phys. Rev. B*, 50:17953, 1994.
- [164] J.P. Perdew, K. Burke, and M. Ernzerhof. *Phys. Rev. Lett.*, 77:3865, 1996.
- [165] J. P. Perdew, K. Burke, and M. Ernzerhof. *Phys. Rev. Lett.*, 77:3865, 1996.
- [166] N. D. Mermin. *Phys. Rev.*, 137:A1441, 1965.
- [167] D. Alfè. *Comp. Phys. Comm.*, 118:31, 1999.
- [168] W. M. Foulkes and R. Haydock. *Phys. Rev. B*, 39:12520, 1989.
- [169] T. Frauenheim, G. Seifert, M. Elstner, T. Niehaus, C. Köhler, M. Amkreutz, M. Sternberg, Z. Hajnal, A. Di Carlo, and S. Suhai. *J. Phys.: Condens. Matter*, 14:3015, 2002.
- [170] M. Elstner, D. Porezag, G. Jungnickel, J. Elsner, M. Haugk, T. Frauenheim, S. Suhai, and G. Seifert. *Phys. Rev. B*, 58:7260, 1998.
- [171] T. Frauenheim, G. Seifert, M. Elstner, T. Niehaus, C. Köhler, M. Amkreutz, M. Sternberg, Z. Hajnal, A.D. Carlo, and S. Suhai. *J. Phys.: Condens. Matter*, 14:3015, 2002.
- [172] P. Koskinen and V. Makinen. *Comp. Mat. Sci.*, 47(1):237–253, 2009.
- [173] M. Elstner, D. Porezag, G. Jungnickel, J. Elsner, M. Haugk, T. Frauenheim, S. Suhai, and G. Seifert. *Phys. Rev. B*, 58(11):7260, 1998.
- [174] A. Gromov, S. Ballenweg, S. Lebedkin, W.E. Hull, and W. Krätschmer. *Chem. Phys. Lett.*, 267:460, 1997.
- [175] B. Aradi, B. Hourahine, and T. Frauenheim. *J. Phys. Chem. A*, 111(26):5678–5684, 2007. <http://www.dftb-plus.info/>.
- [176] J. Hutter. *J. Chem. Phys.*, 118:3928, 118.
- [177] W. Andreoni and A. Curioni. *Parallel Computing*, 26:819, 2000.
- [178] J. Tersoff. *Phys. Rev. B*, 37:6991, 1988.

- [179] S. Baroni, S. de Gironcoli, A. Dal Corso, and P. Giannozzi. *Rev. Mod. Phys.*, 73:515, 2001.
- [180] S. Taioli, P. Umari, and M.M. De Souza. *Phys. Stat. Sol.*, 246:2572, 2009.
- [181] P. Umari, O. Petrenko, S. Taioli, and M. M. De Souza. *J. Chem. Phys.*, 136:181101, 2012.
- [182] G. C. Vougioukalakis, M. M. Roubelakis, and M. Orfanopoulos. *Chem. Soc. Rev.*, 39:817, 2010.
- [183] B.L. Zhang, C.Z. Wang, C.T. Chan, and K.M. Ho. *Phys. Rev. B*, 48:11381, 1993.
- [184] S. G. Kim and D. Tomanek. *Phys. Rev. Lett.*, 72:2418, 1994.
- [185] L. Horvath and T. A. Beu. *Phys. Rev. B*, 77:075102, 2008.
- [186] H. Zettergren, H. T. Schmidt, P. Reinhed, N. Haag, D. Fisher, Z. Berenyi, H. Cedergren, J. Jensen, P. Hvelplund, S. Tomita, B. Manil, J. Rangama, , and B.A. Huber. *Journal of Physics: Conference Series*, 88:012039, 2007.
- [187] S. Hunsche, T. Starczewski, A. l’Huillier, A. Persson, C.-G. Wahlström, B. van Linden van den Heuvell, and S. Svanberg. *Phys. Rev. Lett.*, 77:1966, 1996.
- [188] D. Marx and J. Hutter. *Ab Initio Molecular Dynamics*. Cambridge University Press, 2009.
- [189] R. Car and M. Parrinello. *Phys. Rev. Lett.*, 55:2471, 1985.
- [190] L. D. Landau and L. M. Lifshitz. *Quantum Mechanics: Non-relativistic theory*. Butterworth–Heinemann, 3rd edition, 1977.
- [191] C. Zener. *Proc. R. Soc. London A*, 137:696, 1932.
- [192] M. Barbatti. *Advanced Review*, 1:620, 2011.
- [193] H.P. Kelly. *Many-Body Perturbation Approaches to the Calculation of Transition Probabilities, Atomic Inner-Shell Transition*. Ed. by B. Crasemann, Academic Press, New York, 1975.
- [194] Rainer D. Beck, Jörg Rockenberger, Patrick Weis, and Manfred M. Kappes. *J. Chem. Phys.*, 104:3638–3650, 1996.
- [195] S. Suhai and G. Seifert. *J. Chem. Phys.*, 132:111102, 2010.
- [196] D. Spataru, S. Ismail-Beigi, L.X. Benedict, and S.G. Louie. *Phys. Rev. Lett.*, 92:077402, 2004.
- [197] R.B. Weisman and S.M. Bachilo. *Nano Lett.*, 3:1235, 2003.
- [198] G. Dukovic, F. Wang, D. Song, M.Y. Sfeir, T.F. Heinz, and L.E. Brus. *Nano Lett.*, 5:2314, 2005.

- [199] J. Deslippe, M. Dipoppa, D. Predergast, M.V.O. Moutinho, R.B. Capaz, and S.G. Louie. *Nano Lett.*, 9:1130, 2009.
- [200] W.G. Aulbur, L. Jönsson, and J.W. Wilkins. *Sol. State Phys.*, 54:1, 2000.
- [201] Y.W. Son, M.L. Cohen, and S.G. Louie. *Phys. Rev. Lett.*, 97:216803, 2006.
- [202] L.J. Sham and M. Schlüter. *Phys. Rev. Lett.*, 51:1888, 1983.
- [203] F. Aryasetiawan and O. Gunnarson. *Rep. Prog. Phys.*, 61:237, 1998.
- [204] R.E. Stratmann, G.E. Scuseria, and M.J. Frisch. *J. Chem. Phys.*, 109:8218, 1998.
- [205] M. Petersilka, UJ Gossmann, and EKV Gross. *Phys. Rev. Lett.*, 76(8):1212–1215, 1996.
- [206] M. Cossi and V. Barone. *J. Chem. Phys.*, 115:4708, 2001.
- [207] *J. Chem. Phys.*, 10:5134, 1996.
- [208] G. Onida, L. Reining, and A. Rubio. *Rev. Mod. Phys.*, 74:601, 2002.
- [209] H.N. Rojas, R.W. Godby, and R.J. Needs. *Phys. Rev. Lett.*, 74:1827, 1995.
- [210] W. Kang and M. S. Hybertsen. *Phys. Rev. B*, 82:195108, 2010.
- [211] T. Miyake and S. Saito. *Phys. Rev. B*, 68:155423, 2003.
- [212] E. Chang, G. Bussi, A. Ruini, and E. Molinari. *Phys. Rev. B*, 72:195423, 2005.
- [213] C. Friedrich, M. C. Müller, and S. Blügel. *Phys. Rev. B*, 83:081101(R), 2011.
- [214] P. Umari, G. Stenuit, and S. Baroni. *Phys. Rev. B*, 81:115104, 2010.
- [215] N. Marzari and D. Vanderbilt. *Phys. Rev. B*, 56:12847, 1997.
- [216] P. Umari, O. Petrenko, S. Taioli, and M.M. De Souza. *Comm.: J. Chem. Phys.*, 136:181101, 2012.
- [217] G. Onida L. Reining and A. Rubio. *Rev. Mod. Phys.*, 74:601, 2002.
- [218] M.S. Hybertsen and S.G. Louie. *Phys. Rev. B*, 34:5390, 1986.
- [219] X. Ren, P. Rinke, C. Joas, and M. Scheffler. *J. Mater. Sci.*, 47:7447, 2012.
- [220] F. Bruneval, N. Vast, and L. Reining. *Phys. Rev. B*, 74:045102, 2006.
- [221] M. van Schilfgaarde, T. Kotani, and S. Faleev. *Phys. Rev. Lett.*, 96:226402, 2006.
- [222] C. Rostgaard, K.W. Jacobsen, and K.S. Thygesen. *Phys. Rev. B*, 81:085103, 2010.
- [223] F. Caruso, P. Rinke, X. Ren, M. Scheffler, and A. Rubio. *Phys. Rev. B*, 86:081102(R), 2012.

- [224] M.M. Rieger, L. Steinbeck, I.D. White, H.N. Rojas, and R.W. Godby. *Comp. Phys. Comm.*, 177:211, 1999.
- [225] P. Lautenschlager, M. Garriga, L. Vina, and M. Cardona. *Phys. Rev. B*, 36:4821, 1987.
- [226] F. Sottile. *Ph.D. Thesis presented to École Polytechnique*, 2003.
- [227] L.P. Kadanoff. *Physica*, 2(263):12, 1966.
- [228] K.G. Wilson. *Reviews of Modern Physics*, 47(4):773, 1975.
- [229] S. Daul, I. Ciofini, C. Daul, and S.R. White. *International Journal of Quantum Chemistry*, 79(6):331–342, 2000.
- [230] R. Saito, G. Dresselhaus, and M.S. Dresselhaus. *Physical Properties of Carbon Nanotubes*. Imperial College Press, London, 1998.
- [231] J.P. Perdew and A. Zunger. *Phys. Rev. B*, 23:5048, 1981.
- [232] P. Giannozzi and *et al.* *J. Phys. Condens. Matter*, 21:395502, 2009.
- [233] from the www.quantum-espresso.org website We used the pseudo-potential file: C.pz-vbc.UPF.
- [234] The GWL code can be downloaded from the gww.qe-forge.org website.
- [235] X. Blase, L. X. Benedict, E. L. Shirley, , and S. G. Louie. *Phys. Rev. Lett.*, 72:1878, 1994.
- [236] B. Kozinsky and N. Marzari. *Phys. Rev. Lett.*, 96:166801, 2006.
- [237] C.A. Rozzi, D. Varsano, A. Marini, E.K.U. Gross, and A. Rubio. *Phys. Rev. B*, 73:205119, 2006.
- [238] H. Lin, J. Lagoute, V. Repain, C. Chacon, Y. Girard, J.-S. Lauret, F. Ducastelle, A. Loiseau, and S. Rousset. *Nat. Mat.*, 9:235, 2010.
- [239] M. Rohlfing, P. Rinke, and S.G. Louie. *Phys. Rev. B*, 62:4927, 2000.
- [240] K.S. Novoselov, A.K. Geim, S.V. Morozov, D. Jiang, Y. Zhang, S.V. Dubonos, I.V. Grigorieva, and A.A. Firsov. *Science*, 306:666, 2004.
- [241] A.K. Geim and K.S. Novoselov. *Nat. Mater.*, 6:183, 2007.
- [242] A. Grüneis, C. Attaccalite, T. Pichler, V. Zabolotnyy, H. Shiozawa, S.L. Molodtsov, D. Inosov, A. Koitzsch, M. Knupfer, J. Schiessling, R. Follath, R. Weber, and P. Rudolf. *Phys. Rev. Lett.*, 100:037601, 2008.
- [243] M.I. Katsnelson, K.S. Novoselov, and A. K. Geim. *Nat. Phys.*, 2:620, 2006.
- [244] A.H. Castro-Neto, F. Guinea, N.M.R. Peres, and K.S. Novoselov. *Rev. Mod. Phys.*, 81:109, 2009.

- [245] A. Grüneis and D.V. Vyalikh. *Phys. Rev. B*, 77:193401, 2008.
- [246] A. Nagashima, N. Tejima, and C. Oshima. *Phys. Rev. B*, 50:17487, 1994.
- [247] Y. Gamo, A. Nagashima, M. Wakabayashi, and C. Oshima. *Surf. Sci.*, 374:61, 1997.
- [248] V.M. Karpan, G. Giovannetti, P.A. Khomyakov, M. Talanana, A.A. Starikov, M. Zwierzycki, J. van den Brink, G. Brocks, and P. J. Kelly. *Phys. Rev. Lett.*, 99:176602, 2007.
- [249] M.Y. Han, B. Ozyilmaz, Y. Zhang, and P. Kim. *Phys. Rev. Lett.*, 98:206805, 2007.
- [250] X. Li, X. Wang, L. Zhang, S. Lee, and H. Dai. *Science*, 319:1229, 2008.
- [251] C. Stampfer, E. Schurtenberger, F. Molitor, J. Guttinger, T. Ihn, and K. Ensslin. *Nano Lett.*, 8:2378, 2008.
- [252] Y.-W. Son and S.G. Louie. *Phys. Rev. Lett.*, 97:216803, 2006.
- [253] D.W. Boukhvalov and M.I. Katsnelson. *J. Phys.: Condens. Matter*, 21:344205, 2009.
- [254] M. Farjam and H. Rafii-Tabar. *Phys. Rev.*, 79:045417, 2009.
- [255] S. Ryu, M.Y. Han, J. Maultzsch, T.F. Heinz, P. Kim, M.L. Steigerwald, and L.E. Brus. *Nano Lett.*, 8:4597, 2008.
- [256] F. Schedin, A.K. Geim, S.V. Morozov, E.W. Hill, P. Blake, M.I. Katsnelson, and K.S. Novoselov. *Nat. Mater.*, 6:652, 2007.
- [257] I. Gierz, C. Riedl, U. Starke, C.R. Ast, and K. Kern. *Nano Lett.*, 8:4603, 2008.
- [258] T.O. Wehling, M. Katsnelson, and A.I. Lichtenstein. *Phys. Rev. B*, 80:085428, 2009.
- [259] J. Robertson and E.P. O'Reilly. *Phys. rev. b*. 1987, 35:2496, 1987.
- [260] J. Fink, T. Müller-Heinzerling, J. Pflüger, A. Bubenzer, P. Koidl, and G. Crecelius. *Solid State Commun.*, 47:687, 1983.
- [261] J. Fink, T. Müller-Heinzerling, J. Pflüger, B. Scheerer, B. Dischler, P. Koidl, A. Bubenzer, and R.E. Sah. *Phys. Rev. B*, 30:4713, 1984.
- [262] J.O. Sofo, A.S. Chaudhari, and G.D. Barber. *Phys. Rev. B*, 75:153401, 2007.
- [263] G. Savini, A.C. Ferrari, and F. Giustino. *Phys. Rev. Lett.*, 105:037002, 2010.
- [264] E.J. Duplock, M. Scheffler, and P.J.D. Lindan. *Phys. Rev. Lett.*, 92:225502, 2004.
- [265] D.C. Elias, R.R. Nair, T.M.G. Mohiuddin, S.V. Morozov, R. Blake, M.P. Halsall, A.C. Ferrari, D.W. Boukhvalov, M.I. Katsnelson, A.K. Geim, and K.S. Novoselov. *Science*, 323:610, 2009.
- [266] A. Bostwick, J.L. McChesney, K.V. Emtsev, T. Seyller, K. Horn, S.D. Kevan, and E. Rotenberg. *Phys. Rev. Lett.*, 103:056404, 2009.

- [267] R. Balog and *et al.* *Nat. Mater.*, 9:315, 2010.
- [268] J.P. Robinson, H. Schomerus, L. Oroszl'any, and V.I. Fal'ko. *Phys. Rev. Lett.*, 101:196803, 2008.
- [269] S. Casolo, O.M. Lovvik, R. Martinazzo, and G. F. Tantardini. *J. Chem. Phys.*, 130:054704, 2009.
- [270] M. Amini, S. A. Jafari, and F. Shahbazi. *Europhys. Lett.*, 87:37002, 2009.
- [271] S. Hofmann, R. Sharma, C. Ducati, G. Du, C. Mattevi, C. Cepek, M. Cantoro, S. Pisana, A. Parvez, F. Cervantes-Sodi, A.C. Ferrari, R. Dunin-Borkowski, S. Lizzit, L. Petaccia, A. Goldoni, and J. Robertson. *Nano Letters*, 7:602, 2007.
- [272] A. Grüneis, C. Kramberger, D. Grimm, T. Gemming, M.H. Rummeli, P. Ayala, A. Barreiro, T. Pichler, Ch. Schaman, H. Kuzmany J. Schumann, and B. Büchner. *Chemical Physics Letters*, 425:301, 2006.
- [273] S. Doniach and M. Sunjic. *J. Phys. C: Solid State Phys.*, 3:285, 1970.
- [274] A. Nikitin, H. Ogasawara, D. Mann, R. Denecke, Z. Zhang, H. Dai, K. Cho, and A. Nilsson. *Phys. Rev. Lett.*, 95:225507, 2005.
- [275] A. Nikitin, L.-A. Naslund, Z. Zhang, and A. Nilsson. *Surf. Sci.*, 602:2575, 2008.
- [276] O. Wessely, M.I. Katsnelson, A. Nilsson, A. Nikitin, H. Ogasawara, M. Odelius, B. Sanyal, and O. Eriksson. *Phys. Rev. B*, 76:161402, 2007.
- [277] A. Varykhalov, J. Sanchez-Barriga, A.M. Shikin, C. Biswas, E. Vescovo, A. Rybkin, D. Marchenko, and O. Rader. *Phys. Rev. Lett.*, 101:157601, 2008.
- [278] T. Jones, T. Noakes, P. Bailey, and C. Baddeley. *Surf. Sci.*, 600:2129, 2006.
- [279] S. Höfner. *Photoelectron spectroscopy*. Springer-Verlag, Berlin, 1996.
- [280] A. Grüneis, C. Attaccalite, L. Wirtz, H. Shiozawa, T. Pichler, and A. Rubio. *Phys. Rev. B*, 78:205425, 2008.
- [281] J.A. Vergés and P.L. de Andres. *Phys. Rev. B*, 81:075423, 2010.
- [282] D. W. Boukhvalov, M.I. Katsnelson, and A.I. Lichtenstein. *Phys. Rev. B*, 77:035427, 2008.
- [283] D. Haberer and *et al.* *Nano Lett.*, 10:3360, 2010.
- [284] M.L. Ng. *J. Phys. Chem. C*, 114:18559, 2010.
- [285] S. Yuan, H. De Raedt, and M. I. Katsnelson. *Phys. Rev. B*, 82:115448, 2010.
- [286] A. Ekimov *et al.* *Nature*, 428:542, 2004.
- [287] T. Yokoya. *Nature*, 438:647, 2005.

- [288] J. Nakamura, N. Yamada, K. Kuroki, T. Oguchi, K. Okada, Y. Takano, M. Nagao, I. Sakaguchi, T. Takenouchi, H. Kawarada, R.C.C. Perera, and D.L. Ederer. *J. Phys. Soc. Jpn.*, 77:054711, 2008.
- [289] M.S. Dresselhaus and G. Dresselhaus. *Adv. Phys.*, 30:139, 1981.
- [290] A. Grüneis and *et al.* *Phys. Rev. B*, 80:075431, 2009.
- [291] C. Enderlein, Y. S. Kim, A. Bostwick, E. Rotenberg, and K. Horn. *New J. Phys.*, 12:033014, 2010.
- [292] S. Dedkov and *et al.* *Phys. Rev. B*, 64:035405, 2001.
- [293] S. Dedkov, M. Fonin, U. Rüdiger, and C. Laubschat. *Appl. Phys. Lett.*, 93:022509, 2008.
- [294] J. Barnard, K. Hock, and R. Palmer. *Surf. Science*, 287:178, 1993.
- [295] S. Bunch and *et al.* *Nano Lett.*, 8:2458, 2008.
- [296] S. N. Mott. *Metal Insulator Transitions*. Taylor & Francis, London, 1991.
- [297] T. Gokus, R.R. Nair, A. Bonetti, M. Bohmler, A. Lombardo, K.S. Novoselov, A.K. Geim, A.C. Ferrari, and A. Hartschuh. *Nano*, 3:3963, 2009.
- [298] H. Li, M. Eddaoudi, M. O’Keeffe, and OM Yaghi. *Nature*, 402(6759):276–278, 1999.
- [299] O.M. Yaghi, M. O’Keeffe, N.W. Ockwig, H.K. Chae, M. Eddaoudi, and J. Kim. *Nature*, 423(6941):705–714, 2003.
- [300] M. Eddaoudi, J. Kim, N. Rosi, D. Vodak, J. Wachter, M. O’Keeffe, and O.M. Yaghi. *Science*, 295(5554):469, 2002.
- [301] N.L. Rosi, J. Eckert, M. Eddaoudi, D.T. Vodak, J. Kim, M. O’Keeffe, and O.M. Yaghi. *Science*, 300(5622):1127, 2003.
- [302] A.P. Côté, A.I. Benin, N.W. Ockwig, M. O’Keeffe, A.J. Matzger, and O.M. Yaghi. *Science*, 310(5751):1166, 2005.
- [303] H.M. El-Kaderi, J.R. Hunt, J.L. Mendoza-Cortes, A.P. Côté, R.E. Taylor, M. O’Keeffe, and O.M. Yaghi. *Science*, 316(5822):268, 2007.
- [304] S.S. Han, H. Furukawa, O.M. Yaghi, and W.A. Goddard III. *J. Am. Chem. Soc.*, 130(35):11580–11581, 2008.
- [305] K.S. Park, Z. Ni, A.P. Côté, J.Y. Choi, R. Huang, F.J. Uribe-Romo, H.K. Chae, M. O’Keeffe, and O.M. Yaghi. *Proc. Natl. Acad. Sci.*, 103(27):10186, 2006.
- [306] H. Hayashi, A.P. Côté, H. Furukawa, M. O’Keeffe, and O.M. Yaghi. *Nature Materials*, 6(7):501–506, 2007.
- [307] Bo Wang, Adrien P. Côté, H. Furukawa, M. O’Keeffe, and O. M. Yaghi. *Nature*, 453:207, 2008.

- [308] S.S. Han, J.L. Mendoza-Cortés, and W.A. Goddard III. *Chem. Soc. Rev.*, 38(5):1460–1476, 2009.
- [309] J.R. Li, R.J. Kuppler, and H.C. Zhou. *Chem. Soc. Rev.*, 38(5):1477–1504, 2009.
- [310] S.L. Mayo, B.D. Olafson, and W.A. Goddard III. *J. Phys. Chem.*, 94:8897, 1990.
- [311] A.K. Rappé, C.J. Casewit, K.S. Colwell, W.A. Goddard III, and W.M. Skiff. *J. Am. Chem. Soc.*, 114:10024, 1992.
- [312] G. Garberoglio, A.I. Skoulidas, and J.K. Johnson. *J. Phys. Chem. B*, 109(27):13094–13103, 2005.
- [313] G. Garberoglio. *Langmuir*, 23(24):12154–12158, 2007.
- [314] G. Garberoglio and R. Vallauri. *Micropor. Mesopor. Mater.*, 116(1-3):540–547, 2008.
- [315] S.S. Han, H. Furukawa, O.M. Yaghi, and W.A. Goddard III. *J. Am. Chem. Soc.*, 130(35):11580–11581, 2008.
- [316] E. Klontzas, E. Tylianakis, and G.E. Froudakis. *J. Phys. Chem. C*, 112(24):9095–9098, 2008.
- [317] F. Salles, A. Ghoufi, G. Maurin, R.G. Bell, C. Mellot-Draznieks, and G. Férey. *Angew. Chem. Int. Ed.*, 47:8487, 2008.
- [318] F. Salles, H. Jobic, T. Devic, P.L. Llewellyn, C. Serrë, G. Férey, and G. Maurin. *ACS Nano*, 4(1):143, 2009.
- [319] F. Salles, H. Jobic, A. Ghoufi, P.L. Llewellyn, C. Serre, S. Bourrelly, G. Férey, and G. Maurin. *Angew. Chem.*, 121(44):8485, 2009.
- [320] H. Jobic, N. Rosenbach Jr, A. Ghoufi, D.I. Kolokolov, P. Yot, et al. *Chem. A Europ. J.*, 16(34):10337–10341, 2010.
- [321] D. Fairen-Jimenez, S.A. Moggach, M.T. Wharmby, P.A. Wright, S. Parsons, and T. Duren. *J. Am. Chem. Soc.*, 2011.
- [322] D.C. Ford, D. Dubbeldam, and R.Q. Snurr. *diffusion-fundamentals.org*, 11:78, 2009.
- [323] S. Amirjalayer and R. Schmid. *Micropor. Mesopor. Mater.*, 125:90, 2009.
- [324] K. Seehamart, T. Nanok, R. Krishna, J.M. van Baten, R. Remsungnen, and S. Fritzsche. *Micropor. Mesopor. Mater.*, 125:97, 2009.
- [325] K. Seehamart, T. Nanok, J. Kärger, C. Chmelik, R. Krishna, and S. Fritzsche. *Micropor. Mesopor. Mater.*, 130:92, 2010.
- [326] K. Seehamart, C. Chmelik, R. Krishna, and S. Fritzsche. *Micropor. Mesopor. Mater.*, 143, 2011.
- [327] L. Hertäg, H. Bux, J. Caro, C. Chmelik, T. Remsungnen, M. Knauth, and S. Fritzsche. *J. Memb. Sci.*, 377:36–41, 2011.

- [328] L. Zhao, Q. Yang, Q. Ma, C. Zhong, J. Mi, and D. Liu. *J. Mol. Model.*, 17:227–234, 2011.
- [329] B. Zheng, M. Sant, P. Demontis, and G.B. Suffritti. *J. Phys. Chem. C*, 116(1):933–938, 2012.
- [330] G. Garberoglio Battisti, S. Taioli. *Micropor. Mesopor. Mater.*, 143:46–53, 2011.
- [331] M. Tafipolsky, S. Amirjalayer, and R. Schmid. *J. Comp. Chem.*, 28(7):1169–1176, 2007.
- [332] M. Elstner, K.J. Jalkanen, M. Knapp-Mohammady, T. Frauenheim, and S. Suhai. *Chem. Phys.*, 263(2-3):203–219, 2001.
- [333] G. Zheng, S. Irle, and K. Morokuma. *Chem. Phys. Lett.*, 412(1-3):210–216, 2005.
- [334] M. Elstner. *Theor. Chem. Acc.*, 116(1):316–325, 2006.
- [335] H.A. Witek, K. Morokuma, and A. Stradomska. *J. Theo. Comp. Chem.*, 4:639–655, 2005.
- [336] Steve Kaminski, Michael Gaus, Prasad Phatak, David von Stetten, Marcus Elstner, and Maria Andrea Mroginiski. *J. Chem. Theo. Comp.*, 6(4):1240–1255, 2010.
- [337] V. Buch. *J. Chem. Phys.*, 100:7610–7629, 1994.
- [338] S.J. Goodbody, K. Watanabe, D. MacGowan, J.P.R.B. Walton, and N. Quirke. *J. Chem. Soc., Faraday Trans*, 87:1951, 1991.
- [339] J.G. Harris and K.H. Yung. *J. Phys. Chem.*, 99:12021, 1995.
- [340] W.L. Jorgensen, D.S. Maxwell, and J. Tirado-Rives. *J. Am. Chem. Soc.*, 118:11225, 1996.
- [341] Min Zhou, Qi Wang, Li Zhang, Ying-Chun Liu, and Yu Kang. *J. Phys. Chem. B*, 113:11049, 2009.
- [342] Dahuan Liu, Chengcheng Zheng, Qingyuan Yang, and Chongli Zhong. *J. Phys. Chem. C*, 113:5004, 2009.
- [343] Rees B. Rankin, Jinchun Liu, Anant D. Kulkarni, and J. Karl Johnson. *J. Phys. Chem. C*, 113:16906, 2009.
- [344] Rahul Banerjee, Anh Phan, Bo Wang, Carolyn Knobler, Hiroyasu Furukawa, Michael O’Keeffe, and Omar M. Yaghi. *Science*, 319(5865):939–943, 2008.
- [345] J. Pérez-Pellitero, H. Amrouche, F.R. Siperstein, G. Pirngruber, C. Nieto-Draghi, G. Chaplais, A. Simon-Masseron, D. Bazer-Bachi, D. Peralta, and N. Bats. *Chem. Eur. J.*, 16(5):1560–1571, 2010.
- [346] S.R. Venna and M.A. Carreon. *J. Am. Chem. Soc.*, 132(1):76–78, 2010.

- [347] Wei Zhou, Hui Wu, Michael R. Hartman, and Taner Yildirim. *J. Phys. Chem. C*, 111:16131, 2007.
- [348] J. O. Hirschfelder, C. F. Curtiss, and R. B. Bird. *Molecular Theory of Gases and Liquids*. John Wiley & Sons, New York, 1954.
- [349] E.A. Guggenheim. *Thermodynamics. An advanced treatment for chemists and physicists.*, chapter 4. North Holland, 1985.
- [350] D.S. Sholl. *Acc. Chem. Res*, 39(6):403–411, 2006.
- [351] Jinchen Liu and J. Karl Johnson. *J. Low. Temp. Phys.*, 157:268, 2009.
- [352] R. Babarao and J. Jiang. *Langmuir*, 24(12):6270–6278, 2008.
- [353] Andrew Sirjoosingh, Saman Alavi, and Tom K. Woo. *J. Phys. Chem. C*, 114:2171, 2010.
- [354] T. Düren, L. Sarkisov, O.M. Yaghi, and R.Q. Snurr. *Langmuir*, 20(7):2683–2689, 2004.
- [355] H. Frost, T. Düren, and R.Q. Snurr. *J. Phys. Chem. B*, 110(19):9565–9570, 2006.
- [356] Q. Yang and C. Zhong. *J. Phys. Chem. B*, 110(36):17776–17783, 2006.
- [357] S. Keskin and D.S. Sholl. *J. Phys. Chem. C*, 111:14055, 2007.
- [358] Y.S. Bae, K.L. Mulfort, H. Frost, P. Ryan, S. Punnathanam, L.J. Broadbelt, J.T. Hupp, and R.Q. Snurr. *Langmuir*, 24(16):8592–8598, 2008.
- [359] R. Babarao, J. Jiang, and S.I. Sandler. *Langmuir*, 25(9):5239–5247, 2009.
- [360] D. Keffer, H.T. Davis, and A.V. McCormick. *J. Phys. Chem.*, 100(2):638–645, 1996.
- [361] B. Hess, C. Kutzner, D. van der Spoel, and E. Lindahl. *J. Chem. Theory Comput.*, 4(3):435–447, 2008.
- [362] Bei Liu and Berend Smit. *J. Phys. Chem. C*, 114(18):8515–8522, 2010.
- [363] B. Lukose, B. Supronowicz, P.S. Petkov, J. Frenzel, A.B. Kuc, G. Seifert, G.N. Vayssilov, and T. Heine. *Phys. Stat. Sol. (b)*, 2011.
- [364] B. Assfour and G. Seifert. *Chem. Phys. Lett.*, 489(1-3):86–91, 2010.
- [365] W. Zhou, H. Wu, and T. Yildirim. *Chem. Phys. Lett.*, 499(1):103–107, 2010.
- [366] B. Assfour, S. Leoni, and G. Seifert. *J. Phys. Chem. C*, 114:13381–13384, 2010.
- [367] C. Gücüyener, J. van den Bergh, J. Gascon, and F. Kapteijn. *J. Am. Chem. Soc.*, 132(50):17704–17706, 2010.
- [368] Y. Li, F. Liang, H. Bux, W. Yang, and J. Caro. *J. Memb. Sci.*, 354(1):48–54, 2010.

- [369] Y.S. Li, F.Y. Liang, H. Bux, A. Feldhoff, W.S. Yang, and J. Caro. *Angew. Chem.*, 122(3):558–561, 2010.
- [370] Zhongqiao Hu and Yifei Chen. *Mol. Sim.*, 2012.
- [371] H. Bux, C. Chmelik, R. Krishna, and J. Caro. *J. of Memb. Sci.*, 369(1-2):284–289, 2010.
- [372] MT Luebbers, T. Wu, L. Shen, and RI Masel. *Langmuir*, 26(19):15625, 2010.
- [373] M.J.C. Ordoñez, K.J. Balkus Jr, J.P. Ferraris, and I.H. Musselman. *J. of Memb. Sci.*, 361(1-2):28–37, 2010.
- [374] N.M. O’Boyle, M. Banck, C.A. James, C. Morley, T. Vandermeersch, and G.R. Hutchison. Open Babel: An open chemical toolbox. *J. Cheminf.*, 3:33, 2011.
- [375] Daylight Theory, SMARTS. <http://www.daylight.com/dayhtml/doc/theory/theory.smarts.html>.
- [376] B. Hess, C. Kutzner, D. van der Spoel, and E. Lindahl. *J. Chem. Theo. Comput.*, 4(3):435–447, 2008.
- [377] BL Huang, AJH McGaughey, and M. Kaviani. *Int. J. Heat Mass Trans.*, 50(3-4):393–404, 2007.
- [378] H. Jónsson, G. Mills, and K.W. Jacobsen. Nudged elastic band method for finding minimum energy paths of transitions. In *Classical and Quantum Dynamics in Condensed Phase Simulations*, volume 1, pages 385–404, 1998.
- [379] G. Henkelman and H. Jónsson. *J. Chem. Phys.*, 113:9978, 2000.
- [380] D. Sheppard, R. Terrell, and G. Henkelman. *J. Chem. Phys.*, 128:134106, 2008.
- [381] S. a Beccara, G. Garberoglio, P. Faccioli, and F. Pederiva. *J. Chem. Phys.*, 132:111102, 2010. preprint: arXiv:0909.5381.
- [382] S. a Beccara, P. Faccioli, M. Sega, F. Pederiva, G. Garberoglio, and H. Orland. *J. Chem. Phys.*, 134:024501, 2011.
- [383] E. Haldoupis, S. Nair, and D.S. Sholl. *J. Am. Chem. Soc.*, 132(21):7528–7539, 2010.
- [384] S.V. Penumathsa and N. Maulik. *Can. J. Physiol. Pharmacol.*, 87:275, 2009.
- [385] S.J. Park, F.Ahmad andA. Philp andK. Baar andT. Williams andH. Luo, and H.Ke andH. Rehmann and R. Taussig andA.L. Brown andM.K. Kim andM.A. Beaven and A.B. Burgin andV. Manganiello andJ.H. Chung. *Cell*, 148:421, 2012.
- [386] Y. Hu, J. Wang, and Q. Liu. *Free Radic. Biol. Medicine*, 51:250, 2011.
- [387] S. Quideau, D. Deffieux, C. Douat-Casassus, and L. Pouységu. *Angew. Chem. Int. Ed.*, 50:586, 2011.
- [388] Y.J. Shang, Y.P. Qian, X.D. Liu, F. Dai, X.L. Shang, W.Q. Jia, Q. Liu, J.G. Fang, and B. Zhou. *J. Org. Chem.*, 74:5025, 2009.

- [389] V. Tamboli, A. Defant, I. Mancini, and P. Tosi. *Rapid Commun. Mass Spectrom.*, 25:526, 2011.
- [390] J. Oomens, B. G. Sartakov, G. Meijer, and G. von Helden. *Int. J. Mass Spectrom.*, 254:1, 2006.
- [391] T. D. Fridgen. *Mass Spectrom. Rev.*, 28:586, 2009.
- [392] J. Roithova. *Chem. Soc. Rev.*, 41:547, 2011.
- [393] M. A. Duncan. *Int. J. Mass Spectrom.*, 272:99, 2008.
- [394] L. MacAleese and P. Maitre. *Mass Spectrom. Rev.*, 26:583, 2007.
- [395] L. Mac Aleese, S. Aude, T. B. McMahon, J. M. Ortega, D. Scuderi, J. Lemaire, and P. Maître. *Int. J. Mass Spectrom.*, 249/250:14, 2006.
- [396] R. K. Sinha, P. Maître, S. Piccirillo, B. Chiavarino, and M. E. Crestoni and S. Fornarini. *Phys. Chem. Chem. Phys.*, 12:9794, 2010.
- [397] M. J. Frisch, G. W. Trucks, H. B. Schlegel, G. E. Scuseria, M. A. Robb, J. R. Cheeseman, J. A. Montgomery, Jr., T. Vreven, K. N. Kudin, J. C. Burant, J. M. Millam, S. S. Iyengar, J. Tomasi, V. Barone, B. Mennucci, M. Cossi, G. Scalmani, N. Rega, G. A. Petersson, H. Nakatsuji, M. Hada, M. Ehara, K. Toyota, R. Fukuda, J. Hasegawa, M. Ishida, T. Nakajima, Y. Honda, O. Kitao, H. Nakai, M. Klene, X. Li, J. E. Knox, H. P. Hratchian, J. B. Cross, V. Bakken, C. Adamo, J. Jaramillo, R. Gomperts, R. E. Stratmann, O. Yazyev, A. J. Austin, R. Cammi, C. Pomelli, J. W. Ochterski, P. Y. Ayala, K. Morokuma, G. A. Voth, P. Salvador, J. J. Dannenberg, V. G. Zakrzewski, S. Dapprich, A. D. Daniels, M. C. Strain, O. Farkas, D. K. Malick, A. D. Rabuck, K. Raghavachari, J. B. Foresman, J. V. Ortiz, Q. Cui, A. G. Baboul, S. Clifford, J. Cioslowski, B. B. Stefanov, G. Liu, A. Liashenko, P. Piskorz, I. Komaromi, R. L. Martin, D. J. Fox, T. Keith, M. A. Al-Laham, C. Y. Peng, A. Nanayakkara, M. Challacombe, P. M. W. Gill, B. Johnson, W. Chen, M. W. Wong, C. Gonzalez, and J. A. Pople. Gaussian 03, Revision C.02. Gaussian, Inc., Wallingford, CT, 2004.
- [398] M. W. Schmidt, K. K. Baldridge, J. A. Boatz, S. T. Elbert, M. S. Gordon, J. H. Jensen, S. Koseki, N. Matsunaga, K. A. Nguyen, S. Su, T. L. Windus, M. Dupuis, and J. A. Montgomery. *J. Comput. Chem.*, 13:1347, 1993.
- [399] S. Tosoni, C. Tuma, J. Sauer, B. Civalleri, and P. Ugliengo. *J. Chem. Phys.*, 127:154102, 2007.
- [400] J.P. Perdew, J.A. Chevary, S.H. Vosko, K.A. Jackson, M.R. Pederson, D.J. Singh, and C. Fiolhais. *Phys. Rev. B*, 46:6671, 1992.
- [401] J. Hafner D. Karhánek, T. Buûko. *J. Phys.: Condens. Matter*, 22:265006, 2010.
- [402] J. Paier, M. Marsman, and G. Kresse. *J. Chem. Phys.*, 127:024103, 2007.
- [403] F. Tran, R. Laskowski, P. Blaha, and K. Schwartz. *Phys. Rev. B*, 75:115131, 2007.

- [404] P. Milko, J. Roithova, D. Schröder, J. Lemaire, H. Schwarz, and M. C. Holthausen. *Chem. Eur. J.*, 14:4318, 2008.
- [405] D. M. Goldberg, J. Yan, E. Ng, E. P. Diamandis, A. Karumanchiri, G. Soleas, and A. L. Waterhouse. *Anal. Chem.*, 66:3959, 1994.
- [406] F. Billes, I. Mohammed-Ziegler, H. Mikosch, and E. Tyihak. *Spectrochim. Acta A: Molecular and biomolecular spectroscopy*, 68:669, 2007.
- [407] G. Henkelman, A. Arnaldsson, and H. Jonsson. *Comput. Mater. Sci.*, 36:254, 2006.
- [408] E. Sanville, S. D. Kenny, R. Smith, and G. Henkelman. *J. Comp. Chem.*, 28:899, 2007.
- [409] W. Tang, E. Sanville, and G. Henkelman. *J. Phys.: Condens. Matter*, 21:084204, 2009.
- [410] A. Messiah. *Quantum Mechanics*. Courier Dover Publications, 1999.
- [411] P. Giannozzi and S. Baroni. *J. Chem. Phys.*, 100:8537, 1994.
- [412] M.H. Anderson, J.R. Ensher, M.R. Matthews, C.E. Wieman, and E.A. Cornell. *Science*, 269(5221):198, 1995.
- [413] K.B. Davis, M.O. Mewes, M.R. Andrews, N.J. Van Druten, D.S. Durfee, D.M. Kurn, and W. Ketterle. *Phys. Rev. Lett.*, 75(22):3969, 1995.
- [414] L.P. Pitaevskii and S. Stringari. *Bose-Einstein Condensation*, volume 116. Oxford University Press, USA, 2003.
- [415] C. Pethick and H. Smith. *Bose-Einstein condensation in dilute gases*. Cambridge University Press, 2002.
- [416] F. Dalfovo, S. Giorgini, L.P. Pitaevskii, and S. Stringari. *Rev. Mod. Phys.*, 71(3):463, 1999.
- [417] A.J. Leggett. *Rev. Mod. Phys.*, 73(2):307, 2001.
- [418] K.M. O'Hara, S.L. Hemmer, S.R. Granade, M.E. Gehm, J.E. Thomas, V. Venturi, E. Tiesinga, and C.J. Williams. *Phys. Rev. A*, 66(4):041401, Oct 2002.
- [419] M. Bartenstein, A. Altmeyer, S. Riedl, R. Geursen, S. Jochim, C. Chin, J. Hecker Denschlag, R. Grimm, A. Simoni, E. Tiesinga, C.J. Williams, and P.S. Julienne. *Phys. Rev. Lett.*, 94(10):103201, Mar 2005.
- [420] K. Huang. *Statistical mechanics*. John Wiley & Sons, 1963.
- [421] G. Bruun, Y. Castin, R. Dum, and K. Burnett. *Eur. Phys. J. D*, 7:433, 1999.
- [422] S. De Palo, M.L. Chiofalo, M.J. Holland, and S.J.J.M.F. Kokkelmans. *Phys. Lett. A*, 327(5-6):490, 2004.
- [423] L.M. Jensen. *Arxiv preprint cond-mat/0412431*, 2004.

- [424] M. Bartenstein and *et al.* *Phys. Rev. Lett.*, 94(10):103201, 2005.
- [425] L.P. Gorkov. *Soviet Phys. JETP*, 7:505, 1958.
- [426] A.J. Leggett. *Quantum Liquids. Bose condensation and Cooper pairing in condensed-matter systems*. Oxford University Press, 2008.
- [427] P.-G. de Gennes. *Superconductivity of metals and alloys*. Advanced Book Program, Perseus Books, 1999.
- [428] Randeria M. *Bose–Einstein Condensation*. Cambridge University Press, 1996.
- [429] S. Taioli S. Simonucci, G. Garberoglio. *AIP Conf. Proc.*, 1485:312, 2012.
- [430] S. Simonucci, G. Garberoglio, and S. Taioli. *Phys. Rev. A*, 84:043639, 2011.
- [431] C. Amiot. *J. Mol. Spect.*, 147(2):370–382, 1991.
- [432] R. Rydberg. *Ann. Phys.*, 73:376, 1931.
- [433] O. Klein. *Z. Physik*, 76:226, 1932.
- [434] A. L. G.. Rees. *Proc. Phys. Soc. London*, A59:998, 1947.
- [435] M. Marinescu, HR Sadeghpour, and A. Dalgarno. *Phys. Rev. A*, 49(2):982, 1994.
- [436] J.L. Bohn, J.P. Burke Jr, C.H. Greene, H. Wang, PL Gould, and WC Stwalley. *Phys. Rev. A*, 59(5):3660, 1999.
- [437] E. Anderson, Z. Bai, C. Bischof, S. Blackford, J. Demmel, J. Dongarra, J. Du Croz, A. Greenbaum, S. Hammarling, A. McKenney, and D. Sorensen. *LAPACK Users’ Guide*. Society for Industrial and Applied Mathematics, Philadelphia, PA, third edition, 1999.
- [438] S. Jochim, M. Bartenstein, G. Hendl, J. Hecker Denschlag, R. Grimm, A. Mosk, and M. Weidemüller. *Phys. Rev. Lett.*, 89:273202, 2002.
- [439] S. Taioli, S. Simonucci, L. Calliari, and M. Dapor. *Phys. Rep.*, 493:237, 2010.
- [440] A. Perali, P. Pieri, and G.C. Strinati. *Phys. Rev. A*, 68(3):031601, Sep 2003.
- [441] M. Holland, S.J.J.M.F. Kokkelmans, M.L. Chiofalo, and R. Walser. *Phys. Rev. Lett.*, 87(12):120406, Aug 2001.
- [442] J. Carlson and Sanjay Reddy. *Phys. Rev. Lett.*, 100(15):150403, Apr 2008.
- [443] J. Carlson, S.-Y. Chang, V.R. Pandharipande, and K.E. Schmidt. *Phys. Rev. Lett.*, 91(5):050401, Jul 2003.
- [444] G.E. Astrakharchik, J. Boronat, J. Casulleras, and S. Giorgini. *Phys. Rev. Lett.*, 93(20):200404, Nov 2004.
- [445] E. Burovski, N. Prokof’ev, B. Svistunov, and M. Troyer. *Phys. Rev. Lett.*, 96(16):160402, Apr 2006.

- [446] M. W. Zwierlein, J. R. Abo-Shaeer, A. Schirotzek, C. H. Schunck, and W. Ketterle. *Nature*, 435:1047, 2005.
- [447] BD Esry, H. Suno, and C.H. Greene. Ultracold three-body recombination of fermionic atoms. In *The Expanding Frontier of Atomic Physics*, volume 1, pages 122–129, 2003.
- [448] A. Coc and E. Vangioni. *J Phys. Conf. Ser.*, 202:012001, 2010.
- [449] P. Bonifacio, L. Sbordone, and E. Caffau et al. . *A&A*, 542:87, 2012.
- [450] F. Spite and M. Spite. *A&A*, 115:357, 1982.
- [451] E. Casuso and J.E. Beckmann. *PASJ*, 55:247, 2003.
- [452] B.D. Fields, K.A. Olive, and D.N. Schramm. *ApJ*, 435:185, 1994.
- [453] A. Alibés, J. Labay, and R. Canal. *ApJ*, 571:326, 2002.
- [454] A. M. Boesgaard. *Cosmic Abundances as Records of Stellar Evolution and Nucleosynthesis*, volume 39. ed. T. G. Barnes, III & F. N. Bash (San Francisco, CA:ASPC), 2005.
- [455] F. D’Antona and P. Ventura. *Light elements in the Universe*, volume 268. IAU Symposium, ed. C. Charbonnel et al., 2010.
- [456] M. Pinsonneault. *ARA&A*, 35:557, 1997.
- [457] P. Sestito, S. Degl’Innocenti, P.G. Prada Moroni, and S. Randich. *A&A*, 454:311, 2006.
- [458] M. Asplund, N. Grevesse, J. Sauval, and P. Scott. *ARA&A*, 47:481, 2009.
- [459] A.M. Boesgaard and M.J. Tripicco. *ApJ*, 303:724, 1986.
- [460] S. Balachandran. *1995*, 446:203, ApJ.
- [461] A.M. Boesgaard, C.P. Deliyannis A. Stephens, and D.L. Lambert. *ApJ*, 492:727, 1998.
- [462] G. Michaud. *ApJ*, 302:650, 1986.
- [463] G. Michaud and P. Charbonneau. *Space Sci. Rev.*, 57:1, 1991.
- [464] C. Charbonnel and N. Lagarde. *A&A*, 522:10, 2010.
- [465] P. Eggenberger, G. Meyne, A. Maeder, and *et al.* *A&A*, 519:116, 2010.
- [466] A.D. Andrews, M. Rodonò, and J.L. Linsky. *A&A*, 204:177, 1988.
- [467] S. Palmerini, M. La Cognata, S. Cristallo, and M. Busso. *ApJ*, 729:3, 2011.
- [468] E. Maiorca, L. Magrini, M. Busso, S. Palmerini, and O. Trippella. *ApJ*, 747:53, 2012.
- [469] M. Busso, G.J. Wasserburg, K.M. Nollett, and A. Calandra. *ApJ*, 671:802, 2007.

- [470] J. Nordhaus, M. Busso, G.J. Wasserburg, E.G. Blackman, and S. Palmerini. *ApJ*, 684:29, 2008.
- [471] P.A. Denissenkov, M. Pinsonneault, and K.B. MacGregor. *ApJ*, 696:1823, 2009.
- [472] S. Palmerini, S. Cristallo, M. Busso, and *et al.* *ApJ*, 741:26, 2011.
- [473] J. A. Brown. *ApJ*, 317:701, 1987.
- [474] C. Charbonnel and S. Balachandran. *A&A*, 359:562, 2000.
- [475] B.Y. Kumar, B.E. Reddy, and D.L. Lambert. *ApJL*, 730:L12, 2011.
- [476] S. Uttenthaler and T. Lebzelter. *A&A*, 510:62, 2010.
- [477] T. Lebzelter, S. Uttenthaler, M. Busso, M. Schultheis, and B. Aringer. *A&A*, 538:L36, 2012.
- [478] J. N. Bahcall. *Phys. Rev.*, 126:1143, 1962.
- [479] I.Jr. Iben, K. Kalata, and J. Schwartz. *ApJ*, 150:1001, 1967.
- [480] J.N. Bahcall and C.P. Moeller. *ApJ*, 155:511, 1969.
- [481] P. Debye and E. Hückel. *Phys. Z.*, 24:185, 1923.
- [482] J.N. Bahcall and A.V. Gruzinov. *ApJ*, 490:437, 1997.
- [483] L.S. Brown and R.F. Sawyer. *ApJ*, 489:968, 1997.
- [484] R.F. Sawyer. *Phys. Rev. C*, 83:065804, 2011.
- [485] C.W. Johnson, E. Kolbe, S.E. Koonin, and K. Langanke. *ApJ*, 392:320, 1992.
- [486] M. Busso, R. Gallino, and G.J. Wasserburg. *PASA*, 20:356, 2003.
- [487] M. Busso. *Astronomy with Radioactivities*, volume 812. ed. R. Diehl, D. H. Hartmann, & N. Prantzos, LNP, Berlin: Springer, 2011.
- [488] H.N. Pollack, S.J. Hurter, and J.R. Johnson. *Rev. Geophys.*, 31:267, 1993.
- [489] C. M. R. Fowler. *The Solid Earth: an Introduction to Global Geophysics*. Cambridge: Cambridge University Press, 2005.
- [490] K.K.M. Lee and G. Steinle-Neumann. *Earth Plan. Sci. Lett.*, 267:628, 2008.
- [491] G. T. Emery. *Ann. Rev. Nucl. Sci.*, 22:165, 1972.
- [492] H.P. Hahn, H.J. Born, and J.I. Kim. *Radiochim. Acta*, 23:23, 1976.
- [493] A. Ray, P. Das, and S.K. Saha. *Phys. Lett. B*, 531:187, 2002.
- [494] T. Ohtsuki, K. Ohno, T. Morisato, T. Mitsugashira, K. Hirose, H. Yuki, and J. Kasagi. *Phys. Rev. Lett.*, 98:252501, 2007.

- [495] T. Morisato, K. Ohno, T. Ohtsuki, K. Hirose, M. Sluiter, and Y. Kawazoe. *Phys. Rev. B*, 78:125416, 2008.
- [496] E.G. Adelberger, A. Garca, and R.G.H. Robertson. *Rev. Mod. Phys.*, 83:195, 2011.
- [497] N. J. Shaviv and G. Shaviv. *MNRAS*, 341:119, 2001.
- [498] P. Quarati and A.M. Scarfone. *J. Phys. G*, 36:025203, 2009.
- [499] W.A. Fowler G.R. Caughlan and B.A. Zimmerman. *ARA&A*, 13:69, 1975.
- [500] G.J. Mathews, R.C. Haight, R.G. Lanier, and R.M. White. *Phys. Rev. C*, 28:879, 1983.
- [501] G.M. Fuller and C.J. Smith. *Phys. Rev. D*, 82:125017, 2010.
- [502] S. Taioli, S. Simonucci, and M. Dapor. *Comput. Sci. Disc.*, 2:015002, 2009.
- [503] S. Taioli, S. Simonucci, L. Calliari, M. Filippi, and M. Dapor. *Phys. Rev. B*, 79:085432, 2009.
- [504] C. Abia, S. Palmerini, M. Busso, and S. Cristallo. *A&A*, 548:55, 2012.
- [505] D.L. Lambert, K.H. Hinkle, and V.V. Smith. *AJ*, 99:1612, 1990.
- [506] C. Abia and J. Isern. *ApJ*, 536:438, 2000.
- [507] R. D. McClure. *PASP*, 109:256, 1997.
- [508] L. Pauling. *PNAS*, 88:9208, 1991.
- [509] P.W. Stephens and *et al.* *Nature*, 351:632, 1991.
- [510] R. Mitsuhashi, Y. Suzuki, Y. Yamanari, H. Mitamura, T. Kambe, N. Ikeda, H. Okamoto, A. Fujiwara, M. Yamaji, N. Kawasaki, Y. Maniwa, and Y. Kubozono. *Nature*, 464:76, 2010.
- [511] M. Casula, M. Calandra, G. Profeta, and F. Mauri. *Phys. Rev. Lett.*, 107:137006, 2011.
- [512] O. Gunnarsson. *Rev. Mod. Phys.*, 69:575, 1997.
- [513] H. Alloul. *EPJ Web of Conferences*, 23:00015, 2012.
- [514] W. Andreoni, P. Giannozzi, and M. Parrinello. *Phys. Rev. B*, 51:2087, 1995.
- [515] V. P. Antropov, O. Gunnarsson, and A. I. Liechtenstein. *Phys. Rev. B*, 48:7651, 1993.
- [516] M. Capone, M. Fabrizio, C. Castellani, and E. Tosatti. *Rev. Mod. Phys.*, 81:943, 2009.
- [517] M. Calandra, G. Profeta, and F. Mauri. *Phys. Rev. B*, 82:165111, 2010.
- [518] A. A. Mosto, J. R. Yates, Y.-S. Lee, I. Souza, D. Vanderbilt, and N. Marzari. *Comput. Phys. Commun.*, 178:685, 2008.
- [519] F. Gompf, B. Renker, H. Schober, P. Adelman, and R. Heid. *J. Super.*, 7:643, 1994.